Acoustic emission from domain wall motion in ferroelectric crystals.

Mangion, Louis J. Zammit

Award date:
1982

Awarding institution:
University of Bath

ACOUSTIC EMISSION FROM DOMAIN WALL MOTION IN FERROELECTRIC CRYSTALS

Submitted by
Louis J. Zammit Mangion
for the Degree of
Doctor of Philosophy
of the University of Bath
1982

L. Zammit Mang...

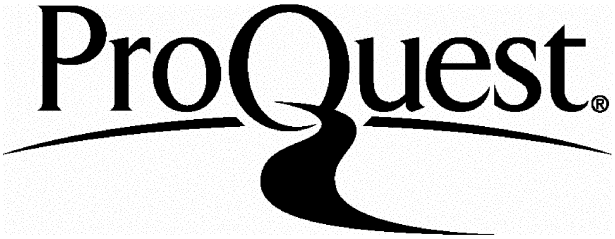

ABSTRACT

The emission of bursts of ultrasound accompanying polarisation reversal has been observed in a number of ferroelectric materials, including lead germanate, Rochelle salt, gadolinium molybdate and terbium molybdate. This acoustic emission (AE) occurs predominantly near the regions of saturation polarisation at the extremities of the hysteresis loop, and has been investigated as a function of sample size and temperature and of the magnitude and frequency of the electric field applied to cause the switching. These measurements indicate that the AE is closely connected with the process of polarisation reversal and therefore with the motion of domain walls within the crystal. In all the materials studied, a threshold electric field has been found below which no AE is produced, even though the hysteresis loop is still saturated and switching still occurs. This threshold field increases steeply as the Curie temperature of the material is approached, a finding which is attributed to a higher voltage being required to induce the AE-generating process as the domain walls become more mobile. Measurements of the crystal polarisation reveal a one-to-one correspondence between this acoustic noise and the electrical Barkhausen pulses also associated with polarisation reversal in ferroelectrics, which indicates that domain nucleation and collapse may be the source of AE. Simultaneous monitoring of the AE and visual observation of the domains in gadolinium molybdate and lead germanate confirm that these particular processes are indeed responsible for the AE produced by ferroelectric crystals.

ACKNOWLEDGEMENTS

My sincere gratitude goes to my supervisor, Professor G.A. Saunders, whose valued advice and sustained enthusiasm have been a constant source of inspiration and encouragement.

My thanks are also extended to the technical staff of the School of Physics, particularly Mr. E.F Lambson, Mrs. W.A. Lambson and Mr. R.C.J. Draper, for their invaluable assistence with the experimental work and in the preparation of this thesis.

I am deeply grateful to my colleagues of the Solid State Physics research group, with whom I had many useful discussions and who helped to make my term as a research student such a happy one.

I would like to thank Dr. G.R. Jones and Dr. E.H. Putley of R.S.R.E. Malvern for their help and support, and particularly for providing the ferroelectric crystals used in this work. The financial support of the Association of Commonwealth Universities is also gratefully acknowledged.

Finally, I warmly acknowledge the constant support of my wife Patricia, whose encouragement and patience cannot go unmentioned.

CONTENTS

CHAPTER 1 - GENERAL INTRODUCTION

Acoustic emission (AE) is the name given to stress waves internally generated during dynamic processes within materials. The dynamic processes may be the result of an externally applied stress or of some other unstable condition within the material. The source of the stress waves depends on the nature of the substance, some examples being dislocation motion and crack growth in metals, fibre cracking in wood and cavitation and boiling in liquids. In its less conventional forms, the AE can be so loud as to be audible to the unaided ear: the creaking of timber structures loaded to the point of failure being one example of this. The seismic waves generated by the failure of rock under stress may also be considered under the heading of acoustic emission. The development of sensitive electronic equipment capable of detecting the extremely low level, ultrasonic pressure waves that are generated by most materials when under stress has spurred the application of AE to the non-destructive testing of materials and structures. It is a particularly useful technique because it has the capability of detecting active flaws which may ultimately lead to failure, well before the failure actually occurs. In fact, the vast majority of publications on acoustic emission deal with the engineering applications of this technique.

Acoustic emission from a ferroelectric material was first reported by Buchman (1972), who observed AE during the ferroelectric phase transition in barium titanate. He also noted that AE was produced when the polarisation in the ferroelectric sample was reversed by the application of an electric field. Acoustic emission from ferroelectric crystals formed the subject of a PhD thesis by Mohamad (1980), of which the present work is a continuation. The properties of ferroelectric materials are discussed in Chapter 2. The remainder of this chapter is devoted to a review of acoustic emission and its many applications.

1.1 Acoustic Emission and its Applications.

Historically, the first use of acoustic emission probably occurred in seismology when the elastic waves produced by an earthquake were analysed to characterise fault movement in terms of the energy released, slip distance, location and depth. Research into the possibility of using microseisms to predict rock bursts in coal mines started as long ago as the late 1930's (Obert 1941). It is proper to point out that these early attempts, crude though they may be by modern standards, laid the ground for future developments. Obert and Duvall (1945) attempted to identify the source of the microseisms by stressing rocks under controlled conditions in the laboratory. Triangulation (using multiple geophones) was also attempted by Obert in order to locate the sources of the microseisms.

Kaiser (1950) is generally credited with the first serious work in the field of acoustic emission. He was the first to use electronic instrumentation to detect stress waves from metals such as zinc, steel, aluminium, copper and lead during deformation. He also observed that AE activity is irreversible, noting that during the reloading of a material no AE is generated until the stress level exceeds the previous maximum. The Kaiser effect, as this phenomenon is known, applies to most metals and has proved to be very useful in AE studies. Several years after Kaiser's work, extensive improvements in instrumentation made possible many advances in AE technology (Schofield et al 1958, Dunegan et al 1964). In particular it was found that the AE from stressed metals is primarily due to dislocation motion accompanying plastic deformation (Tatro and Liptai 1962) and not entirely to grain boundary movement as proposed by Kaiser.

Most of the modern work on AE has concentrated on its

application to non-destructive testing (NDT). Several excellent publications exist, notably the two sets of conference proceedings published by the American Society for Testing and Materials (ASTM 1972, ASTM 1975) and a series of conference papers collected by Nichols (1976). A number of reviews have also been published, such as Lord (1975), Williams (1980) and Ying (1973) which concentrates more on the solid state physics aspects of the subject. Also well worth noting is a comprehensive bibliography compiled by Drouillard (1979), though in a rapidly expanding field this is already somewhat out of date.

Acoustic emission is particularly suited to monitoring structural integrity because the receiving transducer does not have to be close to the source of the emissions or to the area under test. For large structures, AE probes can be placed on the surface of the structure at intervals of up to 10m. When several transducers are used, it is possible to determine the location of the AE source by triangulation (Sinclair 1977). A large variety of structures have been investigated in this way, including nuclear and chemical reactor pressure vessels (Morais and Green 1975, Parry and Robinson 1970) and civil engineering structures such as bridges and buildings (Muenow 1971). Another useful feature of AE as a NDT tool is that it can be used for continuous, in-service monitoring of structural integrity (Holt and Palmer 1974, Gopal et al 1976). A particularly interesting application is the in-flight monitoring of fatigue cracks in aircraft (Hutton and Skerpik 1981).

Acoustic emission has been used to study deformation and failure processes in several materials, including metals (Kaiser 1950, Dunegan and Harris 1969), rocks (Hardy 1970), concrete (Nielsen 1977) and composite materials (Guild et al 1980). Flawed metal specimens have been used to investigate the AE produced by stress concentrations. These AE results have been analysed using fracture mechanics by Dunegan et al (1970), and provide basic data on the techniques used to monitor structural integrity. In fibre reinforced materials, AE provides a means

of identifying nondestructively the various failure modes of the material, such as fibre breakage, matrix cracking and debonding (Mehan and Mullen 1971). Human and animal bones have also been studied using AE, and a clinical method of detecting bone damage and abnormalities without surgery has been described by Yoon et al (1980).

Besides deformation and failure under stress, a number of other processes have been studied using acoustic emission. Perhaps the most important of these from a practical point of view is weld formation (Notvest 1966). It is now possible to monitor the welding process while the weld is being formed, which can offer considerable economic savings (Schwerk and Schearer 1973). The martensitic phase transformation has also been extensively investigated by this technique in a variety of metals and alloy systems. This phase transformation is a diffusionless, shear-type reaction that takes place through the cooperative movement of very many atoms. The transformation is very rapid, each plate or crystallite formed triggering the nucleation of other plates in adjoining regions. Materials investigated include gold-cadmium (Liptai et al 1969) and indium-thallium alloys (Beattie 1971).

Despite the large number of applications described above, acoustic emission as a technique has not lived up to the expectations placed upon it ten years ago. This is partly due to a lack of understanding of the fundamental processes of AE sources, acoustic wave propagation in complex structures and the response of transducers and amplifier systems. Although much work has been done on source characterisation (Schofield 1970, Curtis et al 1981) and transducer response (Sachse and Ceranoglu 1979), many points remain unclear. Brekenridge et al (1975) have modelled the response of an elastic half-space to a point force step, and more recently the response of infinite plates has been calculated (Pao et al 1979). However, while excellent agreement has been found between theoretical and measured results for simulated AE sources, real AE waveforms have proved to be much more intransigent (Hsu et al 1979). Another problem

is that of calibration, which is particularly difficult with piezoelectric transducers in the absence of an absolute standard. An idea of the seriousness of this problem may be gained from the fact that many national AE working groups have recently adopted a 'standard' AE source based on breaking pencil lead (Nielsen 1980). Despite these problems, AE provides an alternative means of investigating physical processes (such as deformation and phase transformations) which complements other, better known techniques, as well as being a powerful NDT tool in its own right.

1.2 Acoustic Emission from Ferroic Materials.

A limited number of publications on AE from ferroic materials have appeared in the literature. A ferroic material may be defined as one which contains two or more possible orientation states or domains: under a suitable driving force (mechanical stress, electric field, magnetic field or a combination of these) the domain walls move and switch the crystal from one state to the other (Aizu 1970). Spanner (1970) first pointed out that the magnetisation process in ferromagnetic materials might be a source of AE. Preliminary investigations by Lord (1975) have shown that this is so and have tentatively correlated the emissions with the well-known magnetic Barkhausen effect. This phenomenon is associated with small, discontinuous changes in the overall magnetisation of a ferromagnetic sample caused by the abrupt displacement of magnetic domain walls (Crangle 1977). Lord (1967) has shown that this sudden change should produce AE through magnetoelastic coupling.

Laughner et al (1979) have observed AE accompanying the formation and motion of Dauphiné twins in quartz under an applied mechanical stress. According to the notation of Aizu (1970), this second-order effect is termed ferrobielastic switching. In a simple but elegant experiment, Miller and

Saunders (1979) have observed AE from ferroelastic lead phosphate. The sample was mounted so that the domain structure could be observed through a polarising microscope while any AE produced could be monitored simultaneously. When the stress applied to the sample exceeded a threshold value, the domain walls were observed to move to the accompaniment of bursts of AE.

In the first reference to AE from ferroelectric crystals, Buchman (1972) reported the observation of AE during the ferroelectric phase transition in barium titanate and from ferroelectric material undergoing polarisation reversal under the influence of an applied electric field. AE from the ferroelectric phase transition has also been reported in triglycine sulphate (Lambson et al 1977) and Rochelle salt (Mohamad 1980). The ferroelectric phase transition is similar in many respects to the martensitic transformation which also produces copious AE.

The first detailed study of AE from ferroelectric crystals undergoing polarisation reversal was carried out by Mohamad (1980). The central finding of this work is the existence of a threshold electric field below which no AE is observed (Mohamad et al 1979). Mohamad attempted to correlate the behaviour of the AE with other ferroelectric phenomena such as the coercive field, the saturation polarisation and the switching time, and speculated that the AE may be related to the sideways motion of domain walls in the material. The objective of the present work is to consolidate and expand these preliminary investigations. After a description of the experimental apparatus and techniques in Chapter 3, the AE from ferroelectrics and how it depends on parameters such as sample size and temperature and the applied electric field are discussed in Chapter 4. These results indicate that the AE cannot be related successfully to bulk quantities such as the spontaneous polarisation and the switching time, but should be correlated with individual domain switching events. Chapter 5 describes the visual observation of domain wall dynamics in ferroelectric materials and how this relates to the AE produced.

CHAPTER 2 - FERROELECTRICITY

We now turn to a discussion of the fundamental properties of ferroelectric materials, with particular reference to domains and the switching process. The chapter concludes with a review of the properties of four particular ferroelectrics which are used in the experimental work described in the remainder of this thesis.

2.1 Basic Principles.

The phenomenon known as ferroelectricity was first observed in 1920 by Valasek who discovered that the polarisation of sodium potassium tartrate tetrahydrate (Rochelle salt) could be reversed by the application of an external electric field. Valasek (1920, 1921) recognised that the dielectric properties of this crystal were in many respects similar in nature to the magnetic properties of ferromagnetic materials such as iron: Rochelle salt exhibits a hysteresis effect in the polarisation-electric field curve, a Curie temperature above which the polar ordering vanishes and an extremely large dielectric and piezoelectric response in and around the ferroelectric region. The similarity of these effects to ferromagnetic phenomena led to the terminology of ferromagnetism being applied to ferroelectricity even though on an atomic scale the two are quite distinct - in fact the term 'ferroelectricity' came about through this analogy and does not imply that ferroelectric materials contain iron or exhibit anomalous magnetic properties.

Depending on their geometry, crystals are commonly classified into seven systems: these systems can again be subdivided into 32 crystal classes (or point groups) according to their symmetry

with respect to a point. These classes are detailed in Table 2.1. Of these 32 point groups, 11 possess a centre of symmetry (which maps a point (x,y,z) onto (-x,-y,-z)) and therefore cannot exhibit any polar properties. If an electric field is applied to such a centrosymmetric crystal, the resulting strain (electrostriction) is unchanged by the reversal of the electric field. Of the remaining 21 non-centric classes, all except one can exhibit the piezoelectric effect: the crystal becomes electrically polarised when subjected to stress, the direction of the polarisation reversing if the stimulus is reversed. Of the 20 piezoelectric crystal classes, 10 are characterised by having a unique polar axis: these are called the polar or pyroelectric crystal classes. These crystals possess a spontaneous polarisation or electric moment, which changes with temperature and gives rise to the pyroelectric effect.

A crystal is said to be ferroelectric when it has two or more orientational states in the absence of an electric field and can be changed from one state to the other by the application of an electric field, the orientation states being identical in crystal structure (or enantiomorphous) and differing only in the direction of the electric polarisation vector at zero electric field. The requirement that the crystal possesses an electric polarisation in the absence of an applied electric field (a spontaneous polarisation) means that the crystal must have a unique polar axis - a ferroelectric must belong to one of the pyroelectric crystal classes. The above definition of ferroelectricity is necessarily empirical because whether or not a material is classed as ferroelectric depends on whether the switching of the polarisation can be experimentally detected. Crystal perfection, electrical conductivity and the temperature and pressure all affect the reversibility of polarisation. It follows that the crystallography alone cannot determine the ferroelectric character of a material, though the possibility of switching usually implies a polar structure characterised by only small distortions from a non-ferroelectric phase with higher symmetry. This phase is termed the prototype phase, and is usually non-polar.

Crystal System	Symbol (International)	Centro-symmetric	Piezo-electric	Pyro-electric
Triclinic	1		X	X
	$\bar{1}$	X		
Tetragonal	4		X	X
	$\bar{4}$		X	
	4/m	X		
	422		X	
	4mm		X	X
	$\bar{4}$2m		X	
	4/mmm	X		
Hexagonal	6		X	X
	$\bar{6}$		X	
	6/m	X		
	622		X	
	6mm		X	X
	$\bar{6}$m2		X	
	6/mmm	X		
Monoclinic	2		X	X
	m		X	X
	2/m	X		
Orthorhombic	222		X	
	mm2		X	X
	mmm	X		
Trigonal	3		X	X
	$\bar{3}$	X		
	32		X	
	3m		X	X
	$\bar{3}$m	X		
Cubic	23		X	
	m3	X		
	432			
	$\bar{4}$3m		X	
	m3m	X		

TABLE 2.1 - The 32 crystallographic point groups. A cross (X) indicates that the point group is centrosymmetric, piezoelectric or pyroelectric, as the case may be.

In a typical ferroelectric, the spontaneous polarisation decreases with rising temperature as its structure becomes closer to that of the prototype, disappearing at the Curie temperature at which a phase change takes place. However, polar crystal classes do not always belong to systems of lower crystal symmetry than non-polar ones, and transitions from non-polar to polar phases as a function of increasing temperature are also known to occur. The ferroelectric phase change represents a special class of structural phase transitions characterised by the appearance of a spontaneous polarisation. In most cases, the non-ferroelectric (or paraelectric) phase is the same as the prototype, though this is not necessarily always so. As the transition temperature is approached from above, the differential dielectric response (or permittivity) of many ferroelectrics diverges in an approximately Curie-Weiss manner, according to:

$$\varepsilon = \frac{C}{(T - T_o)}$$

where the Curie-Weiss temperature T_o is only equal to the transition or Curie temperature T_c in the case of a continuous (or second-order) transition. Below the Curie temperature, the spontaneous polarisation can develop in at least two directions: to minimise the depolarising fields, different regions of the crystal polarise in each of these directions so that the net polarisation of the crystal is very small. Consequently ferroelectric crystals exhibit negligible pyroelectric effects until they are poled by the application of an electric field. The regions of uniform polarisation in the crystal are called domains: it is their presence which gives ferroelectrics their characteristic dielectric properties.

Most textbooks on solid state physics and electromagnetism mention ferroelectricity, at least in passing. Several excellent texts on ferroelectricity have also been published, notably the review of Lines and Glass (1977). Also worth noting

is the comprehensive bibliography compiled by Connolly et al (1970, 1974). Several earlier texts (eg Kanzig 1957, Jona and Shirane 1962, Fatuzzo and Merz 1967) contain extensive reviews of the early develepment of the field, but care must be taken with these references as some of the concepts outlined in them have since been outdated.

2.2 The Ferroelectric Phase Transition.

An understanding of the ferroelectric phase transition is an essential part of any theory of ferroelectricity, for it is at the phase transition that the material acquires its spontaneous polarisation. The first microscopic theories of ferroelectrics, now obsolete, were published by Kurchatov (1933) and Fowler (1935) for Rochelle salt - then the only known ferroelectric - and assumed the presence of rotatable electric dipoles, associated with the water of crystallisation in the lattice, which behave in a manner analogous to the Weiss theory of ferromagnetism. The phase transition in Rochelle salt is still poorly understood, as the structure of this material is extremely complex, having 112 atoms per unit cell. The discovery of simpler ferroelectrics, notably potassium dihydrogen phosphate (Busch and Scherrer 1935) and barium titanate (Wul and Goldman 1945) led to the first microscopic models of ferroelectricity which have, in their essentials, withstood the test of time (Slater 1941, 1950).

In 1960 Jona and Shirane reviewed most of the then known ferroelectrics with a detailed discussion of the basic crystal structures. This was before the introduction of the soft-mode theory, and separate theoretical discussions were included for each structure, with the unifying concepts appearing only at the macroscopic level. The advantage of the macroscopic approach is that the focus can be placed solely on thermodynamic concepts, overlooking the complexities of the atomic level. This approach

was first taken by Mueller (1940). It was later expanded by Ginzburg (1949) and Devonshire (1949, 1954) and has been discussed at some length by Fatuzzo and Merz (1967). The basic idea is to write a free energy as an expansion in powers of polarisation and strain, and assume that the same energy function is capable of describing both the polar and the non-polar phase. Normally the potential chosen is the elastic Gibbs function G_1 relative to the prototype phase, which is expressed as a function of temperature, stress and displacement from the equilibrium prototype state (this displacement being proportional to the polarisation). In the simplest case, for a centrosymmetric prototype, zero external stress and assuming that both the displacement D and the electric field are restricted to one of the crystallographic axes, this can be written as:

$$G_1 = \frac{\alpha}{2} D^2 + \frac{\gamma}{4} D^4 + \frac{\delta}{6} D^6 + \ldots$$

The coefficients are in general temperature dependent: the parameter α can be identified with the dielectric stiffness (or reciprocal permittivity) and is assumed to vary according to:

$$\alpha = \beta (T - T_o)$$

in order to account for the observed Curie-Weiss dependence of the dielectric constant. The coefficients γ and δ are assumed independent of temperature: δ is necessarily positive for stability at large D while the sign of γ has a bearing on the order of the phase transition. The values of the coefficients β, γ and δ can be obtained from a few experimental results, such as the dielectric constant as a function of a biasing electric field and the spontaneous polarisation close to the transition temperature (Fatuzzo and Merz 1967).

Some of the results of this theory are sketched out in Figure 2.1. Note that above the Curie temperature the free energy has only one minimum (at D=0) while below it there are two: these equilibrium displacements define the spontaneous polarisation

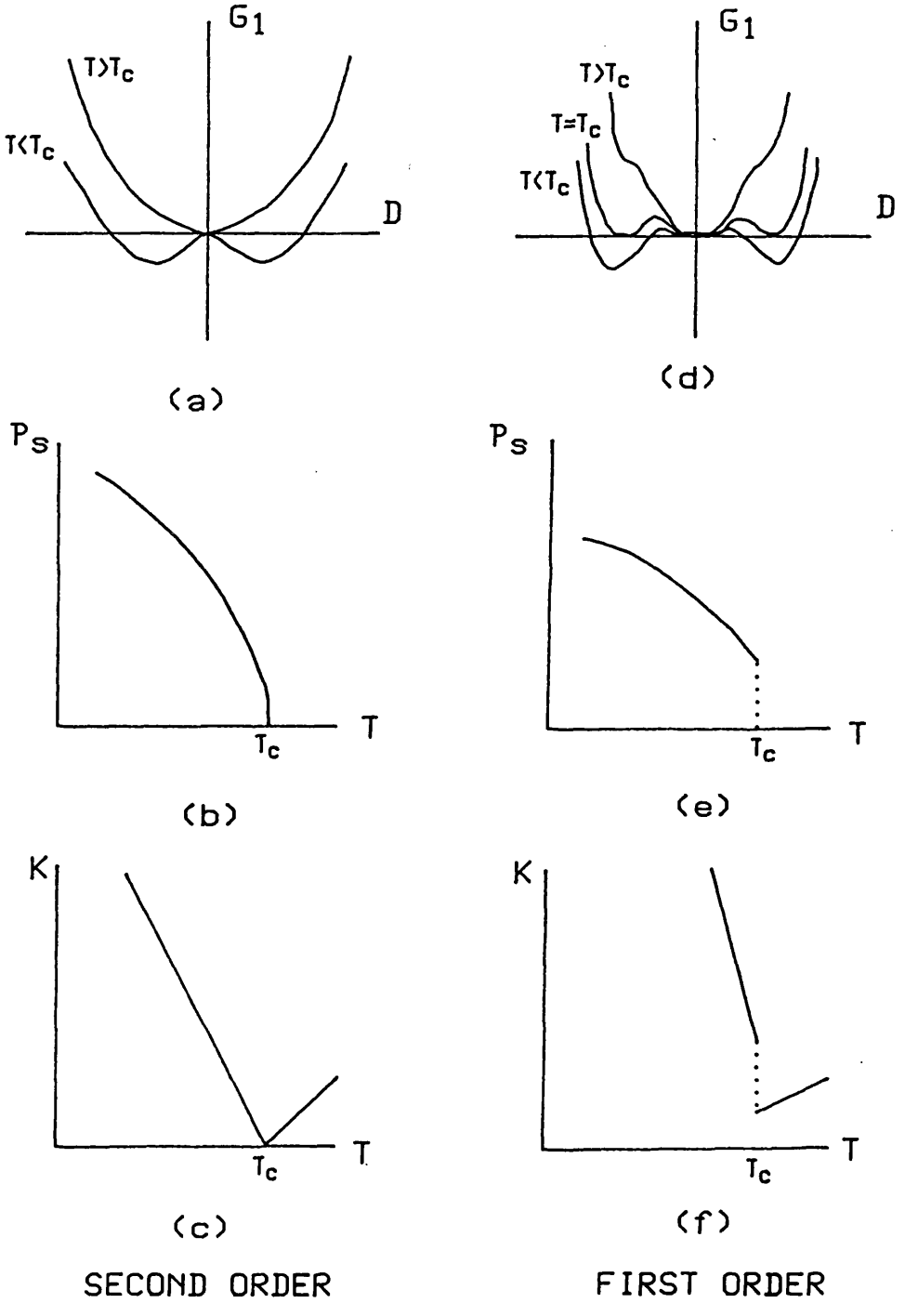

FIGURE 2.1 - Qualitative temperature dependence of the free energy/displacement curves, the spontaneous polarisation P_s and the dielectric stiffness K for first and second order phase transitions.

P_s. For positive γ, the saturation polarisation decreases continuously to zero at the Curie temperature. There is no latent heat associated with the phase transition, which is of second order. The theory gives the ratio of the slopes of the reciprocal permittivity below and above the Curie point (Figure 2.1c) as -2. The theory begins to break down for temperatures far from the transition: as a second-order phase transition requires a singularity in the thermodynamic potential, it should also break down in this case for temperatures very close to the transition (Lines and Glass 1977).

For negative γ, the free energy has three minima at the Curie point: this leads to the Curie-Weiss temperature T_θ being somewhat lower than the Curie temperature T_c. In this case the transition is first order: the saturation polarisation falls to zero discontinuously at the transition, and the ratio of the slopes of the reciprocal permittivity curves in Figure 2.1f should be -8. The shape of the free-energy curves in Figure 2.1d implies the existence of metastable states close to the transition temperature, which results in the transition occurring at a slightly higher temperature when approached from above than when it is approached from below (thermal hysteresis). It also implies that it should be possible to induce the ferroelectric phase above the Curie temperature by the application of a suitable electric field.

The modern era of theoretical understanding began with the realisation that the problem should be cast in terms of lattice dynamics and that the focus should be on a particular lattice mode (the soft mode), involving the motions of all the constituent atoms, which drives the structural instability (Anderson 1960, Cochran 1960). The ferroelectric transition can usually be associated with the condensation of a low-frequency (or soft) mode of lattice vibration at the Brillouin zone centre. The theory of soft modes and the ferroelectric phase transition has been extensively covered by Blinc and Zeks (1974) and reviewed by Lines and Glass (1977). When considering the microscopic details of the phase transition, a distinction is

sometimes made between displacive and order-disorder ferroelectrics. A displacive transition can be thought of as being due to the actual displacement of an atom (or group of atoms) from its equilibrium position in the prototype structure to create the polar phase, while the paraelectric phase of an order-disorder ferroelectric is only non-polar in a thermally averaged sense. While the soft-mode theory was initially developed for displacive systems, it was later extended to order-disorder transitions by considering lattice modes other than damped optic phonons.

Structural transitions triggered by zone-centre soft modes are generally termed ferrodistortive, so the ferroelectric transition can be defined as a ferrodistortive transition involving a polar or optically active mode whose condensation causes the appearance of long-range polar order. An antiferrodistortive transition can take place when the mode softening occurs at some point other than the Brillouin zone centre. Such a transition involving a polar mode leads to an antipolar phase, analogous to a pyroelectric which results from a soft zone-centre polar mode. An antiferroelectric is then defined as an antipolar material in which ferroelectricity can be induced by the application of an electric field and exhibit large dielectric anomalies near the Curie point: this usually involves a low-frequency zone centre mode in addition to the condensing antipolar mode, since these modes primarily influence the dielectric characteristics.

It should now be pointed out that a ferroelectric material is not necessarily ferrodistortive, although the majority are - these are called intrinsic ferroelectrics. In some cases an antiferrodistortive mode couples to a zone-centre polar mode and upon condensing indirectly induce a small spontaneous polarisation - this phenomenon is termed extrinsic (or 'improper') ferroelectricity. In the context of this coupling between polar and other modes, it should be recognised that most ferroelectrics will also exhibit a spontaneous strain, through the piezoelectric effect (or coupling to acoustic modes). If

the strain can be switched by the application of an external stress, the material can be called ferroelastic by analogy with ferroelectrics (Aizu 1969). An intrinsic ferroelastic is associated with the condensation of a zone-centre acoustic phonon. Ferroelasticity is a complementary phenomenon to ferroelectricity, all even-rank tensor properties (such as strain) changing for a ferroelastic phase shift and all odd-rank tensor properties (such as polarisation) changing for a ferroelectric phase shift. These primary ferroic characteristics are by no means mutually exclusive and are often strongly coupled.

Aizu (1969) has determined all the possible species which can exhibit ferroelectricity and/or ferroelasticity, 'species' here being defined as a pair of crystallographic point groups related by a ferroic phase transition. This classification has been extended to include ferromagnetism (Aizu 1970) and also partial or secondary ferroics, not all but some of whose orientation states differ in spontaneous polarisation, strain or magnetisation. Newnham (1974) has reviewed this classification and has discussed its application to several materials. Laughner et al (1979a,b) have observed both ferrobielasticity (where a combination of stresses is required to move the domains) and ferroelastoelectricity (where a combination of stress and electric field is required to move the domains) in quartz, a material whose crystal class (hexagonal 622) does not permit it to possess primary ferroic characterists such as ferroelectricity, ferroelasticity and ferromagnetism.

2.3 Ferroelectric Domains and Domain Walls.

While it is possible to discuss the theory of ferroelectrics in terms of an infinite uniform crystal, the presence of surfaces and imperfections in real crystals has several important

consequences. Perhaps the most fundamental of these is that the polarisation, which is uniform (and equal to the spontaneous polarisation) within a perfect crystal, may change in the vicinity of defects and vanishes at the surfaces of the crystal. Poisson's equation:

$$\text{div } \underline{D} = \text{div } (\epsilon_o \underline{E} + \underline{P}) = \rho$$

can be written as:

$$\text{div } \underline{E} = \frac{1}{\epsilon \epsilon_o} (\rho - \text{div } \underline{P}_s)$$

since in a ferroelectric the polarisation $\underline{P}$ is the sum of the polarisability of the material in the presence of an electric field and its spontaneous polarisation P_s. Therefore the changes in P_s near defects and more importantly at the crystal surfaces gives rise to a depolarising electric field. In contrast with its magnetic analogue, this depolarising field can be compensated by the motion of free charge within the crystal, in its surroundings or round some externally connected circuit.

For an insulating crystal in insulating surroundings this compensation can be very slow. If such a crystal is taken from the paraelectric phase to the ferroelectric phase, different regions of the crystal (or domains) polarise in different directions to minimise the energy associated with the uncompensated depolarising field. In the case of conducting ferroelectrics where the motion of charge within the crystal would rapidly compensate the depolarising field, DiDomenico and Wemple (1967) have observed the formation of single-domain crystals. A common way of obtaining single-domain samples of insulating ferroelectrics is to cool the crystal through the Curie point in the presence of an externally applied electric field. This process is known as poling. The presence of domains in a ferroelectric crystal can affect measurements of physical properties such as the dielectric constant, the pyroelectric coefficient and the specific heat made on the

sample as a whole. Therefore such measurements are normally carried out on poled (single domain) crystals.

The boundaries separating domains in a crystal are referred to as domain walls. In ferroelectrics where the spontaneous polarisation can only take two possible orientations, the domain walls separate regions of antiparallel polarisations and are referred to as 180° domain walls. However, other configurations are possible in materials with more than two orientational states: barium titanate has six (three mutually perpendicular antiparallel pairs), and exhibits 90° domain walls separating regions where the dipoles are oriented at right angles, as well as 180° walls (Hooton and Merz 1955). It is worth noting that since the domains are identical except in the orientation of the polarisation vector, they may be regarded as crystallographic twins and the domain walls as twin planes. The requirement that adjacent domains meet without creating regions of infinite stress or cracks in the lattice means that domain walls can only have certain fixed orientations: these have been determined for all crystal symmetries by Fousek and Janovec (1969). These mechanical compatibility requirements are obeyed by most known ferroelectrics, though slight misorientations have been observed (and may be expected) in the vicinity of crystal surfaces and defects (Chynoweth and Feldmann 1960).

While the formation of domains reduces the energy associated with the depolarising field, it carries a penalty in that a certain amount of energy is also associated with the domain walls, which differ in structure from the bulk crystal. In principle the domain configuration can be determined by minimising the sum of the depolarising and domain wall energies. In practice, complicated domain patterns are observed, which depend on a large number of factors including the crystal symmetry and defect structure, the electrical conductivity, and even the geometry of the sample and its previous treatment. The energy associated with the depolarising field W_E depends on the geometry of the sample and the domain configuration at the surfaces. For a plate sample of volume V and thickness t along

the z-axis, with 180° domain walls in the yz-plane and domains of uniform thickness d along the x-axis, Mitsui and Furuichi (1953) have evaluated this energy as:

$$W_E = \frac{\epsilon^* \; d \; P_o^2 \; V}{t}$$

where P is the polarisation in the centre of a domain and ϵ^* a constant derived from the dielectric constants of the ferroelectric. Note that the depolarising energy is minimised for low d, ie by having a large number of very small domains. Assuming a domain wall energy of σ per unit area, minimising the sum of the two energies gives an equilibrium domain width of:

$$d = \left(\frac{\sigma \; t}{\epsilon^* \; P_o^2} \right)^{\frac{1}{2}}$$

Thus the domain width should vary with the square root of the crystal thickness: this has actually been observed in barium titanate (Mitsui and Furuichi 1953).

The domain wall energy includes contributions from the interaction of the differently aligned dipoles on each side of the wall, and the elastic energy, which includes piezoelectric and electrostrictive contributions. Another contribution, from div $\underline{P}$ at the domain boundaries, is usually minimised by the orientation of neighbouring domains, and is very low in the case of 90° and 180° domain walls (Burfoot 1967). In general these contributions to the wall energy are functions of the wall thickness: by minimising the total energy, the equilibrium wall thickness may be determined, while the minimum value itself gives the domain wall energy. This process has been carried out by Zhirnov (1958) and refined by Kholodenko (1961). Zhirnov obtained a wall thickness of about 5nm for the 180° wall in barium titanate, which agrees with the experimental results of Tanaka and Honjo (1964). Other measurements and calculations of the thickness of ferroelectric domain walls also indicate that the domain walls are usually only a few unit cells wide: this is

in sharp contrast with the ferromagnetic domain wall where the magnetisation changes direction over several hundred unit cells. While the magnetisation changes across a magnetic domain wall by a process of rotation at constant magnitude, the polarisation vector changes in magnitude only, decreasing to zero at the centre of the ferroelectric domain wall. This has been confirmed for the 90° domain wall in barium titanate using electron microscopy (Yakunin et al 1972). Shepherd and Barkley (1972) have shown that Raman scattering from the 180° domain wall in gadolinium molybdate is typical of the paraelectric prototype phase, which represents a structure mid-way between that of the two antiparallel domains. Shepherd and Barkley obtained a domain wall thickness of between 0.8 and 5 microns for this ferroelectric-ferroelastic material: however, Haas and Jaep (1974) have shown that domain walls are likely to be thicker in ferroelastic materials than in pure ferroelectrics.

A number of techniques have been developed for observing domain configurations in ferroelectric materials. The most straightforward method is viewing the sample between crossed polars in a polarising microscope: the domains usually stand out in contrast. The success of this technique is usually due to optical birefringence: all pyroelectric (and therefore all ferroelectric) crystals are optically anisotropic unless the refractive indices happen to coincide accidentally. The optic axes are oriented differently in different domains, so that the elliptical section of the optical indicatrix perpendicular to the wave-front normal of the incident light varies from domain to domain. Therefore the domains appear with different intensities when viewed between crossed polars. This technique generally fails for materials with antiparallel domains since the optical indicatrix is then invariant under domain reversal: however in these cases the domain wall may be visible even though the two domains are indistinguishable. This is the case with the 180° domain wall in barium titanate, and Kobayashi et al (1963) have suggested that this is due to birefringence induced by shear strain in the vicinity of the domain wall. However, birefringence is not the only reason for a difference in

contrast of domains viewed by polarised light. In lead germanate, the 180° domains appear in contrast because of optical rotation (Dougherty et al 1972), which changes sign for antiparallel domains.

Other techniques for viewing domains include differential etching, using an etchant that attacks the crystal at opposite ends of the polarisation vector at different rates. Water acts as a differential etchant on Rochelle salt (Straubel-Fischer 1957). The resultant etch pattern can be viewed under an electron microscope for greater resolution. Colloidal suspensions of charged particles in insulating organic liquids can be used to "decorate" domains on the surface of a crystal (Pearson and Feldman 1959). Domains in thin films of ferroelectrics can also be observed directly under an electron microscope (Tanaka and Honjo 1964). A number of other methods not mentioned here are reviewed by Lines and Glass (1977).

The most convenient method of observing domains in ferroelectrics is undoubtedly using the polarising microscope, providing that the optical properties of the material are suitable. It has the added advantage of not damaging the sample in any way, and can also be used to study domains in motion. This is the method used to study domain patterns in the present work, and some photographs of the domain structure in lead germanate and gadolinium molybdate are shown in Chapter 5. Several plotographs of domains in other ferroelectrics are included in the books by Jona and Shirane (1962) and Fatuzzo and Merz (1967). By depositing transparent electrodes on the crystal surfaces, this technique permits the viewing of domain wall motion under an applied electric field, and alternating field can be used with stroboscopic illumination. The motion of domain walls will be shown to play an important part in the generation of acoustic emission in ferroelectric crystals, and the dynamic properties of domains are discussed in the following section.

2.4 Polarisation Reversal.

The characteristic property of ferroelectrics is that they possess a spontaneous polarisation that can be reversed by an externally applied field. In an ideal dielectric, the polarisation $\underline{P}$ is proportional to the applied electric field $\underline{E}$: clearly the presence of this reversible spontaneous polarisation will affect this relation. The presence of domains in the crystal gives rise to a hysteresis loop when $\underline{P}$ is plotted against $\underline{E}$ similar to the $\underline{B}$-$\underline{H}$ hysteresis loop found in ferromagnets. The ferroelectric hysteresis loop can be displayed on an oscilloscope screen by including the crystal in a simple circuit devised by Sawyer and Tower (1930): this circuit is described in Chapter 3.

A representative hysteresis loop is sketched in Figure 2.2. Starting with an initially unpolarised ferroelectric crystal (with equal regions of antiparallel polarisation), the application of a small electric field along the polar axis initially gives a linear P-E relation, characteristic of a normal dielectric. As this field is increased, the polarisation increases rapidly as the crystal switches. This process ceases when the entire crystal consists of a single domain oriented along the electric field: any further increase in the applied field yields an increase in polarisation due to the dielectric susceptibility of the poled crystal. This saturation polarisation, extrapolated back to zero electric field, is equal to the spontaneous polarisation P_S. If the electric field is reduced to zero, most of the domains remain aligned so that the crystal exhibits a remanent polarisation P_R. In an ideal ferroelectric, P_S and P_R are equal as all the domains remain aligned: however in most cases the presence of internal or externally applied stress, or the inability of the free charge in the crystal to compensate the depolarising field of the domain in each half-cycle of the loop at high frequencies, may lead to "backswitching" when the applied field is removed. To annihilate the net polarisation of the crystal the field must be

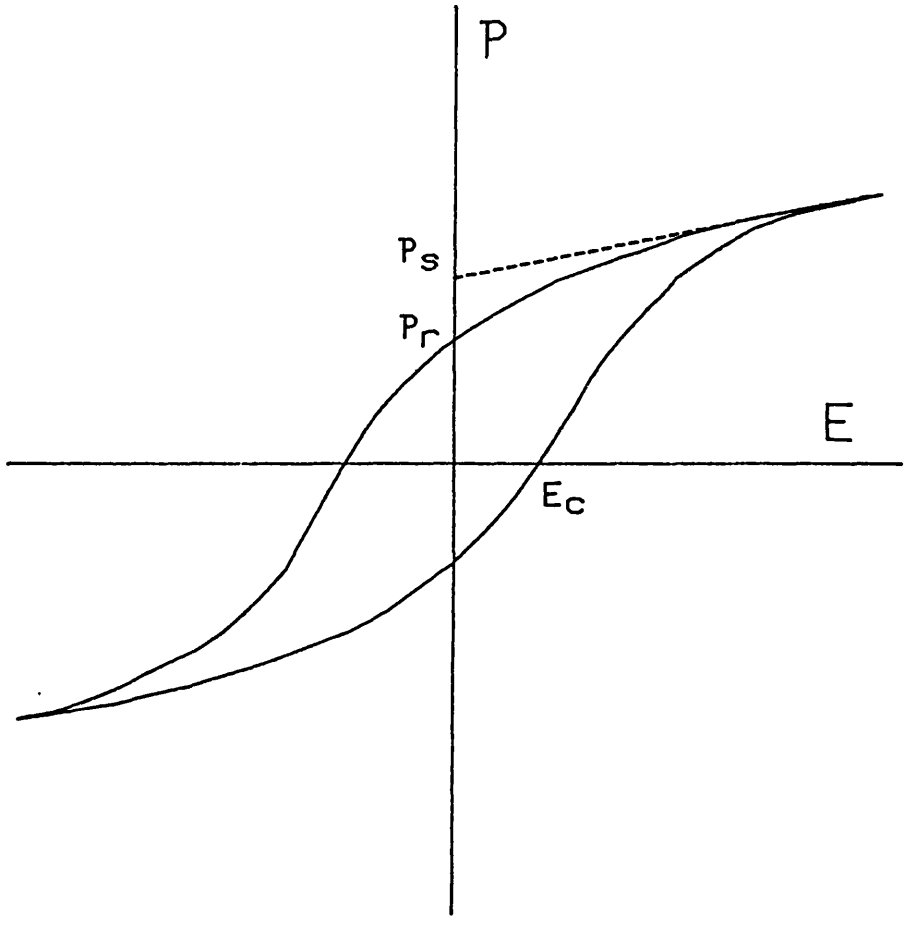

FIGURE 2.2 - Polarisation (P) versus electric field (E) ferroelectric hysteresis loop showing the spontaneous polarisation P_s, the remanent polarisation P_r and the coercive field E_c.

reversed by an amount E_c (the coercive field), when the polarisation again switches rapidly towards saturation in the opposite direction. The coercive field and the saturation polarisation are both frequency dependent, as there is a switching time associated with the polarisation reversal. At high frequencies the switching of the crystal is not complete and "saturation" does not correspond to a single-domain crystal. In addition, most ferroelectrics do not have a true coercive field in that a very low applied field will switch the crystal given enough time, so that in general hysteresis loops can only be obtained over a limited range of frequencies, typically from several seconds per cycle to a few hundred hertz.

There has been a great deal of experimental work on the mechanism of polarisation reversal, both by direct observation of domains during switching and by electrical measurements on the bulk crystal. Much of this work has been carried out on barium titanate. Polarisation reversal is usually accomplished through a combination of the nucleation of domains in a region of oppositely directed polarisation and subsequent growth along the polar axis, the sideways motion of the 180° domain walls formed in this manner (or initially present in the crystal), and the ultimate coalescence of these domain walls to give a single-domain crystal. These processes are sketched schematically in Figure 2.3. For most ferroelectrics in the form of a plate normal to the polar axis, the sideways motion of 180° domain walls seems to be the preferred form of motion (Lines and Glass 1977). In general, the switching of a crystal takes place through the nucleation and growth of a large number of domains, though complete polarisation reversal by the nucleation and subsequent motion of a single domain wall has been accomplished in barium titanate (Miller 1958) and gadolinium molybdate (Kumada 1969). This has also been accomplished in gadolinium molybdate as part of the present work, and a sequence of photographs showing the domain wall traversing the crystal are shown in Chapter 5. The switching behaviour of a ferroelectric is affected by a large number of factors, including the nature of the electrodes (Camlibel 1969)

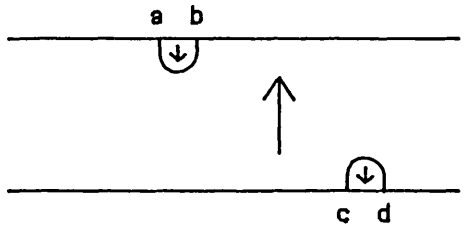

(a)
Nucleation of domains.

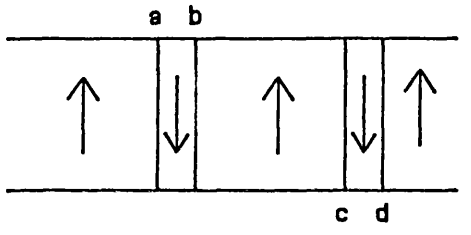

(b)
Forward growth through crystal.

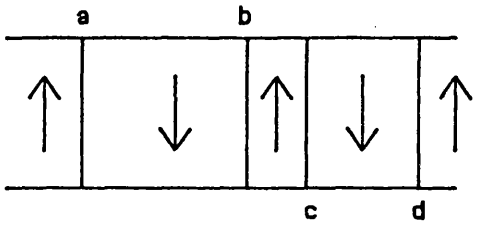

(c)
Sideways motion of domain walls.

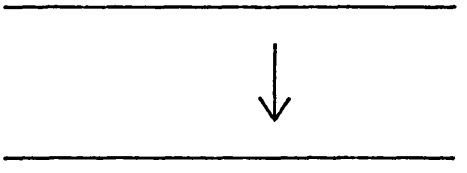

(d)
Coalescence of domains.

FIGURE 2.3 - Simple model for polarisation reversal in a ferroelectric crystal (initially poled 'up') under an electric field (applied in a downward direction).

and the crystal surfaces, the geometry of the sample, the domain configuration (Janta 1971) and the presence of defects.

While visual observation of the domains during switching can identify the various processes by which the polarisation reversal occurs, little quantitative information can usually be obtained. Stadler and Zachmandis (1963) have studied the nucleation of new domains in barium titanate and have found that for moderately high electric fields (over 5kV/cm) the rate of nucleation follows a power law of the form:

$$n = k E^{1.4}$$

At low fields the rate of nucleation is very small, and is generally taken to follow an exponential law: this has actually been observed in potassium dihydrogen phosphate by Mitsui and Furiuchi (1953). Nucleation occurs preferentially near defects and at the surfaces of the crystal, and can be induced in a predetermined region by dimpling the crystal surface (Miller 1958). The forward growth of domains has not been extensively studied, partly because of the difficult geometry and partly because a domain grows through the thickness of the crystal very rapidly once nucleation has occurred. The sideways motion of domain walls seems to be the dominant mechanism of polarisation reversal in most materials. Optical measurements of the domain wall velocity tend to be difficult as the walls can move very rapidly. Miller and Savage (1958) have measured the domain wall velocity in barium titanate by applying an electric field in short pulses and determining the position of the domain wall after each pulse. For low fields they found an exponential dependence of the form:

$$v = v_\infty \exp (-\delta/E)$$

where the constant δ appeared to depend on the defect concentration in the sample. At high fields (above 1kV/cm), Stadler and Zachmandis (1963) found that the domain wall velocity follows a power law similar to that obtained for the

nucleation rate. However, not all ferroelectrics behave in this way: some examples are given in Section 2.6 where the properties of four particular ferroelectric materials are discussed in more detail.

Electrical measurements of the switching process can be much more quantitative, but it is then difficult to separate nucleation from sideways growth. The circuit commonly used is shown in Figure 2.4a. When a voltage step, directed so as to reverse the polarisation in the previously poled ferroelectric sample, is applied to the circuit, the voltage across the load resistance is proportional to the current through the crystal (or rate of change of polarisation). A typical "switching pulse" is shown in Figure 2.4c, which also gives the definitions of the peak current i_m and the switching time t_s. To a first approximation, neglecting the dielectric polarisability of the sample and assuming complete switching, the area under the curve is equal to $2AP_s$, where A is the electrode area and P_s the spontaneous polarisation. The switching time is usually defined as the time taken for the area under the curve to reach a certain fraction (typically 90 or 95%) of this limiting value, or for ease of measurement as the time at which the switching current drops to some fraction (eg 5%) of its peak value. The shape of the curve can be characterised by a form factor f which is 1 for a rectangular pulse: as the area under the curve is constant, to a first approximation the switching time and the peak switching current are related by:

$$i_m = 2 f P_s / t_s$$

The initial current spike is due to the charging of the crystal capacitance: if the voltage step is re-applied in the same direction, so that no switching occurs, the voltage across R has the form of Figure 2.4d, which is characteristic of a linear dielectric.

In most ferroelectrics the peak current and the reciprocal of the switching time appear to follow laws similar to those

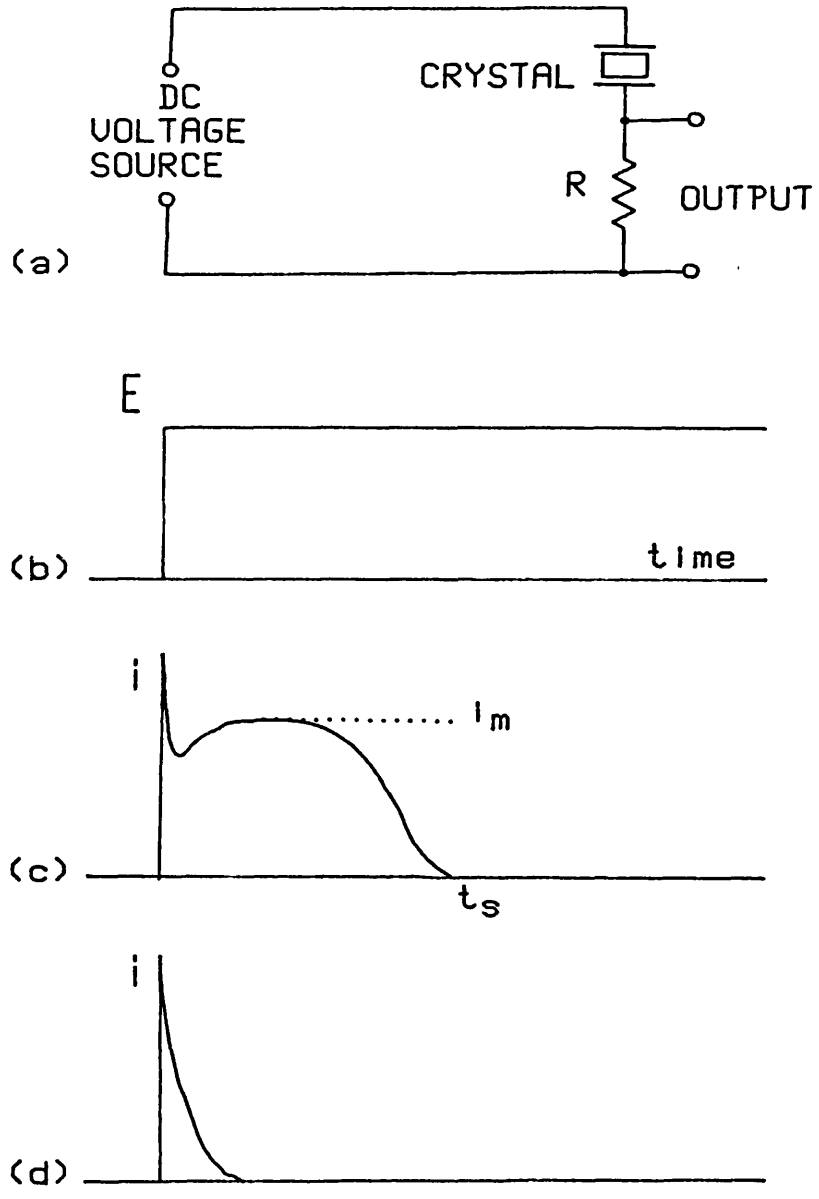

FIGURE 2.4(a) - Schematic circuit for electrical studies of polarisation reversal in ferroelectrics. When a voltage step (b) is applied to the crystal, the output voltage is proportional to the switching current. A typical switching pulse is sketched in (c). The output for a linear dielectric is given in (d).

outlined above for the nucleation rate and domain wall velocity. At low fields, Merz (1954) found that the switching time for barium titanate varies as:

$$t_s = t_o \exp (\alpha/E)$$

while at high fields a power law was found by Stadler (1958):

$$t_s = k E^{-1.5}$$

The parameters in these expressions vary with temperature, switching occurring more rapidly as the transition temperature is approached. This behaviour has also been observed in other materials such as Rochelle salt (Wieder 1958) and lead germanate (Suzuki et al 1978).

A number of transient impulses are often found superimposed on the switching pulse. These current transients are characterised by a relatively large amplitude but short duration. These pulses are referred to as Barkhausen pulses by analogy with a similar ferromagnetic phenomenon, where the change in magnetisation takes place in discontinuous steps associated with the jerky motion of domain walls (Crangle 1977). The ferroelectric Barkhausen effect has been extensively studied in Rochelle salt (Abe 1956) and barium titanate (Chynoweth 1958). Chynoweth found that both the average height of the pulses and the number of pulses larger than some threshold level increase with the applied electric field, while the total number of pulses for complete switching is essentially constant. The total charge carried by all the Barkhausen pulses amounts to only about 0.1% of the total charge switched ($2AP_s$). From these and other observations, Chynoweth concluded that a jerky-wall model cannot be responsible for this effect in ferroelectrics.

Miller (1960) has optically studied the mechanisms which give rise to the Barkhausen pulses. He found that these pulses are associated with the formation of cylindrical domains about a micron in diameter soon after the application of the electric

field, which then expand sideways. When two expanding domains coalesced, Miller found that the approaching domain walls seemed to repel one another, forming a metastable region about one micron across which then suddenly disappeared, again with the production of a Barkhausen pulse. Later measurements by Rudyak et al (1972) revealed subtle differences between pulses originating from these two mechanisms, "nucleation" pulses being larger and with a faster risetime than those associated with the fusion of two domains.

Chynoweth (1958) had considered both these possible sources of the current transients, but ignored the coalescence model because the pulses appear throughout the switching process and not predominantly towards the end. By evaluating the energy of a reversed domain as a sum of the wall energy, the depolarising energy and the electrostatic energy of the reversed domain in the applied electric field, Merz (1954) was able to show that the nucleation rate should vary exponentially with the applied field assuming a flat dagger-shaped domain nucleus. Chynoweth showed that this result also holds for a cylindrical nucleus, in both cases the length being much larger than the width or diameter to minimise the depolarisation energy. He then went on to show that the exponential dependence of the switching time could be explained in terms of this nucleation rate followed by sideways motion of the domain walls, with a velocity proportional to the applied field. Landauer (1957) has shown that the nucleation of domains in the bulk of a ferroelectric crystal by thermal fluctuations is unlikely since the energy of formation of such a domain nucleus is large compared with kT. However, this energy is likely to be considerably smaller near inhomogeneities such as defects and crystal surfaces, which is where domain nucleation is normally observed to occur.

Landauer also showed that since the ferroelectric domain wall is only a few lattice spacings thick, the energy required to move it by one lattice spacing is comparable to the wall energy itself, which is far in excess of the energy gained by moving this distance. Therefore this kind of "sideways motion" is

unlikely. As the experimentally observed field dependences of the nucleation rate and wall velocity are similar, this sideways motion may occur by preferential nucleation on the existing domain wall. Miller and Weinreich (1960) developed a model for barium titanate along these lines which agreed with the measured field and temperature dependences at low values of the electric field. In this model, the shape of the nucleus is taken to be a triangular step, one lattice spacing thick, on the face of an existing wall. The wall velocity is then proportional to the nucleation rate, which varies as:

$$\frac{1}{\tau} = A \exp (-\delta/E)$$

The model was extended by Stadler and Zachmandis (1963) by assuming that nucleation steps of more than one lattice spacing can occur at high values of the applied field, obtaining a power law with an exponent of about 1.3 in good agreement with experiment.

Hayashi (1972) has developed a more general formulation of the problem along similar lines. The situation is complicated by the fact that nucleation can occur on the growing steps of earlier nucleations, and a distinction has to be made between this new nucleation, which increases the wall thickness, and the sideways growth of the steps which effectively decreases it. The change from an exponential to a power law at high fields can then be explained in terms of the relative importance of these two processes: at low fields the nucleation is the limiting factor as in the Miller-Weinreich model but the sideways growth (on the domain-wall face) takes over at high fields. The various factors in these models depend on several material parameters, so it is not surprising that different materials show widely different switching behaviour.

2.5 Applications of Ferroelectrics.

Ferroelectric materials have a number of useful properties in addition to their reversible polarisation. The commonest applications utilise their so-called 'anomalous' properties. Most ferroelectrics have relatively high dielectric and piezoelectric coefficients, which has led to their use in capacitors and piezoelectric transducers: however these properties are often very sensitive to temperature so these applications are limited to cases where high stability is not required. In their day, Rochelle salt and later potassium and ammonium dihydrogen phosphates had the largest known piezoelectric coefficients, and were widely used in applications ranging from record-player pickups to sonar transducers. Nowadays, ceramic lead zirconate titanate is extensively used in piezoelectric transducers, while surface-acoustic-wave devices are commonly fabricated on substrates of lithium niobate. When high voltages are applied to ferroelectrics, non-linear effects become apparent. While these are usually detrimental, some applications based on them have been proposed, including microwave amplification (Billeter et al 1964) and harmonic generation (DiDomenico et al 1962).

The pyroelectric effect is commonly used to detect infra-red radiation. The efficiency of such a detector depends on a number of material parameters, including the pyroelectric coefficient, the dielectric constant, the conductivity and the specific heat. Many ferroelectric materials perform well in this application, notably lithium tantalate and alanine-doped triglycine sulphate (Keve et al 1971). Pyroelectric detectors can be used to record infra-red images either by scanning the image with a single detector or by electrically scanning the image formed on a slab of pyroelectric material. The latter approach is used in the pyroelectric vidicon (Hadni et al 1965), where the image is formed on the front face of a pyroelectric "target", the reverse side of which is scanned by an electron beam. Both triglycine sulphate (Singer and Lalak 1976) and lead

germanate (Watton et al 1976) have been used as target materials.

The non-linear dielectric properties of ferroelectrics give rise to useful electro-optic effects. In its simplest form, the change in dielectric constant (and hence refractive index) under an applied electric field means that the retardation of a beam of light traversing a crystal can be changed by applying a voltage across the crystal. This can be used to modulate the light beam in sympathy with the applied voltage, which has obvious applications in optical communications technology (Spencer et al 1962). The dielectric nonlinearity also makes possible the generation of optical harmonics of intense laser light (Maker et al 1962). These optical applications make stringent demands on the purity and perfection of the crystals, with the result that in many applications the choice of material is dictated by the availability of optically perfect crystals in the required quantity. Materials used in this application include lithium niobate, lithium tantalate and potassium dihydrogen phosphate, the latter mainly because large, optically perfect crystals can be grown from solution even though it has relatively small non-linear coefficients.

While several applications utilising the reversible polarisation of ferroelectrics have been proposed, they have not been particularly successful. One reason for this is the phenomenon known as "ageing", where the switching properties of the material degrade with time and repeated switching. This may be due to the formation of migration of defects during polarisation reversal or to the build-up of space charge near the crystal surfaces (Fatuzzo and Merz 1967, Lines and Glass 1977), which stabilises the domain walls and inhibits the nucleation of new domains. The existence of two stable polarisation states means that ferroelectrics can be used as binary memories, just as ferromagnetic materials are used in ferrite cores and more recently bubble memories. The optical properties of reversed domains means that optical read-out is possible, while optical storage can be achieved by depositing a photoconductive film on the surface of the ferroelectric, making

high-density memories possible (Anderson 1974). These optical properties have also led to the application of ferroelectrics to displays (Anderson 1972) and light valves or shutters (Kumada 1972). However, in the latter application these devices are far slower than those based on the electro-optic effect described above, which do not involve domain-wall motion and polarisation reversal.

2.6 Properties of Four Particular Ferroelectric Materials.

The experimental work described in the following chapters of this thesis was performed on samples of four ferroelectric materials, namely Rochelle salt, lead germanate, gadolinium molybdate and terbium molybdate. In this section, the particular properties of these materials are reviewed. Full details of sample preparation, along with X-ray Laue photographs of these materials, are given in Chapter 3.

(a) Rochelle salt.

Rochelle salt is the name commonly given to the hydrated double tartrate of sodium and potassium (Na K COO.CHOH.CHOH.COO $4H_2O$), first prepared as a laxative around 1655 by Seignette in the French spa town of La Rochelle. The large piezoelectric effect in this material was noticed by the Curie brothers in 1880 and the electro-optic effect by Pockels in 1894. However it was in 1921 that Valasek discovered its anomalous dielectric properties and indeed the phenomenon of ferroelectricity. Rochelle salt was initially extensively investigated as the only known ferroelectric, but interest in it faded with the discovery of simpler materials more amenable to theoretical studies. Even today, the origin of ferroelectricity in Rochelle salt remains poorly understood. There have been few recent publications concerning this material, and the best references seem to be the

earlier ones: the relevant chapters in the books by Jona and Shirane (1962) and Mason (1950) are particularly useful.

One outstanding property of Rochelle salt is that it exhibits two Curie points, at -18 °C and +24 °C. In the range between these two temperatures, the symmetry of the material is monoclinic with point group 2. Both of the paraelectric phases have the same symmetry, orthorhombic point group 222, and are piezoelectric. The polar axis of the polar phase is parallel to the original orthorhombic [100] direction. Although according to the conventions for the monoclinic system the unique polar axis should be called the b-axis, it has become customary to refer to the axes of the polar phase with reference to the prototype: hence the polar axis is given the label a. The first X-ray investigation of the structure of Rochelle salt was made by Beevers and Hughes (1941). The differences between the three phases are extremely small, at least as far as X-ray diffraction is concerned. The lattice parameters in the orthorhombic phase at +35 °C are (Ubbelohde and Woodward 1946):

$$a = 11.878 \text{ Å} \qquad b = 14.246 \text{ Å} \qquad c = 6.218 \text{ Å}$$

Although it was originally believed that the complex system of hydrogen bonding in the material was responsible for the spontaneous polarisation, Frazer et al (1954), using neutron diffraction, revealed that the most relevant contribution to the phase change is due to the orientation of the hydroxyl (OH) groups of the tartrate molecule. Diagrams of the structure of Rochelle salt as obtained from X-ray and neutron scattering are included in the references given above.

Rochelle salt shows pronounced anomalies in the small-signal dielectric constant ϵ_{11} measured along the a-axis at the transition temperatures: no thermal hysteresis has been observed, and the transitions are believed to be second order. Measurements of the spontaneous polarisation and the coercive field as a function of temperature have been made by Wieder (1958) among others: both these quantities go to zero

continuously (as far as could be determined) at the transition temperatures, and reach a maximum at about +4°C.

The domain configuration in Rochelle salt has been extensively studied (eg Mitsui and Furuichi 1953). Rochelle salt has 180° domain walls, which can lie on ab- or ac- planes: domains separated by these walls are called b- and c- domains respectively. These configurations are sketched in Figure 2.5a. Despite having 180° domain walls, these domains are visible under a polarising microscope: although the optical indicatrices in each domain are identical, they are rotated relative to one another as a result of the spontaneous strain (this has been exaggerated in Figure 2.5a). Therefore the positions of the polariser for extinction of the two domains differ by a small amount, which Mitsui and Furuichi (1953) have measured as 2.5° at +17°C, and varies with temperature. Both b- and c- domains can coexist in a single sample, in which case domains terminate within the crystal, becoming wedge-shaped. Marutake (1925) found that domains can also become wedge-shaped along the a-direction, resulting in a layered structure of b- and c- domains.

The dynamic properties of domains in Rochelle salt have also been extensively studied, and are broadly similar to the properties of barium titanate discussed in Section 2.4. Mitsui and Furuichi (1953) found that the nucleation rate varied exponentially with the applied field (similar to barium titanate), but that the sideways velocity of domain walls had a linear dependence according to:

$$v = \mu (E - E_o)$$

where E_θ is a critical field below which no sideways motion is observed, being about 80V/cm at +11°C. Wieder (1958) found no evidence for a threshold field below which no switching occurs, and also obtained values for the domain wall mobility far higher than those of Mitsui and Furuichi: however, Wieder measured the switching of an entire crystal, where the nucleation of domains

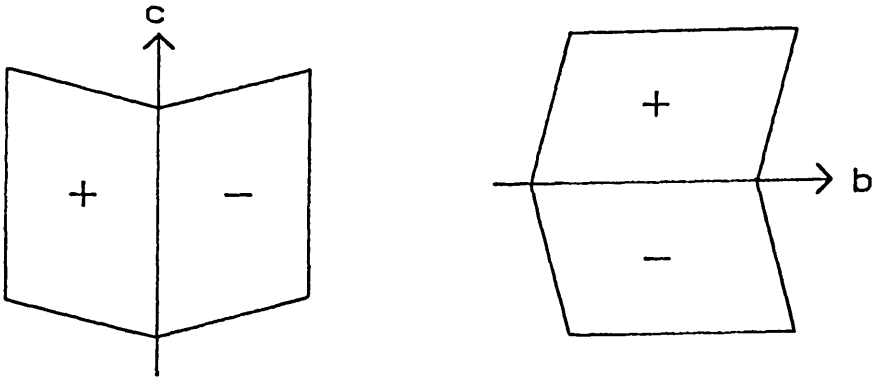

(a)

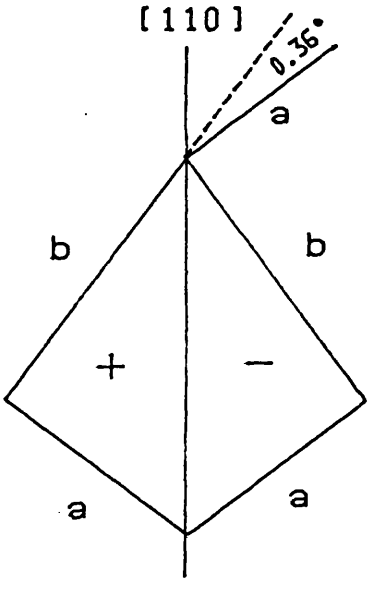

(b)

FIGURE 2.5 - Domain wall orientations in (a) Rochelle salt and (b) gadolinium molybdate. The signs + and - indicate the direction of the polar axis, into and out of the plane of the diagram respectively.

and the sideways motion of several domain walls all occur in parallel.

(b) Lead Germanate.

Ferroelectricity in lead germanate ($Pb_5 Ge_3 O_{11}$) was discovered independently by Iwasaki et al (1971) and Nanamatsu et al (1971). At room temperature, where the material is ferroelectric, the crystal has trigonal symmetry (point group 3), with lattice constants (Iwasaki et al 1971):

$$a = 10.250 \text{ Å} \qquad c = 10.685 \text{ Å}$$

The polar axis is the three-fold c-axis in this structure. Lead germanate has a Curie point of 177°C, above which it has hexagonal symmetry (point group $\bar{6}$). The crystal structure in both phases has been studied using X-ray and neutron diffraction (Newnham et al 1973, Iwata 1977).

Lead germanate is optically active with a rotary power of 5.6°/mm at room temperature. The direction of rotation changes on inversion of the polar c-axis, so that domains can be viewed using a polarising microscope. The mechanical compatibility relations of Fousek and Janovec (1969) indicate no strong preference for any particular orientation of the walls between antiparallel domains: however Dougherty et al (1972) found a clear preference for $\{1\bar{1}00\}$ planes, particularly for small domains which tend to be hexagonal in shape, while for larger regions the wall orientations become less distinct. They also measured the switching time using cinematographic techniques, finding a power law:

$$t = k (E - E_o)^{-1.5}$$

no switching being observed below E_o, which was found to be about 3kV/cm. Measurements made by Suzuki et al (1978) indicate that the switching behaviour is similar to that in barium

titanate, the switching time depending exponentially on the applied field for low fields (less than about 7kV/cm) and according to a power law at higher fields.

(c) Gadolinium and Terbium Molybdates.

Gadolinium molybdate ($Gd_2 (Mo O_4)_3$) and terbium molybdate are two members of a series of ferroelectric rare-earth molybdates having similar properties (Borchardt and Bierstedt 1967). This discussion will concentrate on gadolinium molybdate (GMO), on which most of the work on this series of ferroelectrics has been carried out. GMO is ferroelectric at room temperature, with an orthorhombic (though nearly tetragonal) crystal structure, with point group mm2, the polar axis being the c-axis. The lattice constants at room temperature are (Jeitschko 1972):

$$a = 10.39 \text{ Å} \qquad b = 10.42 \text{ Å} \qquad c = 10.70 \text{ Å}$$

Above the Curie point of about 160°C, the structure is tetragonal (point group $\bar{4}2m$), with a unit cell half the volume of that in the ferroelectric phase. Comprehensive X-ray studies of the crystal structure of GMO have been carried out by Keve et al (1971) and Jeitschko (1972).

GMO has a very small dielectric anomaly at the transition temperature, although significant anomalies in some elastic constants have been observed by Hochli (1972). The phase transition is first order, and the spontaneous polarisation is accompanied by a spontaneous strain which can be switched by an externally applied stress. In GMO, ferroelectricity and ferroelasticity are so closely coupled that the spontaneous strain and polarisation always switch simultaneously, and can be driven either by an electric field or an applied stress (Smith and Burns 1969). These observations initially led to the suggestion (Cross et al 1968) that GMO is intrinsically ferroelastic (through an elastic instability) but extrinsically

ferroelectric. However, the true character of the phase transition was later deduced by Pytte (1970), based on the doubling of the unit cell through a soft zone-boundary phonon mode. Therefore GMO is intrinsically antiferrodistortive but extrinsically both ferroelectric and ferroelastic. Petzelt and Dvorak (1971) identified the soft mode in question, and the matter was finally settled by a neutron scattering study on terbium molybdate by Axe et al (1972).

GMO has 180^0 domain walls, but as in Rochelle salt the opposed domains have slightly different intensities when viewed between crossed polars. Viewed down the polar c-axis, the extinction directions on opposite sides of a domain wall differ by less than 1^0. The domain walls stand out in sharp contrast against the nearly uniform background, being light or dark according to the setting of the polarisers: Flippen (1975) has attributed this to the material in the relatively wide domain wall being similar in structure to the prototype phase and therefore non-birefringent. The domain walls appear on {110} planes. This is shown in Figure 2.5b, which also indicates how the a- and b- axes axes are interchanged on polarisation reversal. This distortion involves a change in crystal shape when the polarisation is switched, which may have useful applications (Lemons and Geary 1978). Switching in GMO takes place largely through the sideways motion of a small number of domain walls, nucleation being difficult and only occurring at high fields and at suitable sites on the crystal surface. The sideways velocity of domain walls has been measured by Flippen (1975) who found a linear relation:

$$v = \mu (E - E_o)$$

where no switching occurs below E_o (typically 1.4kV/cm). This relation holds for fields up to about 10kV/cm, above which the nucleation of additional domain walls occurs. A similar relation has also been found for the mobility of the domain wall under an applied mechanical stress.

CHAPTER 3: EXPERIMENTAL METHODS FOR THE DETECTION AND MEASUREMENT OF ACOUSTIC EMISSION FROM FERROELECTRICS.

This chapter describes the experimental procedures followed in the measurement of acoustic emission from ferroelectric crystals as a function of temperature, applied electric field and other sample parameters. The operating principles of the equipment are described.

Sample preparation is also covered in this chapter. This includes X-ray alignment, cutting and polishing of the bulk material and the application of electrodes to the flat surfaces of the plates thus prepared. Preparation details are given for the four materials investigated, namely Rochelle salt (RS), lead germanate (PGO), gadolinium molybdate (GMO) and terbium molybdate (TMO).

3.1 Experimental Setup

The basic experimental configuration used for the acoustic emission (AE) experiments is shown in Figure 3.1, and a photograph of a typical setup is shown in Figure 3.2a. A brief description of the complete installation is given below, while the individual components are described in detail in later sections of this chapter.

The specimen, generally a flat plate of single-crystal ferroelectric material with flat surfaces perpendicular to the polar axis, was coupled to a transducer which sensed any acoustic emissions produced. A coupling fluid, such as silicone grease, was used between sample and transducer to improve transmission across the interface. The sample dimensions were typically a centimetre across and a millimetre thick so that in most cases the sample could be mounted directly on the

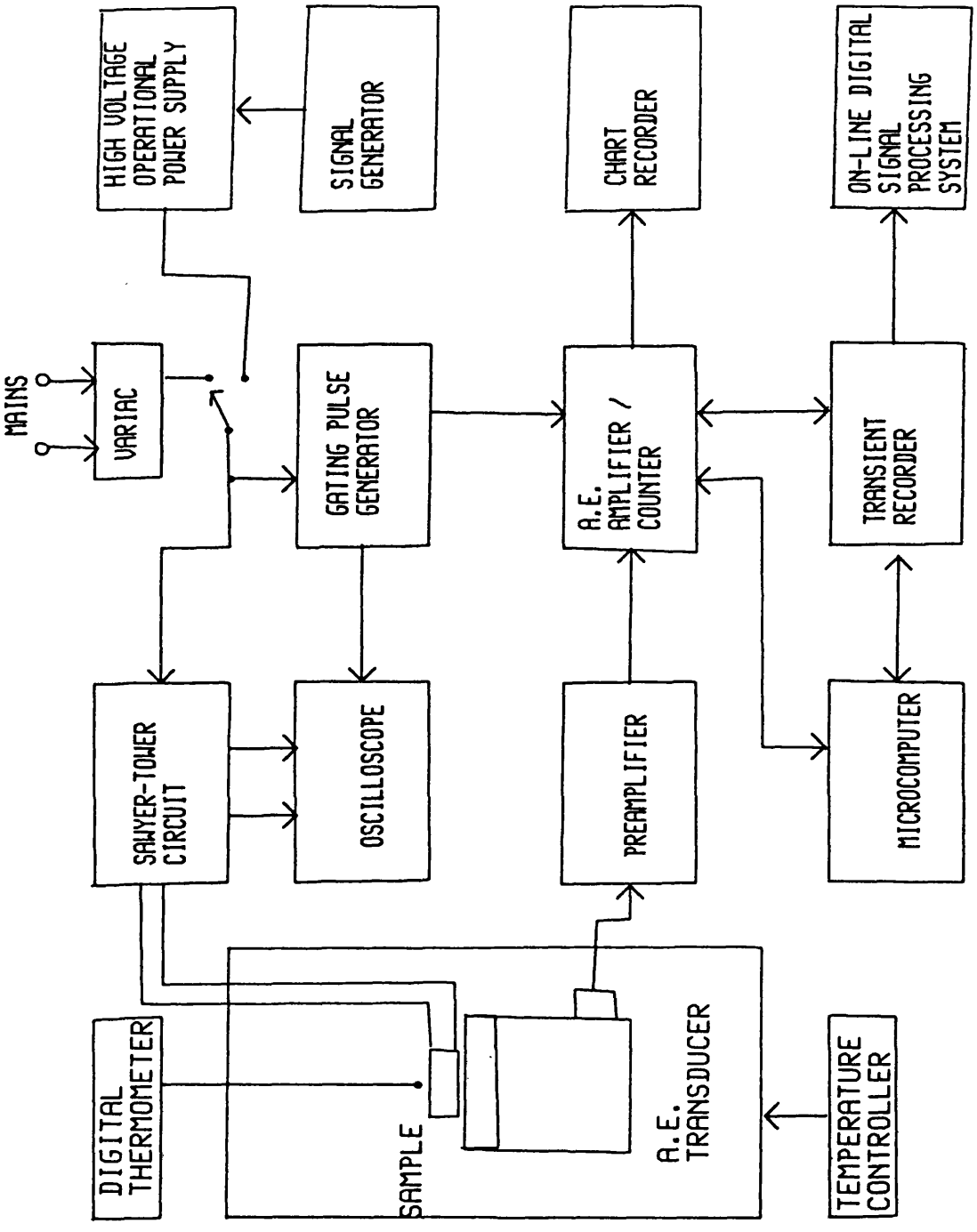

FIGURE 3.1 - Block diagram of the apparatus used to investigate acoustic emission from ferroelectric crystals.

FIGURE 3.2(a) - Photograph of a typical acoustic emission experiment. The thermoelectric module and its controller are visible on the extreme right.

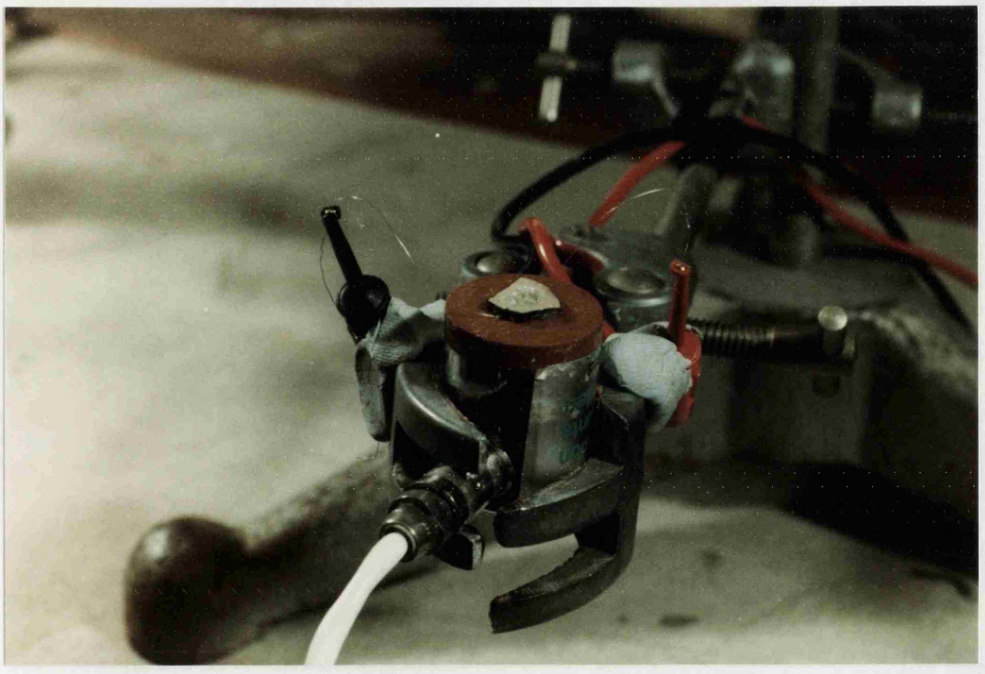

FIGURE 3.2(b) - Close-up photograph of a lead germanate sample mounted on an AC1500L transducer.

transducer, which was considerably larger (Figure 3.2b). When the sample temperature had to be varied, the sample was mounted in a furnace or a thermoelectrically cooled chamber as necessary. In this case an acoustic waveguide was interposed between sample and transducer so as to isolate the transducer from any potentially harmful temperature changes. A digital thermocouple thermometer was used to monitor the sample temperature to within 0.1°C.

The AE monitoring system employed was the Model 105 supplied by Acoustic Emission Consultants Ltd. This is an industrial system and has the advantage that its components, including the transducers, are quite robust. The system comprises a transducer, a fixed-gain preamplifier and a main amplifier/counter unit which is capable of performing ring-down and envelope (event) counting on the incoming signal. The amplified AE signal is available at a connector on this unit, and could be captured on a transient recorder for further analysis. A Hewlett-Packard 9825A minicomputer was used to coordinate and control the data acquisition process. All the experimental data was stored on magnetic tape, using a standard file format as far as possible to simplify the subsequent processing and plotting of the data. Since the AECL 105 counter was not designed for computer control, a custom interface had to be constructed.

In order to induce polarisation reversal in the sample, a high voltage (typically several hundred volts) must be applied along its polar axis. To this end, electrodes were deposited on the flat surfaces of the plate samples and these were connected to a suitable voltage source, normally derived from the mains. A simple circuit, due to Sawyer and Tower (1930) was used to display the resulting $\underline{P}$-$\underline{E}$ hysteresis loop on one channel of an oscilloscope, while the AE signal could be simultaneously displayed on the other. A delayed pulse generator, synchronised to the driving field, could be used to gate the AE counter to operate only on specific regions of interest of the hysteresis cycle. A high-voltage operational power supply was also used to provide a variable-frequency, variable-waveform electric field

for measurements of the frequency dependence of the AE.

3.2 Specimen Characterisation and Preparation.

Defects in ferroelectric crystals can seriously influence domain wall motion in ferroelectrics and hence their dielectric properties and switching behaviour (Lines and Glass 1977). Poor crystals also tend to be copious sources of AE but do not give reproducible results. The starting material from which the samples used in the present work were prepared were therefore single crystals grown to a high degree of purity and perfection.

The specimens used for the acoustic emission experiments were in the form of rectangular or disc-shaped flat plates, about 1cm across and 0.3 to 3mm thick. The plates were oriented with the flat surfaces perpendicular to the polar axis so that electrodes deposited on these faces could be used to apply an electric field along this axis. Back-reflection X-ray (Laue) diffraction was used to line up the boule, mounted on a goniometer. Two parallel cuts were made perpendicular to the polar axis using a slow-speed peripheral diamond saw to produce a correctly oriented slice ready for polishing.

The cut slices were first stress relieved by lightly polishing the edges, using 600 grit aloxite. This was particularly necessary for thin samples of non-circular section which tended to break up during the polishing process due to stress concentrations left by the cutting action of the saw. The diamond saw could not be used to cut slices less than about a millimetre thick without running the risk of breaking the sample. Therefore thinner specimens were prepared by polishing down to the required thickness, again using 600 grit aloxite. The actual polishing techniques used varied according to the nature of the material to be polished, and are described in greater detail below. The flat faces of the sample were generally required to possess an optical finish and a

parallelism of at least 5' of arc.

Electrodes were then deposited on the flat surfaces of the plate. Intimate contact between the electrode and the sample surface is essential because otherwise sparking may occur between the two at the high electric fields used, giving rise to the so-called Schonfeld effect (Abe 1956). Aluminium electrodes, vapour deposited in vacuo through a mask of known area, were used for the lead germanate, GMO and TMO specimens. The deposited electrodes were carefully painted over with a silver dag preparation for protection against scratching. This technique could not be used with Rochelle salt which dehydrates under vacuum. Therefore electrodes were painted on samples of this material using silver dag.

Fine copper wires (0.12mm diameter) were attached to the electrodes using a small drop of silver dag and soldered or clipped to the high-voltage leads of the apparatus (Figure 2.2b). The lower electrode connection was usually brought round the side of the crystal with a thin track of silver dag so that the connection to this electrode could also be made on the upper face of the sample: this leaves a flat lower surface to couple efficiently to the AE transducer. This technique could not be used with GMO and TMO where the surfaces of the crystal must be completely electroded for reliable switching (Cummins 1970). With these materials the connection was made directly to the lower surface with no apparent degradation of the sample-transducer bond.

The four materials studied are characterised separately below. Their principal properties relevant to this work are summarised in Table 3.1. The values given in this table were measured on typical samples prepared as above. The coercive field is included in this table as an indication of the voltage required to switch the polarisation of the sample: the actual value can vary substantially from sample to sample, with the past history of the sample and with the conditions under which the measurement is made.

Material	Curie Temperature Tc °C	Dielectric Constant (1kHz)	Spontaneous Polarisation (0.1Hz) Ps $\mu C/cm^2$	Coercive Field (0.1Hz) Ec kV/cm
Rochelle salt	-18,+24	400	0.25	0.5
Lead germanate	177	50	4.2	3.4
Gadolinium molybdate	159	10.3	0.19	5.5
Terbium molybdate	157	11.4	0.21	4.9

TABLE 3.1 - Summary of the principal properties of the four materials studied relevant to the present work. All measurements were made at room temperature (20 °C), except those for Rochelle Salt which were made at 4 °C. The spontaneous polarisation Ps and coercive field Ec were measured directly off the oscilloscope display of a 0.1Hz hysteresis loop for typical samples of the material about 1mm thick.

(a) Sodium potassium tartrate hydrate $NaKC_4H_4O_6.4H_2O$
(Rochelle salt)

A number of large crystals of Rochelle salt were available, and samples were cut from these. These crystals had been grown many years previously and no information was available about them. Rochelle salt is grown from water solution (Cady 1946) and the crystals all contained small water inclusions, typically about a tenth of a millimetre across, which were easily visible under a microscope. It was not possible to cut a completely inclusion-free sample from any of the crystals available.

Rochelle salt has a monoclinic crystal structure (point group 2) between -18°C and +24°C, where it is ferroelectric (Jona and Shirane 1962). In this phase, the polar axis is the unique two-fold a-axis (with Rochelle salt, the notation for the crystallographic axes in the non-polar orthorhombic phase is customarily retained for the polar phase: according to the conventions for monoclinic crystals, this axis should be designated the b-axis). A Laue photograph taken in the direction of this axis is shown in Figure 3.3a. Since the upper Curie temperature is so close to room temperature, the crystal was cooled to around 10°C during the exposure of this photograph.

This material proved difficult to polish to a satisfactory finish. Polishing was carried out by hand on successively finer diamond polishing cloths (down to 1 micron), using Hyprez fluid as a lubricant, until an acceptable surface finish was achieved. A simple jig was used to ensure parallelism of the opposite faces. A little water could be added in the final stages to improve the finish, but over-polishing quickly led to a dimpled "orange-peel" effect on the surface. Rochelle salt is soluble in water and decomposes at temperatures above about 50°C. As the crystal contains water of crystallisation and effluoresces readily in excessively dry conditions, crystals of this material have to be stored and treated with care. Rochelle salt does not exist in an anhydrous form so that this effluorescence leads to

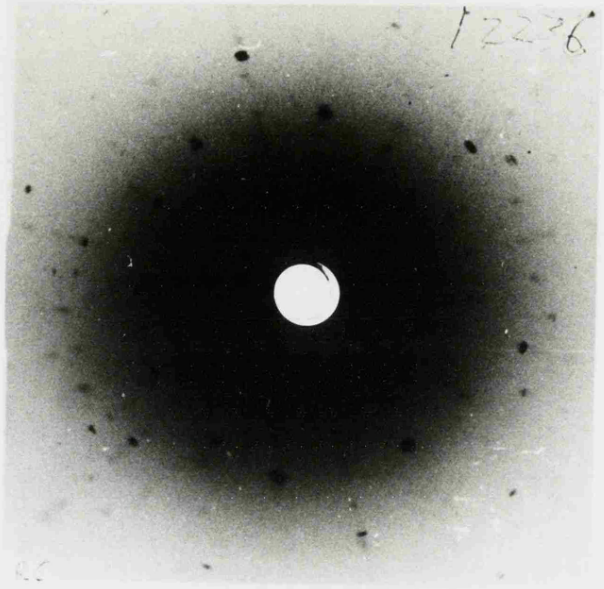

FIGURE 3.3(a) - X-ray Laue photograph taken down the polar a-axis in Rochelle salt, showing two-fold symmetry.

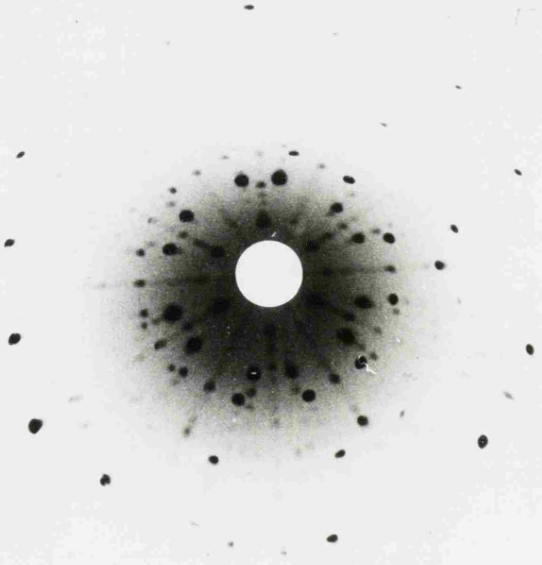

FIGURE 3.3(b) - X-ray Laue photograph taken down the polar c-axis in lead germanate, showing three-fold (pseudo six-fold) symmetry.

the decomposition of the crystal. The crystal also deliquesces under conditions of high humidity.

(b) Lead germanate $Pb_5 Ge_3 O_{11}$

Optical quality single crystals of lead germanate, grown by the Czochralski technique (Houlton et al. 1975) in boules ranging in size from 7x7x40mm to 40x40x100mm, were kindly provided by Dr. G.R. Jones of R.S.R.E. Malvern. These crystals were intended for use as targets in pyroelectric vidicon cameras for infrared imaging (Watton et al. 1976) and are among the most perfect examples of their kind ever grown. Since lead germanate has the trigonal point group 3 at room temperature, the polar axis lies in the [001] direction of the unit cell and exhibits three-fold symmetry. A Laue photograph taken along this axis is shown in Figure 3.3b. Although at first sight this seems to exhibit six-fold symmetry, there are a few weak reflections which appear only in positions of three-fold symmetry. In addition, the existence of antiparallel domains (with the c-axis reversed) also tends to give the crystal the appearance of six-fold symmetry about this axis.

Lead germanate is a difficult material to polish as it cracks readily under stress and so cannot be fixed to a polishing jig with adhesives. In the technique used, the cut slices were placed in a Tufnol template and polished on an expanded polyurethane or nylon polishing disc in a Buehler Minimet polishing machine, using "Cyton" fluid which gives a semichemical polishing action.

(c) Gadolinium molybdate $Gd_2(Mo O_4)_3$

A boule of gadolinium molybdate, approximately 11mm in diameter and 8mm long, grown by the Czochralski technique (Borchardt and Bierstedt 1966) was provided by Dr. G.R. Jones (R.S.R.E. Malvern). At room temperature the crystal structure is

orthorhombic (point group mm2). The polar axis in this ferroelectric phase is the two-fold c-axis. A Laue photograph taken down this axis is shown in Figure 3.4a. Although classed as orthorhombic, the unit cell is almost tetragonal as the a- and b- axes differ in length by less than 0.3% (Jeitschko 1972), and this gives the Laue photograph the appearance of four-fold symmetry.

This material presented no particular polishing problems. The cut slices were mounted in a jig using cyanoacrylate adhesive and hand polished on successively finer diamond cloths (down to 1 micron) until a satisfactory surface finish was achieved. For visual observation of domain walls, some samples were polished to a higher standard using 14 and 6 micron diamond in "Hyprez" fluid on a Logitech PM2 precision polishing machine.

(d) Terbium molybdate $Tb_2 (Mo O_4)_3$

This material resembles GMO very closely in its physical properties (Borchardt and Bierstedt 1967) and samples were prepared in a similar fashion. Fragments of Czochralski-grown boules of terbium molybdate were made available by Dr. G.R. Jones (R.S.R.E. Malvern) and several samples could be prepared from these. A Laue photograph taken down the polar axis is shown in Figure 3.4b. The crystal structure is almost identical to that of GMO which accounts for the similarity of this photograph to Figure 3.4a.

3.3 Acoustic Emission Transducers.

The transducer is the heart of any acoustic emission system, as it converts the mechanical energy of the incident ultrasound into electrical impulses for amplification and processing. The vast majority of transducers used for acoustic emission work rely

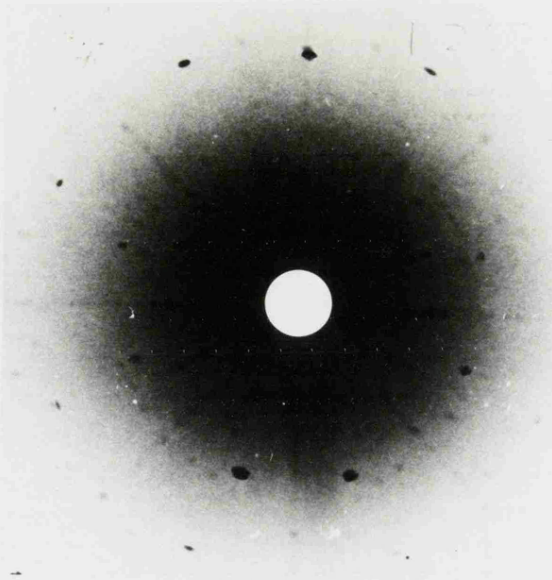

FIGURE 3.4(a) - X-ray Laue photograph taken down the polar c-axis in gadolinium molybdate, showing two-fold (pseudo four-fold) symmetry.

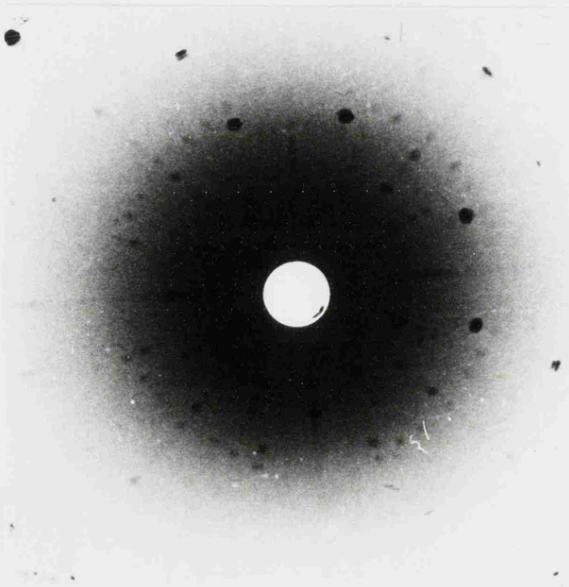

FIGURE 3.4(b) - X-ray Laue photograph taken down the polar c-axis in terbium molybdate.

on the piezoelectric effect. These types of transducer offer a high sensitivity, small size and a large degree of mechanical ruggedness essential in industrial applications. However they suffer from a poor frequency response and each transducer must be individually calibrated, as the performance depends on the behaviour of the piezoelectric sensing element and its mounting.

There are two other types of transducer also worth mentioning, as they overcome both these drawbacks. The first uses optical laser scanning of the displacements of the lower surface of the sample produced by the acoustic waves (Kline and Green 1978) and therefore directly measures the amplitude of these waves. The second, the capacitance transducer, uses these minute displacements to effectively change the gap of a parallel-plate capacitor, one surface of the sample forming one plate of the capacitor. This change in capacitance can be translated to a voltage pulse for amplification. This method has been brought to a high degree of perfection by Scruby et al. (1978). Their transducer has been used by Abey (1979) to detect AE from ferroelectric lead germanate with some success. The output of this type of transducer is very low (of the order of nanovolts) and special electronic techniques must be used to amplify it with an acceptable signal-to-noise ratio. A low noise, high gain charge preamplifier specially designed for this purpose has recently been produced by E.M.I. Ltd. (Model 6306), so that the construction of a usable capacitance transducer for the detection of AE from ferroelectrics may now be a practical proposition.

Piezoelectric transducers generally exhibit a strongly resonant behaviour with peaks in the sensitivity at frequencies corresponding to the normal vibrational modes of the sensing element. In the transducers used for acoustic emission detection, the sensing element is in the form of a disc and exhibits a fundamental thickness resonance mode where the wavelength is twice the thickness of the disc. The response of such a transducer to an impulse is generally a damped sine wave as the sharp leading edge of the acoustic wave excites the sensing element to ring at its resonant frequency. This

technique permits the use of a high degree of amplification as heavy filtering can be used to isolate the narrow band of frequencies containing this resonance, thus improving the signal-to-noise ratio.

While resonant transducers offer the greatest sensitivity, most of the information regarding the frequency content of the incoming acoustic wave is lost. When this information is important, the use of a wideband transducer, with an electrical output which closely follows the form of the input acoustic signal rather than being dominated by transducer resonances, is essential. Various means of linearising the frequency response of piezoelectric transducers have been discussed by Brown and Weight (1974), but this type of transducer is fundamentally unsuited to this application and the best result is neccessarily a poor compromise between bandwidth and sensitivity.

The transducers used in this work were industrial types, based on the piezoelectric ceramic PZT-5 (a form of lead zirconate titanate). In these transducers, the actual sensing element is mounted in a metal case for protection and electrical screening (Figure 3.2b). The active surface of the transducer is made of a silicone rubber which couples acoustic energy to the sensor while affording mechanical protection. The transducers feature a differential output, with the sensing element electrically isolated from the case of the transducer which is connected to earth through the cable shield. The two electrodes on the sensor are connected to a differential amplifier through a two-way cable. As any electromagnetic interference would induce the same voltage in both leads and the differential amplifier responds only to differences between the two inputs, this configuration affords a high immunity to electrical noise pickup.

The transducers were all individually calibrated by the manufacturer against a known standard and a frequency response curve included with each unit. These curves are reproduced in Figure 3.5. For general counting purposes, a resonant

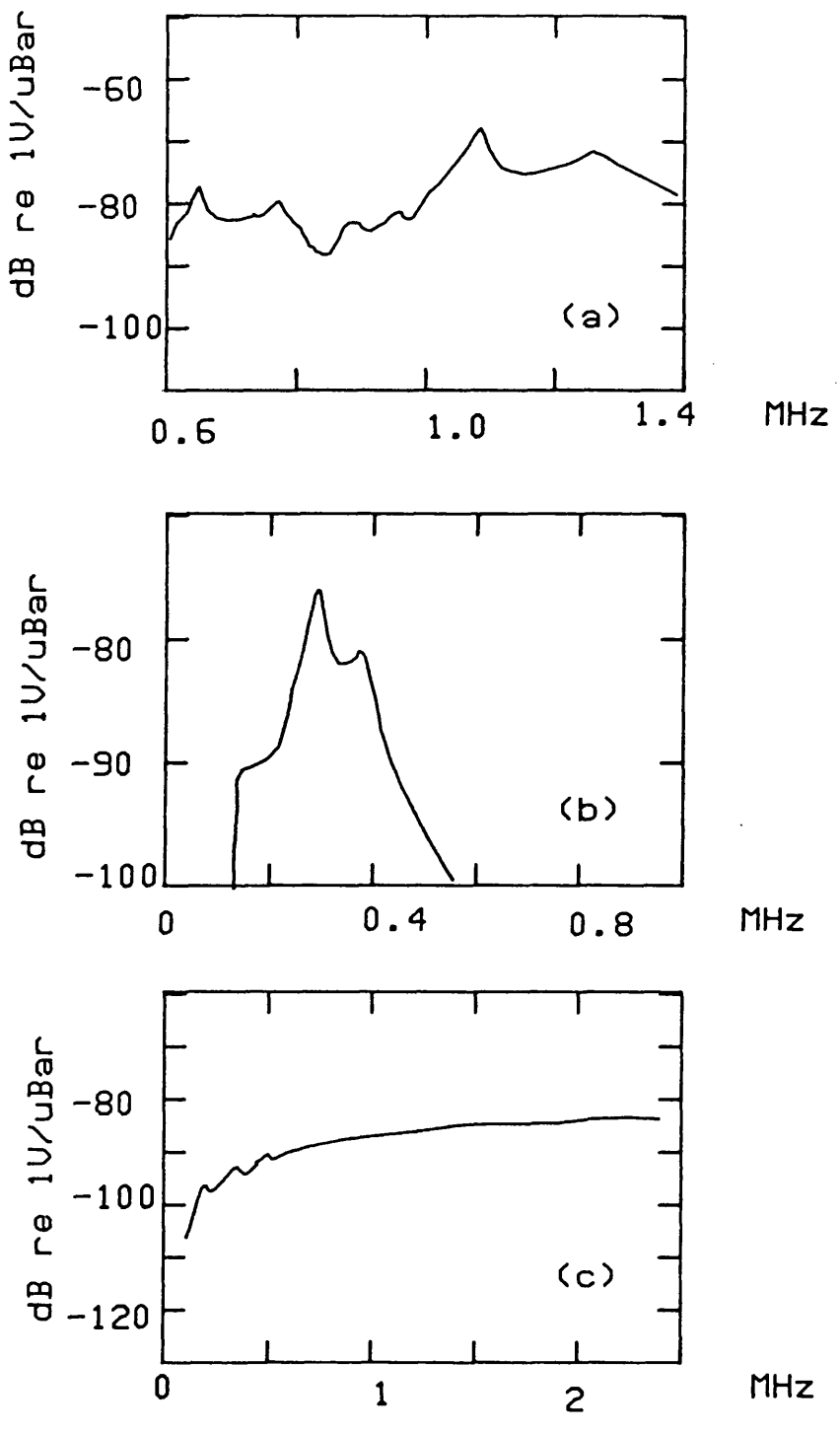

FIGURE 3.5 - Frequency response curves of the Acoustic Emission transducers used

(a) AECL AC1500L
(b) Dunegan-Endevco D140B
(c) AECL FAC500 wideband transducer

transducer was used as these give the highest sensitivity. Most of the measurements were performed using an AECL 1500L transducer which had a nominal resonance frequency of 1.1MHz and a bandwidth of 600kHz to 1.4MHz. In some cases, such as with thicker samples which produced AE of a lower average frequency, a Dunegan D140B transducer was used. This transducer had a resonance frequency of 225kHz with a bandwith of 100kHz to 500kHz. When the actual waveform of the AE signal was to be recorded, an AECL FAC500 wideband transducer was used. This transducer had an essentially flat frequency response between 500kHz and over 2MHz. As Figure 3.5 shows, this transducer exhibited a sensitivity of about 25dB less than the resonant transducers, when the latter were operated at their resonant frequencies.

3.4 Coupling.

The bond between specimen and transducer plays an important part in the transfer of acoustic energy from one to the other. A simple solid-solid interface is particularly poor in this respect as it may contain voids or air gaps, so a coupling fluid is used between the two. The effects of the couplant medium and the thickness of the bond on the transmission of acoustic emission across an interface have been studied by Hill and El-Daridy (1977). They conclude that in certain cases the sample-transducer interface can influence markedly the sensitivity and overall performance of the measurement system. Therefore it is essential to obtain a reliable bond before performing any acoustic emission measurements.

To obtain a good bond, both transducer and specimen surfaces must be flat, clean and free of dust. Care was therefore taken to avoid scratching either sample or transducer surfaces. Before forming a bond, the two surfaces to be mated were carefully swabbed with acetone to remove surface dust and left to dry. A small amount of couplant fluid was then applied to

both surfaces and then the sample was pressed down on the transducer surface, with a slight sliding motion to expel any trapped air. It is essential that only a thin film of couplant remains between sample and transducer, as the attenuation of sound in the fluid is relatively high. If an acoustic waveguide is used, the above considerations apply to both the sample-waveguide and the waveguide-transducer interfaces.

The coupling media used were silicone (stopcock) grease and a special couplant fluid made by Acoustic Emission Consultants Ltd. (type SC3). The former was by far the most convenient to use and proved perfectly adequate as a bonding material. The latter had a very high viscosity and retained its viscosity even at high temperatures, so it was used in most of the temperature dependence measurements. In use, no differences in performance between the two coupling media could be observed.

3.5 Signal Amplification and Counting.

The output from an AE transducer is of the order of microvolts, and so has to be amplified before it can be processed. As a piezoelectric element is basically a charge source, it is highly sensitive to capacitative loading from cables and amplifier inputs. To avoid problems of this kind, a specially designed low-noise preamplifier is placed close to the transducer and connected to it by as short a lead as possible. The signal is then fed to the main amplifier, which can be conveniently sited some distance from the transducer.

The Acoustic Emission Consultants Ltd. Model 105 Stress Wave Processor was used to amplify and process the AE signals. This system consists of a main amplifier/counter unit and a matched preamplifier which has a fixed gain of 40dB and features a differential high impedance input stage to match the piezoelectric transducers. The main amplifier has

switch-selectable gain which can be varied from 0 to 65dB in steps of 1dB. The gain of the amplifier is calibrated to an accuracy of 0.1%. A schematic diagram of this system is reproduced in Figure 3.6.

The first step in processing the amplified signal is to filter off unwanted parts of the frequency spectrum. Usually, low frequencies are susceptible to mechanical noise while high frequencies may contain mains-borne interference or unwanted transducer resonances. Therefore the Model 105 contains four switch-selected bandpass filters of known response to modify the basic 20kHz to 2MHz response of the unfiltered amplifier.

At this point the AE signal has an amplitude of several hundred millivolts and is in a suitable form for display on an oscilloscope or digital storage on a transient recorder. The Model 105 provides an audible indication of acoustic emission by mixing this signal with an internally generated beat frequency. The unit also incorporates counter circuitry to provide a quantitative measure of the AE signal. The counter outputs are available in binary form for digital recording, and an analogue output is also provided to drive a chart recorder. A timer is provided to reset the counter at preset time intervals so that the counter output indicates the average count rate over the selected time interval.

There are two methods of deriving a count from an acoustic emission signal. The first, known as ring-down counting, involves counting the number of times the signal exceeds a preset threshold level. In the idealised case, where an acoustic impulse excites the transducer to ring at its resonant frequency, the amplifier output is an exponentially damped sinusoid (Figure 3.7a). In general, such a signal may exceed the threshold more than once and therefore one event can register as more than one count (Figure 3.7b). As a large impulse will record more counts than a small one, the ringdown count provides an estimate of the acoustic energy incident on the transducer (Harris and Bell 1970). If two events overlap,

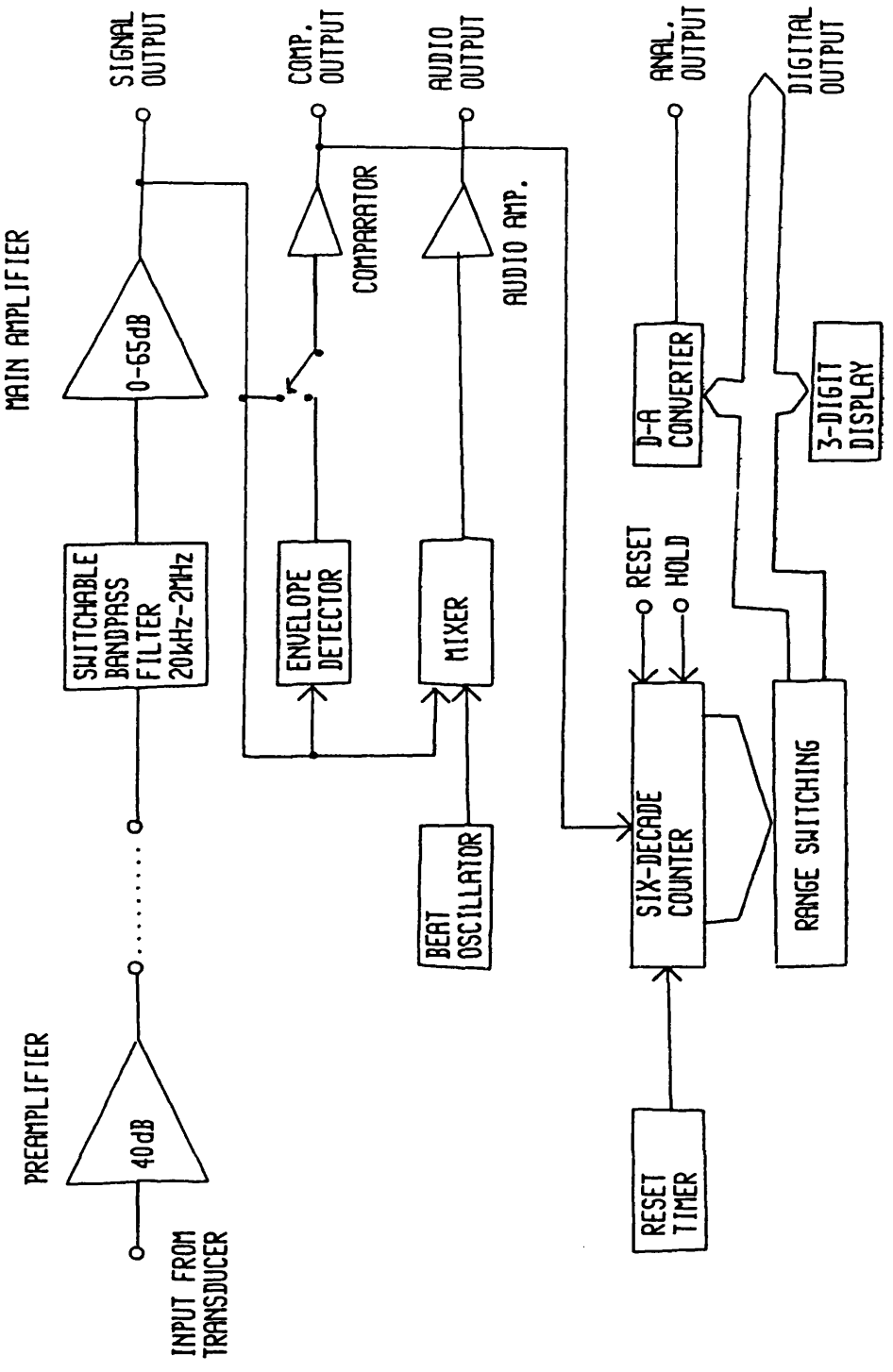

FIGURE 3.6 - Schematic diagram of the AECL 105 Acoustic Emission signal processor.

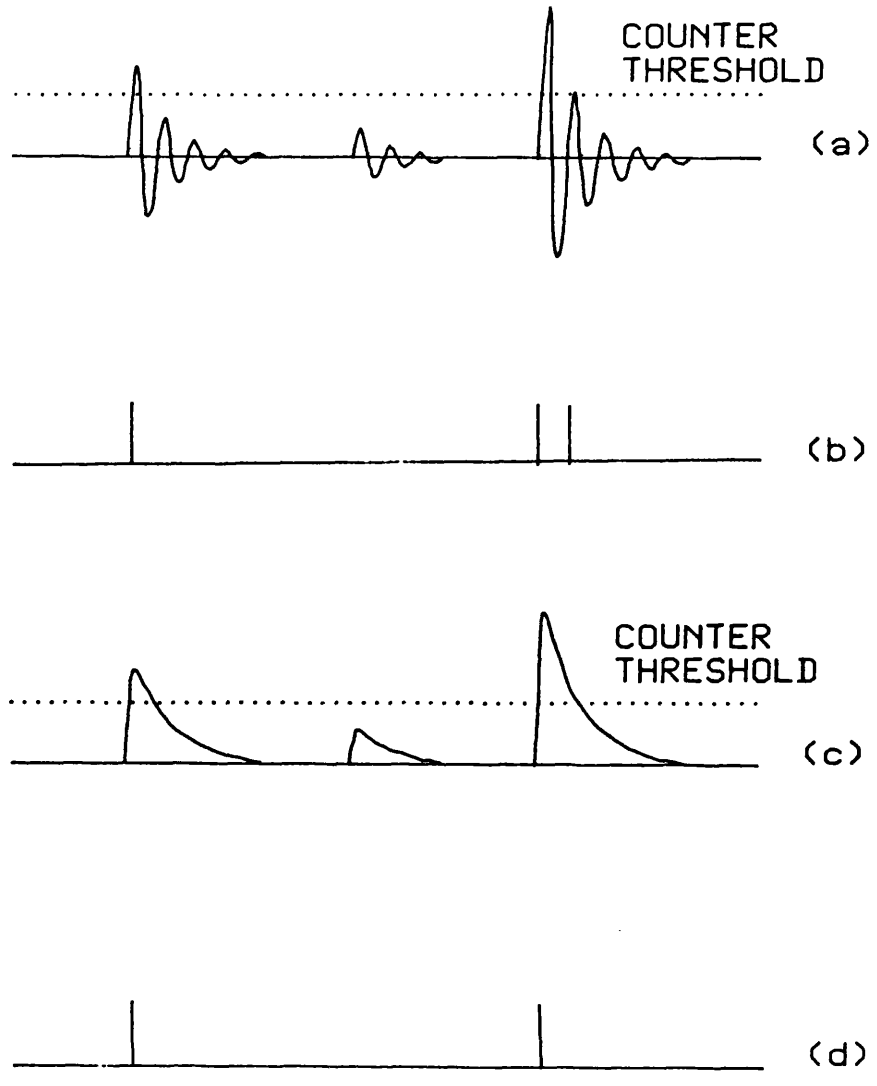

FIGURE 3.7 - Acoustic Emission counting techniques.
(a) The idealised transducer output consists of a train of damped sinusoids.
(b) The ringdown count is the number of times the signal crosses a preset threshold level.
(c) Envelope detector output for the signal in (a).
(d) The event count is the number of times the envelope of the signal crosses the threshold.

then in general the ring-down count will be higher as the two signals add algebraically, reflecting the fact that more energy is incident on the transducer.

The second method, known as event counting, passes the signal through an envelope detector (Figure 3.7c) so that each impulse is counted only once (Figure 3.7d). The envelope level must fall below the threshold before a new event can be counted. Any information about the size of the AE signal is lost. This method only works well in the idealised case. If two or more events occur in close succession, the envelope detector output will follow the sum of the two sinusoids and the counter may only count one event. This dead time can be several microseconds long and may introduce a considerable error at high count rates. The situation is complicated by the fact that real signals do not always approximate to damped sinusoids. In practice, the event count rate was generally found to be very erratic and so ringdown counting was more commonly used.

Counting techniques are no longer so commonly used in AE non-destructive testing as they are being superseded by the so-called energy analysis of the AE pulses (Williams 1980). The principle behind energy analysis is that the energy contained in a signal is the area under a graph of the square of the amplitude against time. By squaring and integrating the signal from the transducer, a measure of the acoustic energy incident on the transducer may be obtained. As an AE energy processing unit was not available, it was not possible to assess the utility of this relatively new technique as applied to the measurement of AE from ferroelectric crystals.

The ringdown count rate for a given signal is a function of the amplitude of the signal and the threshold level at which the counter is set to operate. As a typical AE signal consists of a series of distinct bursts, comparing count rates for different threshold levels yields information about the amplitude distribution of the signal. Although the threshold level in the Model 105 was internally preset at 1.0V, a similar effect could

be obtained by varying the gain setting of the amplifier and hence varying the signal amplitude with respect to this threshold. This process was limited by noise and overloading at one extreme and losing the signal completely at the other. However a plot of the count rate as a function of amplifier gain resulted in an acceptable cumulative amplitude spectrum of the input signal.

A typical AE measurement consisted of averaging the count rate over a period of time as a function of amplifier gain setting and other experimental parameters. Therefore it was an ideal subject for computer control. Although the AECL Model 105 was not designed to be externally controlled, it was modified internally to interface with the Hewlett Packard 9825A minicomputer through a 98032A 16-bit I/O interface. This enabled the computer to control the gain setting of the amplifier and all the counter functions, and to read out the counter contents when a count had been completed. Details of the interface and the software required for a typical experimental run are given in Appendix B.

3.6 Digital Signal Processing.

The amplified AE signal could be digitised and stored on a Datalab DL920 transient recorder. This instrument samples the input signal at a maximum rate of 20MHz (50nS per sample) and stores it in a digital memory as a sequence of up to 4096 8-bit words. The stored information can then be played back at a slower rate on an oscilloscope or on a chart recorder for a permanent record. Thus it is an ideal instrument for use in AE work, where the signal occurs in distinct, randomly spaced bursts so that the more conventional techniques of recording and signal processing cannot be used.

The transient recorder is particularly suited to recording single-shot events because of its pretrigger function. In this

mode the memory recirculates continuously and is only stopped after the trigger pulse, so that it is possible to observe not only the triggering event itself but even for a preset time in advance of it. This window into the past is not obtainable with conventional storage oscilloscopes, which all too often miss out the leading edge of the desired signal.

The DL920 transient recorder was connected to a matching DL4000 data processing system, based on the DL450U microprocessor unit. The functions of this unit and its application to the analysis of acoustic emission signals have been discussed by Mohamad (1980). This system was mainly used to perform fast Fourier transforms (FFT) on the acoustic emission signal to evaluate its frequency spectrum. However this unit was limited in its capabilities as it could only output results to a chart recorder. Therefore the DL920 transient recorder was also interfaced to the HP9825A minicomputer, which provided mass storage of the digitised signals, processing of the stored data (including FFT's), and printing or plotting of the final results in a suitable format. Details of this interface and driving software are given in Appendix C.

The transient recorder was also used in the investigation of the switching transients and Barkhausen pulses in ferroelectrics by connecting it to the circuits providing the high-voltage driving field to the crystal. While the transient recorder did not have the speed of a fast storage scope, the pretrigger facility was invaluable for the storage and display of Barkhausen pulses, which are of very short duration but widely spaced out in time.

3.7 Hysteresis Loop Circuit.

A ferroelectric is characterised by having a spontaneous

polarisation which can be reversed by the application of an electric field. This polarisation normally cannot be measured directly as any surface charge on the material is neutralised by the motion of free charge within the crystal and in its surroundings. However, this motion of charge which must accompany each polarisation reversal constitutes an electric current which can be measured. The first demonstration of polarisation reversal was in fact performed in this way (Valasek 1920). By repeatedly switching the polarisation in the sample, the resulting hysteresis loop can be displayed on an oscilloscope screen (Sawyer and Tower 1930).

The circuit actually employed, shown in Figure 3.8, differed from that of Sawyer and Tower in that one side of the crystal was connected to earth, as it was undesirable to have high voltages applied to the surface of the AE transducers. The voltage applied to the crystal was derived from the mains at a frequency of 50Hz. A step-up transformer (primary 250V, secondary 3000V rms) provided the necessary high voltage, while a variac was used to adjust the actual voltage applied to the sample. An RC filter was interposed between the transformer secondary and the sample to remove any mains-borne interference.

When an electric field is applied across the sample, any movement of charge in the crystal also appears on the reference capacitor C_o and develops a voltage across it. The voltage on C_o is proportional to the charge moved and therefore, as a first approximation, to the polarisation of the crystal. This voltage is applied to the Y-plates of the oscilloscope, while the sample voltage is applied to the X-plates. Thus, if an alternating electric field is applied to the sample, a plot of the polarisation $\underline{P}$ against the electric field $\underline{E}$ is continuously traced out on the oscilloscope screen. However, the polarisation $\underline{P}$ measures only the charge density on the sample surface whereas the movement of free charge round the circuit is governed by the electric displacement $\underline{D}$, where:

$$\underline{D} = \varepsilon_o \underline{E} + \underline{P}$$

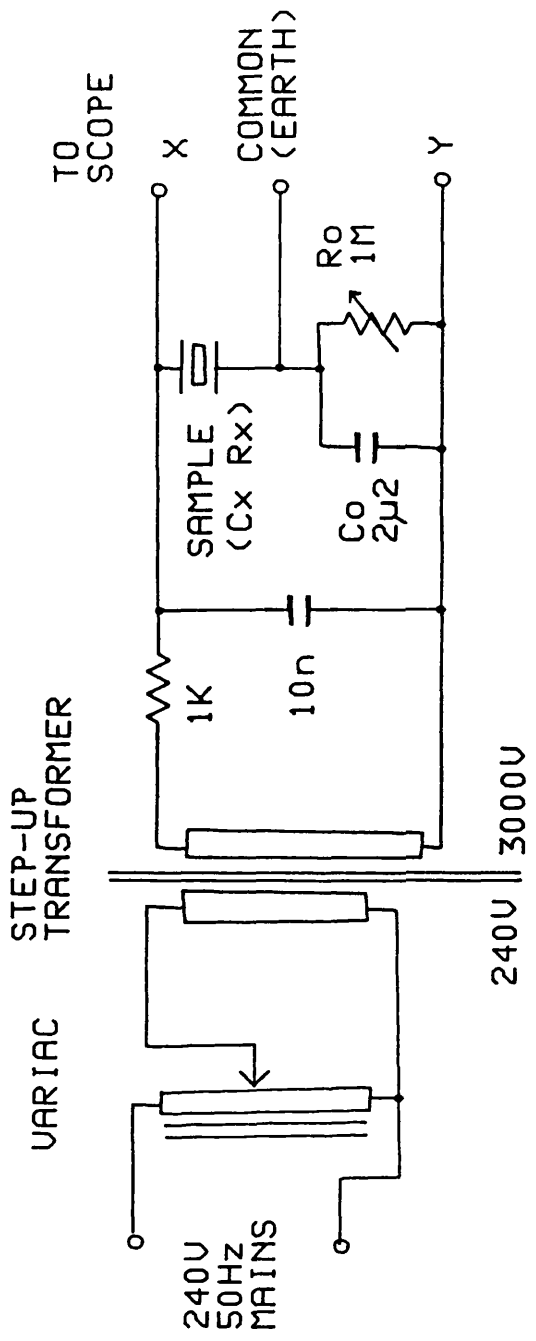

FIGURE 3.8 - Circuit diagram of the hysteresis loop generator (modified from Sawyer and Tower 1930).

This means that the voltage on C_o is not strictly proportional to the polarisation of the sample but carries an additional contribution of $\epsilon_o E$. At an electric field of 20kV/cm, the value of $\epsilon_o E$ is approximately 1.8×10^{-5} Cm^{-2}, while the lowest spontaneous polarisation P_s of the ferroelectrics studied is about 2×10^{-3} Cm^{-2}. Therefore, the $\epsilon_o E$ contribution is typically less than 1% of the total charge on the reference capacitor, and can be neglected unless accurate measurements are to be made from the hysteresis loop display.

The resistance R_o across the reference capacitor C_o serves to compensate for the resistive component (R_x) of the impedance in the upper branch of the circuit, which contains the sample. This resistive component includes both the linear dielectric loss in the sample and the shunting effect of the oscilloscope X-amplifier. The circuit must be compensated for these losses before any measurements can be made from the hysteresis loop display. The balance condition is given by the bridge formula:

$$R_x C_x = R_o C_o$$

In practice R_o was a variable resistor which was adjusted for the best loop shape on the oscilloscope screen. Figure 3.9 shows typical (a) uncompensated and (b) compensated hysteresis loops in Rochelle Salt.

In this work, the main function of the hysteresis loop circuit was to apply an alternating field to the sample so as to cause it to emit stress waves. The hysteresis loop display was mainly used to monitor the amplitude of the applied voltage and the timing of the AE relative to the hysteresis cycle. With the hysteresis loop displayed on one trace of a two-channel oscilloscope, and the AE signals on the other, the two could be superimposed by switching the scope Y-amplifier to the "ADD" mode. In this mode the display clearly shows the phase relation of the AE bursts to the hysteresis cycle. A typical example (from lead germanate) is shown in Figure 3.9c.

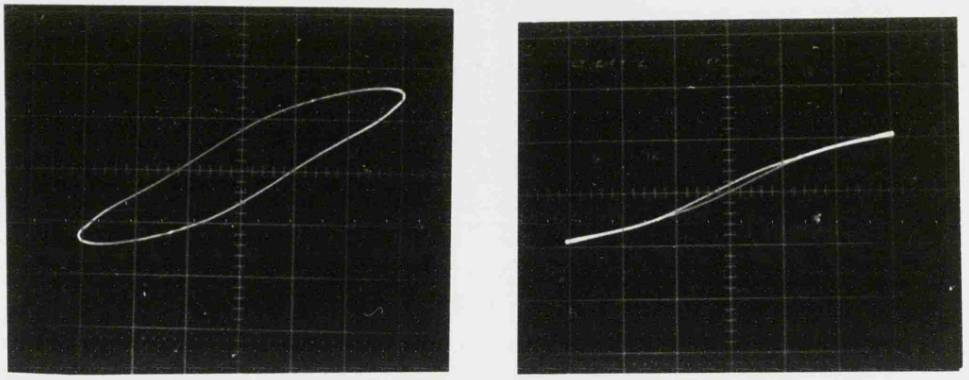

(a) (b)

Horizontal scale 200V/cm per div.

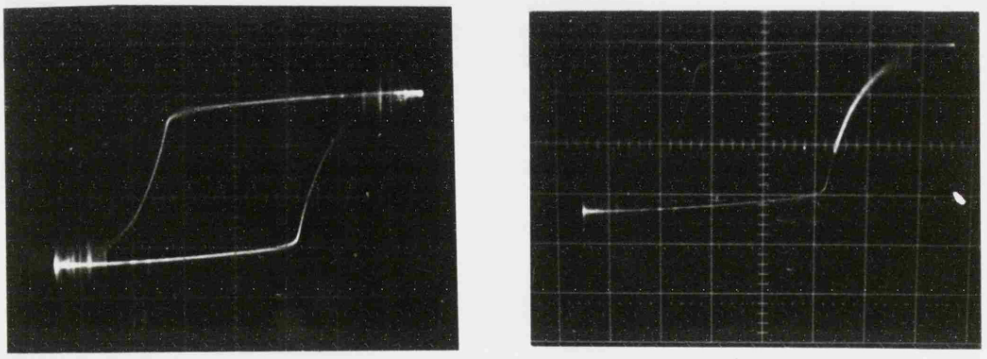

(c) (d)

Horizontal scale 2000V/cm per div.

FIGURE 3.9 - Typical hysteresis loops at 50Hz.
(a) Uncompensated Rochelle salt loop.
(b) RS loop compensated for crystal leakage.
(c) Lead germanate loop with superimposed A.E.
(d) Lead germanate loop with AE and counter gating pulse (brightened portion of loop).

In many circumstances it was required to gate the AE counter to operate only on regions of interest in the hysteresis cycle. To achieve this, a delayed pulse generator synchronised to the mains was used to provide a pulse suitable for gating the counter. A schematic of this unit is shown in Figure 3.10. The unit generated a pulse of variable width which could be positioned over any part of the loop by adjusting the delay from the triggering point, which was derived from the mains. This pulse was used to enable the counter and was also applied to the Z-modulation input of the oscilloscope to intensify the trace in the selected region. This effect is shown in Figure 3.9d, where only the AE bursts in the bright portion of the trace were counted.

3.8 High Voltage Power Supply.

The circuit described in section 3.7 could provide a wide range of voltages across the sample but was limited to the 50Hz sinusoidal waveform of the mains supply. To investigate the effects of the frequency and waveshape of the driving field, a high-voltage operational power supply system was constructed. This could provide a voltage of up to 2KV peak-to-peak, over a frequency range of DC to 200Hz, with lower voltages available outside this range, depending on the waveform used. The power supply was controlled by a conventional signal generator and could provide sine, triangular, trapezoidal and square waveforms, limited to a maximum slew rate of about 10V/μS.

A schematic of this power supply system is shown in Figure 3.11. The system was built around a Kepco OPS 5000-50 operational power supply which was capable of supplying up to 5000V at a current of 5mA. This unit consisted of an uncommitted preamplifier and a power output stage which were interconnected so that a small voltage at the input (0 to 5V) controlled the full 0 to 5000V swing available at the output.

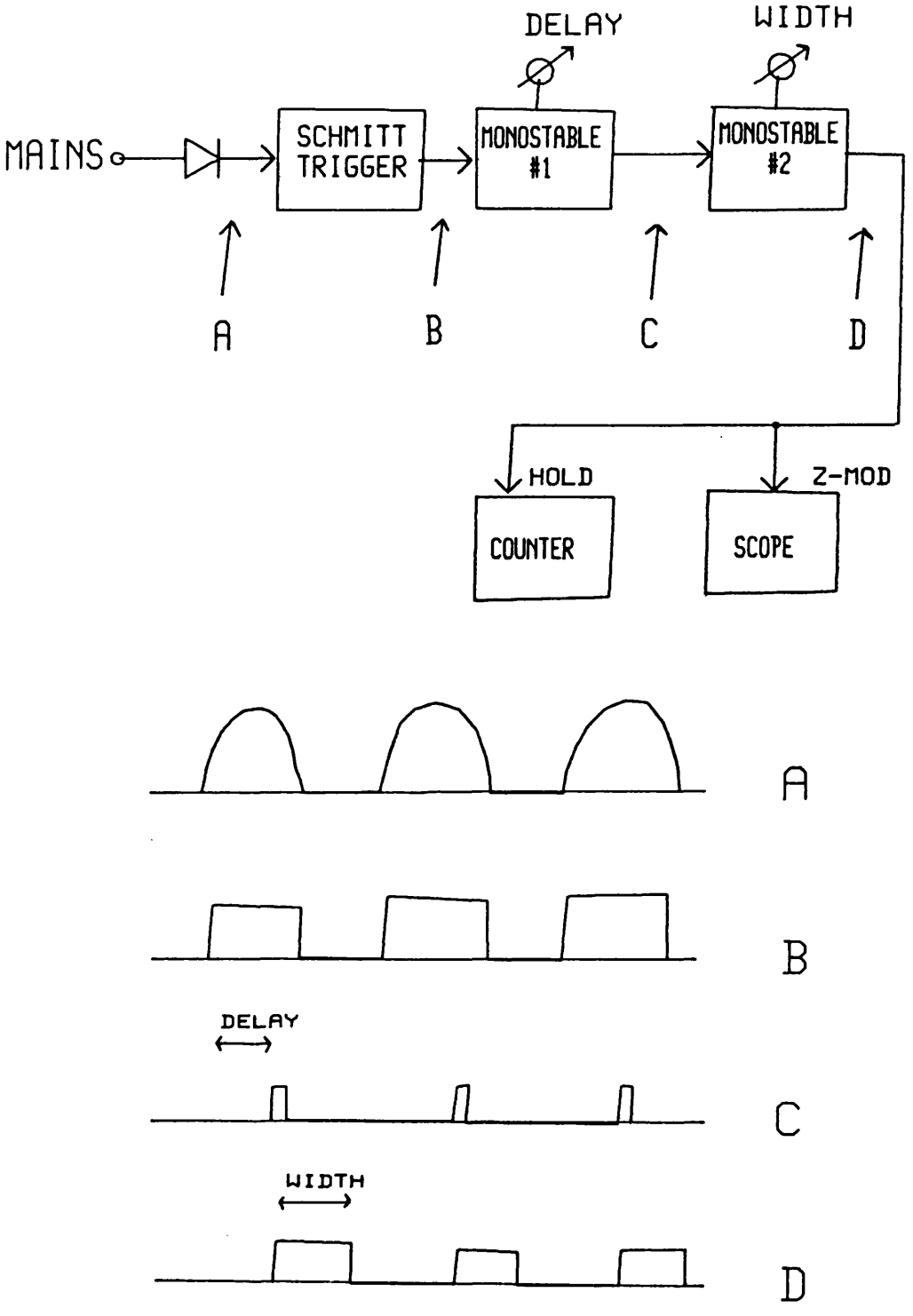

FIGURE 3.10 - Block diagram and principle of operation of the delayed pulse generator used to gate the A.E. counter in synchronism with the applied field.

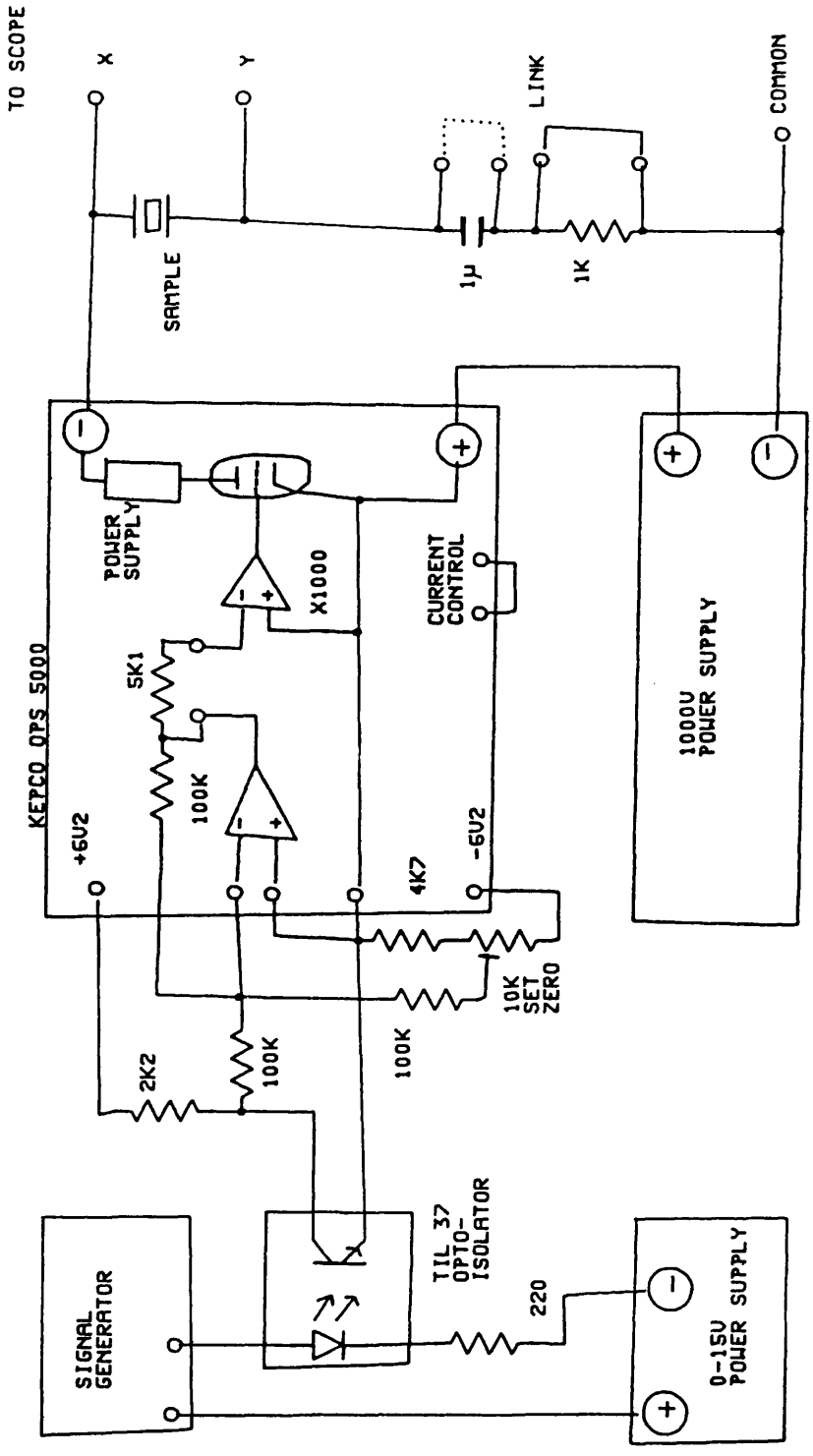

FIGURE 3.11 - Circuit diagram of the high voltage operational power supply capable of providing 2000V p-p at up to 200Hz. To investigate the switching pulse the link is replaced across the 1μF capacitor.

The control voltage was supplied by a Feedback Ltd. TWG 500 signal generator, which could provide the range of waveforms and frequencies required (sine, square, triangular or trapezoidal waves, from 0.001Hz to 1000Hz). For safety reasons, an opto-isolator was used to isolate the high-voltage side of the circuit from the signal generator. An additional low-voltage power supply (0 to 15V) was required to provide the correct bias voltage for the LED in the opto-isolator. If necessary, adjusting this power supply enabled the output waveform to be made asymmetric about ground.

While the voltage across the crystal must be able to swing both negative and positive to reverse the polarisation in the sample, the Kepco power supply was unipolar and could only provide a negative voltage. To obtain the required bipolar output, a Brandenberg 475R photomultiplier power supply was connected in series with the Kepco unit. The maximum offset which could be applied was limited to 1kV by the insulation rating of the Kepco supply, and this effectively limited the available output to 2kV peak-to-peak. Typical output waveforms from the power supply system are shown in Figure 3.12. Figure 3.12(d) shows the loading effect of a typical ferroelectric sample (nominal capacitance 100pF) on a 200Hz 2kVp-p square wave. The unloaded waveform is shown in Figure 3.12(c) for comparison. This waveform represents the upper frequency limit of the system and the loading effect decreases rapidly at lower frequencies.

The output from the power supply system was applied to the crystal via a Sawyer-Tower circuit. With this system, it was not possible to earth one of the crystal electrodes because one side of the Brandenberg power supply had to be connected to earth. In the circuit shown in Figure 3.11, the earthy side of the crystal is offset above ground by the voltage across the reference capacitor. Although this potential is very low (a few millivolts in practice), more care had to be taken with screening and with preventing short circuits to earth. A slight increase in the noise level in the AE system was also apparent with this arrangement.

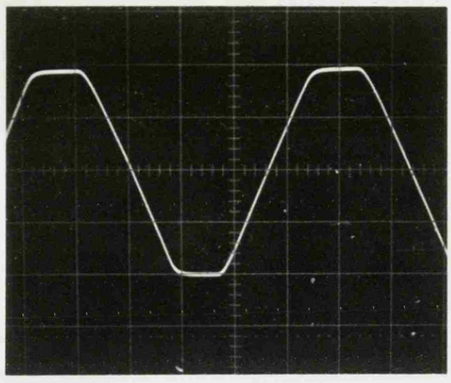

(a)

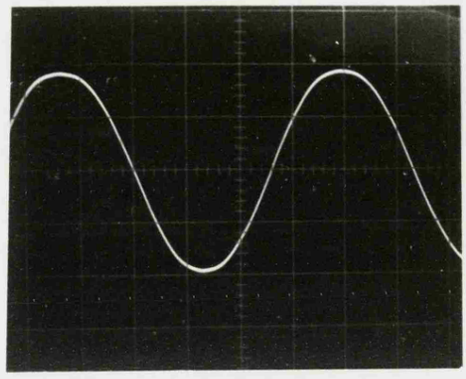

(b)

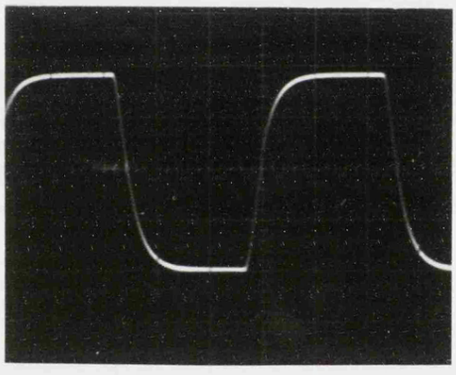

(c)

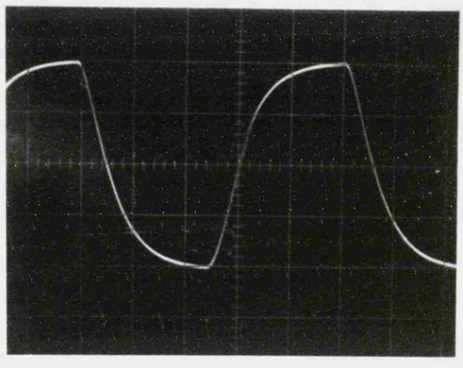

(d)

FIGURE 3.12 - Operational power supply output waveforms.
Vertical scale is 500V per division.
(a) 20Hz trapezoidal waveform.
(b) 20Hz sine wave.
(c) 200Hz square wave. This represents the upper frequency limit of the system.
(d) 200 Hz square wave showing the loading effect of a typical ferroelectric sample.

By using this power supply, hysteresis loops at very low frequencies (down to 0.001Hz) could be obtained. Such low frequencies were required to minimise the frequency dependent errors associated with the measurement of some ferroelectric properties, such as the saturation polarisation Ps. A storage oscilloscope was used to display the loop in these cases, and a high-impedance buffer interposed between the Y-amplifier input and the reference capacitor in the Sawyer-Tower circuit which would otherwise discharge in the long time period between polarisation reversals.

In the configuration shown in Figure 3.11, the circuit functions as a normal hysteresis loop generator. If however the shorting link is removed from across the resistor and placed across the capacitor, the circuit then becomes suitable for the study of switching transients (Fatuzzo and Merz 1967). In this case the voltage across the resistor is proportional to the switching current through the crystal, and thus to the rate of change of polarisation. This arrangement is also suitable for the investigation of Barkhausen pulses (Abe 1956), in which case the output is connected to the transient recorder so that the non-repetitive impulses can be studied. In this mode, the operational power supply serves to provide either a slowly-changing voltage or a step function, as required, by the simple manipulation of a low-voltage control.

As the operational power supply system had so many interrelated controls, and as in most cases the symmetry of the applied field about earth was of great importance, a simple oscilloscope display was no longer sufficient to set up the required voltage swing across the sample. Therefore a circuit was constructed to measure the magnitude and offset of the output of the power supply system and display the two readings on separate indicators. The schematic for this unit is shown in Figure 3.13. Two peak detectors were used to measure the positive and negative peaks of the signal (relative to ground). The algebraic sum of the outputs of the peak detectors

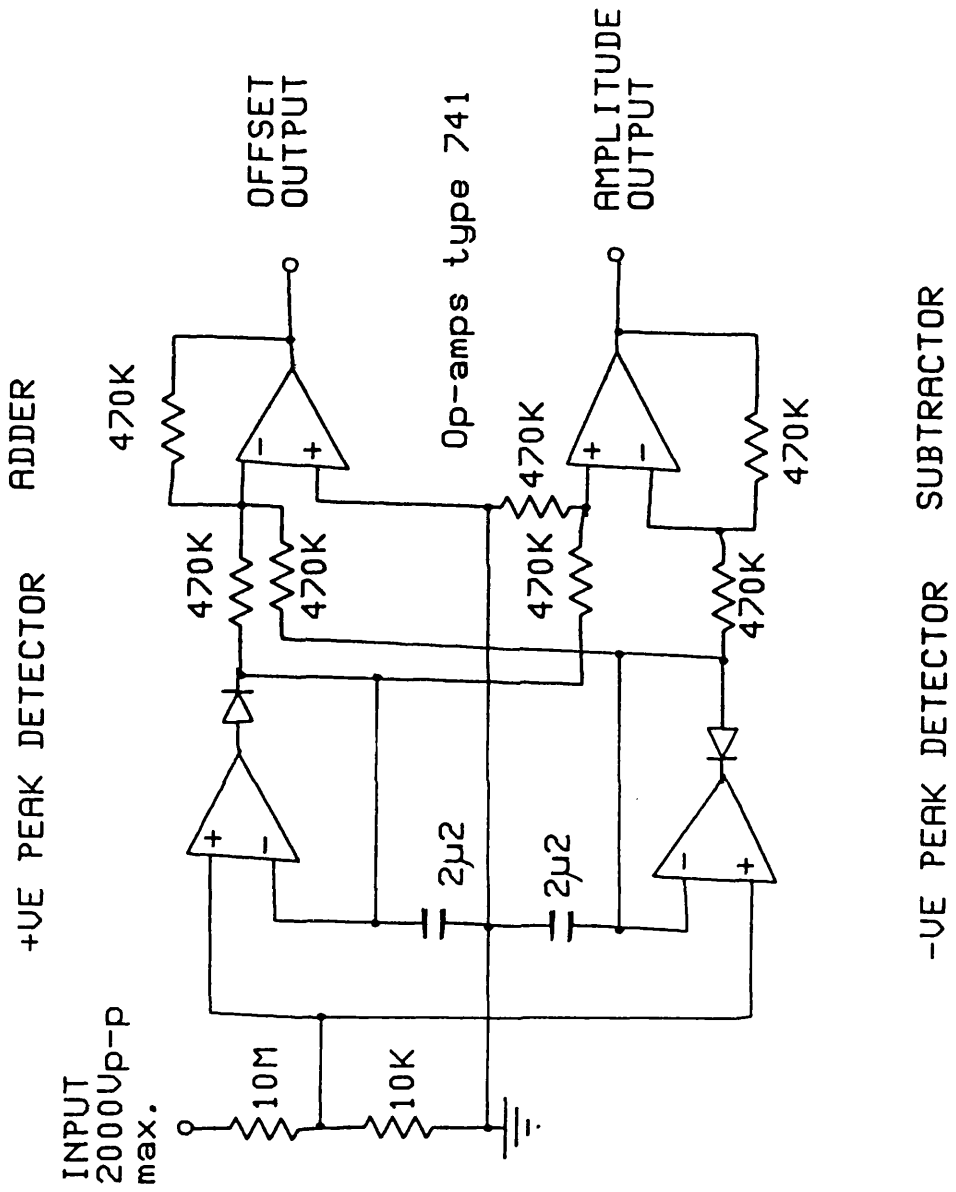

FIGURE 3.13 - Circuit diagram of the dual peak detector used to measure the output amplitude and offset of the high voltage operational power supply.

represented the offset of the signal about earth while the difference gave the peak-to-peak amplitude. The time constant of the peak detectors was set to about half a second, which enabled the indicators to respond to control changes at a reasonable rate, while retaining the accuracy of the unit at frequencies down to about 2Hz.

Due to the wide range of frequencies available with the operational power supply system, the delayed pulse generator used to gate the acoustic emission counter with the mains-driven circuit was no longer adequate. With this system, a Farnell PG5122 pulse generator, triggered by a square-wave output from the signal generator, was used to provide the delayed gating pulse.

3.9 Controlling the Sample Temperature.

While the majority of the acoustic emission experiments were carried out at room temperature, it was often required to change the temperature of the sample, and to be able to take the crystal through its ferroelectric phase transition(s). For lead germanate this occurs at around 180°C, while for gadolinium and terbium molybdates the transition is around 160°C. For these materials, a vertical furnace capable of reaching 250°C was used.

This arrangement is illustrated in Figure 3.14. As the transducer could be damaged by temperatures above 60°C, an acoustic waveguide was used to carry the emissions from the hot sample to the transducer which was kept at room temperature. This waveguide was 24cm long and was turned from a solid bar of aluminium. Aluminium was selected for the waveguide material as it has a very low ultrasonic attenuation in the frequency range of interest. The upper and lower surfaces of the waveguide, where an acoustic bond had to be made, were polished flat on 600

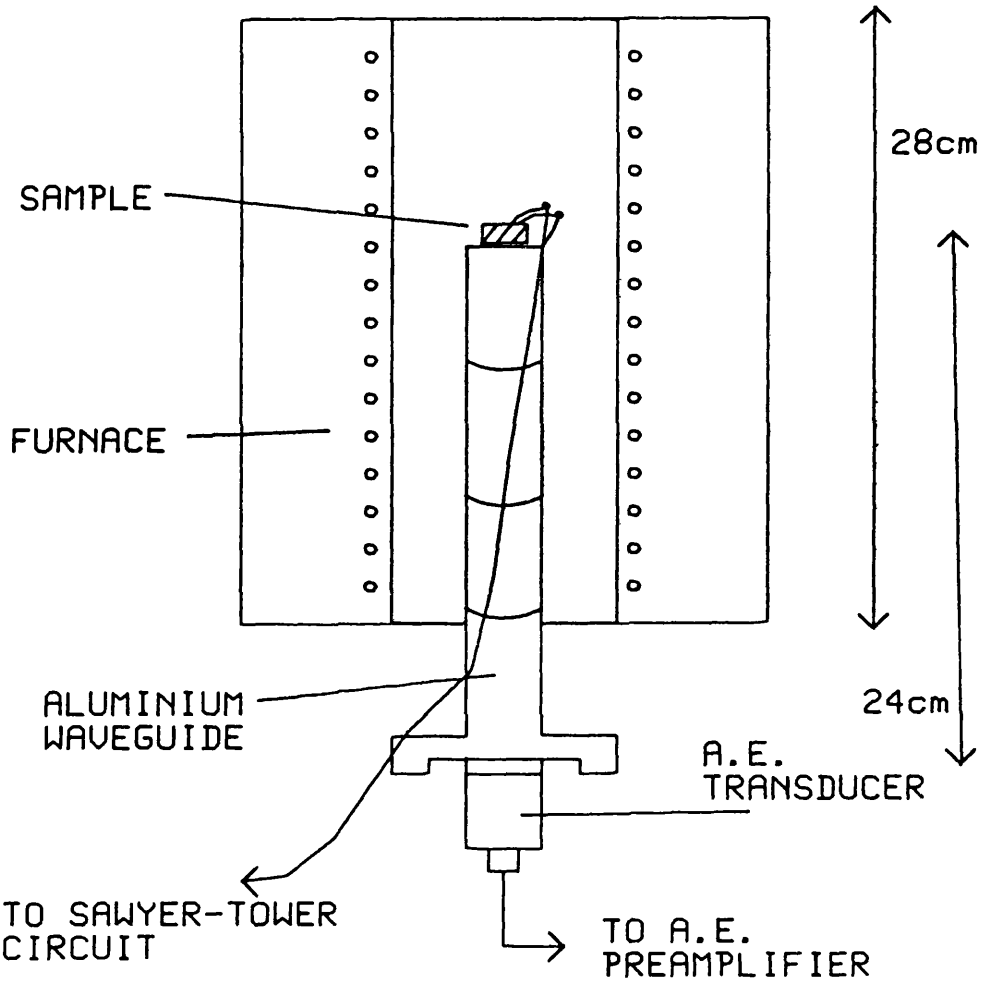

FIGURE 3.14 - Sectional diagram of the vertical furnace and acoustic waveguide used for A.E. measurements at temperatures of up to 250°C.

grit aloxite. As the waveguide was earthed, the upper surface was given a thin coat of black paint to insulate it from the sample. A thermocouple was attached to but electrically insulated from the sample by a small blob of silicone rubber. The sample electrodes were soldered to a pair of PTFE-insulated wires which were tied to the side of the waveguide. These wires were then connected to the high voltage supply leads from the Sawyer-Tower circuit outside the furnace. The waveguide, with the sample mounted upon it, was inserted into the furnace from beneath. The transducer was then attached to the bottom of the waveguide using a strong rubber band. When operating with sample temperatures above 150°C, enough heat was conducted down the waveguide to raise the temperature of the transducer surface above its rated maximum of 60°C. In these circumstances a small electric fan was used to cool the transducer to an acceptable temperature.

Various means of stabilising the furnace temperature were tried. Although a commercial temperature controller (Eurotherm PID/SCR) provided the best temperature stability (better than 0.1°C), the thyristor switches in this unit generated an unacceptable level of interference in the AE detection system. The method chosen used a stabilised DC power supply capable of providing 50V at 1A. This could provide sufficient power into the 40-ohm winding of the furnace to enable a temperature of over 250'C to be reached. With the furnace well insulated from its surroundings with ceramic fibre (Kaowool), the sample temperature was found to remain constant to within 0.3°C over a period of several hours, without adjusting the power supply.

One of the interesting features of Rochelle salt is that it has two transition temperatures and is only ferroelectric between -18°C and +24°C. To study this material over this temperature range, a thermoelectrically cooled chamber and temperature controller capable of covering the range -25°C to +50°C were constructed. This unit was based on a Cambion 806-1006-01 watercooled thermoelectric module which had a heat capacity of 10W. As the capacity of the module was so limited,

the enclosure had to be well insulated and as small as possible to miminise heat leakage. Therefore the transducer was mounted outside the sample chamber, and an acoustic waveguide used to carry the AE to it. The waveguide had to combine low ultrasonic attenuation with a low thermal conductivity and Pyrex glass was chosen for this application. This waveguide was a cylindrical rod 35mm long and 11mm in diameter, with the ends hand polished to an optical finish on successively finer diamond polishing cloths (down to 1 micron), using a simple jig to ensure parallelism of the opposing faces. The sample chamber itself consisted of a small box (40 x 20 x15mm high) made of 0.5mm thick copper sheet with soldered edges, which was mounted on top of the thermoelectric module and coupled to the active elements by a thin layer of thermally conductive grease (Figure 3.15). The sample was mounted on the end of the waveguide, using the high-viscosity couplant SC3 to hold it in this inverted position. The whole assembly was surrounded by 50mm of styrofoam insulation. The thermocouple and high-voltage leads were taped to the side of the waveguide to reduce the number of apertures in the insulation. A thin mica plate was placed in the bottom of the chamber to prevent the lower surface of the crystal from short-circuiting to the earthed copper box.

In most cases, the convection of air within the sample chamber was sufficient to transfer heat to and from the sample, although as this process is not very efficient the sample could take several minutes to reach the desired temperature. When a faster settling time was required, the sample enclosure was filled with transformer oil. However, rapid temperature changes were generally avoided to prevent excessive thermal stresses being applied to the sample. Once the temperature had stabilised, the temperature difference between the upper and lower surfaces of the sample was found to be less than 0.1°C over the entire temperature range the module was capable of attaining.

The thermoelectric module required a bipolar power supply at currents of up to 10A. At a constant sample temperature, the current drawn by the module is a measure of the rate of heat

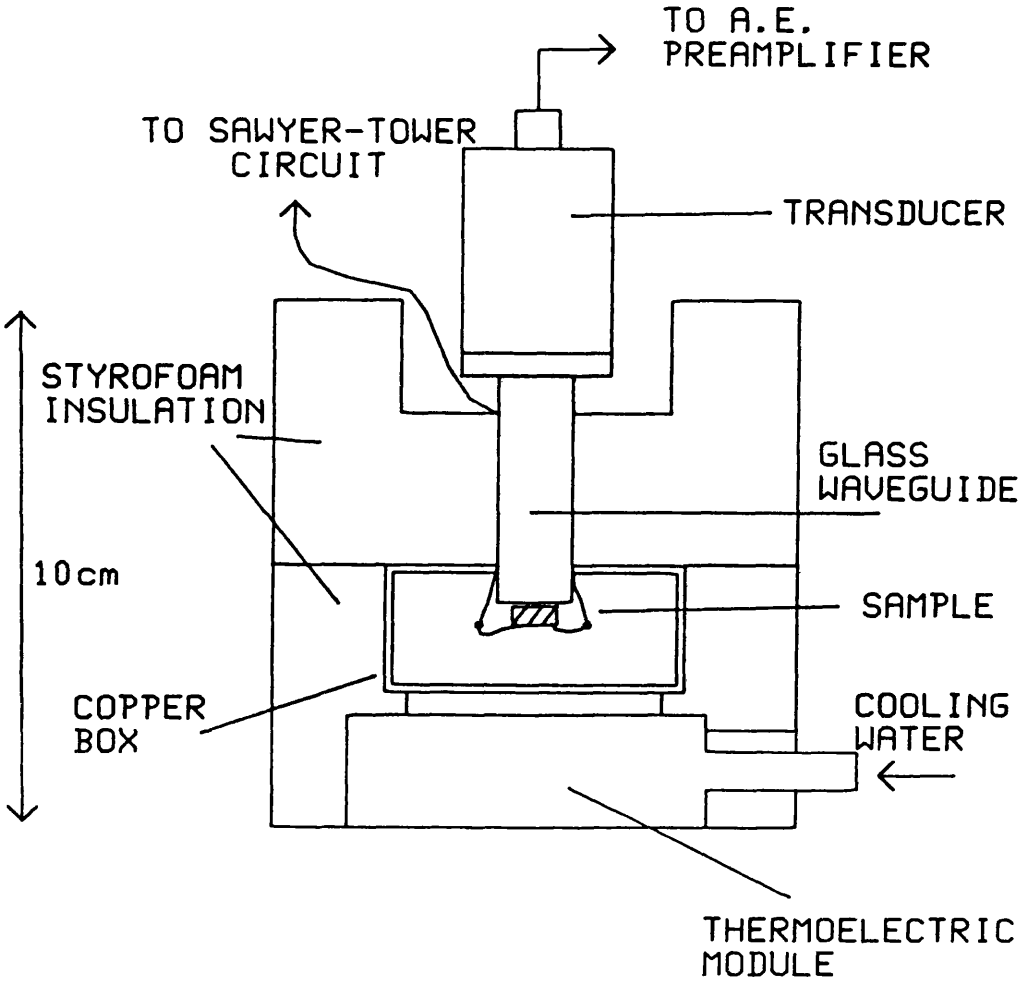

FIGURE 3.15 - Sectional diagram of the thermoelectrically cooled sample chamber used to cover the range -18°C to +24°C over which Rochelle salt is ferroelectric.

transfer through the module, so that a current-stabilised power supply was required. The circuit of the controller used is shown in Figure 3.16. A multi-turn potentiometer was used to set the module current in the range -10A (cooling) to +5A (heating). The controller circuit monitors the module current and adjusts the voltage across the module to maintain the selected current. This in itself proved sufficient to stabilise the chamber temperature to within 0.2°C, without any temperature feedback. An input was provided so that the module current could be modulated by an externally applied voltage. A slow ramp generator was available which could cover the entire temperature range in about 12 hours, at a fairly constant rate of change of temperature of about 0.1°C per minute.

As the thermoelectric module had a limited cooling capacity, the heat dissipated by the sample when an electric field was applied could adversely affect the temperature stability of the sample chamber. This was only apparent near the Curie temperatures of Rochelle salt, where the dielectric loss factor rises sharply. With a large electric field applied, it was not possible to reach the lower Curie point even with the module running at maximum capacity. Near the upper Curie temperature, the application of a sufficiently high electric field could result in thermal runaway, which generally resulted in the decomposition of the crystal. The linear dielectric loss of Rochelle salt is very low away from the transition temperatures. In the ferroelectric region, additional power is dissipated through the non-linear dielectric loss which is measured by the area enclosed within the hysteresis loop. In Rochelle salt, this reaches a maximum at around 0°C (Sawyer and Tower 1930). This power dissipation is low enough to be handled by the temperature controller, and the temperature stability at this temperature was found to be unaffected by the application of an electric field across the sample.

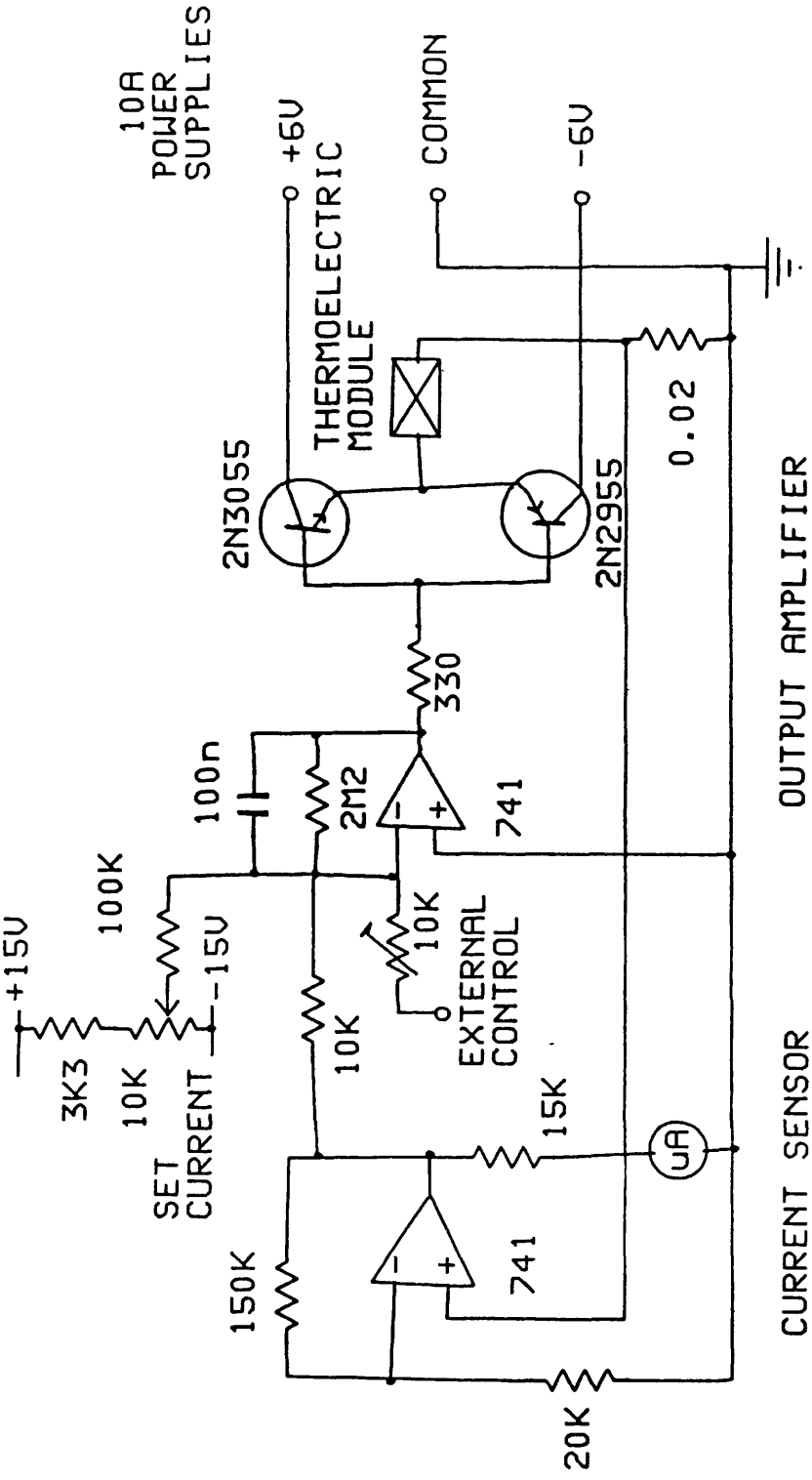

FIGURE 3.16 - Circuit diagram of the constant current thermoelectric module controller.

3.10 Problems Encountered with Acoustic Emission Measurements.

The problems associated with acoustic emission measurements could be divided into two groups: those originating from the limitations of the equipment and those arising from the nature of the sample and the phenomena being investigated. The major problem with the equipment, due to the low level of signal generated, was noise and interference. Since the AE signal is non-repetitive, conventional techniques such as signal averaging and phase-sensitive detection could not be used to improve the signal to noise ratio. The presence of an alternating high voltage in close proximity to the transducer also caused problems in this respect, and great care had to be taken to screen the sample, transducer and the connections between the various pieces of equipment. The high voltages involved also presented a safety problem, so that interlocks had to be incorporated to prevent the application of potentially lethal voltages while the sample was at all accessible.

In practice, the overall gain of the system had to be as high as 85dB (40dB in the preamplifier plus 45dB in the main unit) to detect the weakest signals. When the system was correctly set up and the transducer connected, a total gain of over 90dB could be achieved before the counter started counting on noise. The main source of noise at this point was in fact electrical pickup from nearby mains cables, and an excessively high noise level was generally due to a faulty interconnection between the transducer and the preamplifier. A quick test of the performance of the system could be made by lightly brushing the dry transducer surface with a fingertip. At a system gain of 80dB, this would cause several thousand (ringdown) counts to be recorded.

Although the transducers were supplied with individual calibration curves, it was not possible to compare directly results taken with different transducers. As far as possible, one transducer (AC1500L) was used for all measurements. As the transducer-sample interface could seriously influence results, a

standard coupling technique was devised (section 3.4) and applied in all cases. As far as possible, results to be compared were taken at one sitting and without disturbing the sample and transducer.

Since it was possible that the acoustic waveguides could influence results, a detailed examination of the transmission characteristics of the waveguides was made. The frequency spectrum of a simulated signal produced by lightly tapping the top of the Pyrex glass waveguide (the one used with the thermoelectric unit) with a screwdriver blade is shown in Figure 3.17a. The waveguide exhibits a strong resonance at 73.2 $\pm$ 2.4kHz, which is well below the working frequency range of the transducers and therefore should not influence the results. This frequency corresponds to the fundamental mode of vibration where the wavelength is twice the length of the cylindrical waveguide. The resonant frequency is given by:

$$f = \frac{v}{2\ell}$$

where ℓ is the length of the cylinder (35.9mm) and v the velocity of longitudinal waves in the material. For a thin rod, v is given by:

$$v = \sqrt{\frac{E}{\rho}}$$

where ρ is the density and E the Young's modulus for the material. The density and elastic constants can vary considerably with the composition of the glass, and most references (eg Yarwood and Castle 1979) give a wide range for these values. Typical values of E (6×10^{10} Nm^{-2}) and ρ (3×10^{3} kgm^{-3}) give a velocity of about 4500m/s and a resonance frequency of around 67kHz. To obtain a closer estimate, the velocity of longitudinal waves at 10MHz in the waveguide was measured using a pulse-echo technique and found to be 5469m/s, which gives a resonant frequency of 76.1kHz. However, the wavelength of these waves (around 0.5mm) is much less than the diameter of the waveguide (10.9mm) so that the thin rod

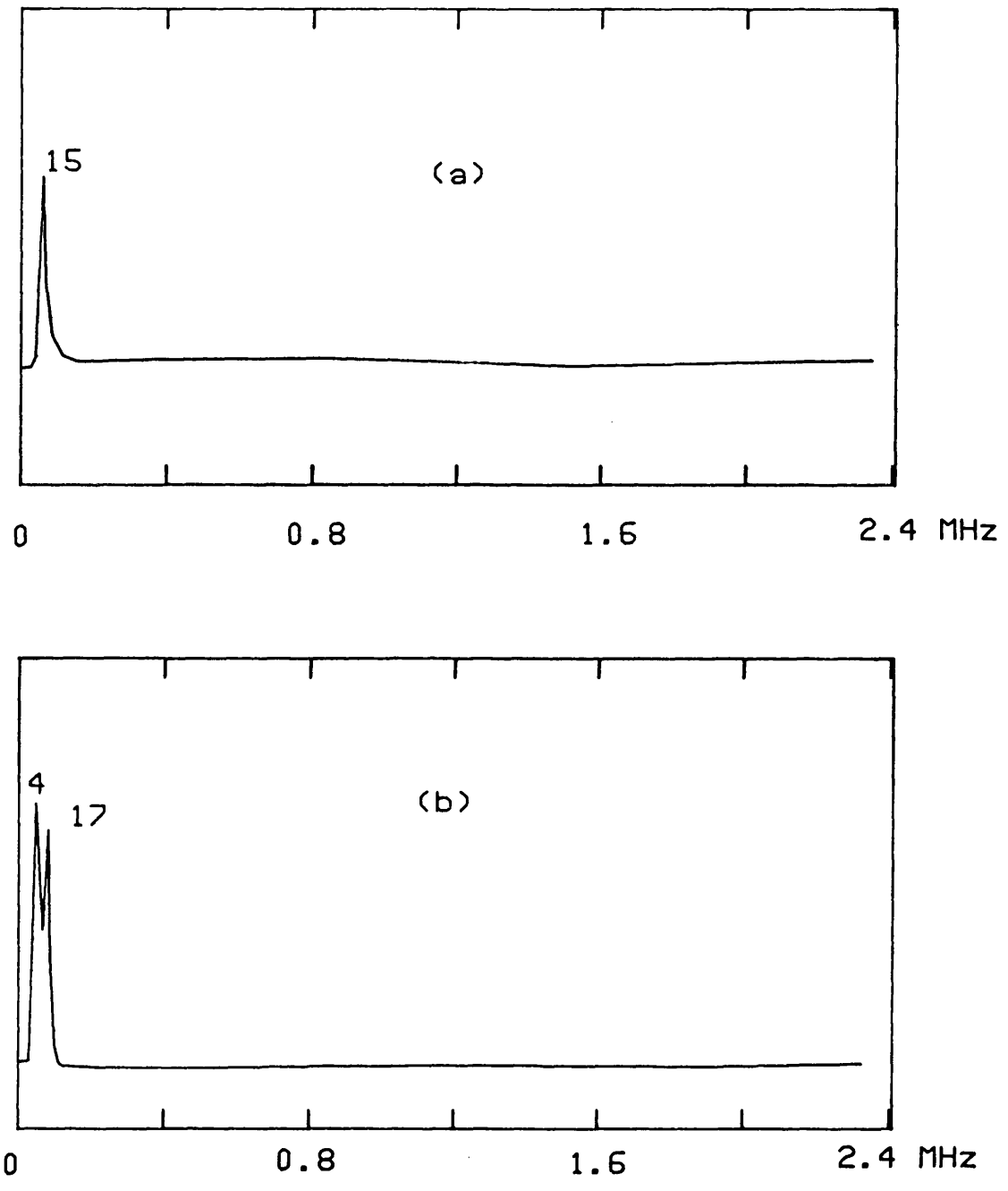

FIGURE 3.17 - FFT power spectra of simulated AE signals showing the resonance frequencies of the (a) Pyrex glass and (b) aluminium acoustic waveguides.
The numbers by the peaks refer to the cursor address on the peak and correspond to 4.88kHz per point.

approximation is no longer valid. The Young's modulus of the material can be calculated from a combination of the longitudinal and shear wave velocities c_ℓ and c_t (Pain 1970), and is given by:

$$E = \rho c_t^2 \frac{(3 c_\ell^2 - 4 c_t^2)}{(c_\ell^2 - c_t^2)}$$

The velocity of shear waves at 10MHz was also measured and found to be 3365m/s. Substituting into the above equation gives a velocity of 5203m/s and a resonance frequency of 72.5kHz, which agrees well with the measured value.

It was not possible to assess directly the effect of the waveguide on the shape of the received signal because individual AE impulses vary so much from one to the other. By comparing several events recorded with and without the waveguide, no significant differences in signal shape or frequency content that could be attributed to the waveguide (and not to natural variation) could be observed.

Again using the pulse-echo apparatus, the ultrasonic attenuation in the waveguide was estimated to be approximately 23% (2.3dB) for the round trip (twice the waveguide length). Assuming that the signal amplitude decays exponentially with distance and neglecting losses on reflection and at the waveguide-transducer interface, the attenuation after traversing the waveguide once should be half the dB value, ie around 1.1dB, corresponding to a loss in amplitude of about 12%. Experiments carried out with an emitting ferroelectric sample (a) placed directly on the transducer and (b) on the waveguide revealed that using the waveguide led to a reduction in count rate by approximately 20%. Alternatively, the same count rate could be maintained by increasing the amplifier gain by about 3dB. This means that the use of the waveguide reduced the signal amplitude by about 30%, much of which could probably be attributed to the additional interface between sample and transducer. These measurements were repeated at different count rates produced by

varying the amplifier gain and the sample voltage. In all cases, the effect of the waveguide was simply to reduce the count rate by about 20%. Figure 3.18 shows the variation of count rate with electric field for a Rochelle salt sample. Using the waveguide does not alter the shape of the curve but merely shifts it down the (logarithmic) count rate axis.

The characteristics of the aluminium waveguide used with the vertical furnace have been investigated by Mohamad (1980). His conclusion that this waveguide does not substantially alter the count rate nor the form of the received signals has been verified in independent experiments. The mechanical resonances of the waveguide, measured by taking the frequency spectrum of the signal produced by lightly tapping the waveguide end, were found to be at 20kHz and 83kHz (Figure 3.17b) and again are below the usable frequency ranges of the transducers.

As the acoustic emission occurs in sporadic bursts, counting had to be performed over an extended period of time in order to gather a statistically significant count. In addition it was desirable to segment the counting period into several smaller intervals so that any drift or excessive variation in the count rate could be signalled, as this would have led to an erroneous value for the mean count rate. In practice, measurements were generally taken over ten 10-second periods, although this was extended when very low count rates were encountered. The distribution of the individual counts was found to be approximately Gaussian in shape with the standard deviation generally lying between 5% and 20% of the mean. An excessively large standard deviation was generally due to mains-borne interference from other equipment (such as power tools) being used in the vicinity, or to an actual variation in the count rate either because the conditions of the experiment (temperature, voltage etc.) changed during the course of the measurement or because of the time-dependent effects discussed below. During the measurement period, a running mean was calculated and the variance of the individual counts evaluated as a measure of the uniformity of the count rate. At the end of the run, the final

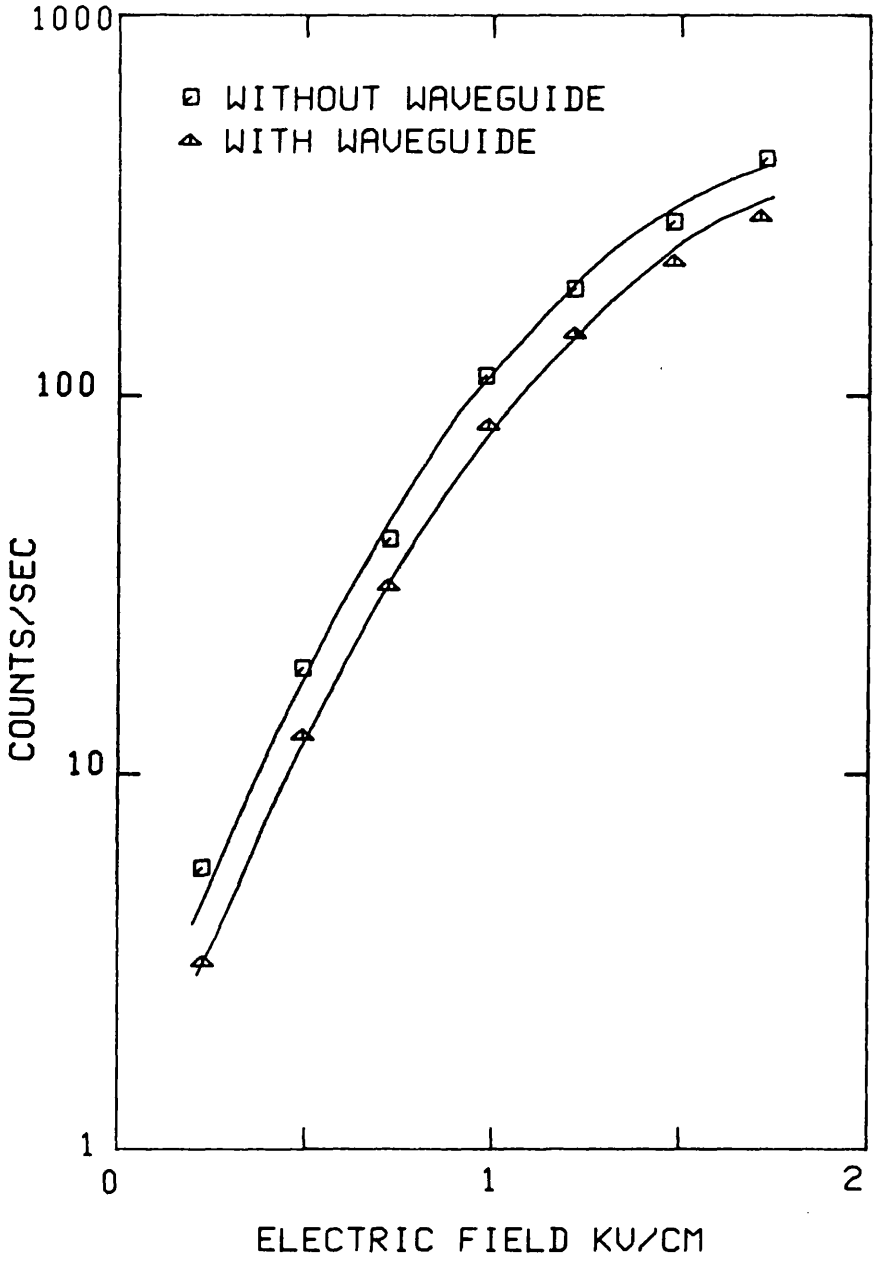

FIGURE 3.18 - AE count rate as a function of applied electric field for a Rochelle salt crystal. The effect of the Pyrex glass waveguide is to reduce the count rate uniformly by about 20%.

mean and standard deviation (calculated as the square root of the variance) were presented. The measurement was repeated if the calculated standard deviation exceeded 20% of the mean. The program listing in Appendix B was designed to perform this process automatically.

In addition to the statistical problem, the AE output of the sample is strongly dependent on its past history and on time. Figure 3.19(a) shows the variation of AE count rate with time for a lead germanate sample at room temperature with a 50Hz electric field of 15kV/cm peak applied across it. The sample was heated to above the Curie temperature for 2 hours and then left to cool slowly for 24 hours before the voltage was applied. This behaviour is typical of all the materials studied. The initial count rate is always very high, but usually stabilises after a few hours. It is essential that this plateau is reached before any measurements are taken. After about 300 hours (for this sample) the count rate becomes unstable and this is then generally followed by the destruction of the crystal.

The effect of changing the electric field is shown in Figure 3.19(b). A crystal of lead germanate, prepared as described above, was cycled at 15kV/cm for two hours. The electric field was then increased to 18kV/cm (at zero time on the graph). Immediately following the change, the count rate is unstable but usually stabilises within a few minutes.

As these time-dependent effects can seriously affect results, the following precautions were taken with each measurement:
(a) Before taking any measurements, the crystal was first cycled for at least 12 hours, at a sufficiently high voltage to ensure polarisation saturation.
(b) If the experiment was suspended for any reason (eg. overnight), the crystal was left cycling, again at a sufficiently high voltage to ensure saturation.
(c) When any experimental parameter was changed, the crystal was allowed to stabilise for at least an hour before resuming the measurements.

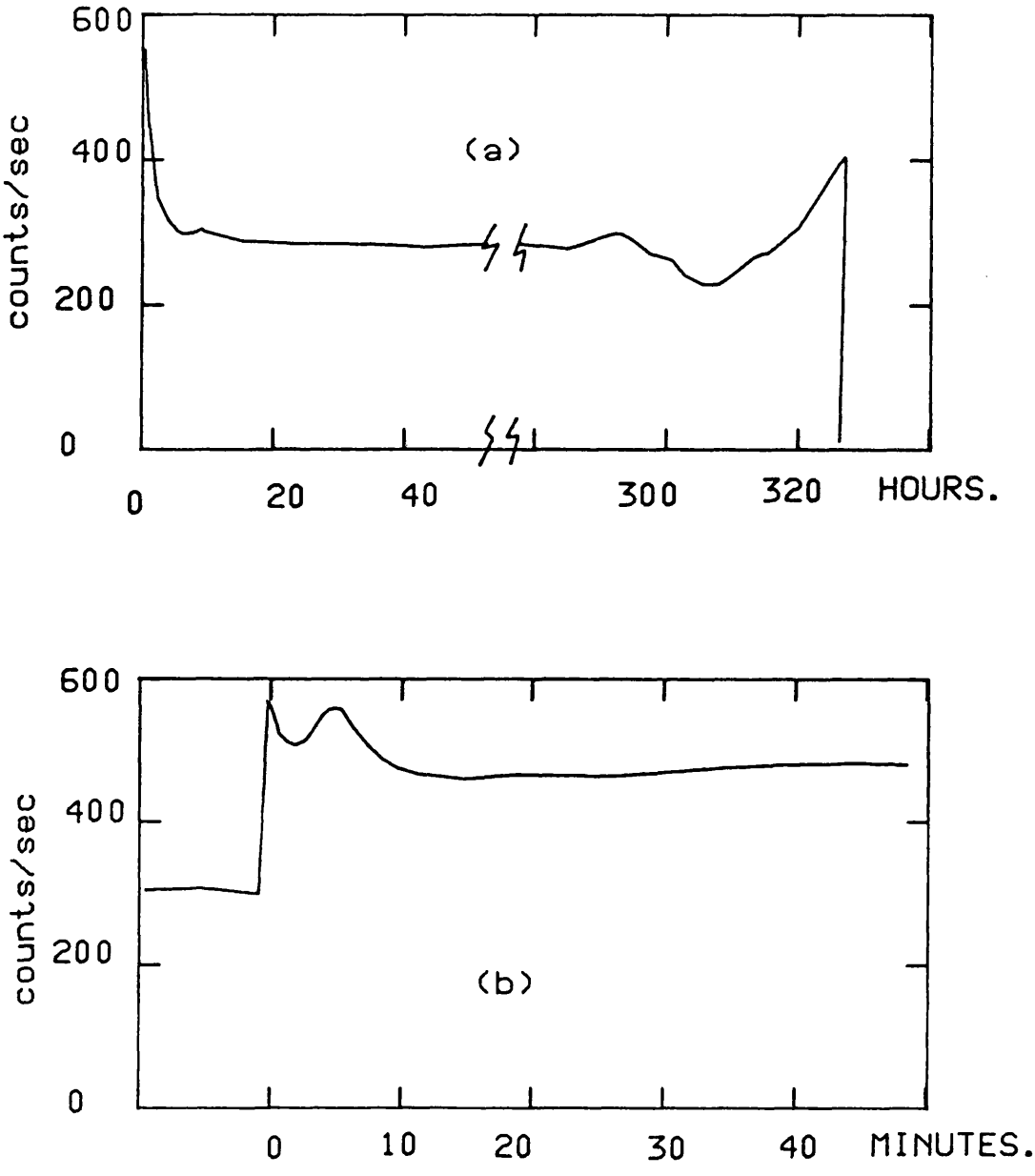

FIGURE 3.19 - Variation of AE count rate with time.
(a) Count rate from PGO sample cycled at 15kV/cm 50Hz. The crystal broke up after about 300 hours.
(b) Count rate from PGO sample cycled at 18kV/cm after being cycled at 15kV/cm for 2 hours. The count rate stabilises in about 10 minutes after which the crystal behaves as in (a).

CHAPTER 4 - ACOUSTIC EMISSION FROM FERROELECTRIC CRYSTALS.

We now turn to the experimental investigation of the acoustic emission produced by ferroelectric crystals undergoing polarisation reversal. The first sections of the chapter describe the AE signal in terms of its frequency and amplitude spectra and its timing with respect to the hysteresis cycle, and how these vary with the magnitude of the applied electric field. This leads to the concept of a threshold electric field below which no AE is produced. Various ways of determining this threshold field are described. The remainder of the chapter is devoted to a discussion of how the AE, and in particular the threshold field, vary with experimental parameters such as sample size, temperature and the frequency and waveform of the applied electric field.

4.1 - AE from Ferroelectrics undergoing Polarisation Reversal.

When a ferroelectric is cycled round the P-E hysteresis loop by the application of an alternating electric field, bursts of ultrasound are emitted. Figure 4.1a shows a typical loop from a crystal of lead germanate under the influence of a 50Hz sinusoidal electric field. The acoustic emission from the sample is superimposed on the hysteresis loop display as described in Section 3.9. The quantity of ultrasound emitted varies as a function of the amplitude of the applied electric field. Figure 4.2 shows the development of the hysteresis loop and AE from a lead germanate sample as the voltage is increased. From displays such as these, several observations can be made which indicate that the production of AE is closely linked to the process of polarisation reversal in the sample. These points are discussed in greater detail in the following sections of this chapter.

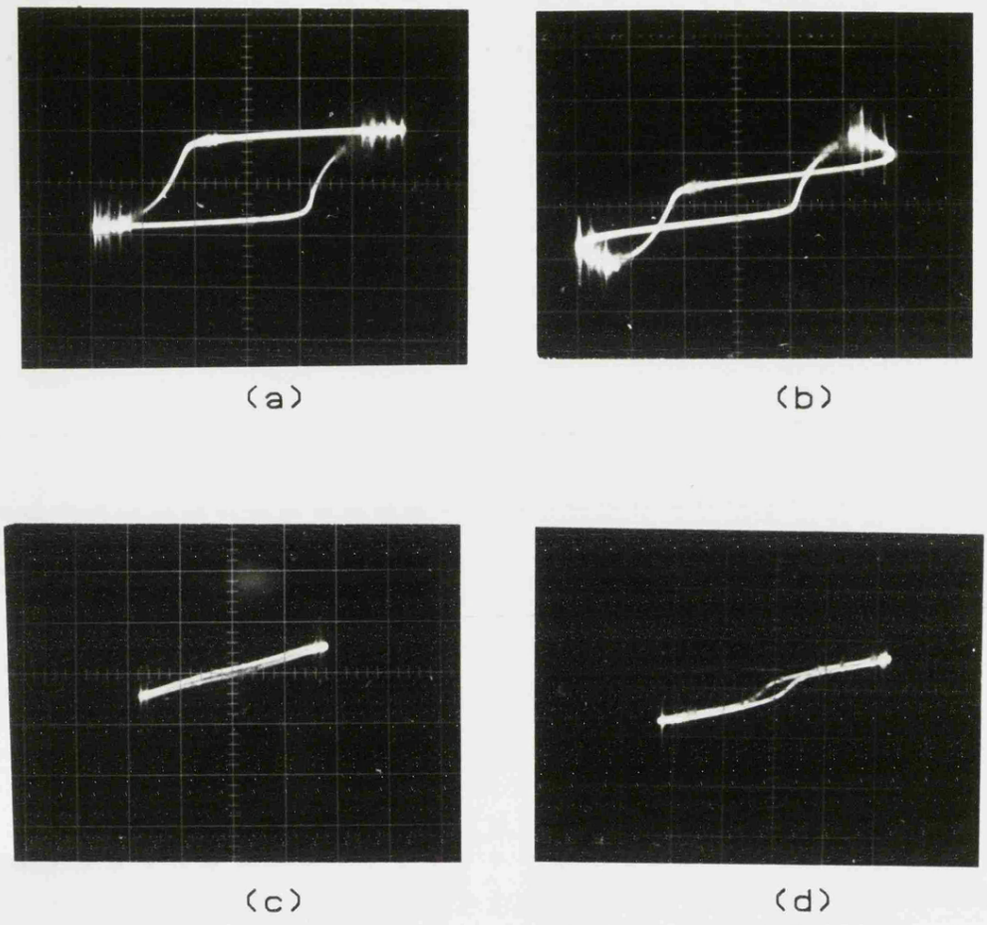

FIGURE 4.1 - Acoustic emission from ferroelectric samples cycled round the hysteresis loop at 50Hz.
(a) AE from lead germanate sample 1.13mm thick. Horizontal scale 500V/div.
(b) Lead germanate loop distorted to show the timing of the AE relative to the loop.
(c) AE from gadolinium molybdate sample 1.25mm thick. Horizontal scale 500V/div.
(d) AE from Rochelle salt sample 1.09mm thick, showing background AE all round the loop. Horizontal scale 100V/div.

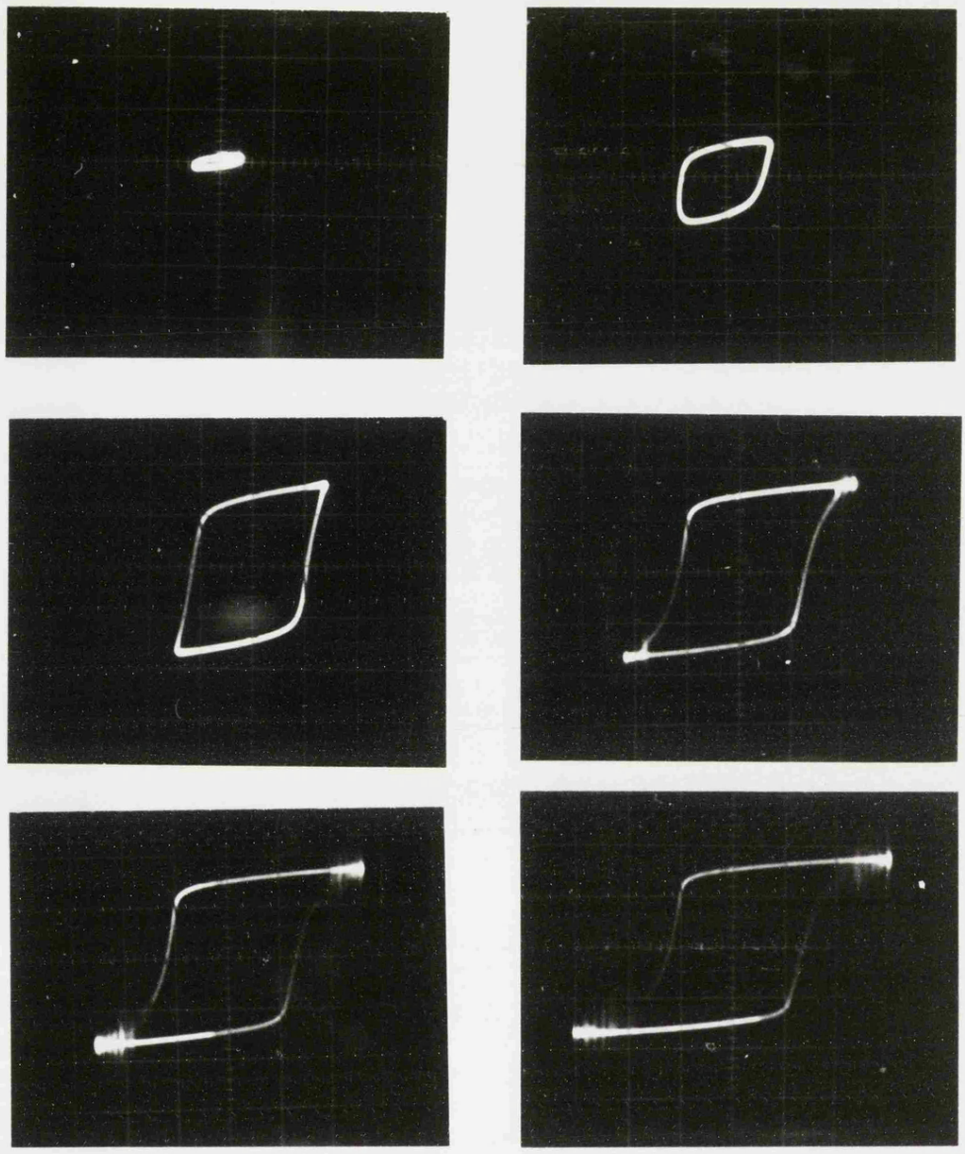

FIGURE 4.2 - Hysteresis loop with superimposed AE for a lead germanate sample 1.13mm thick as a function of the applied field.
Horizontal scale is 500V/div.
The AE first appears in the fourth photograph of the series at an applied field of around 10kV/cm.

(a) The emission occurs in a specific region of each hysteresis half-cycle, corresponding to the approach to saturation polarisation. In the oscillographs of Figures 4.1 and 4.2, the electron beam traces out the loop in an anticlockwise direction, so the AE occurs before, but not after, saturation is reached. The AE ceases once the saturation is achieved (which may occur before the electric field reaches its peak value in the cycle), and no further AE is generated until the polarisation has switched and saturation in the other direction is approached. No AE is observed on the flat portions of the loop, which correspond to saturation. This is clearly shown in Figure 4.1b, where the hysteresis loop display has been deliberately distorted by reducing the value of the compensating resistance in the Sawyer-Tower circuit (Section 3.7) below the optimum value which just balances the sample leakage. This causes the reference capacitor to discharge during the relatively long period of time when the sample is saturated and no movement of charge is taking place, thereby "opening up" the displayed loop.

(b) At a fixed amplifier gain, the observed number and amplitude of the bursts of ultrasound increase with the amplitude of the applied electric field. No AE is observed unless the amplitude of the applied field is sufficient to switch the polarisation in the sample, as indicated by a well-formed hysteresis loop. However, a well-formed loop is not a sufficient condition for the production of AE, as shown in Figure 4.2 for lead germanate where the AE onsets abruptly at some threshold voltage which is greater than that required to switch the sample. In the other materials studied, this threshold effect is not as abrupt as it is in lead germanate, but it is still present.

(c) The quantity of AE varies with temperature, going to zero at the Curie point. No AE is observed outside the ferroelectric region.

(d) No AE is observed when similar voltages are applied to non-ferroelectric samples (such as glass and mica) or to ferroelectric samples but at right angles to the polar axis.

These patterns of behaviour have been observed in a number of ferroelectric materials, including Rochelle salt, lead germanate, gadolinium and terbium molybdate and triglycine sulphate. Although different materials produce hysteresis loops with different shapes and require different voltages to induce polarisation reversal, qualitatively their behaviours are very similar.

A typical hysteresis loop from a sample of gadolinium molybdate is shown in Figure 4.1c. This loop is not fully compensated as insufficient adjustment was available in the Sawyer-Tower circuit with this sample. However, the occurrence of the AE at the ends of the hysteresis loop can be seen. The behaviour of terbium molybdate is essentially identical to that of gadolinium molybdate. A typical hysteresis loop from a Rochelle salt sample is shown in Figure 4.1d. With this material, a background of AE is observed throughout the hysteresis cycle in addition to the high-amplitude bursts which occur at the onset of saturation. These large bursts correspond to the AE observed in the other materials, and follow the observations listed above. The background emission occurs all round the hysteresis loop and can be observed even at very low values of the applied field which are insufficient to switch the sample. This background emission has been correlated with the presence of visible defects in the sample, and is discussed later (Section 4.7).

A third type of AE has been observed which is attributed to dielectric breakdown in the sample or arcing between the electrodes. This AE, which is usually only apparent at very high values of the applied field, can be easily distinguished from its timing within the hysteresis cycle. Although the AE again onsets abruptly at some point in the cycle, it then invariably continues beyond the point where the voltage across the sample reaches its peak value, until the voltage drops below the value at which the AE started. This means that this type of AE always appears on the flat portions of the loop. In

addition, severe arcing is generally accompanied by distortion of the hysteresis loop display. This kind of AE can also be observed at much lower voltages when the electrodes do not make intimate contact with the sample surface. In this case, sparking occurs between the electrode and the sample surface.

While the materials listed above all behave in a similar manner, the ferroelectric barium titanate ($Ba\ Ti\ O_3$) differs in that AE is observed throughout the hysteresis cycle, with no particular increase in activity at the approach to saturation. In addition, AE is observed at very low values of electric field, even before the loop is well formed. Barium titanate differs from the other materials studied in that it posesses 90° domain walls, whereas in the other materials the polarisation can assume only two directions (parallel or antiparallel to the polar axis). Therefore, barium titanate can be expected to have a fundamentally different domain structure and mechanism of polarisation reversal. Mohamad (1980) has speculated that this difference in behaviour may be attributed to this cause. However, in view of the behaviour of the Rochelle salt crystals described above, it is possible that the behaviour observed merely reflects the quality of the barium titanate crystals available.

4.2 Frequency Analysis of the AE Signal.

Although individual AE impulses vary considerably from one to another, some comments may be made about their general characteristics. A typical burst of AE is shown in Figure 4.3a. This particular burst was recorded from a sample of lead germanate 1.22mm thick being cycled by a 50Hz 1300V peak applied voltage. The sample was mounted on a wideband transducer, and the signal was amplified by 80dB before being recorded on a transient recorder. The trigger level on the transient recorder

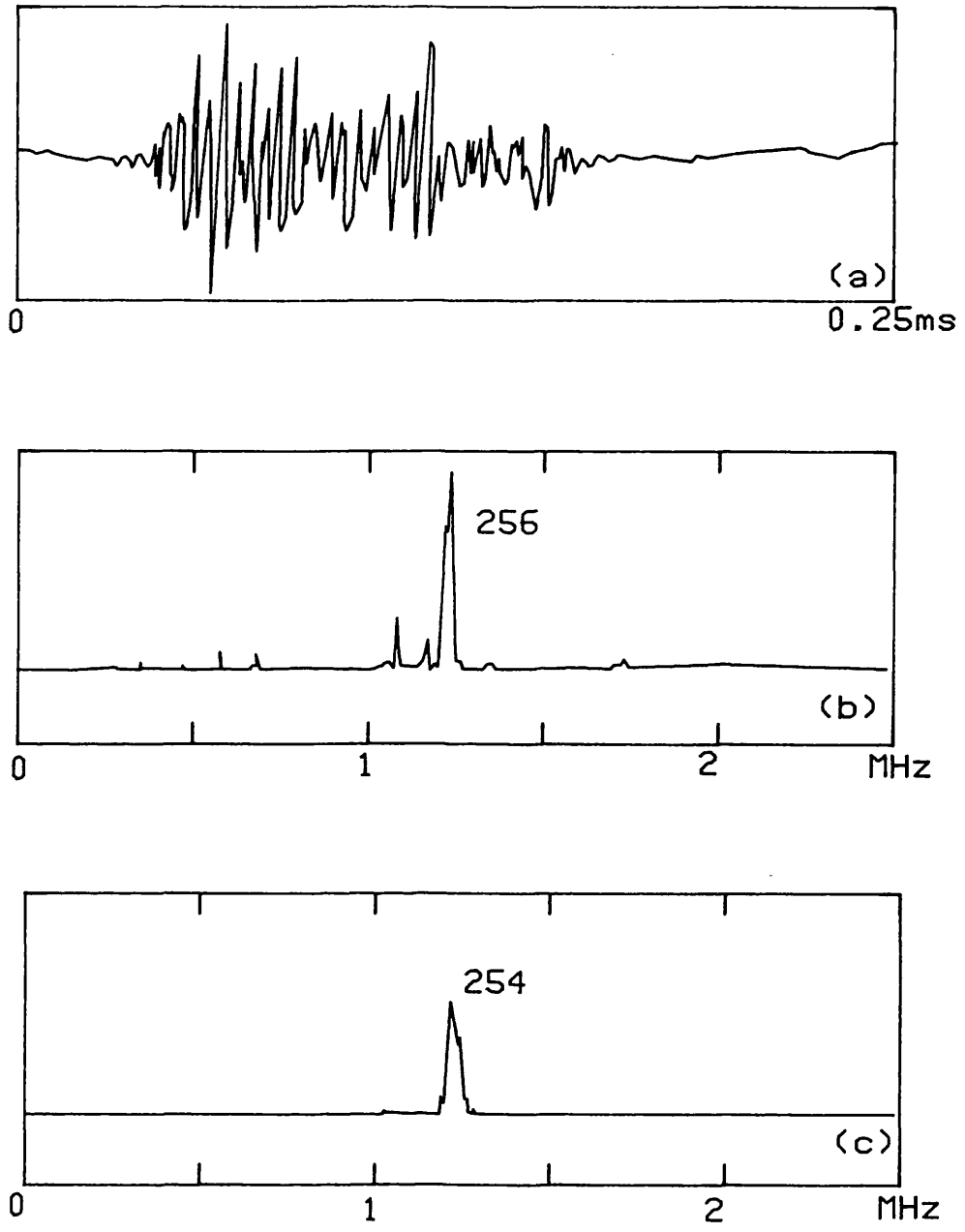

FIGURE 4.3 - Frequency analysis of AE from a lead germanate sample 1.22mm thick.
(a) Typical AE signal.
(b) FFT power spectrum of above signal.
(c) Average of 20 power spectra as in (b).
Frequency resolution 4.88kHz per point.

was set so that only bursts of relatively high amplitude would be recorded, thereby ensuring a good signal to noise ratio in the captured signal. The amplitude of the signal at the transient recorder input was about 200mV peak-to-peak, which means that the transducer output was of the order of 20μV p-p. The duration of the AE bursts is around 0.2ms, though this tends to increase as the amplitude of the burst increases. At high values of the applied field, AE is emitted more copiously and the bursts tend to run together and overlap. Distinct bursts, such as that in Figure 4.3a, can only be resolved with the minimum value of applied field which will cause the production of AE.

The AE burst typically consists of an initial high-amplitude portion which then decays to a sustained ringing. The complex decay envelope evident in Figure 4.3a is characteristic of ringing systems (such as church bells) where energy can be interchanged between a number of vibrational modes, each with its own frequency and attenuation factor (Wood 1944). The crystal-interface-transducer combination forms a complex system of this type. In the signal shown in Figure 4.3a, the trace crosses the mean level at approximately equal time intervals, indicating that the signal contains a single predominant frequency component. The fact that a mode frequency is absent in a recorded signal does not imply that the mode is not excited, as the recording system may not be sensitive to that particular mode. In particular, the FAC500 wideband transducer used to record the signal in Figure 4.3a is ineffective at frequencies below about 300kHz.

Egle and Tatro (1967) have shown that the frequency components of an AE signal are likely to be affected by the acoustic properties of the specimen. Simulated AE experiments in thin plates and bars have shown that a disturbance detected by a surface transducer may have its response concentrated at certain discrete frequencies determined by the thickness of the plate or bar, provided that the initial disturbance has sufficient frequency content to excite these resonances (Egle and Brown

1975). These observations were made on specimens of steel and other alloys in an attempt to explain the characteristics of AE from crack growth and other failure modes in the specimen. In fact, AE frequency analysis can be used in the non-destructive testing of materials and structures (Graham et al 1975).

To determine whether the ultrasound emitted by ferroelectrics is also affected by the geometrical resonances of the sample, the recorded AE signals were analysed in terms of their frequency components by the fast Fourier transform (FFT) technique. The theory and practice of the FFT method have been covered in several texts (eg Brigham 1974). Figure 4.3b shows the power spectrum obtained by taking the FFT of the signal shown in Figure 4.3a, after removing the DC component, scaling appropriately and multiplying by a sharp bell windowing function to ensure that the signal goes to zero at the extremities of the interval over which the FFT is performed. Windowing is neccessary because the FFT assumes a periodic signal. The windowing function neccessarily distorts the signal, the distortion being greatest near the ends of the interval. To minimise this distortion, the pretrigger time on the transient recorder was adjusted to locate the AE burst near the centre of the recording interval. The FFT proper provides an amplitude spectrum with phase information carried in the real and imaginary parts of the solution. The real and imaginary parts are combined (through a sum of squares) to give the power spectrum.

The power spectrum in Figure 4.3b shows that the signal in Figure 4.3a has a strong component at a frequency of 1.25MHz. The spectrum also contains components at other frequencies, but these are relatively minor. The strong component at around 1.25MHz appears in all the AE signals emitted by this particular sample, although the details of the spectra differ. This is shown in Figure 4.3c, where the power spectra of 20 different AE bursts captured at random from the sample have been summed together. The only feature of this average power spectrum is the strong peak at a frequency of 1.24MHz. The individual

spectra usually contain other peaks in addition to the central resonance (for example the peak at 1.1MHz in Figure 4.3b), but this detail varies from signal to signal. Only the central peak is common to all the spectra, so the other features are not evident in the averaged spectrum. This strong monochromaticity of the AE signal is shown by all the materials investigated, although different samples exhibit different resonant frequencies. It is also independent of the magnitude of the electric field applied to the sample, as long as this is sufficient to generate AE. At high values of the applied field, individual AE impulses overlap and the recorded signals are very complex. However, although the power spectrum tends to contain more low-frequency detail, the central peak is still predominant. The frequency of this peak is independent of the magnitude of the applied field.

If the strong frequency component is indeed due to a sample resonance, the resonant frequency should be dependent upon the dimensions of the sample. Mohamad (1980) has shown that in lead germanate this resonant frequency f is inversely proportional to the thickness of the sample, following the relation:

$$f = v / 2d$$

where d is the thickness of the sample and v the velocity of longitudinal waves down the polar c-axis of the material, taken as 3587m/s (Yamada et al 1972). The other materials studied have been found to behave similarly. The power spectra of AE from Rochelle salt samples of different thicknesses at a temperature of 20°C are shown in Figure 4.4. The resonant frequencies, calculated from a longitudinal wave velocity down the polar a-axis at this temperature of 3738m/s (Kawashima and Tatsuzaki 1973), are indicated on each spectrum by an arrow. The measured and calculated resonance frequencies for these samples are tabulated in Table 4.1. The measured resonance frequency was obtained from an average of 20 power spectra for each sample, which accounts for the good agreement with the predicted values. The actual resonance frequencies for individual traces could be as much as 5% away from the mean

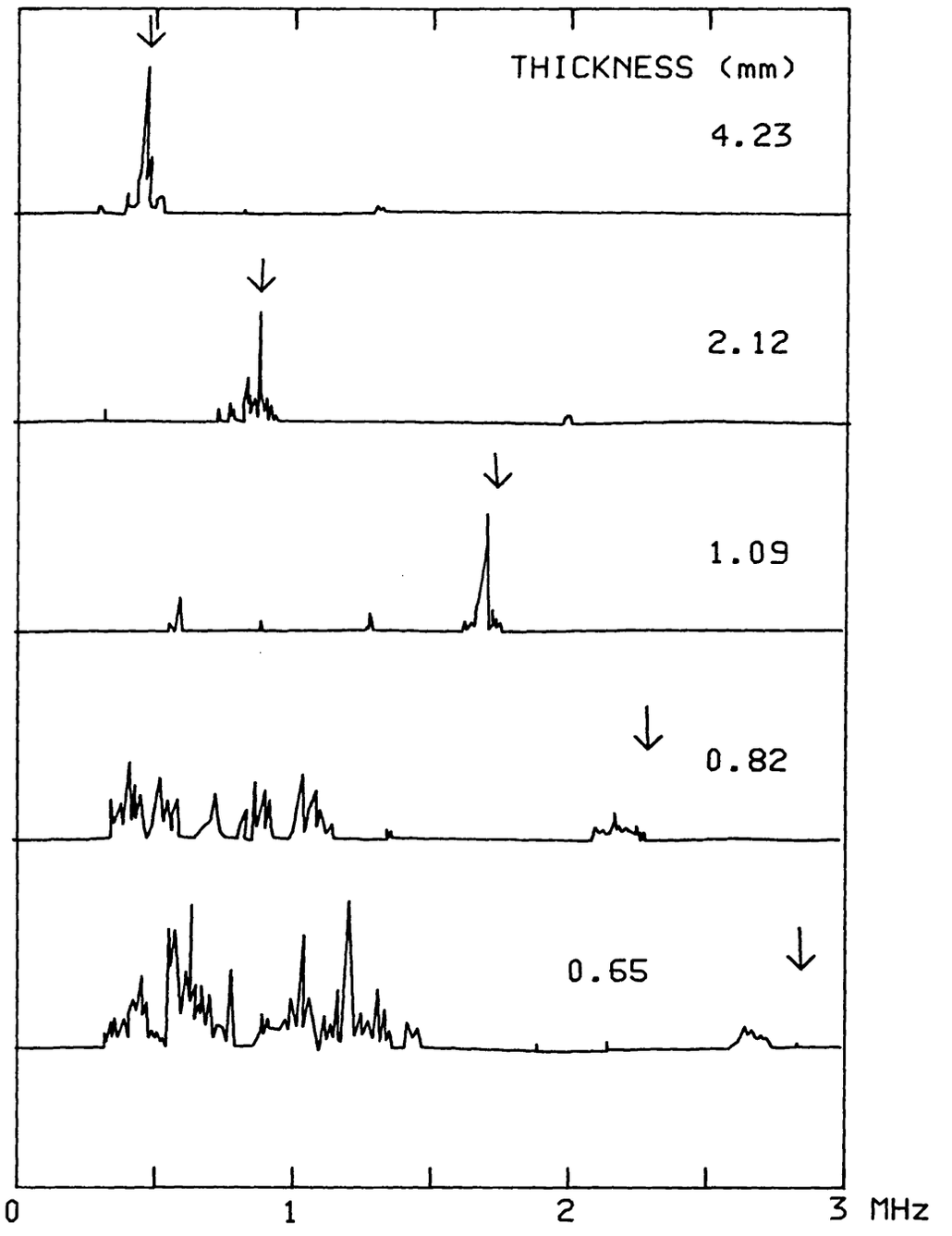

FIGURE 4.4 - AE power spectra for Rochelle salt samples of different thicknesses at 20 °C. The arrows indicate the calculated resonance frequencies. Note that the spectra are plotted on different vertical scales.

Sample Thickness (mm)	Measured Resonance (kHz)	Calculated Resonance (kHz)	Percentage Difference
4.23	449	442	+1.6
2.12	875	882	-0.8
1.38	1370	1355	+1.1
1.09	1740	1715	+1.3
0.82	2220	2279	-2.6
0.65	2619	2875	-8.9

TABLE 4.1 - Frequencies of the central peaks in the power spectra of AE signals from Rochelle salt crystals of different thicknesses compared with the fundamental thickness resonance frequencies calculated from a longitudinal wave velocity down the polar axis of 3738m/s. These measurements were made at a temperature of 20 °C.

value. Measurements of the dominant frequency in the AE signal have also been made in lead germanate and gadolinium molybdate samples of different thickness. The wave velocity of gadolinium molybdate has been taken as 4646m/s (Hochli 1972). These results are shown in Tables 4.2 and 4.3. The results for all three materials are summarised in graphical form in Figure 4.5, where the dominant frequency has been plotted against the reciprocal of the sample thickness. Straight lines on the graph indicate the expected resonance frequencies if the above relation is satisfied.

For specimens thinner than about 1mm, the measured resonant frequency becomes appreciably lower than the calculated value. Mohamad (1980) has observed a similar tendency in lead germanate, and has attributed it to the greater damping experienced by the thinner samples, which leads to a downward shift in the resonant frequency. However, Figure 4.5 shows that in all three materials this discrepancy becomes significant at frequencies above about 2MHz, which is the upper frequency limit of the passband of the AE detection system. Although this in itself should not affect the frequency of the peak, the signal strength drops sharply above this frequency. Figure 4.4 shows that for these thinner sample, the resonance peak becomes small and diffuse. Determining the frequency of the peak in these circumstances is bound to be inaccurate.

Note that the power spectra of Figure 4.4 are only intended to show the frequency relations between the signals from different samples. The individual spectra have been plotted on different vertical scales, and no comparison can be made between the amplitudes of the various components in different signals. The apparently large low-frequency components in the signals obtained from the thinner specimens are a consequence of this arbitrary scaling. These components are also present in the other spectra, but are insignificant in comparison with the height of the central peak. As the frequency of the peak moves outside the passband of the system, these small, low frequency components account for a greater proportion of the recorded

Sample Thickness (mm)	Measured Resonance (kHz)	Calculated Resonance (kHz)	Percentage Difference
2.50	720	717	+0.4
1.67	1080	1076	+0.4
1.22	1450	1475	-1.7
0.73	2300	2451	-6.6
0.60	2600	2989	-15.0

TABLE 4.2 - Frequencies of the central peaks in the power spectra of AE signals of lead germanate samples of different thicknesses compared with the calculated resonance frequencies of the crystals.

Sample Thickness (mm)	Measured Resonance (kHz)	Calculated Resonance (kHz)	Percentage Difference
1.88	1270	1239	+2.4
1.46	1620	1587	+2.0
0.94	2330	2478	-6.4
0.80	2750	2942	-7.0

TABLE 4.3 - Frequencies of the central peaks in the power spectra of AE signals of gadolinium molybdate samples of different thicknesses compared with the calculated resonance frequencies of the crystals.

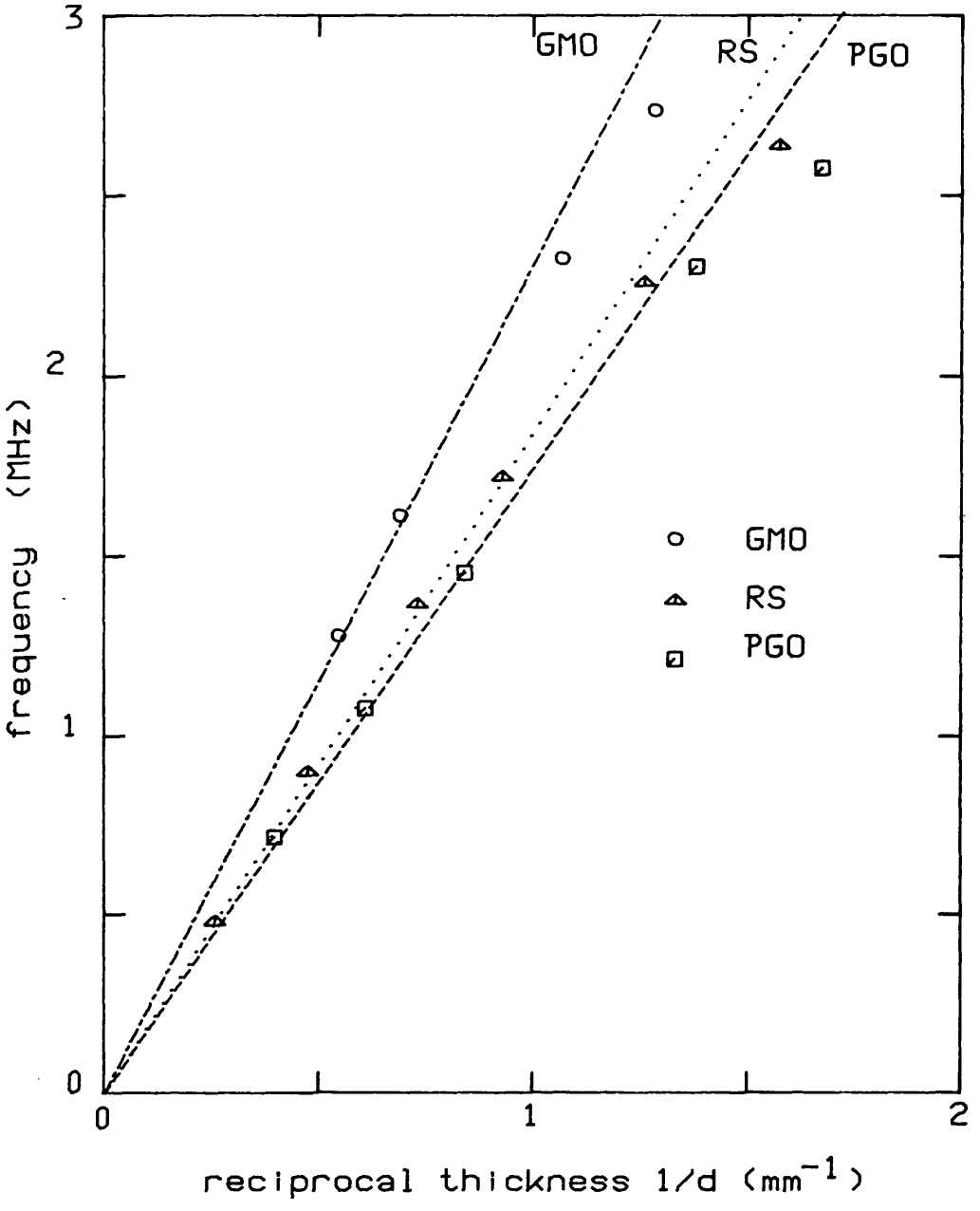

FIGURE 4.5 - Resonant frequency versus reciprocal sample thickness for a number of samples of different materials.
The straight lines have slopes proportional to the speed of sound in each of the three materials.

signal.

When initially prepared, the 1.09mm Rochelle salt sample was found to produce bursts of AE on the flat portions of the hysteresis loop. This was later diagnosed as being caused by sparking between the electrode and the sample surface, probably because the sample had not been thoroughly degreased before the silver dag electrodes were applied. Small pits, presumably caused by the sparks, were visible under a microscope in the regions the electrode had separated from the sample surface. The power spectrum of the AE generated by this crystal is shown in Figure 4.6a. The transient recorder was then gated to trigger only on signals which occur on the flat parts of the loop, which yielded the power spectrum in Figure 4.6b. The power spectrum of the AE generated by the sparks was essentially identical to the spectrum of the AE produced in other samples where this problem did not occur. To ensure that the AE being analysed was caused by sparking and not by the ferroelectric mechanism, the process was repeated with the sample heated to 28°C, which is above the Curie temperature. The wave velocity at this temperature is less than 1% higher than it was at 20°C, even though the material now has a different crystal structure (Kawashima and Tatsuzaki 1973), so there should be no appreciable change in the resonance frequency. The AE recorded yielded the power spectrum in Figure 4.6c. Finally, the faulty electrodes were removed from the sample, which was thoroughly cleaned and new electrodes deposited. The behaviour of the sample was then entirely in line with the others, and the power spectrum of AE generated on the approach to saturation polarisation is shown in Figure 4.6d. The spectra of Figure 4.6 are all essentially identical.

The conclusion to be drawn is that the AE signal recorded is entirely dominated by the effects of sample resonance, and that this type of signal is produced whenever the crystal is excited into resonance by an impulse of sufficiently short duration, irrespective of the nature of the impulse. In fact, electric sparks have been proposed as a wideband source of simulated AE

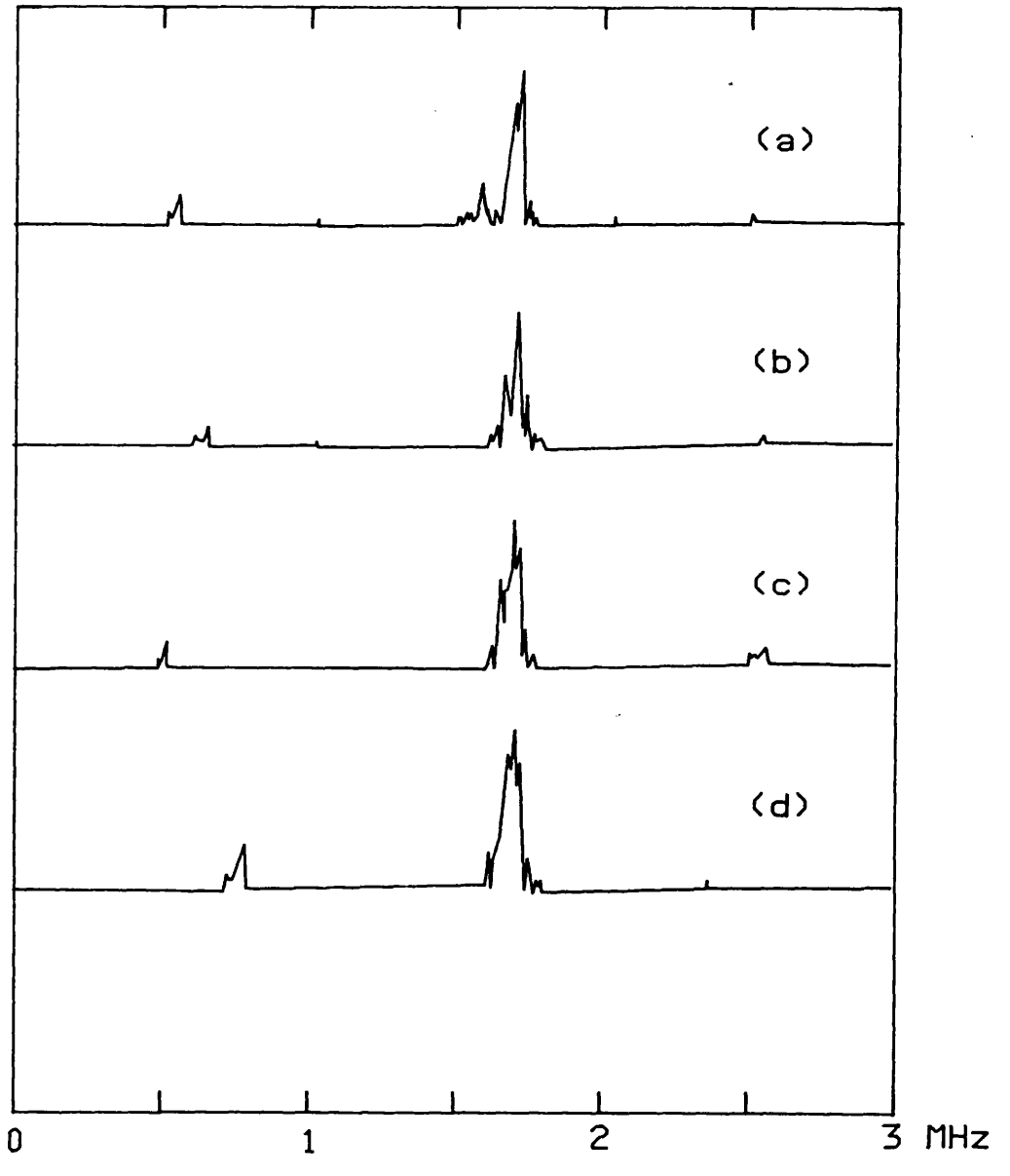

FIGURE 4.6 - Averaged power spectra of AE from a Rochelle salt sample 1.09mm thick.
(a) AE from sample with faulty electrodes.
(b) AE from the flat portion of the loop.
(c) AE from sample heated to 28°C
(ie above the transition temperature).
(d) AE from sample after replacing the faulty electrodes.

for the calibration of piezoelectric transducers (Sachse and Ceranoglu 1979). The only information that frequency analysis yields about the source of the AE is an upper limit to the duration of the source event, as the impulse has to have sufficient frequency content to excite the resonance. The highest resonance frequency recorded was 2.75MHz in a 0.8mm thick gadolinium molybdate sample. This places an upper limit of about 300ns on the duration of the event, although this is likely to depend on the sample thickness and will differ from one material to another. In theory, additional information about the nature of the source event can be gleaned from the shape of the waveform before the resonance oscillation in the sample has had time to build up, which takes at least one transit time of the crystal or one half-cycle of the waveform. However, this analysis can only be carried out with systems which have a much larger bandwidth than the 2MHz available with the piezoelectric transducers and the amplifiers used, and may form the basis of future study.

4.3 The Amplitude Distribution of the AE Signal.

As the AE is generated in distinct bursts which can differ considerably from one to another, the amplitude of the AE produced under a given set of conditions has to be described in terms of an amplitude distribution or amplitude spectrum. Amplitude distribution analysis, also known as amplitude sorting, is often used to interpret AE results in materials testing (eg Nakamura et al 1971, Guild et al 1980). It is particularly useful because different failure mechanisms generally produce AE with distinctive amplitude signatures. Therefore the amplitude spectrum of the AE produced by the specimen can be used to identify how the material fails under different conditions without necessarily destroying the specimen. The analysis is usually carried out using a dedicated

instrument which simultaneously compares the peak amplitude of the amplified AE burst with a number of reference levels and increments a bank of counters accordingly. However, a crude amplitude sort can be carried out by measuring the AE count rate as a function of amplifier gain as described in Section 3.5, assuming that the production of AE remains constant over the long period of time required to complete this process.

Figure 4.7a shows how the AE count rate from a crystal of lead germanate 1.13mm thick cycled by a 50Hz 1500V peak applied electric field varies with the gain of the detection system. The horizontal axis in this graph has been calibrated in terms of the signal amplitude which is obtained by negating the amplifier gain setting. Thus a signal detected at a gain of 60dB is defined as having an amplitude of -60dB relative to the 1.0V internal reference of the AECL 105 AE counter unit. This was done so that the graphs have low signal amplitude (high amplifier gain) on the right hand side, which is the conventional way to display an amplitude spectrum. As it is the peak amplitude of the individual AE bursts that is of interest, the AE counter was set to operate in the event counting mode (Section 3.5). As the AE counter counts all bursts with an amplitude greater than the reference level, the graph of Figure 4.7a represents a cumulative distribution function. Thus the number of bursts whose amplitude lies within a given range is measured by the count rate at the upper end of the range less the count rate at the lower end. As measurements were taken at (constant) gain intervals of 2dB, the amplitude distribution can be obtained from the data in Figure 4.7a by subtracting each reading from the previous one (made at a higher gain setting). The amplitude distribution obtained from the data in Figure 4.7a is shown in Figure 4.7b. For a given point (x,y) in this graph, y gives the number of AE bursts with an amplitude in the range [x,x+2dB]. The amplitude spectrum shows a peak at around -75dB. This means that most of the AE bursts have an amplitude close to some mean value (here about -75dB) which can be used to describe the AE produced under a given set of conditions. The increase in count rate at signal strengths below about -80dB is

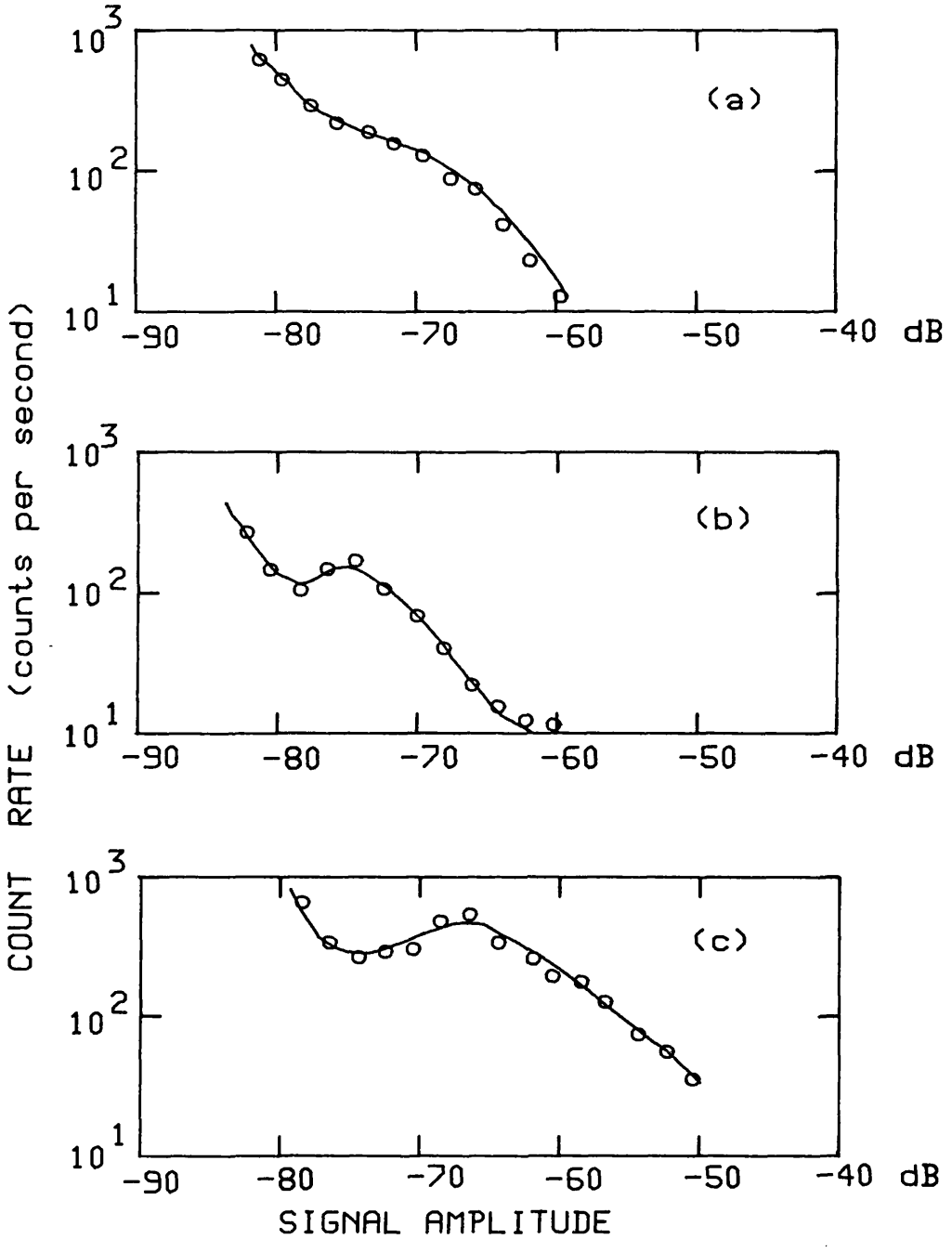

FIGURE 4.7 - Amplitude distribution of the AE from a lead germanate sample 1.13mm thick.
(a) Event count rate as a function of signal amplitude (or amplifier gain) with a peak applied voltage of 1500V.
(b) Amplitude spectrum obtained from (a).
(c) Event count rate as a function of gain with a peak applied voltage of 2000V.

due to amplifier noise, which becomes increasingly apparent as the gain of the system is increased.

The major problem with event counting is the dead time associated with the envelope detector which follows the outline of the AE burst. This leads to a reduced count as the count rate increases. Figure 4.7c shows how the (event) count rate varies with amplifier gain with a sample voltage of 2000V. This graph should be compared to Figure 4.7a. The count rate actually decreases as the gain is increased from 65 to 75dB. It is not possible to regard this graph as a cumulative distribution function, which is necessarily monotonic. The problem arises because the AE is emitted over a short period in the hysteresis cycle, leading to very high instantaneous count rates although the mean count rate (averaged over the entire cycle) is not excessive.

As it was not possible to use event counting to obtain a satisfactory amplitude spectrum, ringdown counting had to be used. This suffers from the opposite problem, namely that high amplitude bursts may be counted more than once, leading to an overestimated count rate at high gain (ie an overestimated cumulative count at low signal amplitudes). It is possible to calculate how the ringdown count varies with amplifier gain for an ideal signal such as a damped sinusoid. However, in view of the complex shape of real AE signals (Figure 4.3a), the value of this approach is doubtful. An empirical approach was found to be more useful.

Figure 4.7b shows that the amplitude spectrum is likely to be peaked or bell-shaped. The hysteresis loop displays of Figure 4.2 show that the amplitude of the AE increases as the magnitude of the applied field is increased. Therefore, the amplitude spectrum may be expected to be a peaked curve which shifts towards high amplitude (low gain) as the applied voltage is increased. Figure 4.8 shows how the ringdown count rate (for the same lead germanate sample described above) varies with amplifier gain for three values of the applied field. The large

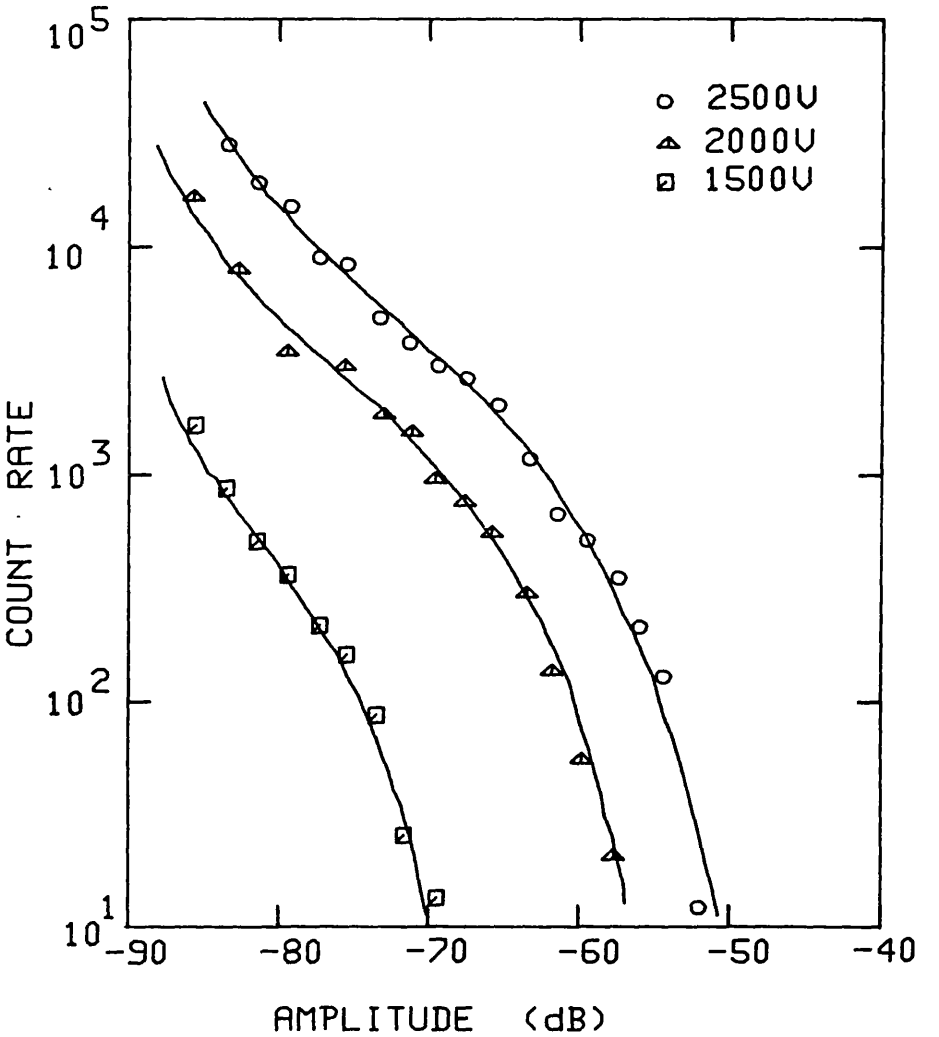

FIGURE 4.8 - Ringdown count rate as a function of amplifier gain for a lead germante sample 1.13mm thick at three values of the applied electric field.

increase in count rate at high gain can again be attributed to amplifier noise. The steep right hand part of each curve, corresponding to high signal amplitude, must be caused by the AE bursts. This occurs at lower signal amplitudes as the applied field is reduced, as expected. Finally, the centre portion of each curve is approximately linear and has approximately the same slope in all three curves. This part of the curve gets shorter as the applied field is reduced and is not very pronounced in the 1500V curve. If the steep part of each curve is assumed to account for all the AE produced, the central linear portion must represent the increased count rate caused by the ringdown counting of a fixed number of events all greater than the counter threshold. If each event is counted only once, then this portion of the curve would have a slope of zero. Therefore, the slope of this linear region is a measure of how much the ringdown counting technique overestimates the event count and can be used to correct the measured (ringdown) count rates. As Figure 4.8 has been plotted on a logarithmic scale, the linear region can be described by:

$$\log_{10} c(G) = \log_{10} c(G-x) + kx$$

or:

$$c(G) = c(G-x) \cdot 10^{kx}$$

where c(G) is the count rate at a gain G, x is the 2dB increment between readings and k is the slope of the line. The value of k, obtained from the mean of the slopes of the linear portions of the curves in Figure 4.8, is 0.043/dB. Assuming that this relation describes how the ringdown count overestimates the event count, a corrected count rate c' is defined by:

$$c'(G) = c(G) - c(G-x) \cdot 10^{kx}$$

When c' is plotted as a function of amplifier gain, a cumulative distribution similar to that obtained by the event counting technique (Figure 4.7a) is produced. The amplitude spectrum is

then derived from this data as described above.

Amplitude spectra obtained in this way from the data in Figure 4.8 are shown in Figure 4.9. These graphs have the desired peaked curves shifting towards high amplitude as the applied field is increased. However, this is not necessarily meaningful as the correction process was designed to produce curves of this type. The increase in count rate at high gain caused by amplifier noise is also evident in these graphs. As the sample voltage is decreased, the peak is eventually lost in the noise. This means that the peak in the amplitude spectrum cannot be followed down to very low signal amplitudes. The amplitude at which this peak occurs is plotted as a function of applied voltage in Figure 4.10. The curve can be extrapolated towards the high-gain regions that cannot be investigated directly because of amplifier noise. This extrapolation indicates a cutoff at around 1000V beyond which no further AE would be detected even with an ideally noise-free infinite gain amplifier. This points to the existence of a threshold field for the production of AE, which is discussed further in Section 4.6.

The height of the peak in the amplitude spectrum decreases as the voltage across the sample is reduced (Figure 4.9). A graph of the height of the peak against sample voltage is similar to Figure 4.10 and also extrapolates towards a cutoff at around 1000V. However, at high gains amplifier noise contributes towards the height of the peak and this tends to flatten the curve away from a cutoff. Although this contribution can be compensated for, plotting the position of the peak (as in Figure 4.10) leads to a sharper cutoff than plotting the height.

At low values of the applied field and at low amplifier gain settings, very small count rates can be recorded. Figure 4.8 shows count rates as low as about 10 per second, which at a 50Hz driving frequency means that on average one count is being recorded in every 10 half-cycles. This does not necessarily mean that some AE is not being produced on every half-cycle, as

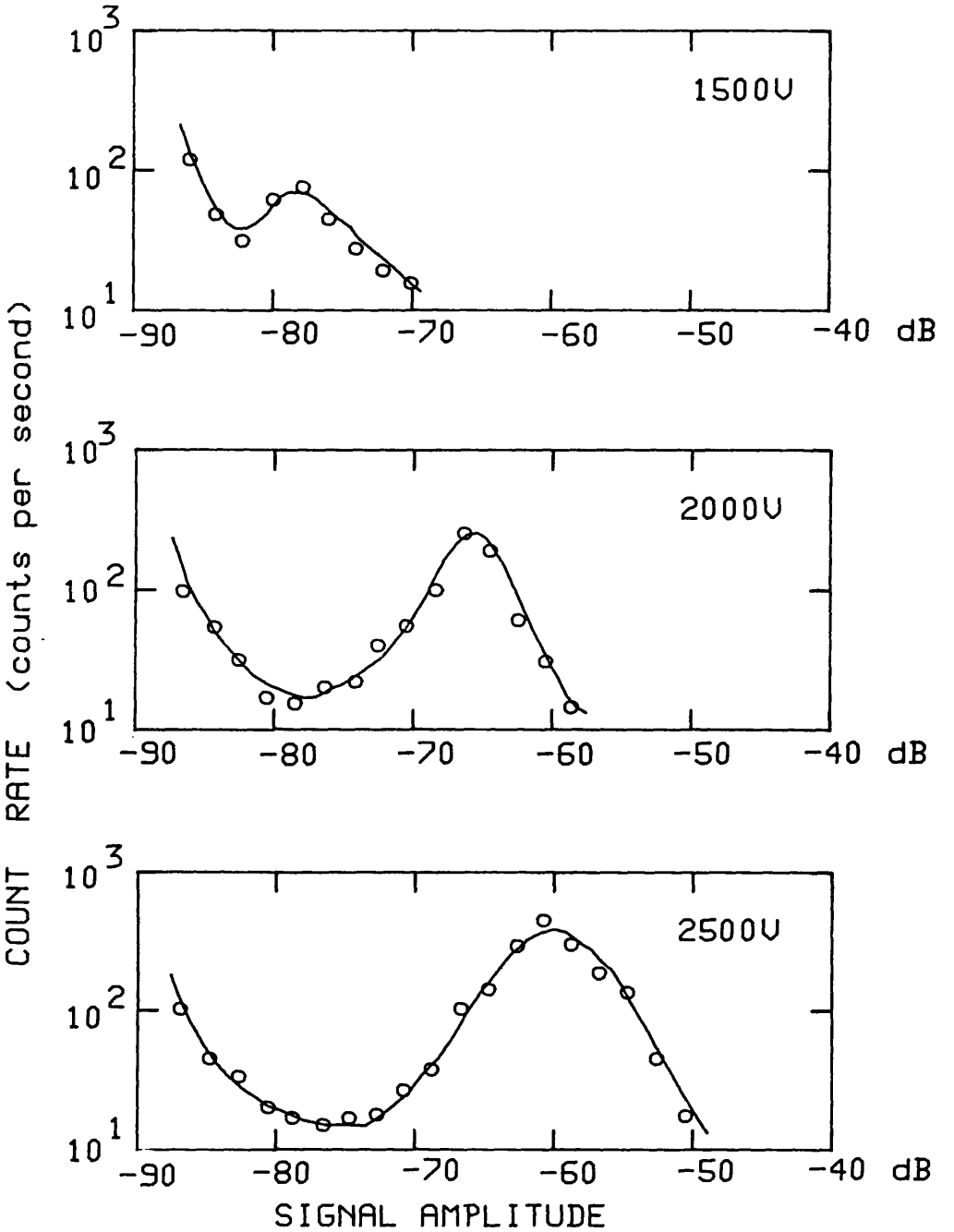

FIGURE 4.9 - Amplitude distribution curves obtained from the data in Figure 4.8.

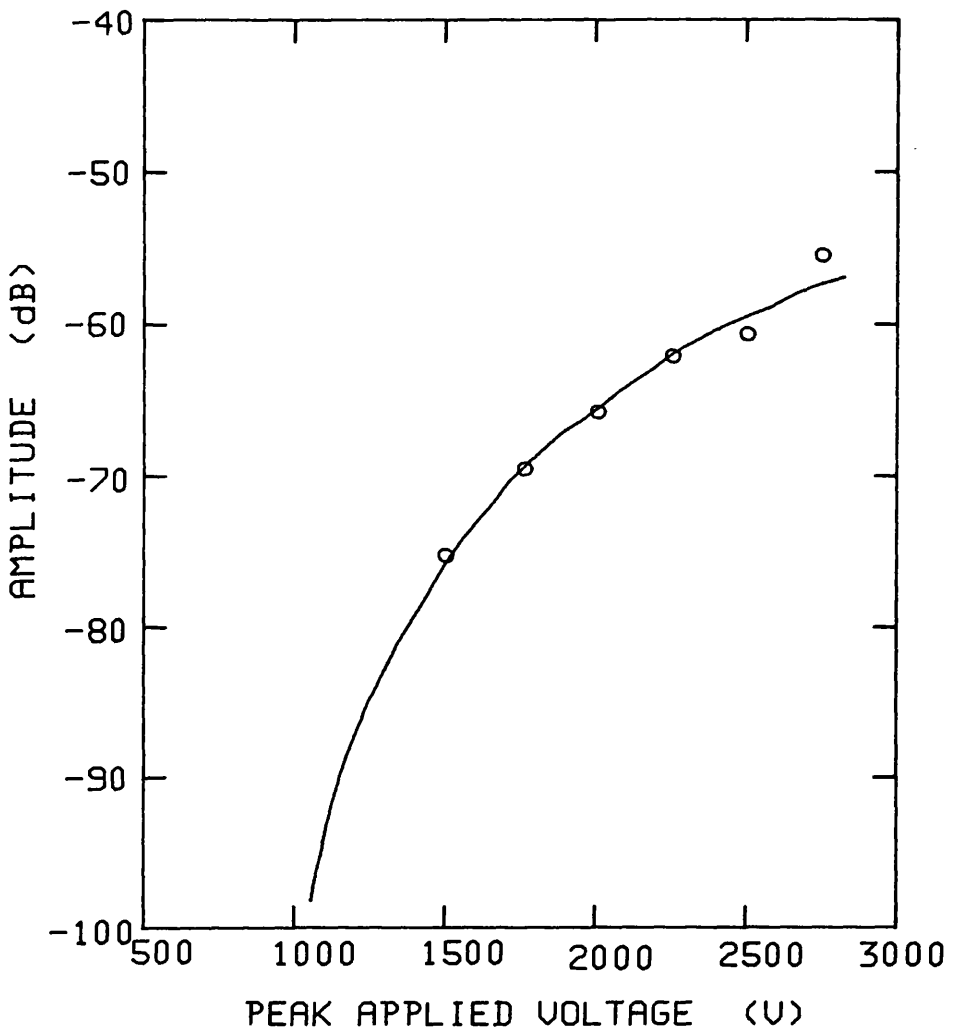

FIGURE 4.10 - Signal amplitude corresponding to the peak in the AE amplitude distribution plotted as a function of the applied voltage.

not all the AE produced is recorded by the counting system. These conditions correspond to the high amplitude tail in the amplitude spectrum, such as at -50dB and 2500V in Figure 4.9, where the probability is relatively low. The bulk of the AE produced at this particular voltage has too low an amplitude (-60dB) to be recorded, and the counter only records the relatively infrequent high amplitude pulses.

4.4 The Timing of the AE within the Hysteresis Cycle.

The occurrence of AE within a specific region of the hysteresis cycle is one of the strongest indications that the generation of AE is intimately connected with the process of polarisation reversal in the sample. Although the AE is restricted to this very definite region, the occurrence of the AE bursts within this region is not so well defined. The individual AE bursts occur randomly within this region on successive cycles. On the oscilloscope display, the AE appears as a continuous blur, a fact that cannot be brought out in the oscillographs of Figures 4.1 and 4.2. It is difficult to estimate the point in time where the onset of AE occurs from a display of this kind.

To determine the distribution of the AE round the hysteresis loop, the AE counter was gated to operate for only a short time within each hysteresis cycle, thereby counting only those AE bursts which occur in that period. By positioning the counter gate at different points in the cycle, the distribution could be built up. Although the gate period should be short to provide adequate time resolution, the shorter the gate the smaller the number of events that occur within the gate period. In addition, the AE bursts have a finite duration (about 0.2ms) which imposes a lower limit on the gate time. As the AE occurs twice in each hysteresis cycle, it is sufficient to consider only half the cycle, which for a 50Hz loop frequency takes 10ms.

This interval was divided into 20 consecutive 0.5ms gate periods, which provided an acceptable compromise between time resolution and count rate. Even so, counting had to be performed over an extended period of time (typically 300s) to gather a statistically significant cumulative count. An even shorter gate time (down to 0.1ms) was used to determine the onset and termination of the AE more accurately. However, this short gate time produces such an erratic count rate that it can only be used to determine the presence (or otherwise) of a signal.

The following measurements were all carried out on a lead germanate sample 1.13mm thick. The gain of the AE detection system was fixed at 60dB. The distribution of AE within a hysteresis half-cycle for three different values of the applied electric field is shown in Figure 4.11. For these graphs, zero time was defined as when the electric field reaches its peak negative value. The first few milliseconds represent the period where the sample is saturated in the negative direction. After 5ms, when the instantaneous voltage is zero, the sample is still saturated. The point in the cycle where the coercive field is reached is marked on each graph by an arrow. The AE onsets abruptly towards the end of the half-cycle, reaching a maximum close to the point where the applied field reaches its peak positive value, beyond which the cycle repeats itself. No AE occurs in any other part of the half-cycle. As the voltage across the sample is increased, the AE onsets earlier in the cycle. The quantity of AE produced also increases with the sample voltage.

The timing of the AE produced in the two separate half-cycles was always found to be very similar. In some samples, a considerable difference was found in the quantity of AE produced at the two ends of the hysteresis loop. This is evident in the oscillograph of the Rochelle salt hysteresis loop in Figure 4.1d, where more AE is visible on the approach to positive saturation (right-hand end of the loop) than at the other end of the hysteresis loop. This asymmetry must be inherent in the

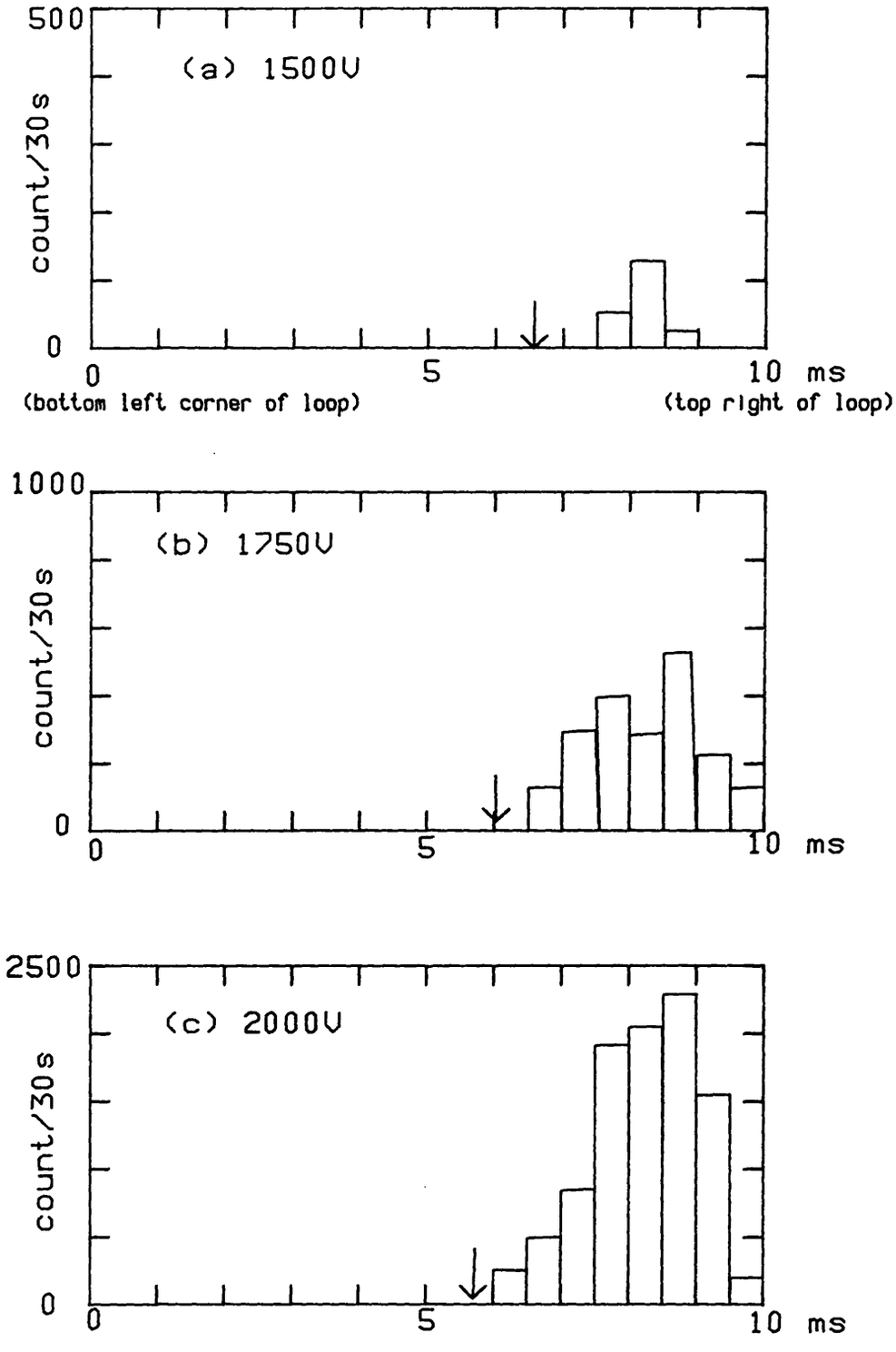

FIGURE 4.11 - Distribution of AE within the hysteresis cycle for a lead germanate sample 1.13mm thick at three values of the applied field. Zero time corresponds to peak negative voltage across the sample. The arrows indicate the position of the coercive field.

crystal as the greater amount of AE is produced at the opposite end of the loop when the connections to the crystal are reversed. Despite this difference in the quantity of AE produced, the timing of the AE in the two half-cycles remains essentially identical.

The timing of the onset of AE as a function of the applied peak voltage is shown in Figure 4.12. The zero of the horizontal (time) axis is again taken to be the point of peak negative voltage across the sample, so that the left-hand end of the graph at time t=5ms corresponds to zero (instantaneous) voltage across the sample. On this graph, points of constant sample voltage are represented by curves, such as curve A which represents an instantaneous sample voltage of 500V. Curve B is the locus of the points at which the instantaneous polarisation of the sample is zero (ie. at the coercive field). The shape of this curve is close to that of curve A which indicates that the coercive field does not change appreciably as a function of the peak applied voltage. Curve C represents the onset of AE in the cycle. The shape of this curve is markedly different from that of curve A, indicating that the onset of AE does not occur at a constant voltage. Finally, curve D represents the points in the cycle where the AE terminates. This graph clearly shows that the onset of AE always occurs at a later point in the cycle than the coercive field, and that the AE terminates before the voltage across the sample reaches its peak value at the end of the half-cycle.

The data in Figure 4.12 is presented in a different form in Figure 4.13. In this graph, the points are plotted in terms of the instantaneous sample voltage on the horizontal axis against the peak applied voltage on the vertical axis. The diagonal (dashed) line across the graph represents the case of the instantaneous voltage equaling the peak voltage and therefore corresponds to the case of t=10ms in Figure 4.12. The horizontal axis represents zero instantaneous voltage which occurs at t=5ms. Curves B, C and D retain their definitions as in Figure 4.12. Curve B shows that the coercive field changes

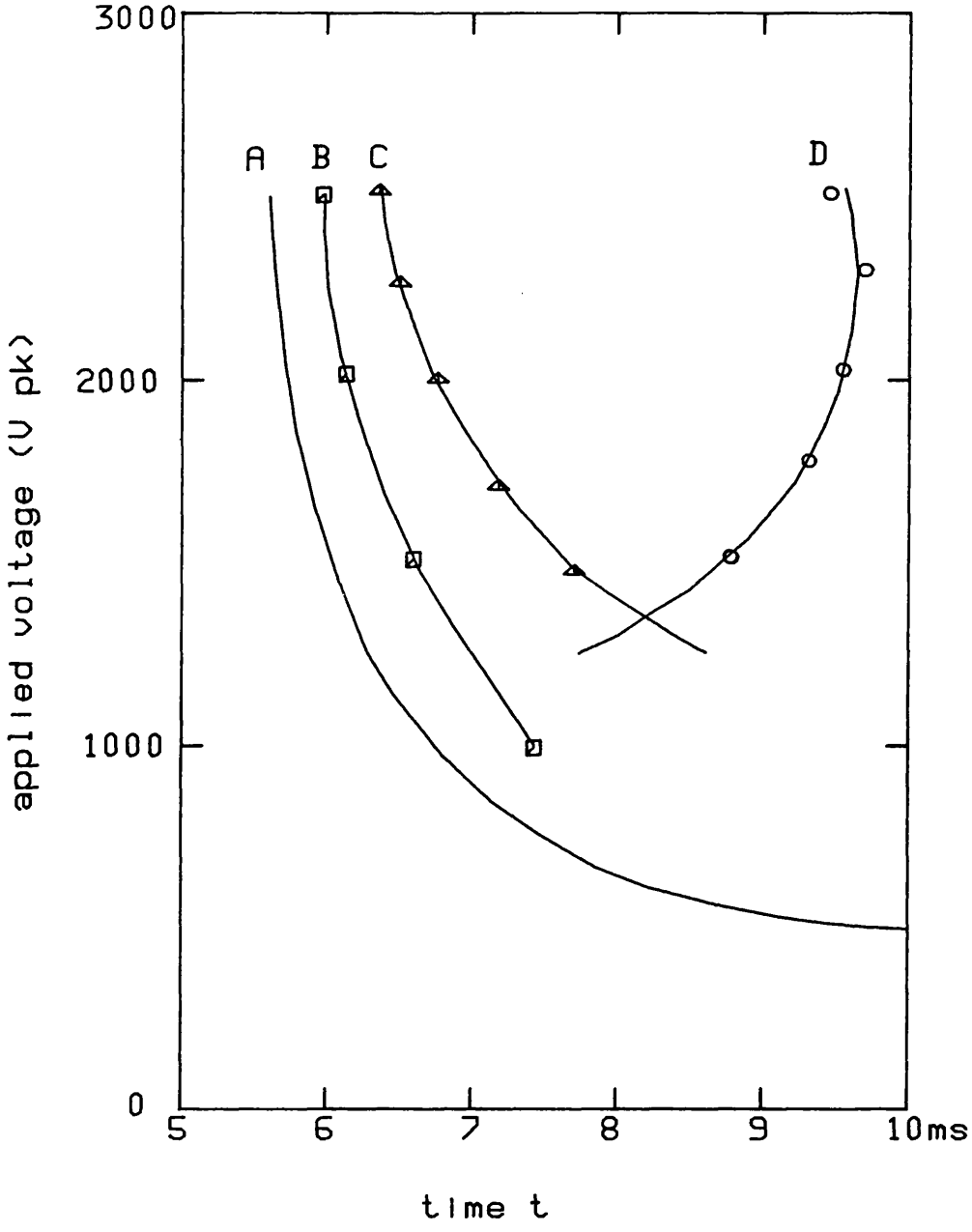

FIGURE 4.12 - Timing of the AE within the hysteresis cycle as a function of the applied electric field. Zero time is defined at peak negative sample voltage. The curves represent:
(A) an instantaneous sample voltage of 500V.
(B) the coercive field
(C) the onset of AE
(D) the termination of AE.

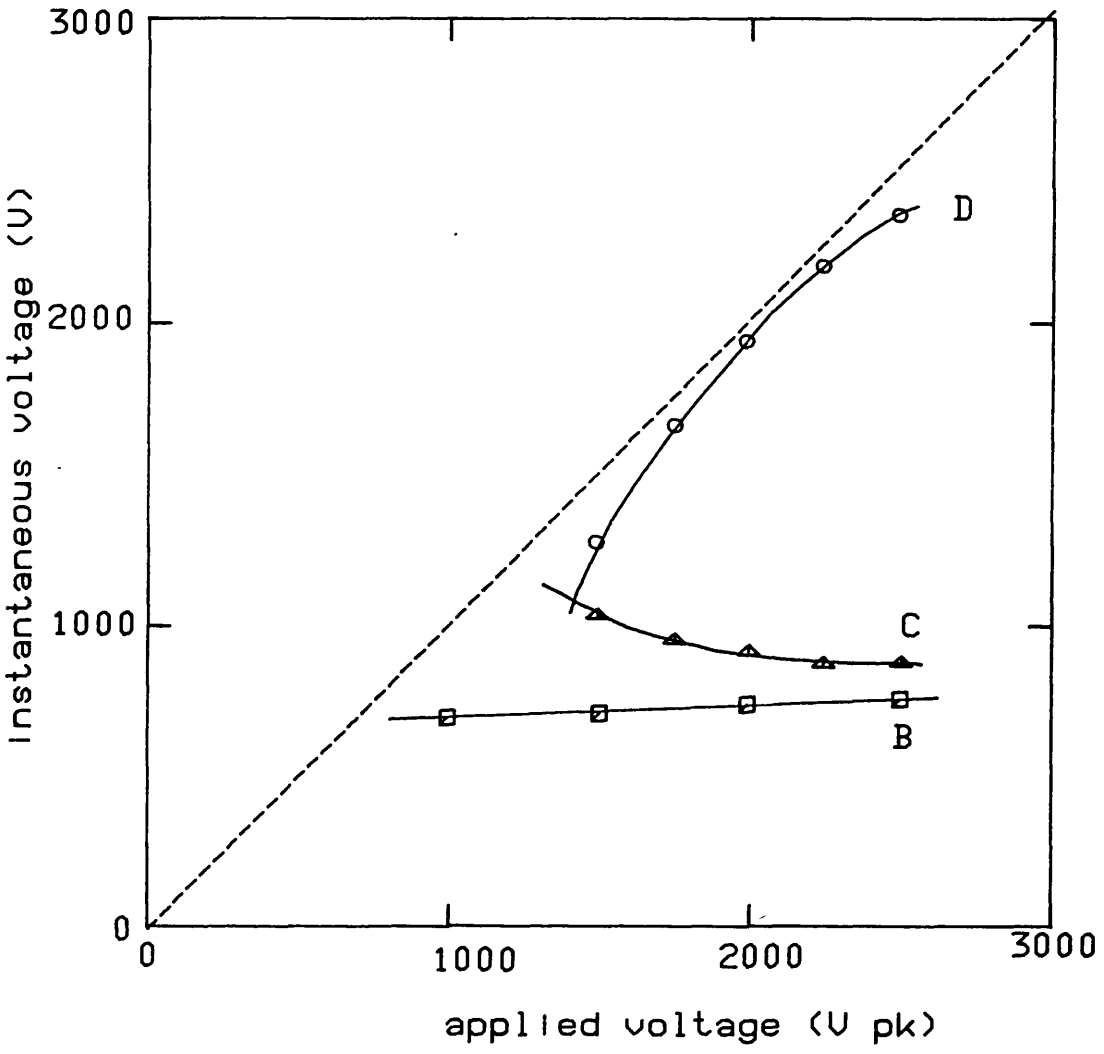

FIGURE 4.13 - Timing of AE within the hysteresis cycle as a function of applied electric field referred to the instantaneous sample voltage. The data plotted is the same as that in Figure 4.12.

only slightly as a function of the applied field. Curve C shows that the onset of AE occurs at a lower (instantaneous) voltage as the peak applied voltage is increased. This means that although a high peak voltage is required to generate the AE, the AE is generated while the instantaneous voltage across the sample is relatively low. For example, at an applied field of 1500V peak, the AE onsets at 1000V and terminates at 1200V, even though no AE is observed with a peak voltage across the sample of 1200V. As the peak voltage is increased, the voltage at the onset of AE production tends towards the coercive field. No AE is observed at (instantaneous) voltages lower than the coercive field, even at very high values of the peak applied voltage.

The upper portion of curve D indicates that at high values of the peak applied field the AE terminates at a progressively higher voltage below the peak applied voltage. This tendency is apparent in Figure 4.12 as the termination of AE occurs earlier in the cycle. Figure 4.1b shows the AE terminating just before the end of the cycle. When this happens, the polarisation always reaches its maximum value before the production of AE ceases (ie the loop is always flat beyond the point where the AE terminates). There are some indications that curve D flattens out at very high values of the applied field, implying that the termination of AE occurs at some (constant) maximum voltage. However, it was not possible to investigate this tendency any further as higher voltages tended to produce sparking and dielectric breakdown in the sample.

In both Figures 4.12 and 4.13, when curves C and D are extrapolated towards lower voltages, they intersect at a point which corresponds to the lowest voltage at which AE should be observed. The vertical distance between curves C and D represents the region over which AE is produced, and as this goes to zero when the curves intersect, in practice no AE is actually detected until the voltage is raised slightly beyond this point. This intersection of the extrapolated curves can be regarded as the threshold for the detection of AE under the conditions of the experiment. This point is not a threshold for

the production of AE as the effect of varying the gain of the AE detection system has not yet been considered. In Section 4.3, the amplitude spectrum of the AE was shown to extend to very low amplitudes, particularly at lower values of the applied field. If the sensitivity of the system is increased, weaker AE impulses can be detected and the threshold is found to occur at a lower voltage. This is shown in Figure 4.14 where the voltage at which curves C and D intersect is plotted as a function of amplifier gain. A smooth curve fitted to the data (ignoring the last three points) flattens out at high gain, indicating that no AE can be detected at lower voltages whatever the gain of the system. This happens at a peak applied voltage of around 1000V for this sample. The tailing off of the last three data points in the graph is due to the effect of amplifier noise, which becomes more apparent as the gain is increased. The effect of amplifier noise is to increase the count rate for a given sample voltage, so that when the curves C and D in Figure 4.13 are extrapolated the intersection occurs at a lower voltage. The measurement of the threshold field for the production of AE is discussed further in Section 4.6.

4.5 The Dependence of the AE upon the Applied Electric Field.

The production of AE in a ferroelectric crystal is strongly dependent on the magnitude of the applied alternating field. In the previous sections of this chapter, the effect of the electric field upon the amplitude and timing of the AE have been described. In this section, the quantity of AE produced (as measured by the ringdown count rate) and how this varies with the applied field is discussed. The general form of this dependence is readily obvious from the hysteresis loop displays such as those shown in Figure 4.2. As the applied voltage is increased from zero, the hysteresis loop takes shape and at a particular voltage the first signs of AE become evident near the

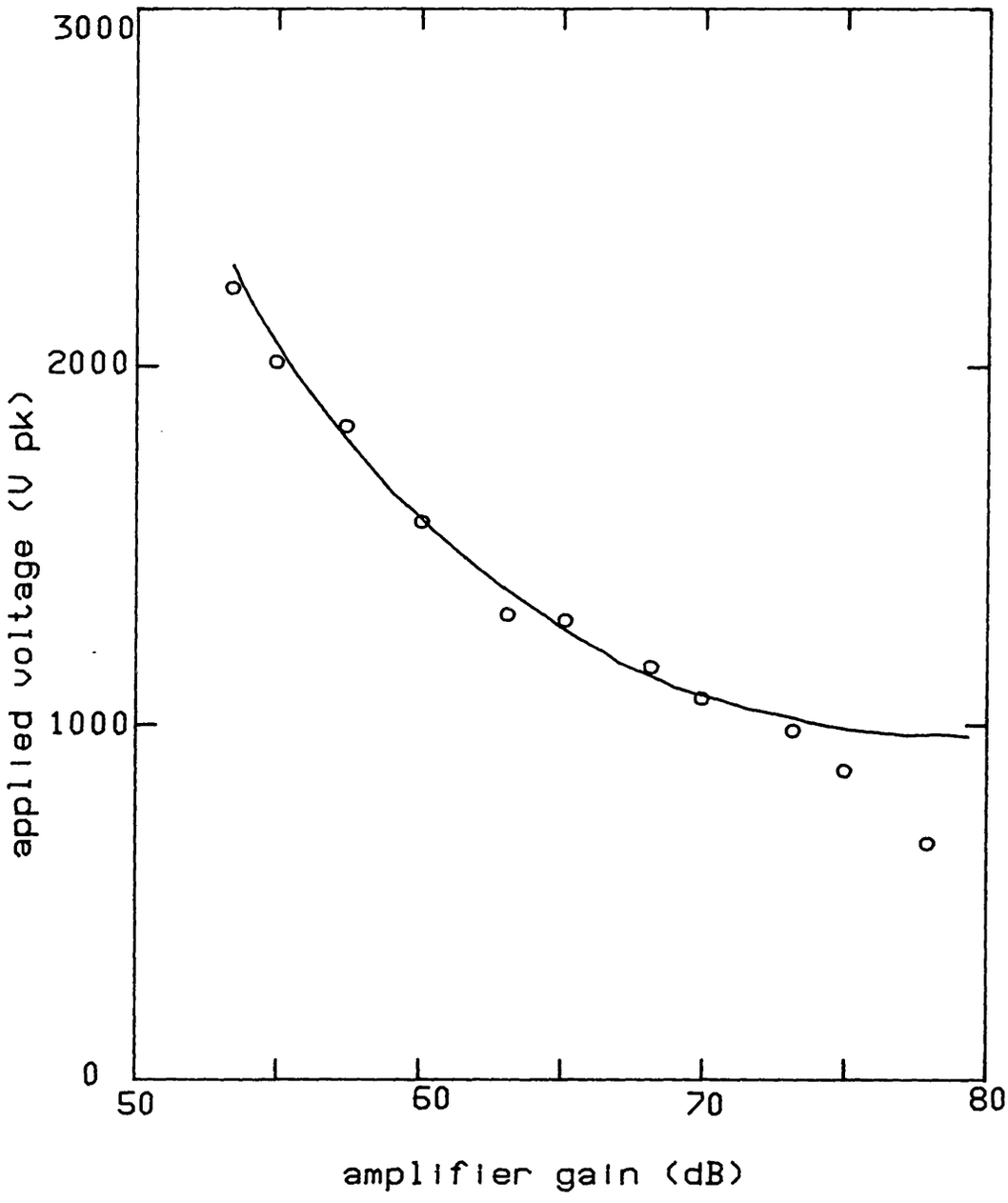

FIGURE 4.14 - Threshold voltage for the detection of AE (as defined in Section 4.4) plotted as a function of amplifier gain.

edges of the loop. As the voltage is increased further, the quantity of AE produced increases dramatically.

These general observations can be quantified by measuring the AE ringdown count rate as a function of the applied voltage. A family of such curves, measured at different amplifier gain settings, are shown in Figure 4.15. These particular measurements were made on a lead germanate sample 1.13mm thick, though the other materials studied also give curves of this shape. The count rate increases steeply at low voltages, but rises less rapidly at high values of the applied field. The count rate was observed to continue increasing up to the highest voltage that could be applied, in all the materials investigated. However, this does not imply that the number of AE bursts also continues to rise as the voltage is increased, because the ringdown count is a function of the amplitude as well as the number of the AE bursts. In Section 4.3, the average amplitude of the AE was shown to increase with the applied voltage, so that the ringdown count rate increasingly overestimates the number of AE events occurring at high values of the applied field.

The technique described in Section 4.3 could be used to estimate the number of AE events occurring from the ringdown count rate. However, the data in Figure 4.15 was recorded by varying the voltage at each of the different gain settings, so that the measurements involved in the correction procedure (those made at the same voltage at each gain setting) were actually made some hours apart and perhaps at slightly different values of the applied field. In addition, the measured count rate depends on the history of the sample (which includes any changes in the voltage across the sample), and in general the measurements obtained depend upon the order in which they are made. This may be seen by comparing the data in Figure 4.15 with that in Figure 4.8, where the count rate was measured as a function of gain. The values recorded in the two cases are generally similar, but not identical, even though the conditions of gain and applied field were reproduced as closely as the

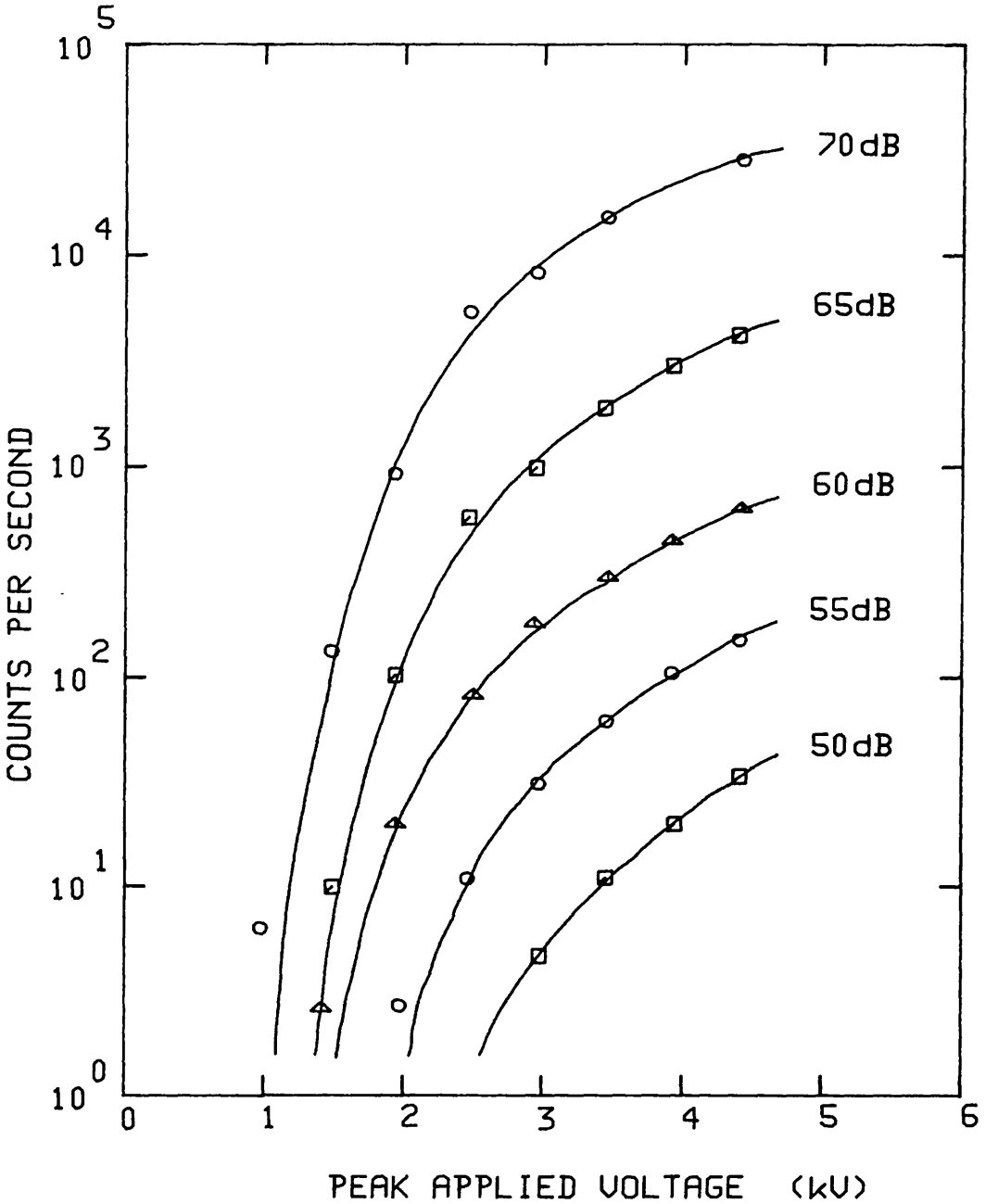

FIGURE 4.15 - Ringdown count rate as a function of peak applied voltage for five different amplifier gain settings, from a lead germanate sample 1.13mm thick.

equipment permitted. Therefore, the measurements in Figure 4.15 do not satisfy the fundamental assumption in the correction procedure that the AE signal remains essentially unchanged while the measurements at different gain settings are made. Despite this reservation, the correction has been applied to the data in Figure 4.15 and the result is shown in Figure 4.16. As expected, there is considerable scatter in the calculated points but the trend towards a saturation in the number of events, especially at the higher gain settings, is evident. Although the curves do not have a definite knee, this saturation tends to occur at lower voltages as the gain is increased. It is interesting that irrespective of the gain setting, as the voltage is increased the curves all tend towards the same limiting value of the event rate. This indicates that as the voltage is increased, the number of AE events reaches a limiting value.

The steep parts of the curves in Figure 4.15 have been extrapolated towards lower voltages. As the voltage is reduced, each curve becomes steeper and beyond a certain value of the applied field becomes essentially vertical. This value of the applied field can be considered a threshold field below which no AE can be detected at that particular setting of the amplifier gain. A threshold field for the detection of AE has been defined in Section 4.4 in terms of the timing of the AE within the hysteresis cycle. At each gain setting, the threshold fields measured by the two methods should be similar. In Figure 4.17, the values of the electric field at which the count rate/voltage curves in Figure 4.15 become vertical are plotted as a function of amplifier gain. This graph may be compared with Figure 4.14, which shows the results obtained from the timing of the AE. The agreement between the two sets of measurements is generally quite good. The accuracy in extrapolating the curves in Figure 4.15 is particularly dependent on the accuracy of the points measured at low voltages. Unfortunately, the count rate at these voltages is very small, sometimes only a few counts in 10 seconds. The odd extra count caused by noise or interference can seriously degrade the accuracy of these points, particularly at high amplifier

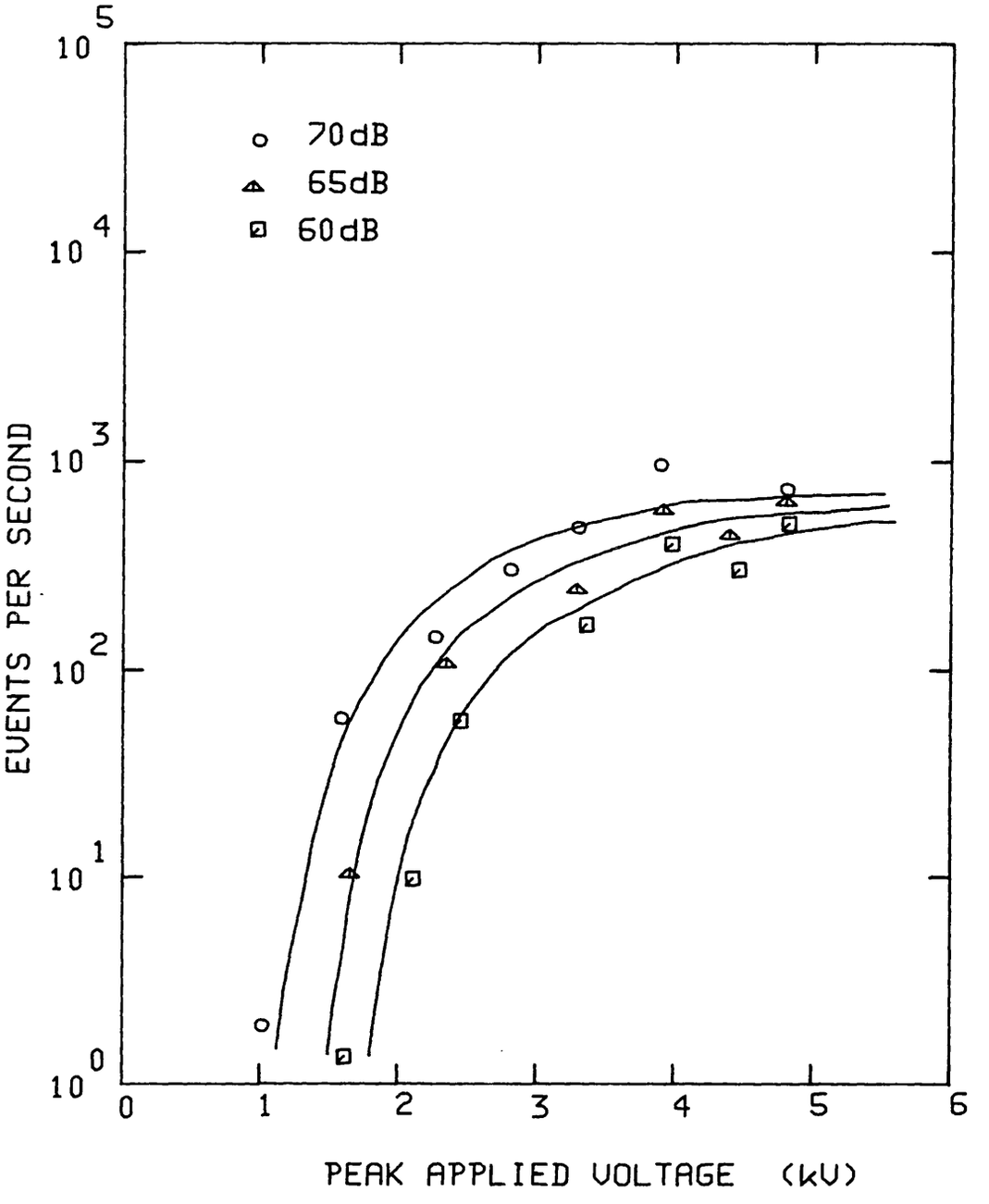

FIGURE 4.16 - Event count rate (calculated from the data in Figure 4.15) as a function of the peak applied voltage.

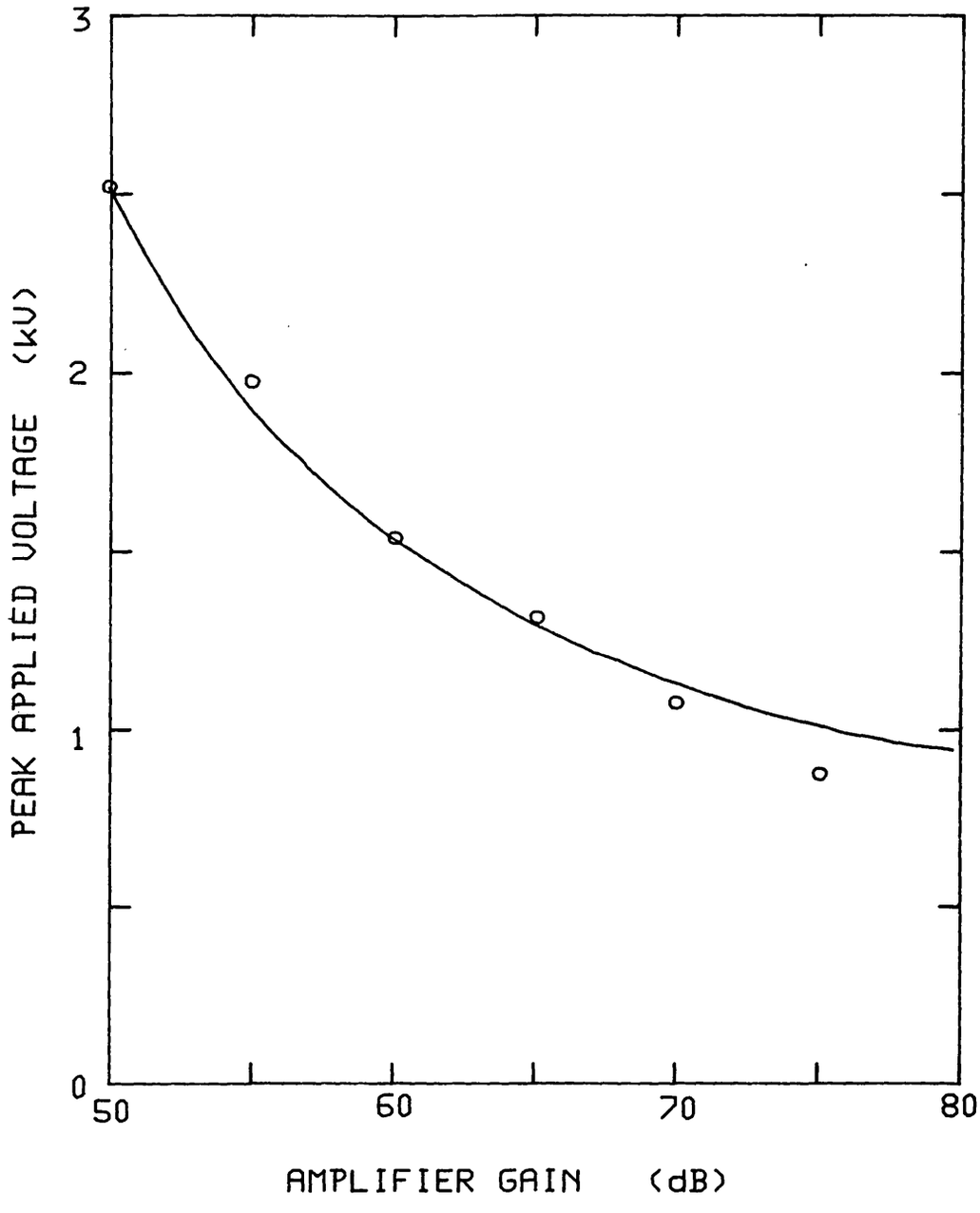

FIGURE 4.17 - Threshold field for the detection of AE (as defined in Section 4.5) plotted as a function of amplifier gain. This graph may be compared with Figure 4.14 which shows the threshold fields obtained from the timing of the AE within the hysteresis cycle.

gain settings. This has the effect of reducing the slope of the curve and indicating a slightly lower threshold field. However, because the slope in this part of the curve is so steep, this has a relatively small influence on the voltage at which the threshold occurs. Because of this, the effect of amplifier noise on the data points measured at high gain in Figure 4.17 is much less pronounced than it was in Figure 4.14. In both graphs, the tendency is towards a threshold voltage, around 1kV peak, below which no AE can be detected even at infinite gain.

The data in Figure 4.17 was obtained by extrapolating the count rate curves by hand. The accuracy of the process can be improved by fitting a function to the data points and performing the extrapolation on a computer. The problem lies in finding a suitable function to model the curves in Figure 4.15. While a third or fourth order polynomial provides a reasonably good fit to the upper portion of the curves, the slope does not increase sufficiently rapidly as the threshold field (for that particular gain setting) is approached to tend towards an infinite slope. Several other simple functions were tried, the most promising being of the form:

$$y = A + B \log (x - C)$$

where y is the logarithm (to base 10) of the ringdown count rate and x is the peak applied electric field. This function is particularly useful because C gives the threshold field corresponding to the gain setting at which the measuremants were made. However, this function does not model the entire curve accurately. By suitable choice of parameters A, B and C, it can be fitted separately to the upper and lower portions of the curve, but not to both simultaneously. When fitted to the lower portion of each curve, this function gives threshold field values which agree well with those obtained by manual extrapolation. The decision as to which points to neglect in fitting the curve has to be made subjectively, so this method does not offer any substantial improvement over extrapolating the curves by hand.

Mohamad (1980) has found that when the logarithm of the (ringdown) count rate is plotted against the reciprocal of the applied field, two straight lines can be fitted to the data in the high and low field regions respectively. He drew a similarity between this behaviour and the variation of the switching time in a ferroelectric with the applied field, and compared the constants describing the dependence of the AE on the applied field with the published data on the switching time in lead germanate. It is not clear why the ringdown count rate should vary with the applied field in the same way as the switching time. The ringdown count rate is a complex combination of the amplitude and number of the AE bursts, and any correlation between the AE count rate and other ferroelectric parameters has to take this into account. In any case, these observations could not be reproduced in full, possibly because the computer-controlled equipment used in these measurements afforded a greater resolution at low count rates than could be achieved by the previous worker. A typical plot of the ringdown count rate against the reciprocal of the peak voltage applied to the sample is shown in Figure 4.18. Although a straight line can be fitted to the data at high field (low 1/E), the low field region is distinctly curved. It is obvious that this must be the case, because the count rate falls steeply to zero as the threshold field for that particular gain setting is approached. The relations adopted by Mohamad, which were of the form:

$$\log C = A - B / E$$

where C is the count rate and E the applied field, do not provide for this observation. In the above equation, C can only be zero when the applied field E is zero, which is not what is observed.

With the exception of the low field region, Figure 4.18 closely follows the observations made by Mohamad. At infinite field (1/E=0), the curves extrapolate towards a maximum count rate

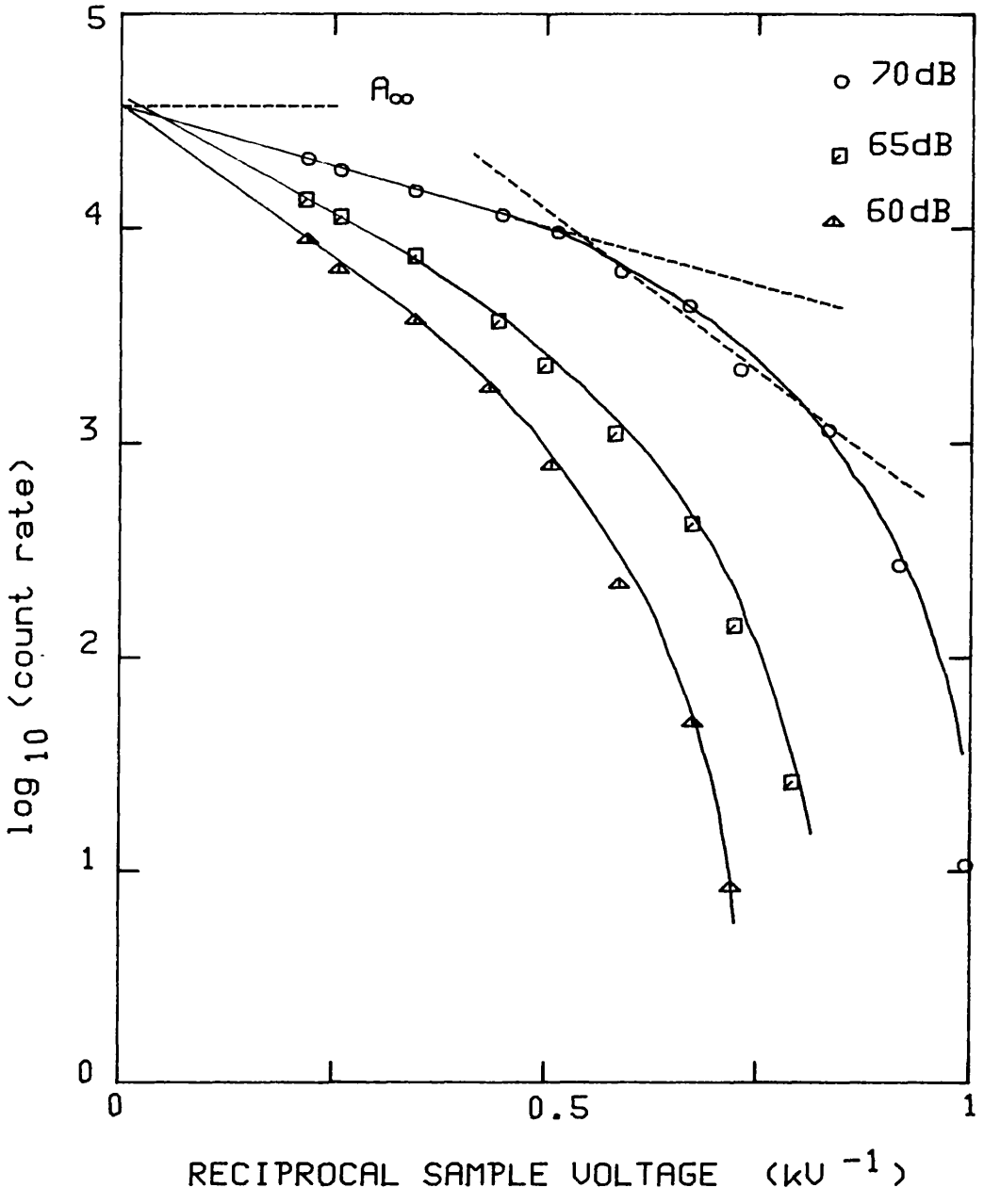

FIGURE 4.18 - Log count rate as a function of the reciprocal of the sample voltage for a lead germanate sample 1.13mm thick. .

which is independent of amplifier gain. This means that both the number and the amplitude of the AE bursts tend toward a limiting value at high field, which supports the observation made above that the number of AE events tends towards a maximum value as the applied field is increased. This limiting count rate, denoted by A_∞ in Figure 4.18, can be used as a measure of the amount of AE produced by a given sample, as it does not refer to a particular amplifier gain setting or peak applied voltage across the sample.

Another interesting feature in Figure 4.18 is the existence of two separate regions which can be correlated with a similar demarcation in the field dependence of the switching time. While this demarcation into high and low field regions is not particularly sharp in Figure 4.18, it can be taken to occur at the point where the curves depart from linearity. By ignoring the measurements made at the lowest values of the applied fields, the low field region may be approximated to by a straight line, which then intersects the high field linear dependence at a well defined point, as observed by Mohamad. This knee occurs approximately where the curve departs from the straight line fitted to the high field data, and can be used to provide a less subjective, though rather artificial, measure of the electric field which separates the two regions. This demarcation occurs at lower voltages as the amplifier gain is increased. An estimate of the true value of this critical field (where the knee occurs) can be obtained by extrapolating towards high gain. This is shown in Figure 4.19, where the critical field is plotted against amplifier gain. Mohamad obtained a value of around 11kV/cm for this critical field, which agrees with the voltage at which the knee in the switching time curve occurs (Suzuki et al 1978). The limiting critical field obtained from Figure 4.19 is 12.5kV/cm, which is slightly higher than the reported value. However, these parameters are known to vary considerably with the dimensions and the past history of the sample. The switching time of this particular sample was measured and a knee found in the voltage dependence at around 12kV/cm. The measurement of the switching time is discussed

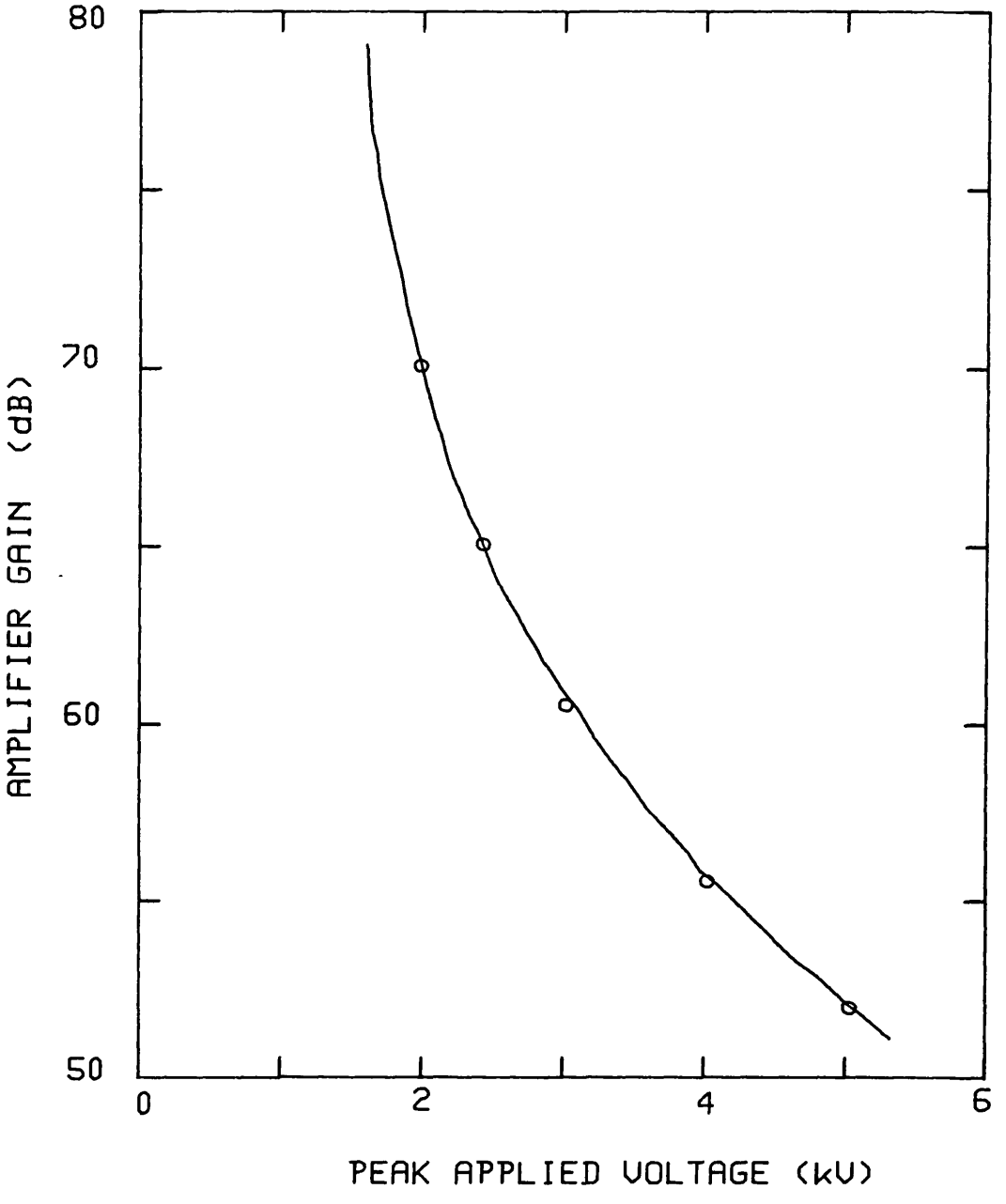

FIGURE 4.19 - Critical voltage separating the high and low field regions in Figure 4.18 plotted as a function of amplifier gain. At high gain, the curve extrapolates towards a limiting voltage of 1.4kV which corresponds to an electric field of 12.5kV/cm.

further in Chapter 5.

The existence of two separate regions in the AE count rate dependence is also evident in Figures 4.15 and 4.16. In particular, the voltages plotted in Figure 4.19 (corresponding to the knee in the count rate curves) are similar to those at which the computed AE event count begins to saturate (Figure 4.16). The demarcation of the switching time dependence into high and low field regions is generally believed to be due to the existence of two competing mechanisms of polarisation reversal. The measurement of the switching time usually starts off with a completely poled crystal, so that the first step in the reversal process must be the nucleation of antiparallel domains. The number of optically visible nuclei has been found to increase exponentially with the applied field in potassium dihydrogen phosphate (Mitsui and Furiuchi 1953) and most other ferroelectrics are believed to follow this law. This behaviour can explain the observed low field dependence of the switching time (Lines and Glass 1977). At high fields, the switching process is dominated by the sideways motion of the domain walls and no further nucleation is observed (Merz 1954). It is tempting to correlate this behaviour with the observed saturation in the number of AE events which occurs at around the same voltage. If this is so, it follows that the AE is generated by the nucleation of domains in the crystal and not by the subsequent sideways motion of the domain walls. However, it must be stressed that the measurement of the switching time relates to a completely different set of conditions than those under which the AE is observed. The switching time is usually measured in a poled crystal, reversing the voltage across it in a very short time. In contrast, when a crystal is cycled at 50Hz it is usually never fully saturated and the voltage changes sinusoidally (and therefore relatively slowly) through the hysteresis cycle.

4.6 The Threshold Field for Acoustic Emission.

In materials such as lead germanate, the existence of a threshold value of the peak electric field applied to the sample below which no AE is produced is evident from the way the quantity of AE detected varies with the applied voltage. With even the most basic equipment the AE can be seen to appear suddenly at some particular value of the applied field, as shown in the oscillograms in Figure 4.2, and this value can be used as a first approximation to the threshold field. For a more accurate estimate, and also with other materials in which the onset of AE is not as rapid as it is in lead germanate, a more quantitative approach must be used. This threshold behaviour is apparent in all aspects of the AE from ferroelectrics which vary as a function of the applied field. In the preceding sections of this chapter, such behaviour has been observed in the amplitude and the timing of the AE impulses, as well as in the raw ringdown count data.

By definition, the threshold field can only be determined by extrapolation towards the point where the quantity of AE produced is zero. This point cannot be determined directly because some AE must be produced to be detected at all. In addition, any threshold field determined in this way gives the point at which AE can first be detected, and because of the amplification and noise limits of the equipment a second extrapolation may be necessary to find the true theshold field. This distinction between the threshold field for the detection of AE (which depends on amplifier gain) and the true threshold field for the production of AE has been made in Section 4.4. The ideal method of determining the threshold field should minimise the number of extrapolations made, as each extrapolation makes certain assumptions about the behaviour of the curve beyond the last data point and introduces errors. In addition, it should provide a well defined value for the threshold field without invoking subjective decisions on the part of the experimenter, for example as to which points to

ignore when extrapolating a curve. Finally, in the interests of expediency and accuracy, it should be amenable to computer solution.

The methods described so far do not meet the above criteria. The main reason that they have been described is that they provide an insight into the behaviour of the AE as the threshold field is approached. The method described in Section 4.3, based on the amplitude distribution of the AE bursts, makes certain assumptions and approximations about the relation of the ringdown count to the amplitude of the signal that may not be valid for all materials and under all conditions. The other two methods both require two levels of extrapolation to reach a final answer. The easiest method described so far is undoubtedly that described in Section 4.5, based on the variation of the ringdown count rate with the applied field. However, the extrapolation of these curves towards an infinite slope remains a problem, particularly as a suitable function to model the curves and enable the extrapolation to be performed numerically could not be found.

The best method available to provide a quick, easy estimate of the threshold field is that originally described by Mohamad et al (1979). It is an extension of the method described in Section 4.5, based on the raw ringdown count data, but the reasoning behind it (which was not included in the original publication) is slightly more complex. Referring to Figure 4.15, as the gain is increased the count rate curves shift horizontally towards the threshold field, vertically towards ever higher count rates, and become steeper. If these tendencies are extrapolated to the limit, at infinite gain the curves tend towards a vertical line at $x=E_{\infty}$, the threshold field. At infinite gain, no AE would be observed below the threshold field and a very large (ringdown) count rate immediately above it. In other words, every point (x,y) on each curve tends towards (E_{∞}, y) as the gain is increased, and a plot of the electric field required to produce a given count rate should extrapolate towards the threshold field. The voltage at

which the count rate curves become vertical, which was plotted as a function of gain in Figure 4.17, is just a special case of this with zero count rate.

The values of the peak applied voltage for constant y in Figure 4.15 are plotted in Figure 4.20. The curves all extrapolate towards a limiting value of the electric field as the gain is increased. This technique has two advantages over using just the values at zero count rate, as was done in Section 4.5. First, the data plotted in Figure 4.20 is obtained by interpolating the count rate curves, which is an easier and more reliable process than extrapolation. Secondly, as the procedure can be repeated for a number of values of y, a check on the final answer is available. The curves should all meet at the same value of the electric field. If they do not, the area enclosed by the intersecting curves is a measure of the error inherent in the measurement. Obviously, the more measurements taken at different amplifier gain settings the more points will be available to define the curves which are extrapolated towards the threshold field. Although Figure 4.15 shows only the measurements made at five gain settings to avoid cluttering up the graph, readings were generally taken at 1 or 2dB increments from about 45dB up to the highest usable gain, typically around 75dB.

In theory, the points can be interpolated off the count rate curves at any fixed value of the count rate. However, there are practical constraints on the choice of the constant y. Too high a value will limit the number of points that can be taken because the high count rate will not be attained at low gain even with the highest voltage applied to the sample. Low count rates are generally somewhat inaccurate because of noise and interference. The range of values over which suitable curves result has to be found by trial and error, but generally corrsponds to log count rates of between 1 and 3.

In Figure 4.20, the curves extrapolate towards a limiting voltage of 925V. Dividing this by the thickness of the sample

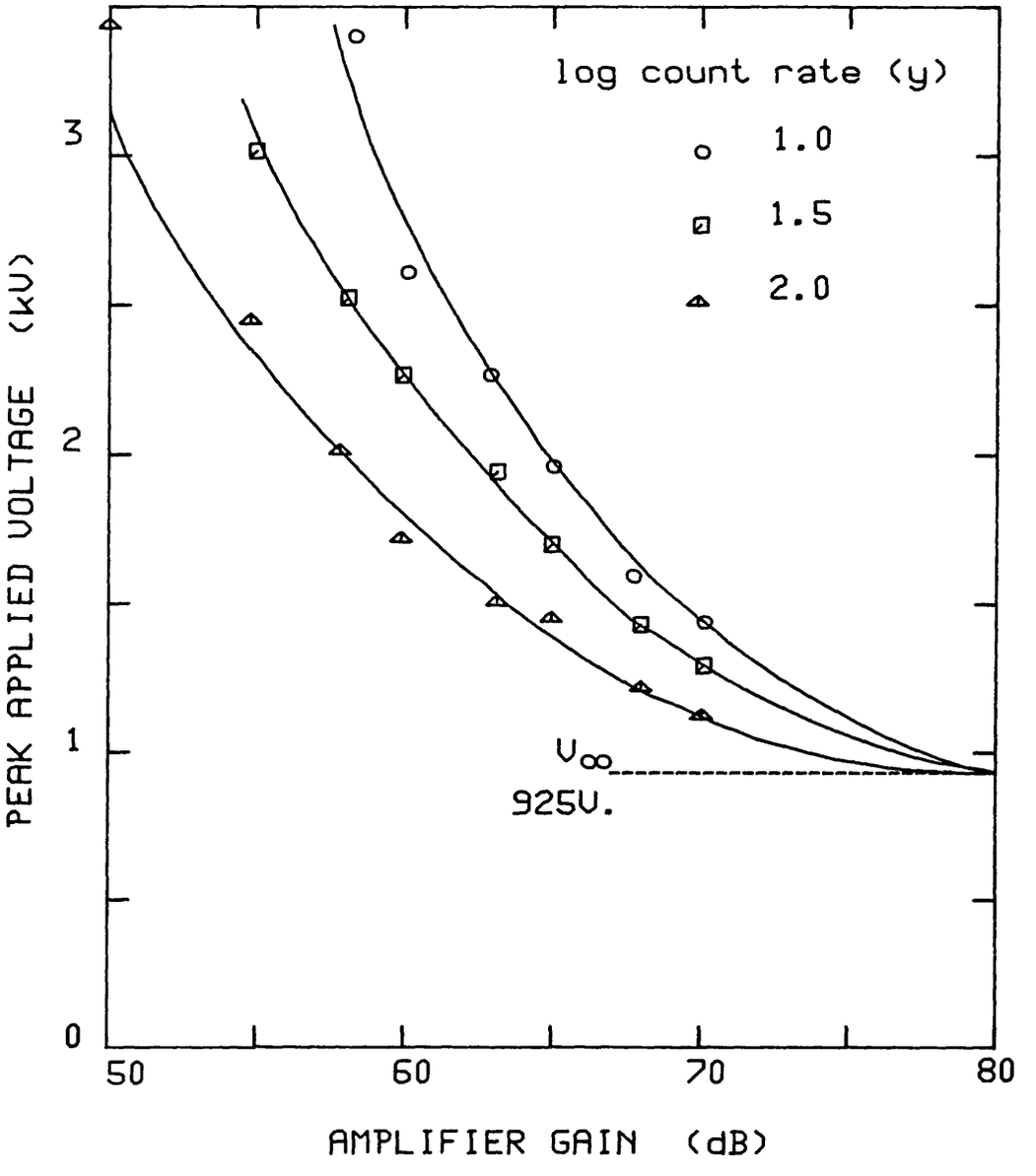

FIGURE 4.20 - Voltage required to produce a given count rate (from Figure 4.15) plotted as a function of amplifier gain. The curves extrapolate towards a limiting voltage of 925V which gives a threshold electric field for this 1.13mm thick lead germanate sample at room temperature of 8.2kV/cm.

(1.13mm) gives a threshold electric field of 8.2kV/cm. The gain at which the curves converge is a measure of how rapid the onset of AE is at voltages abobe the threshold field. For materials with a well-defined threshold, this usually occurs near the highest gain setting before the amplifier starts counting noise (typically 80dB). When the threshold is less sharp, the curves merge at higher gains and at shallower angles, requiring a longer and less reliable extrapolation.

In practice, the threshold field calculations were generally performed on a microcomputer. The count rate curves were first modelled by a cubic polynomial using a least squares technique. A fourth order polynomial was used if sufficient data points were available. As described in Section 4.5, although a polynomial cannot reproduce the observed behaviour of the count rate as the threshold field is approached, it can be used to interpolate between the data points with reasonable accuracy. The regression process typically returned correlation coefficients better than 0.9. To ease the subsequent interpolation, the axes in Figure 4.15 were effectively reversed by considering the peak applied voltage (y) as a function of the amplifier gain (x). The points for subsequent extrapolation could then be obtained by substituting the corresponding values of x into the polynomials whose coefficients have just been computed. The next step in the process was to fit a cubic polynomial to each set of points obtained as above, and extrapolate these polynomials towards the threshold field. This was done by interfacing the computer to a graph plotter and reading the threshold field off the resulting plot. A polynomial does not give the threshold behaviour that is actually observed, so that in general the polynomials plotted do not merge at the threshold field as desired. However, they are generally found to intersect at a value of the electric field close to that found by manual extrapolation. In the interests of simplicity, this point is defined as the threshold field (as discussed below, great accuracy here is not essential). When the curves do not intersect at a single point, the centre of the area enclosed by the curves is taken as the threshold value.

The regression program used was based upon a library subroutine from the Hewlett Packard 9825A program library. As the programs to perform the curve fitting and plotting were already available, a single program to determine the threshold field from the raw data was not written. While the use of a number of shorter programs involved a certain amount of extra work in transferring data, it allowed the process to be monitored continuously. The numerical methods used are all standard and can be carried out on any computer or programmable calculator.

The threshold curves can generally be estimated from extrapolated curves like those in Figure 4.20 to an accuracy of around 10%. However, this order of accuracy is largely meaningless because subsequent measurements of the threshold field in the same sample can vary markedly. As described in Section 4.5, the AE count rate at a given voltage cannot be reproduced exactly once the voltage across the sample is changed. Any subsequent measurement of the threshold field is effectively made under a different set of conditions (ie upon a sample with a different history). The largest change observed between successive threshold field measurements in the same crystal was a difference of 57% in a Rochelle salt sample. While some part of this discrepancy is doubtless due to inaccuracies in the measurement procedure, it is too large to be explained in terms of experimental error alone. No definite pattern to these changes could be found, although there seems to be a tendency for the threshold field to increase with time (and the number of repeated measurements). After taking a crystal through the ferroelectric phase transition, the threshold field is generally found to revert to a relatively low value. However, not enough measurements have been carried out on any one sample to draw any definite conclusions about this variation in the threshold field. The actual threshold field in the crystal undoubtedly also changes over the few hours required to complete the measurement of the threshold field. This contributes to the error in determining the threshold field by making the curves in Figure 4.20 tend towards different limits.

This discussion may have given the impression that AE measurements vary so much, even when made on the same sample and under the same conditions, that no useful observations can be made from them. While these variations certainly exist, and are hard to quantify, in most cases sufficient confidence could be placed on the results to allow some genaral observations to be made: the determination of the threshold field, involving a large number of individual count rate measurements, is a case in point. A measure of the reliability of the measurement can be obtained from the spread in the individual readings when measuring the mean count rate (as described in Section 3.10), or from the way the extrapolated curves intersect when determining the threshold field. If the measured quantity shows signs of changing excessively during the measurement process, the measurement must be regarded as unreliable. However, most of the measurements made do not show problems of this sort and typical accuracies of 20% or so can generally be achieved. In addition, the ways in which the AE count rate and the threshold field vary with parameters such as sample size and temperature, which are described in the following sections of this chapter, show a number of interesting trends which indicates that the reliability situation may be better than has been indicated above.

While the above discussion has concentrated on lead germanate, the other materials studied behave similarly. The determination of the threshold field in a gadolinium molybdate crystal 0.94mm thick is shown diagrammatically in Figures 4.21 and 4.22. The threshold field for this particular sample was found to be about 12kV/cm. Terbium molybdate behaves very much like gadolinium molybdate and samples of similar thickness show broadly similar threshold fields, subject to the considerations discussed above. Rochelle salt is a special case as the measured AE count rate is affected by the existence of a background AE which is produced throughout the hysteresis cycle. This background emission, and its influence on the determination of the threshold field in Rochelle salt, is discussed in Section 4.7.

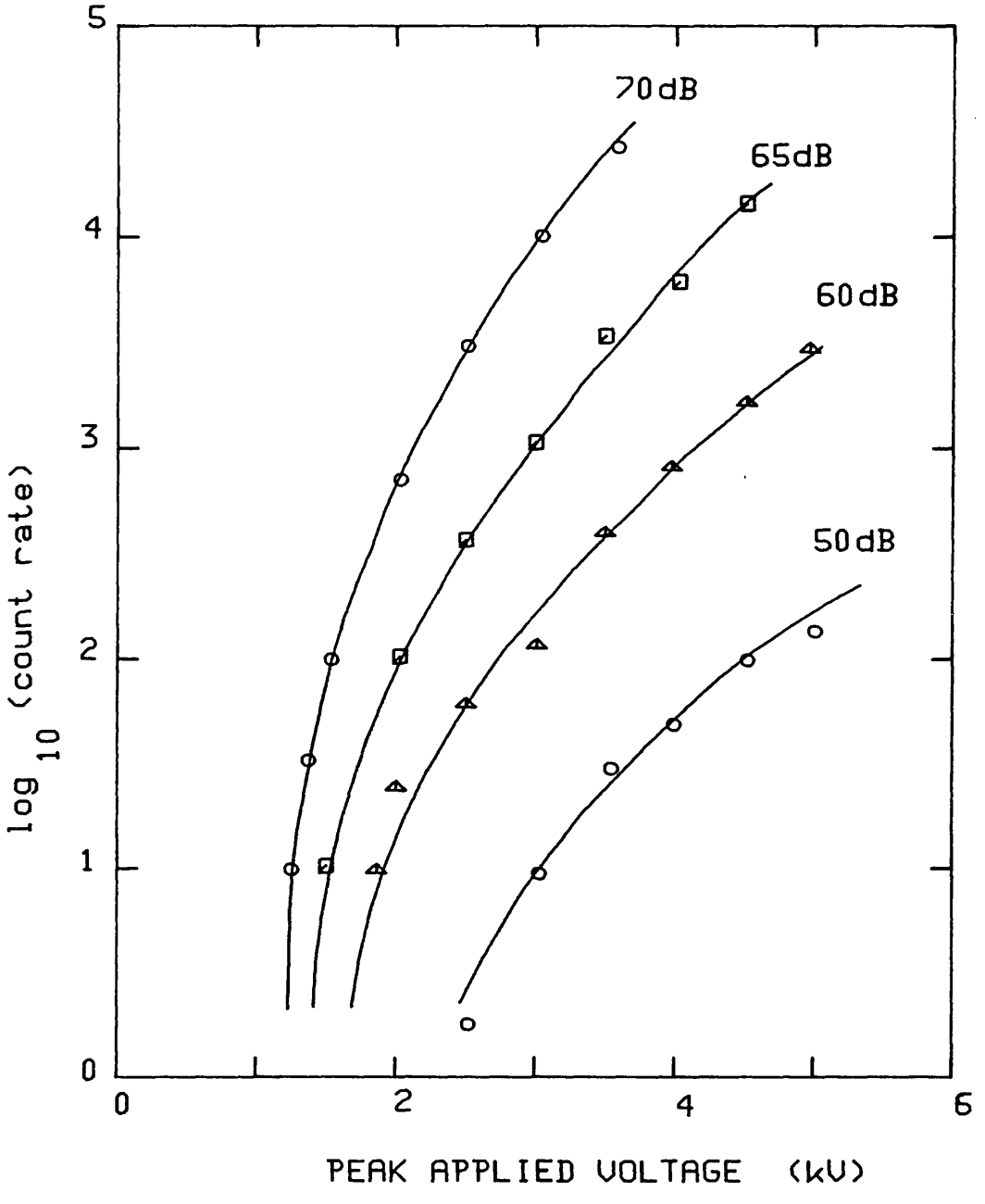

FIGURE 4.21 - Ringdown count rate as a function of peak applied voltage from a gadolinium molybdate sample 0.94mm thick at four settings of the amplifier gain.

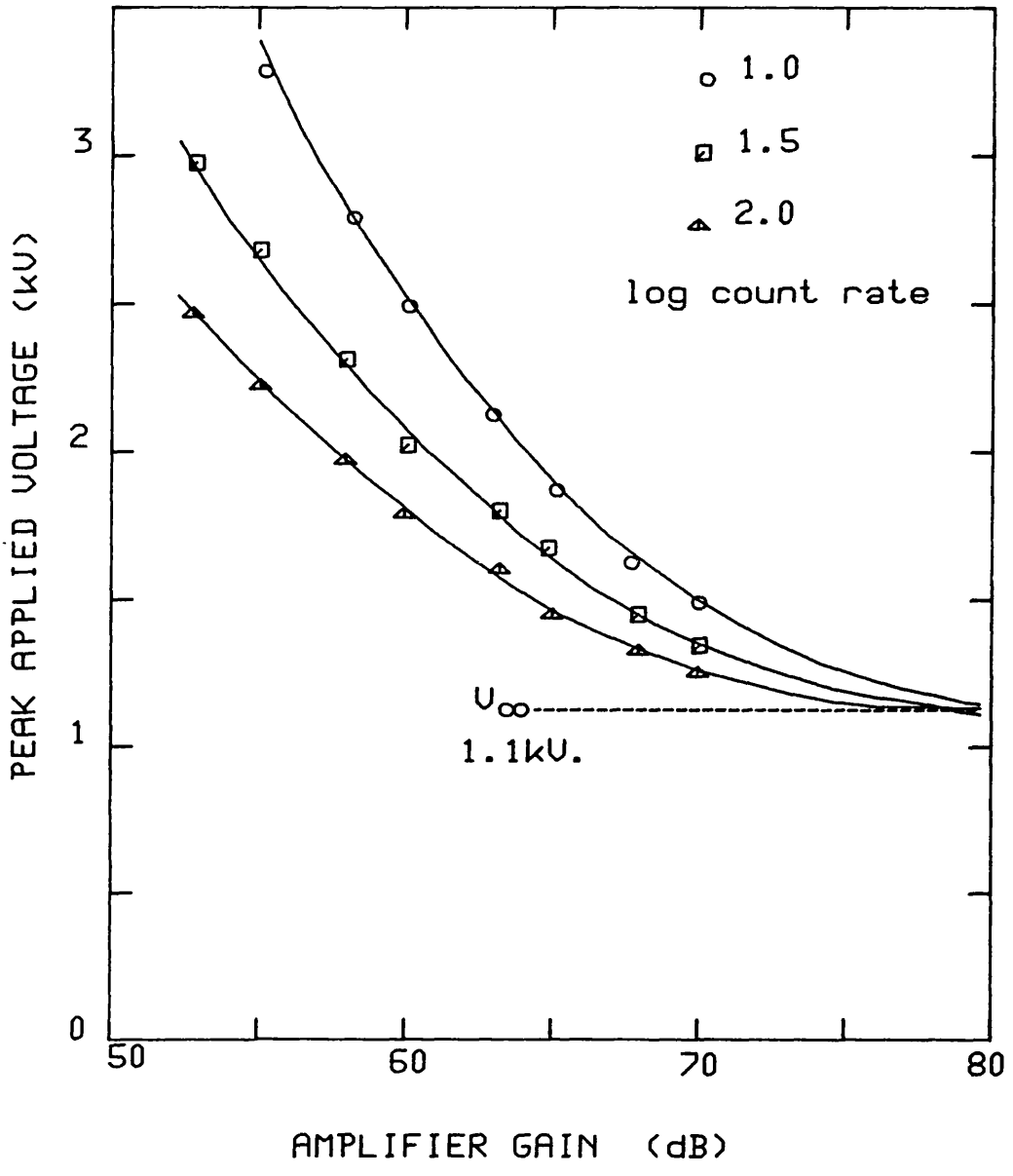

FIGURE 4.22 - Voltage required to produce a given count rate plotted as a function of amplifier gain for the data in Figure 4.21. The curves extrapolate towards a limiting voltage of 1.1kV which gives the threshold field for this 0.94mm thick gadolinium molybdate sample at room temperature as 11.7kV/cm.

Finally, it should be pointed out that a finite (ie non-zero) threshold field has been found in all the ferroelectrics which exhibit pronounced AE activity near the ends of the loop that have been studied. Mohamad (1980) had found no evidence for a threshold field in triglycine sulphate (TGS). As AE can be observed from this material at values of the applied field down to 300V/cm for a crystal 1.02mm thick, it is clear that any threshold field in this material is very low indeed. With the increased resolution afforded at lower count rates by the longer measuring times possible with the computer controlled system, a threshold field of around 100V/cm has been found in this material. This is shown in Figures 4.23 and 4.24.

4.7 The Background Emission in Rochelle Salt.

The Rochelle salt samples studied differed from all the specimens of the other materials investigated (with a few exceptions that will be discussed later) in that a background of AE was emitted throughout the hysteresis cycle in addition to the large bursts near the ends of the loop which have been described in the preceding sections of this chapter. Although this background is generally far lower than the AE produced near the ends of the loop, it does not appear to exhibit a threshold field and so it dominates the AE measurements made at low values of the applied voltage. In fact, the sample seems not to have a threshold field when considering the AE produced as a whole, although the large bursts at the extremities of the loop first appear at a well-defined threshold. In addition, the background AE is also present, albeit at lower levels, above the Curie temperature where the 'ferroelectric' AE is absent. Clearly, two distinct mechanisms are at work here and some means of separating their effects has to be found.

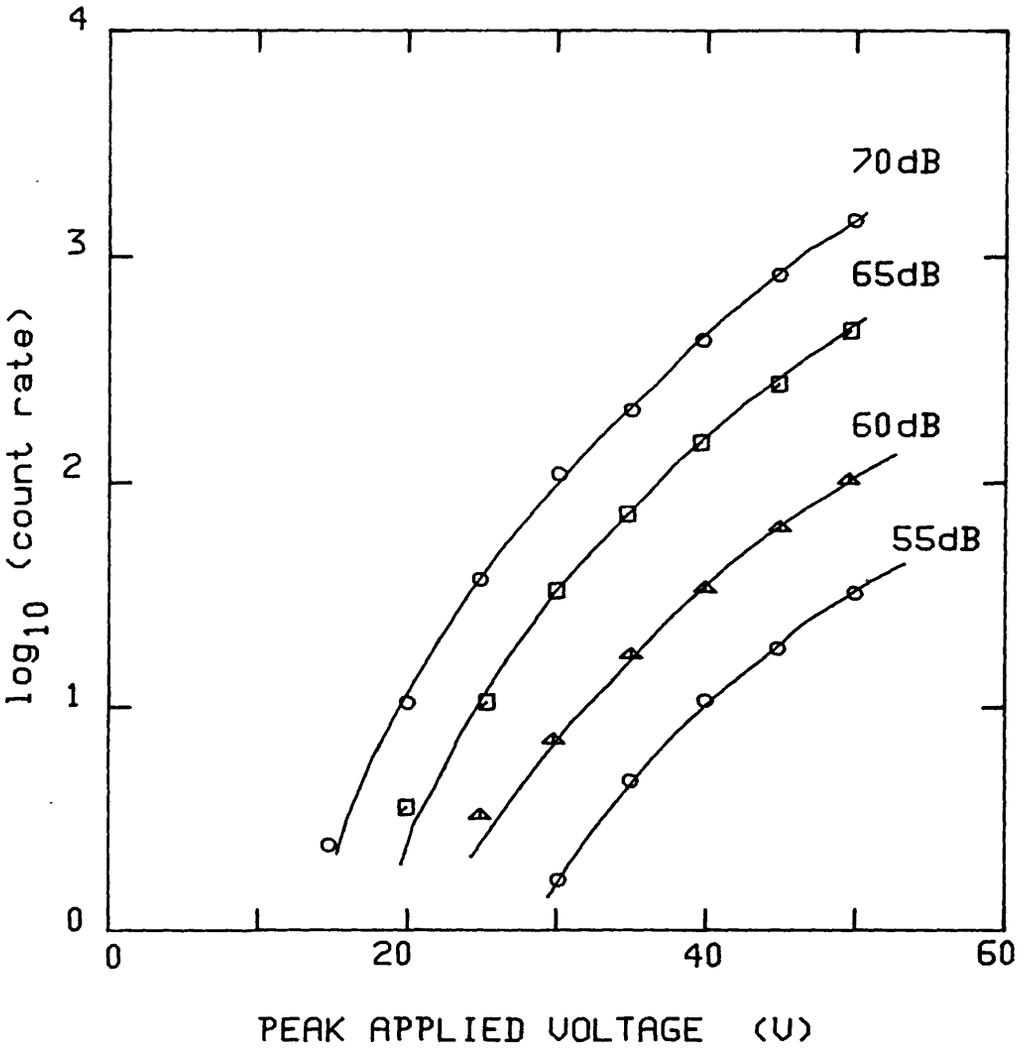

FIGURE 4.23 - Ringdown count rate as a function of the peak applied voltage from a triglycine sulphate sample 1.02mm thick at four settings of the amplifier gain.

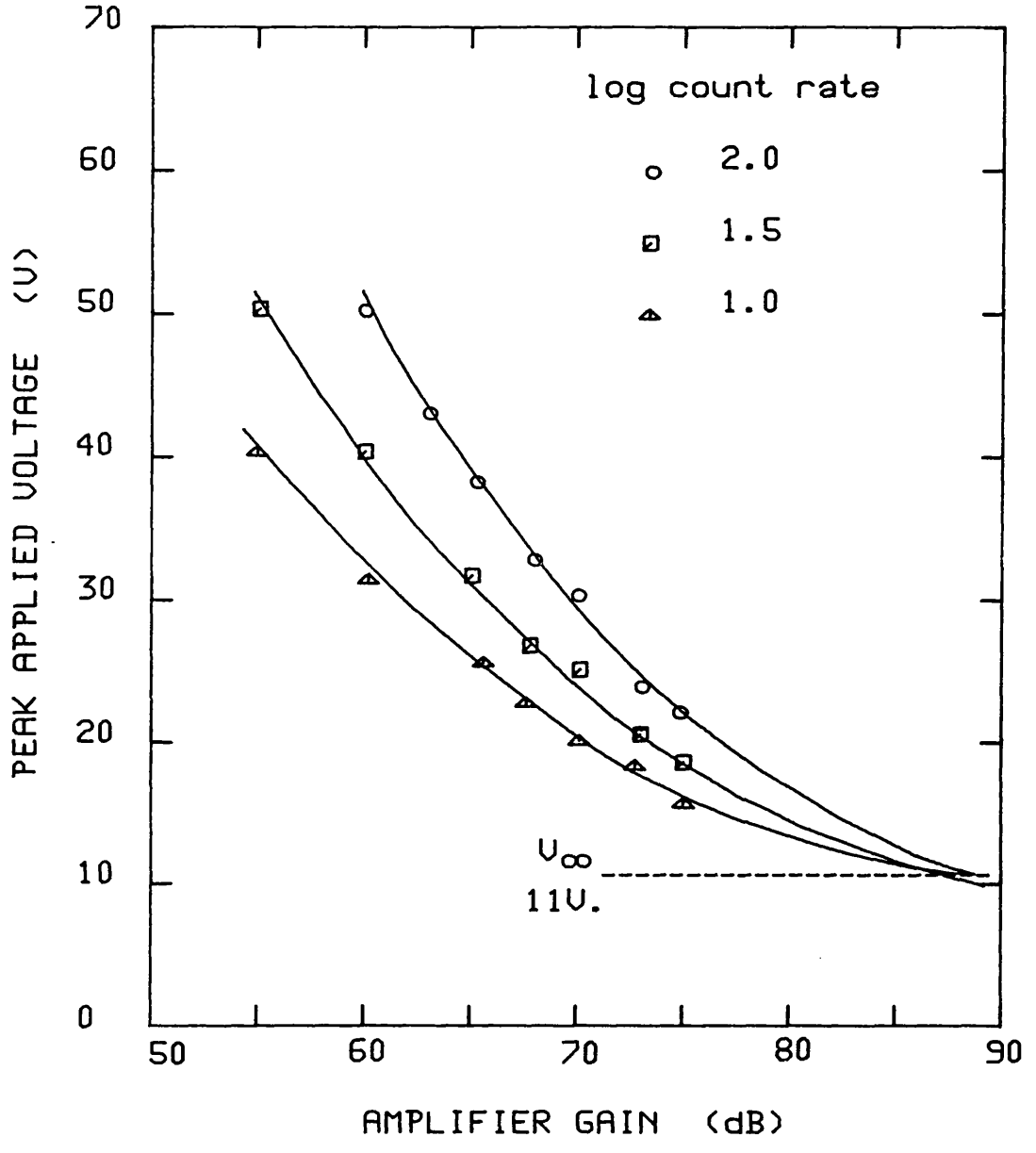

FIGURE 4.24 - Voltage required to produce a given count rate plotted as a function of amplifier gain for the data in Figure 4.23. The curves extrapolate towards a limiting voltage of 11V which gives the threshold field for this 1.02mm thick triglycine sulphate sample at room temperature as 108V/cm.

Since the most obvious way in which the background AE differs from the AE that has been described earlier is its timing, this is discussed first. The timing of AE in lead germanate has been described in Section 4.4, and a histogram of the distribution of the AE within the hysteresis cycle for this material was shown in Figure 4.11. Similar histograms for the AE from Rochelle salt are shown in Figure 4.25. As in Section 4.3, zero time (t=0) is taken as the point at which the instantaneous voltage across the sample reaches its peak negative value (ie the bottom left-hand corner of the hysteresis loop). These measurements were all made on a sample 1.09mm thick. With this sample at a temperature of 20°C (ie within the ferroelectric region), the onset of large bursts of AE was observed to occur at a peak applied voltage of about 400V, corresponding to a threshold field of around 3.7kV/cm. Figure 4.25a shows the timing of the AE produced under these conditions. This diagram shows that some AE is emitted throughout most of the half-cycle in addition to the large bursts near the end. Most of this background activity is concentrated near the middle of the half-cycle, at around t=5ms. When summed over the entire half-cycle, the background count amasses a sizable total. As the voltage across the sample is increased, the quantity of AE produced near the ends of the loop rises very rapidly and the background count becomes insignificant. However, as Figure 4.25a shows, it can introduce a considerable error in measurements of the 'ferroelectric' AE at low values of the applied field.

The timing of the background AE can be seen more clearly by going to a lower voltage, below the threshold field for the production of the 'ferroelectric' AE. This is shown in Figure 4.25b for a peak applied voltage of 30V. The background activity is greatest near the middle of the half-cycle and is practically zero at the ends. The amount of (background) AE produced appears to be roughly symmetric about t=5ms. In fact the rate of AE production in Figure 4.25b seems to follow the rate of change of the applied field (in the chosen coordinate system, at t=0 the instantaneous voltage is at a maximum and its rate of change is zero: at t=5ms, the voltage is zero and its slope is

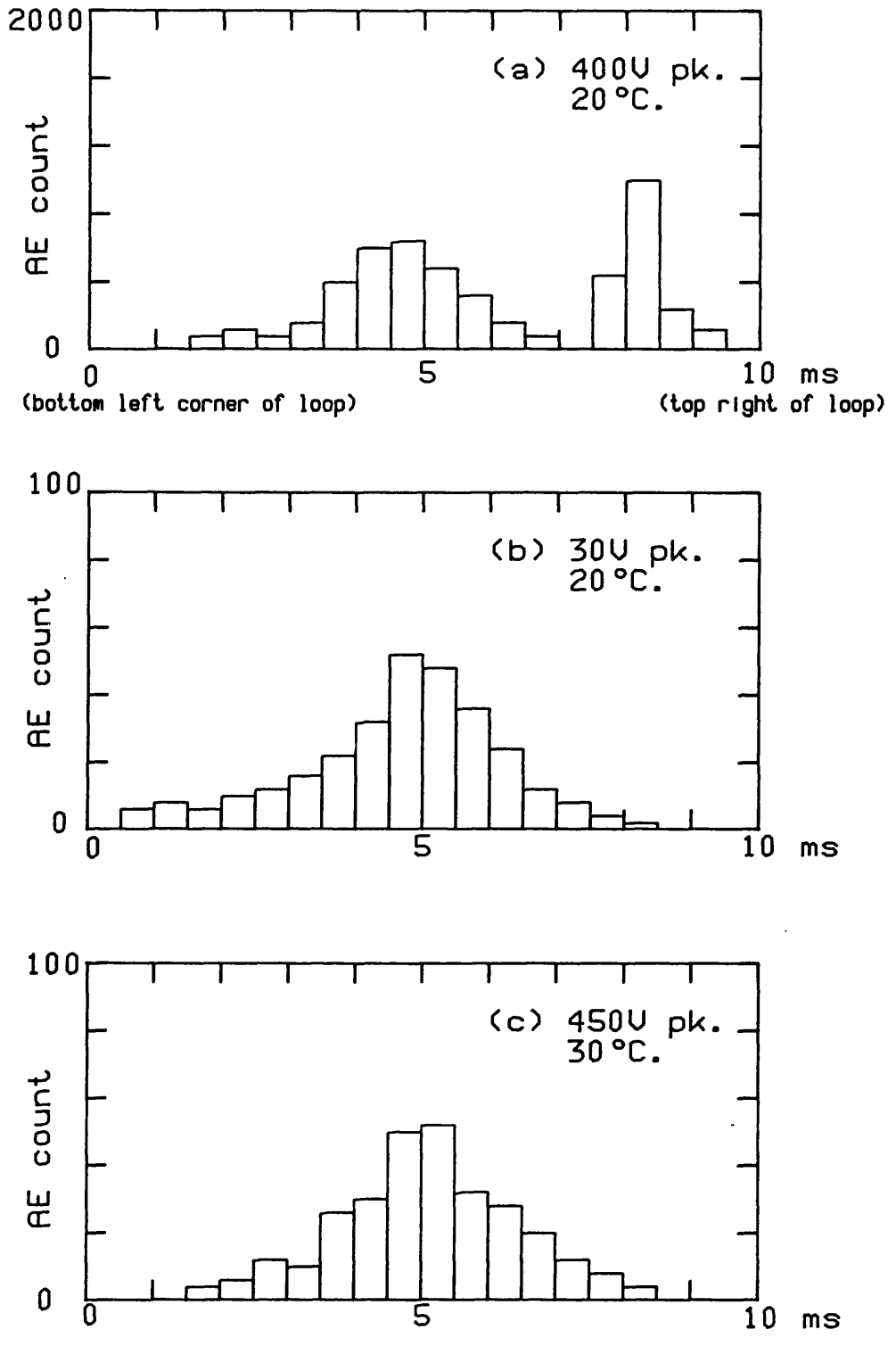

FIGURE 4.25 - Distribution of AE in the hysteresis cycle for a Rochelle salt sample 1.09mm thick under different conditions of temperature and voltage.

greatest). This indicates that the background AE may be related to the piezoelectric effect, which causes the crystal to change its dimensions in sympathy with the applied field (in fact, in some cases a low buzz can be heard emanating from the sample).

The other major way in which the background AE differs from the 'ferroelectric' AE is that it is also present above the Curie temperature. Figure 4.25c shows the timing of the AE at a temperature of 30°C. This measurement has been made at a peak applied voltage of around 450V to obtain a count rate similar to that recorded at 20°C with a peak applied voltage of only 30V. The similarity between Figures 4.25b and 4.25c is obvious: it appears that the background AE is essentially the same (except in magnitude) whether the sample is ferroelectric or not. Rochelle salt is of course still piezoelectric above the Curie temperature, although the piezoelectric coefficients are much smaller. However, piezoelectric coefficients do not have much meaning within the ferroelectric region at the high values of electric field employed. In this case, the piezoelectrically induced strain is no longer proportional to the electric field, but exhibits hysteresis and saturation (Cady 1946). Measurements made by Hinz (1939) show that at a temperature of 21°C the piezoelectric strain induced at an electric field of 300V/cm (corresponding to an applied voltage of 30V, as in Figure 4.25b), is about 15 times greater than that produced by the same voltage at 30°C. Assuming that the piezoelectric effect is linear outside the ferroelectric region up to such a high field, the voltage applied in Figure 4.25c (4.5kV/cm) to produce the same level of AE activity as in Figure 4.25b would produce the same strain in the crystal. This supports the hypothesis that the piezoelectric effect is responsible for the background AE observed in this material. However, this cannot be the complete answer, as all ferroelectrics are necessarily also piezoelectric (at least within the ferroelectric region), and yet most of the samples studied did not exhibit this background emission.

The apparent symmetry of the background AE about the centre of

the half-cycle provides the means of separating it from the AE at the ends of the loop. The AE count rate in the quarter cycles 0-5ms and 5-10ms should be approximately equal in the absence of the 'ferroelectric' AE. This has been verified at low fields below 24°C and at high fields above the Curie temperature. Figure 4.26 shows the count rate obtained from these two regions in the hysteresis cycle at low values of the applied field. Note that this graph has been drawn on a linear vertical scale, not a logarithmic one like most of the other count rate plots presented, to show how the curves extrapolate towards the origin. Above the Curie temperature, similar results are obtained for both quarter-cycles. However, at 20°C the curves diverge rapidly above about 300V. This is because of the onset of the 'ferroelectric' AE, which is present only in the 5-10ms region, at around this voltage. While the background AE count increases relatively slowly with the applied field, the other curve rises very steeply - which is why a logarithmic scale is generally used when plotting count rate curves.

When the 'ferroelectric' AE is being investigated, the effect of the background emission can be taken into account by measuring the AE count rate in each of the two quarter-cycles. Assuming that the background count is the same in both measurements, the count rate due to the 'ferroelectric' AE can be estimated simply by subtracting the two readings. This is not an exact procedure because in general the ringdown count of the sum of two signals is not equal to the sum of the counts obtained from each signal individually. However, this correction is most significant at low count rates, where the ringdown effect is not likely to introduce too great an error. The count rates from this sample, corrected in this way, are plotted as a function of the applied field in Figure 4.27. These curves are similar to those obtained from other materials where this problem is absent (Figures 15, 21, 23): this indicates that the correction procedure works well and gives a true measure of the 'ferroelectric' AE. For comparison, the count rate measured over the entire hysteresis cycle at a gain of 70dB has also been plotted in this graph. At high field,

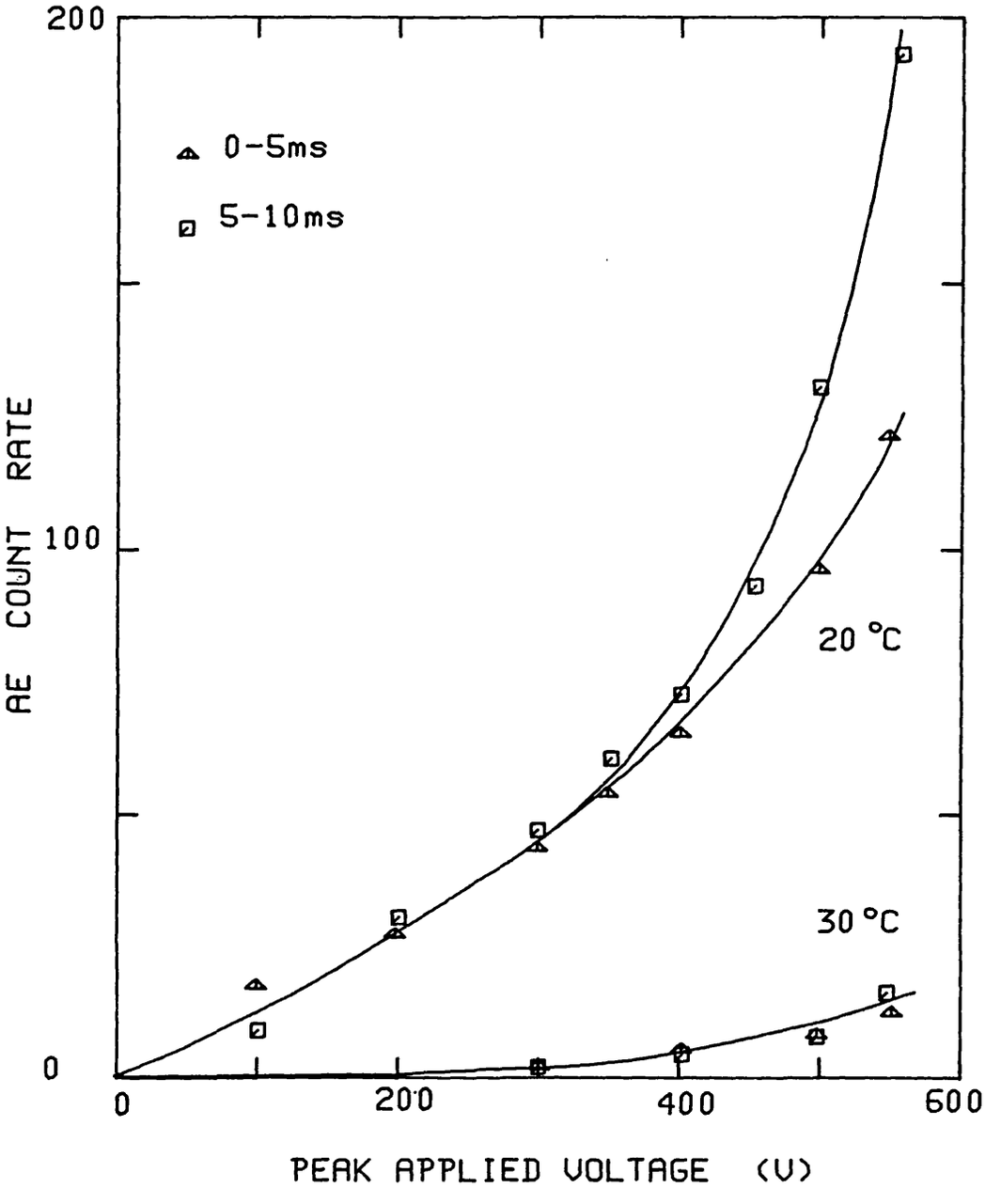

FIGURE 4.26 - AE count rate per quarter-cycle as a function of applied voltage in Rochelle salt. The curves extrapolate towards zero count rate at zero applied voltage.

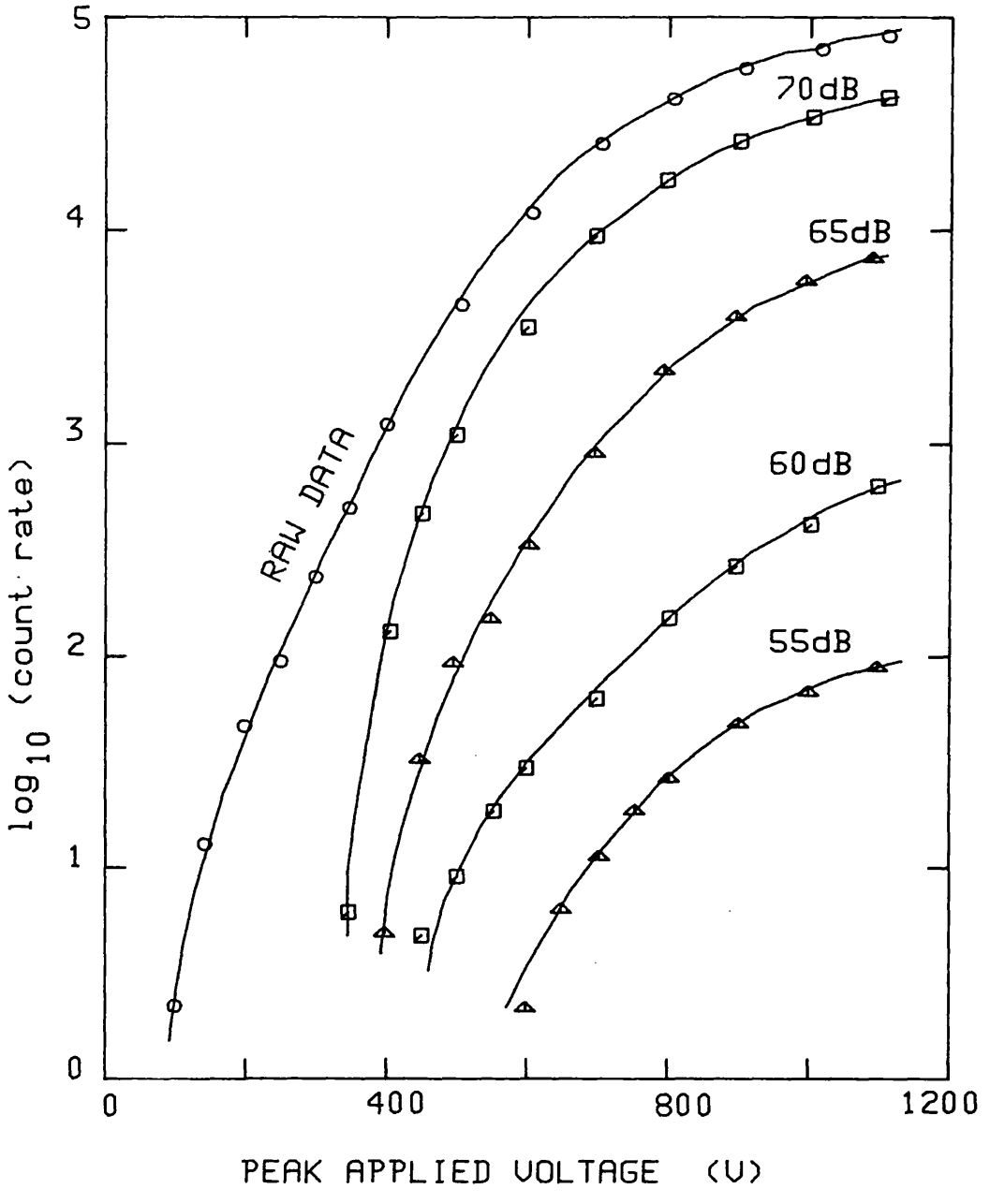

FIGURE 4.27 - Corrected count rate as a function of applied field at four amplifier gain settings for a Rochelle salt sample 1.09mm thick at 20°C. The uncorrected count rate over the entire hysteresis cycle at a gain of 70dB is also shown for comparison.

this curve matches the corrected curve shifted upward by about 0.3 on the logarithmic (to base 10) y-axis, which means that the count rates are approximately doubled (this is because the corrected curves only count the AE at one end of the loop). At low field, the two curves diverge, because of the background AE. The uncorrected curve shows no evidence of threshold field behaviour: in fact, although the curve steepens at low field it tends towards the y-axis giving a zero threshold field. However, the corrected curves do give a satisfactory value for the threshold field of the 'ferroelectric' AE. From Figure 4.28, this occurs at a peak applied voltage of 310V which gives a threshold field of about 2.8kV/cm.

The existence of the background emission has been correlated with the presence of visible defects in the crystal. As described in Section 3.2, the Rochelle salt samples prepared all contained a number of small water inclusions. Three samples were prepared with similar dimensions (10x10x1mm) and the number of defects visible on the surface of each sample was counted. The AE activity from each sample was then measured, and the results are shown in Table 4.4. Although the 'ferroelectric' AE is generally similar in all three samples, the background AE count is around six times higher in sample A, which had the greatest number of visible defects, than in sample C which had the fewest. Therefore it seems likely that the background emission is caused by the piezoelectric strains in conjunction with defects in the material. Defects such as cracks, notches and voids caused by faulty welds are well known sources of AE in stressed structures (Kelly et al 1975), even though the exact mechanism by which these sources produce ultrasound is not completely understood. In this respect the background AE in Rochelle salt may be closer to the more commonly encountered AE produced by strained materials and structures than the phenomena which form the central theme of this study.

On this hypothesis, no background AE was observed in samples of the other materials studied because the crystals did not have any defects capable of causing sufficient AE to be detected. In

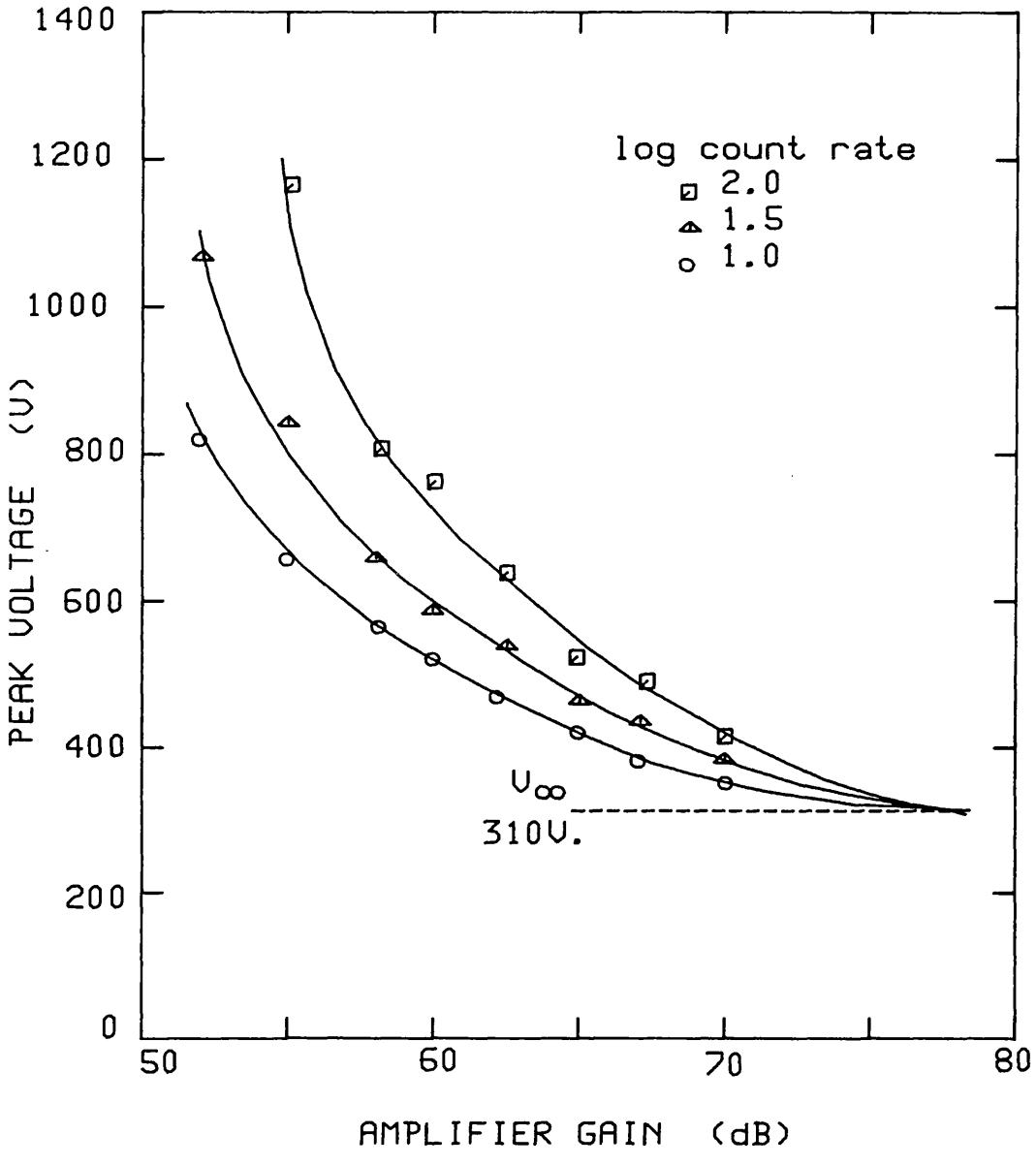

FIGURE 4.28 - Voltage required to produce a given count rate plotted as a function of amplifier gain for the data in Figure 4.27. The curves extrapolate towards a limiting voltage of 310V which gives the threshold field of this 1.09mm thick Rochelle salt sample at 20°C as 2.8kV/cm.

Specimen:	A	B	C
Number of visible surface defects	14	10	4
Typical AE count on whole cycle	30319	13512	5598
AE count 0-5ms (background)	7427	3219	1200
AE count 5-10ms	8034	3765	1772
Difference of above two count rates ('ferroelectric' AE)	607	546	572
Threshold electric field (kV/cm)	3.1	2.6	2.9

TABLE 4.4 - Acoustic emission from three Rochelle salt samples of similar dimensions (10x10x1mm) at a temperature of 20 °C related to the number of visible defects on the surface of the crystal. The AE counts shown above were measured over 10 seconds at a gain of 60dB with a peak voltage of 700V applied to the samples.

fact, this type of background AE has been observed in two circumstances from samples of lead germanate. One was a very old crystal that had been taken through the ferroelectric phase transition several times and had a number of tiny cracks within it that could be seen under the microscope. The other was the sample that was cycled at a high applied field to destruction to study the long-term variation of AE with time as discussed in Section 3.10. Shortly before the crystal cracked and split into five small pieces, the AE count rate became erratic: this was accompanied by a gradually increasing background of AE all round the loop. It is not unreasonable to suppose that the final demise of the crystal was preceded by the formation and growth of a number of small cracks within the crystal, which because of the piezoelectric strains induced in the sample would produce AE of the type described above.

4.8 The Variation of the AE with Sample Size.

The dependence of the AE upon the dimensions of the sample can be considered in two parts: the variation with the area (perpendicular to the polar axis) of the plate-shaped sample, and the effect of sample thickness. When making AE measurements on ferroelectric crystals, one is generally limited to plate samples because a large area is desirable to mate with the AE transducer while the dimension along the polar axis must be small so that a high electric field can be applied with a reasonably low voltage. In both cases, there are two major parameters of interest: the AE count rate at a given value of the applied field, and the way the count rate varies with the applied field, which is embodied in the threshold field. The effect of the surface area of the plate sample is described first.

As the electric field between two parallel electrodes is

largely confined to the volume between the electrodes, and as the ferroelectric material not affected by the electric field is not expected to contribute to the AE produced, the easiest way to investigate this is to actually measure the effect of electrode area. This can be done simply by depositing different electrodes on the same sample, thereby ensuring that the other parameters (such as sample thickness) are reproduced as closely as possible. Preliminary experiments were made by completely covering one surface of the plate with a silver dag electrode and evaporating aluminium electrodes of different sizes on the upper surface. Although this method worked well and gave results that were qualitatively similar to those described below, the asymmetric electrode configuration gives rise to a non-uniform electric field which varies as the relative size of the two electrodes is changed, and this might influence the results.

The ideal method is to deposit two identical electrodes on to the opposite faces of the sample, but the problem here is ensuring accurate vertical registration between the two electrodes. The solution finally chosen involved making up a special set of masks. Each mask consists of two square pieces of copper sheet, fixed together face to face along two opposite edges with an epoxy adhesive. A hole of the required area was punched through both sheets simultaneously. The sample could then be inserted between the copper sheets, and an aluminium electrode vacuum deposited on each face in turn through the holes in the mask. After measuring the AE produced, the electrodes were removed by lightly swabbing the surface of the crystal with a dilute solution of sodium hydroxide, in which the aluminium dissolves. However, lead germanate is slightly soluble in sodium hydroxide (which is used as an echant during the chemical polishing of this material) so the solvent had to be used sparingly. The sample was then ready for the next set of electrodes. A number of masks were made up to produce electrodes of different areas. While most of the masks were intended to produce circular electrodes, two were prepared with square cut-outs to investigate the effect of the shape of the

electrodes.

The following measurements were carried out on a slice of lead germanate 1.25mm thick and 22mm in diameter, prepared as described in Section 3.2. The measurements were made in order of increasing electrode area. The lead germanate plate was marked so that successive electrodes could be placed in different positions on the sample. As the AE count rate is influenced by the history of the ferroelectric material being switched, it was desirable to distribute the active regions as evenly as possible over the sample surface. The whole process was repeated three times to obtain a measure of how the AE changes with the removal and re-application of the electrodes and the repeated application of an electric field. In the event, the values obtained on the different runs were quite close. The results of this experiment are tabulated in Table 4.5.

Table 4.5 shows that the threshold field remains essentially unchanged when the electrode area is varied. However, the mean AE count rate (at a constant value of the applied field) rises as the area of the electrodes is increased. These results are plotted out in Figure 4.29, which shows that the AE count rate varies in direct proportion with electrode area. The two sets of measurements made with square (as opposed to circular) electrodes also lie close to this line, showing that the area and not the shape of the electrodes is the important parameter.

The ringdown count rate plotted in Figure 4.29 is a function of both the amplitude and the number of the AE bursts produced. The amplitude distribution of the AE signal produced at two different electrode areas was calculated as described in Section 4.3: the resulting amplitude spectra are shown in Figure 4.30. Although these spectra might seem different, the important point is that in both cases the peak occurs at about -62dB: the difference in the height of the peak merely reflects the difference in the measured count rates obtained with different electrode areas. What Figure 4.30 shows is that the mean

Electrode Description	Area (mm^2)	Threshold Field (kV/cm)			AE Count Rate		
		Run: 1	2	3	1	2	3
5mm diam.	20	7.8	7.6	7.9	181	222	173
8mm diam.	50	7.9	7.8	7.3	405	412	453
10mm diam.	79	7.2	7.1	7.4	650	643	701
10mm square	100	7.5	7.8	7.9	920	935	743
12mm diam.	113	7.3	7.8	7.8	891	945	992
14mm diam.	154	7.7	7.4	7.3	1182	1201	1245
16mm diam.	201	7.2	7.5	7.8	1630	1882	1956
15mm square	225	7.8	7.2	7.1	1884	2045	1952
18mm diam.	255	7.5	6.8	7.1	2557	2282	2439

TABLE 4.5 - AE production as a function of electrode area in a lead germanate sample 1.25mm thick. Each measurement was repeated three times (Runs 1, 2 and 3). The AE count rates in the right-hand columns of the table were measured with a peak applied voltage of 2kV and at an amplifier gain of 60dB.

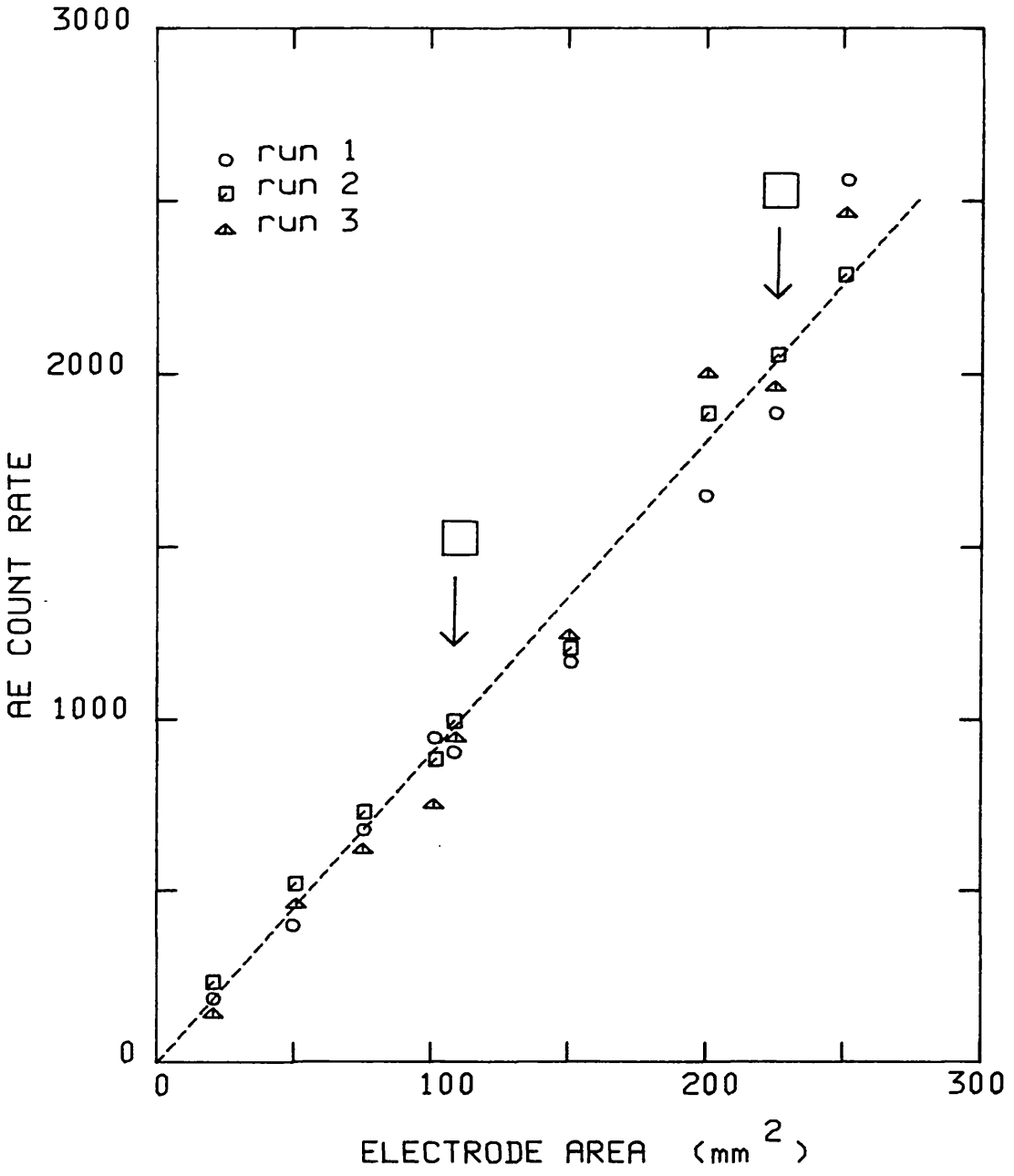

FIGURE 4.29 - AE count rate as a function of electrode area for a lead germanate sample 1.25mm thick, measured at a peak applied voltage of 2kV and an amplifier gain of 60dB. The two measurements made with square electrodes (the rest were made with circular electrodes) are marked in the graph.

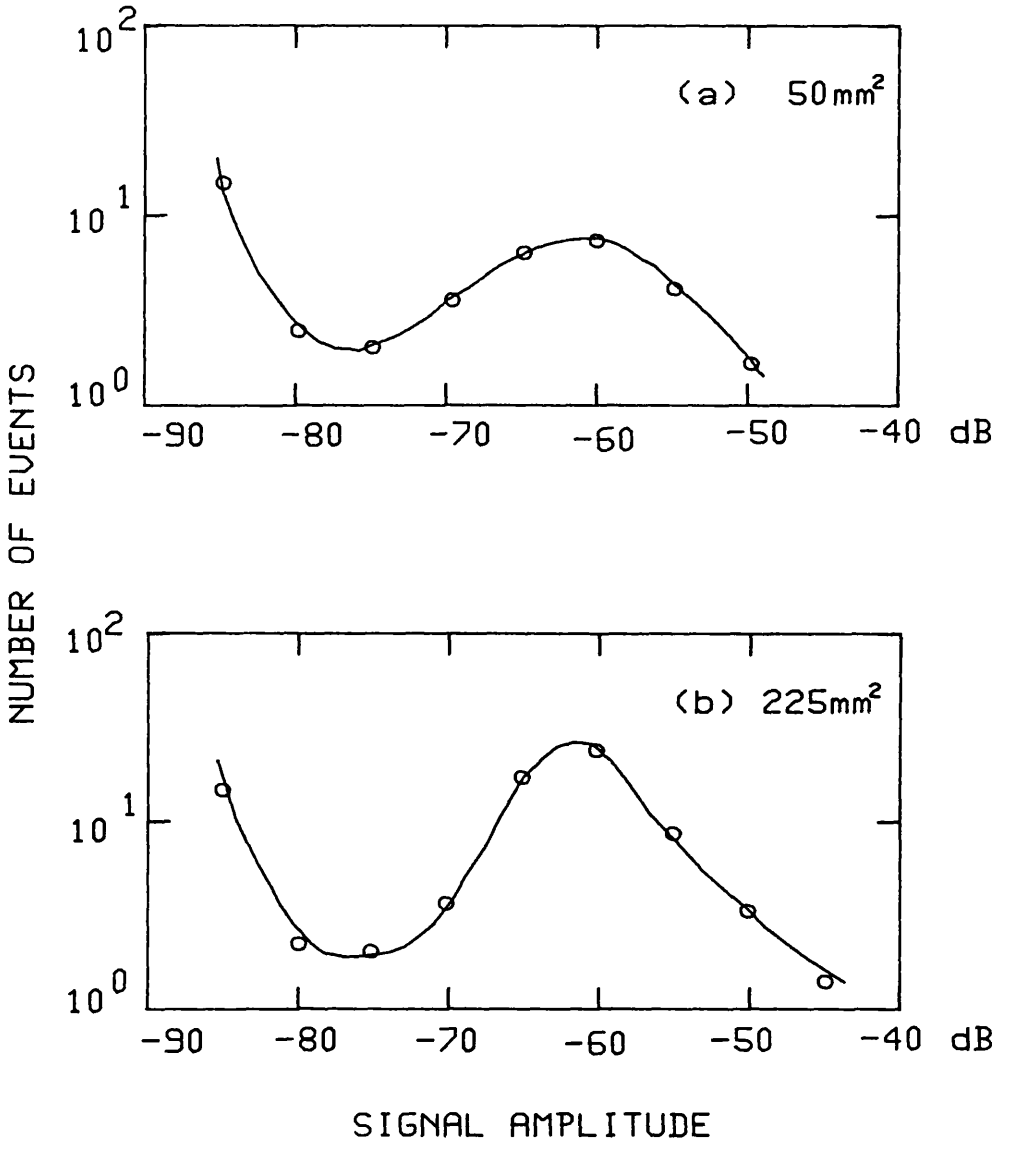

FIGURE 4.30 - Amplitude spectra of the AE produced by a lead germanate sample 1.25mm thick with electrodes of different areas. The amplitude distribution of the AE in the two cases is quite similar, with a peak at about -62dB.

amplitude of the AE bursts is not affected by changing the electrode area, and if this is so then the only thing that does change must be the number of bursts. Given a constant amplitude distribution, the linear relationship between the ringdown count rate and the electrode area means that the number of AE events is also proportional to the area of the electrodes, and therefore to the volume of ferroelectric material being switched. This is consistent with the sources of AE being uniformly distributed through the volume of the crystal, at least in the plane perpendicular to the polar axis.

A similar experiment has been carried out on a Rochelle salt sample, with the same results: the threshold field is unaffected by the change in electrode area, while the AE count rate at a fixed voltage is proportional to the area of the electrodes. Similar experiments could not be carried out in gadolinium and terbium molybdate samples because insufficient raw material was available to prepare large specimens.

4.9 The Variation of the AE with Sample Thickness.

When measuring the dependence of the AE upon the thickness of the sample, a number of problems arise. First of all, it is no longer possible to carry out all the measurements on the same sample, as it is not practical to polish repeatedly an initially thick sample down to each required thickness. The AE produced by different samples of the same material, of similar size and under the same conditions can vary considerably. The history of the sample and the concentration of impurities and defects in the crystal are known to contribute to this variation in the AE produced. To minimise these effects, the samples used were all freshly cut from the same boule of raw material. Electrodes were then deposited through the same mask (8mm diameter) on to each sample, so that the electrode area was also constant. To

minimise the effects of previously applied electric fields, the sequence of voltages applied to each sample was recorded and repeated on each of the other samples.

A second problem arises from the way in which the frequency of the AE produced depends on the sample thickness. As described in Section 4.2, the AE is predominantly emitted with a frequency inversely proportional to the thickness. This means that a wideband transducer had to be used when comparing AE count rates obtained from samples of different thicknesses, and as this transducer is less sensitive than the resonant types (Section 3.3), counting had to be performed over a longer time to gather a statistically significant total count. The frequency response of the amplifier falls off sharply above 2MHz, so that these comparisons are limited to samples thicker than about 1mm (Figure 4.5). These considerations do not substantially affect the measurement of the threshold field in the sample. The determination of the threshold field requires an extrapolation towards zero count rate, and is not dependent (in theory at least) on what fraction of the total AE produced is actually being measured. However, in practice the accuracy of the extrapolation is dependent on accumulating a high count rate, so the fall-off in signal strength with thin samples adversely affects the accuracy of the measurement. To maximise the count rate, a resonant transducer was used to determine the threshold field. Mohamad (1980) found that measuring the threshold field with a wideband transducer always gave a higher threshold field than with a resonant one: this can be attributed to the lower sensitivity of the wideband transducer requiring a higher voltage applied to the sample before the AE is of sufficient amplitude to be detected. With the greater resolution at low count rates afforded by the AE measurement system used in the present work, no substantial differences between the threshold fields measured with the two transducers could be found, at least for samples thicker than about 1mm where the frequency of the AE produced lies within the frequency range of the measuring system.

Figure 4.31 shows how the AE count rate, measured using a wideband transducer and at a constant amplifier gain setting of 70dB, varies with the applied electric field for six lead germanate samples of different thickness. Note that this graph has been plotted with the electric field on the horizontal axis, not the sample voltage as in the previous graphs of this type. Assuming a uniform field, the electric field is obtained by dividing the voltage across the sample by its thickness d. While for any one sample the terms voltage and electric field are practically interchangeable, being related by a constant (the sample thickness d), this is no longer so once the thickness becomes a variable.

The count rate at a given value of the electric field can be obtained from Figure 4.31 by reading off the intercepts on a vertical line at the required value of the electric field. The AE count rate at an applied field of 25kV/cm is plotted as a function of sample thickness in Figure 4.32. This graph clearly shows the sharp fall in count rate for crystal thicknesses less than about 1mm, caused by the dominant frequency of the AE falling outside the amplifier passband. For thicker crystals, the count rate should not be affected by the limited frequency response of the amplifier/transducer system. However, even here the trend seems to be that the count rate falls for thinner crystals.

The ringdown count rate at a constant value of the applied electric field is not a fair measure of the AE activity of samples of different thickness because the threshold field also varies with sample thickness. Figure 4.31 shows that the threshold field of thick samples is lower than for thin ones, and so the AE count rate at a given value of the electric field is expected to fall as the sample thickness is reduced. As described in Section 4.5, when the log count rate is plotted against the reciprocal of the applied field, the curves extrapolate to a limiting count rate at high field that is independent of amplifier gain (Figure 4.18). This limiting value, denoted by A_∞ , can be used to provide a measure of the

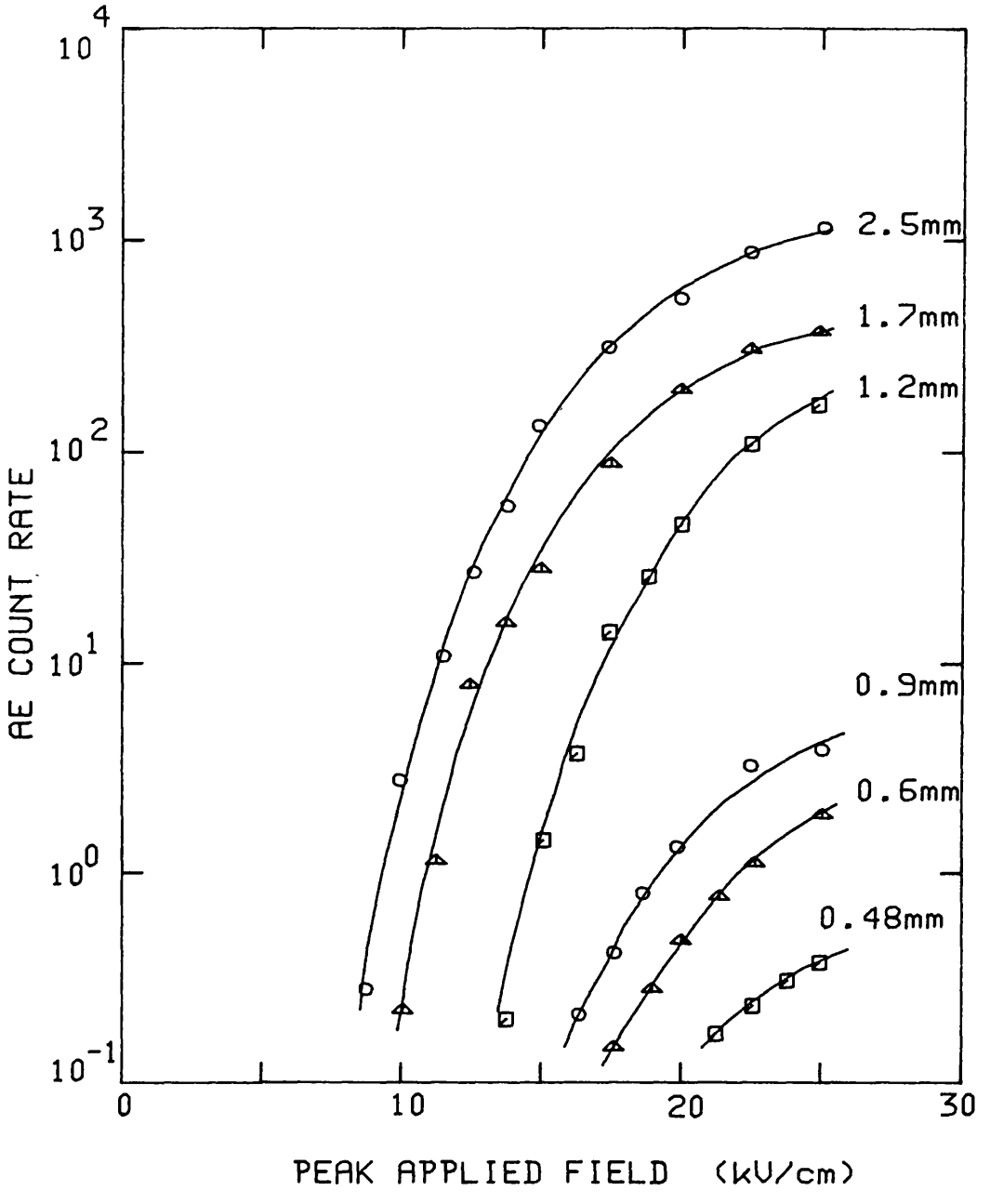

FIGURE 4.31 - AE count rate (measured with a wideband transducer at an an amplifier gain of 70dB) as a function of the applied electric field for six lead germanate samples of different thicknesses.

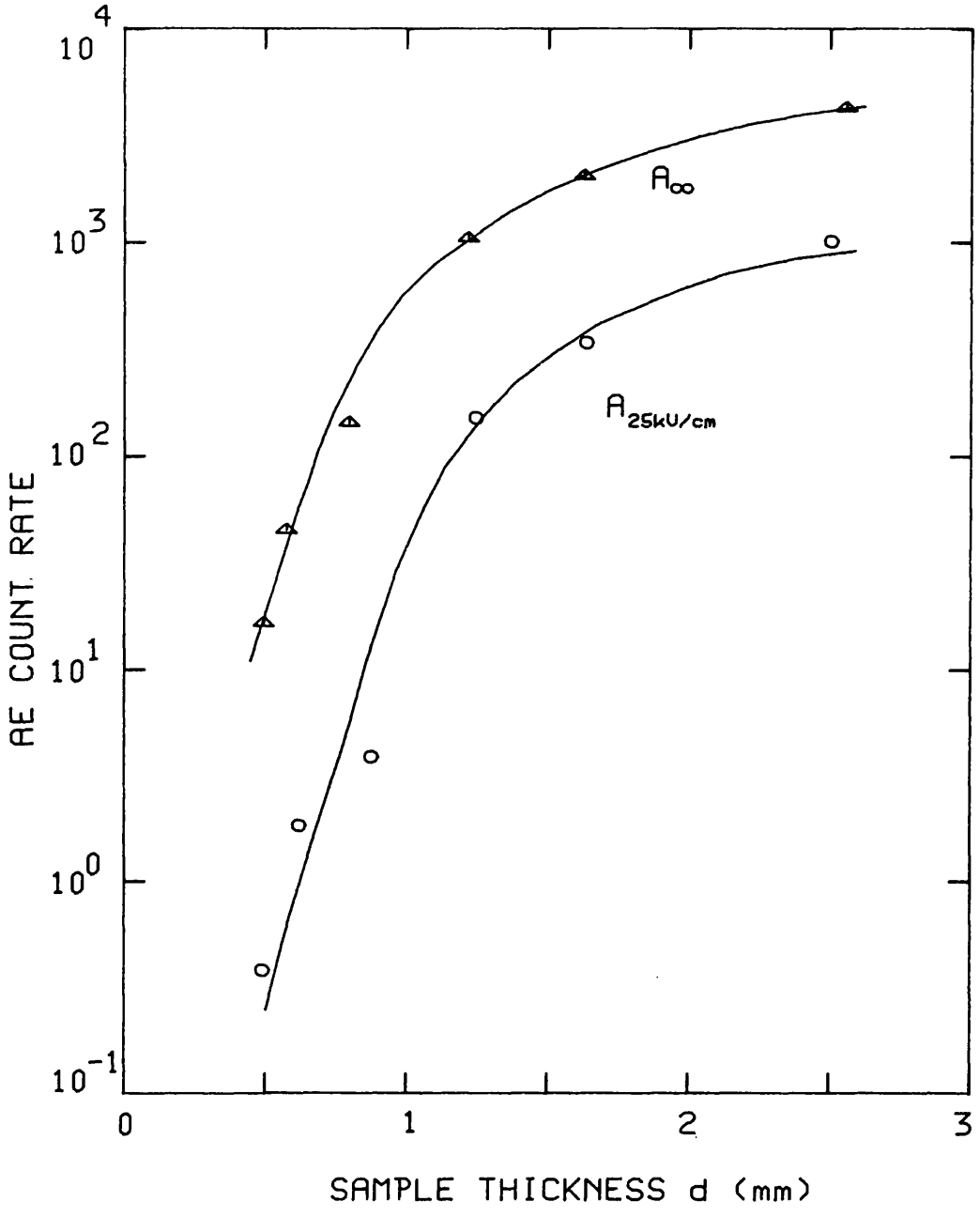

FIGURE 4.32 - AE count rate at a gain of 70dB and an applied electric field of 25kV/cm ($A_{25kV/cm}$) and the limiting count rate A_∞ (as defined in Section 4.5) plotted as a function of sample thickness, from the data in Figure 4.31.

AE activity of the sample that is independent of the threshold field. A plot of A_∞ as a function of sample thickness is included in Figure 4.32. Again, the count rate falls sharply for thinner samples. Because the amplifier frequency response dominates measurements of this kind, comparing the AE count rates from samples of different thicknesses cannot be expected to yield much useful information, and this approach has not been investigated any further.

The measurement of the threshold field for AE as a function of sample thickness is a much more promising approach, as the changing resonant frequency of the sample should not dominate these results. Figure 4.31 shows that all the curves show a threshold behaviour (even though this occurs at very low count rates for the thinner crystals) and that the threshold field is lower in thick crystals than in thin ones. This can be seen from Figure 4.33, where the threshold field of each sample is plotted as a function of thickness. The error bars on this graph become larger for thinner crystals, reflecting the longer extrapolation made necessary by the low count rates obtained from these samples. As described in Section 4.6, the threshold field is determined by extrapolating a number of curves towards high gain, and in practice these curves do not converge at a single point. The ends of the error bars represent the extremities of the area enclosed by the intersecting curves: the threshold field for that sample is taken as the mean of these two extreme values. Admittedly, this is a crude estimate of the accuracy of the measured values, and the fact that smooth curves can be drawn very close to the data points indicates that the accuracy of these points is better than implied by the length of the error bars.

The data in Figure 4.33 can be displayed in a more informative way by plotting the threshold field as a function of the reciprocal of the sample thickness (Figure 4.34). This graph can be divided into two regions: for thick crystals, the threshold field increases almost linearly with 1/d, while for crystals thinner than about 0.9mm the threshold field remains

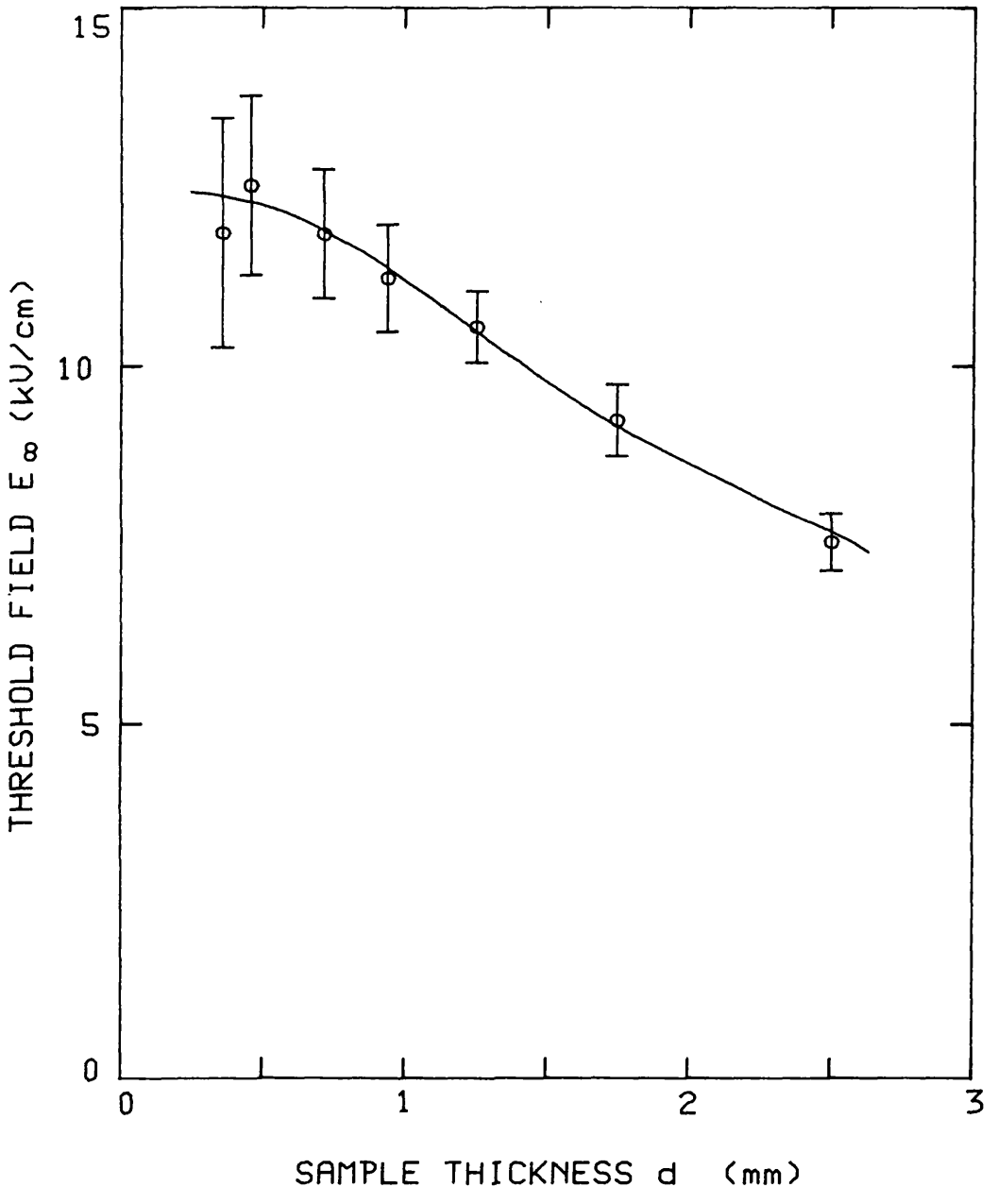

FIGURE 4.33 - Threshold electric field for acoustic emission as a function of sample thickness for lead germanate at room temperature.

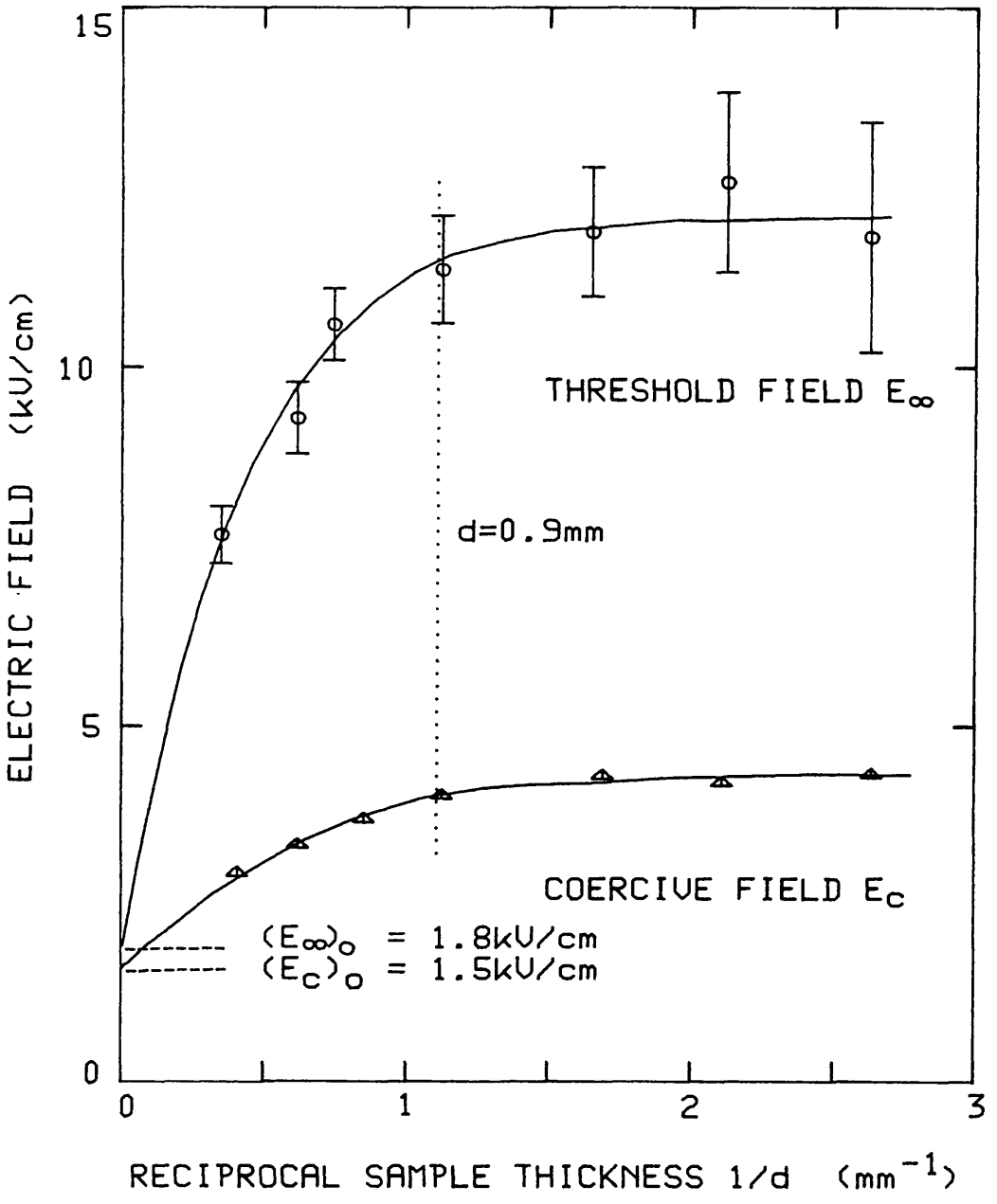

FIGURE 4.34 - Threshold field E_∞ and coercive field E_c plotted as a function of reciprocal sample thickness 1/d for lead germanate. The curves have been extrapolated towards low 1/d, ie towards infinite sample thickness.

essentially constant. This contrasts with the observations of Mohamad (1980) who reported that the threshold field continues to increase linearly with 1/d for crystals as thin as 0.3mm, where he measured a threshold field of over 30kV/cm. However, such large values of the threshold field have not been found in lead germanate, and the data in Figure 4.34 clearly shows that the threshold field stops rising for samples thinner than 0.9mm, even allowing for the full length of the error bars. As described above, the signal strength available from these thinner crystals is very low, and the comparatively primitive techniques used by Mohamad would almost certainly grossly overestimate the threshold field in these circumstances.

For thick crystals, the threshold field E_∞ increases approximately linearly with the reciprocal of the crystal thickness (1/d). This behaviour can be represented by the straight-line equation:

$$E_\infty = (E_\infty)_o + A / d$$

where A is a constant and $(E_\infty)_o$, which is the intercept of the line on the y-axis, represents the threshold field in the bulk crystal (infinitely thick sample). From Figure 4.34, $(E_\infty)_o$ is about 1.8kV/cm.

This linear dependence recalls the behaviour of the coercive field E in barium titanate reported by Merz (1956). Most ferroelectrics do not have a true coercive field as a very low electric field will ultimately switch the crystal given enough time (Lines and Glass 1977). However, a coercive field can be defined under a given set of conditions (notably a fixed frequency of the driving field) as the point where the P-E hysteresis loop intersects the horizontal E-axis (P=0). Even so, this coercive field varies with the peak applied voltage: this can be seen in the sequence of photographs in Figure 4.2. The coercive field for a lead germanate sample 1.22mm thick is plotted as a function of the peak voltage across the sample in Figure 4.35. At low field, the coervive field increases with

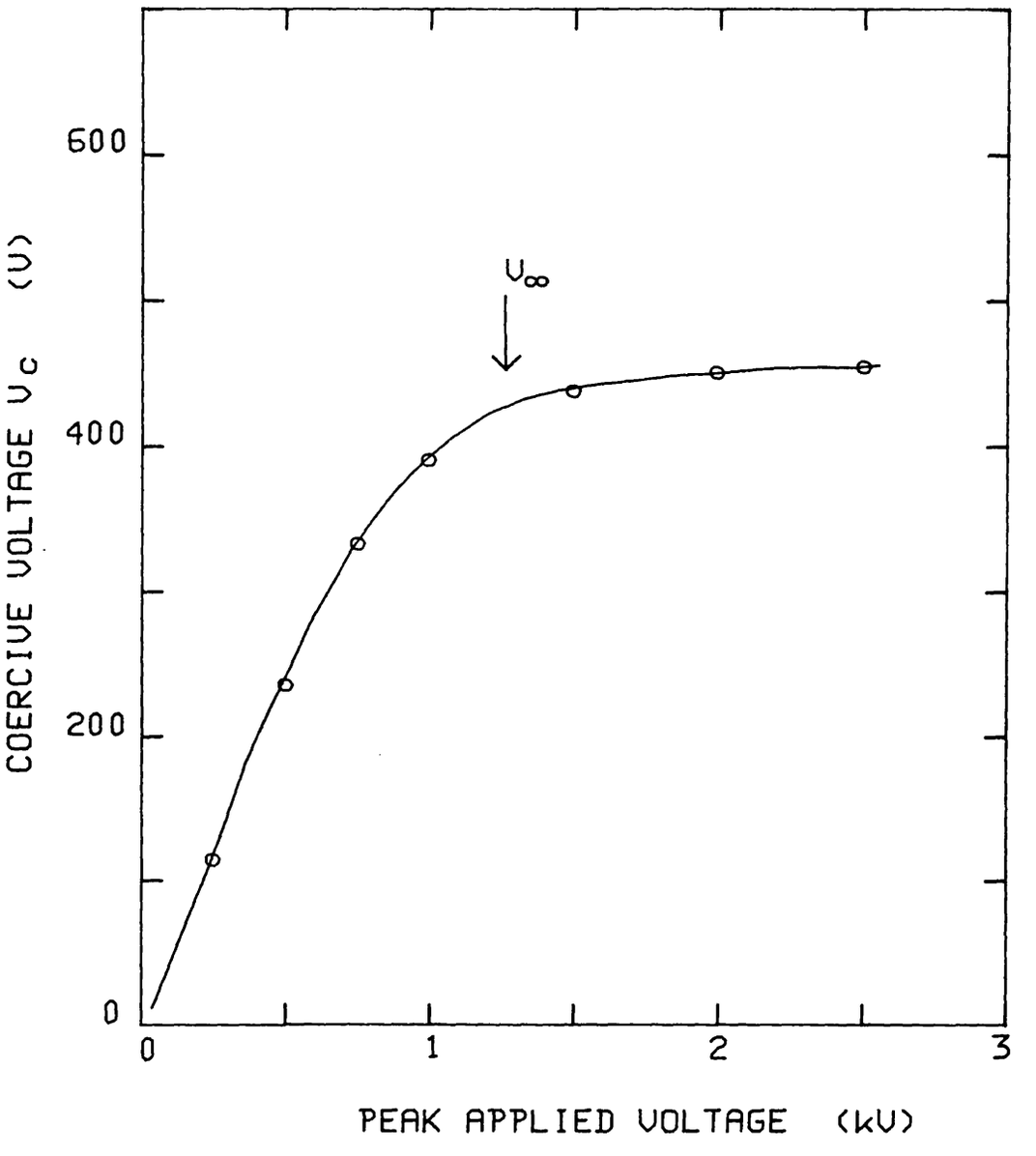

FIGURE 4.35 - Coercive Voltage (defined as the instantaneous voltage across the sample to produce zero polarisation at 50Hz) plotted as a function of the peak applied voltage for a lead germanate sample 1.22mm thick. The threshold voltage for acoustic emission V_∞ in this sample (1.3kV) is also indicated in the graph.

the applied field but reaches a limiting value: this can be defined as the true coercive field for that frequency, in this case 50Hz. It is interesting to note that the coercive field reaches its limiting value at around the threshold field for acoustic emission for the sample, which is also indicated in Figure 4.35. This behaviour has been observed in all the samples studied, and seems to be a general rule: it is a more precise way of saying that the onset of AE occurs once a well-formed and fully saturated loop is obtained.

A plot of the coercive field against 1/d is included in Figure 4.34. Like the threshold field for acoustic emission, the coercive field becomes constant for samples thinner than 0.9mm. For thick crystals, the behaviour of the coercive field E_c is approximately linear and, again like the threshold field, can be represented by an equation of the form:

$$E_c = (E_c)_o + B / D$$

where $(E_c)_o$ measures the threshold field for the bulk crystal. From Figure 4.34, this intercept occurs at about 1.5kV/cm, which is close to (and certainly within experimental error of) the limiting value of the threshold field $(E_\infty)_o$. The behaviour of the coercive field in lead germanate shown in Figure 4.34 agrees well with that reported by Mohamad (1980), who measured a limiting coercive field for the bulk crystal $(E_c)_o$ of 1.54kV/cm, a maximum threshold field (at high 1/d) of 3.75kV/cm and a knee in the curve at about d=0.8mm.

The coercive field in barium titanate has been observed to depart from its linear dependence on the reciprocal thickness for very thin crystals, in a way similar to that in Figure 4.34. Callaby (1966) has shown that this can be explained by proposing the existence of a surface layer beneath each electrode where the domain wall mobility is less than in the bulk. However, the thickness of these layers is only a few microns, and the coercive field in barium titananate becomes constant for thicknesses below 25 microns: this is almost two

orders of magnitude less than the point where the coercive field in lead germanate becomes constant. Surface layers of thicknesses comparable to that in barium titanate have also been observed in other ferroelectric materials (Lines and Glass 1977). Hence it is probable that the departure of the coercive and threshold fields from a reciprocal dependence on the sample thickness in lead germanate is due to some other cause.

The above behaviour has also been observed in Rochelle salt. Figure 4.36 shows how the threshold field in this material (at 20 °C) varies with the reciprocal of the sample thickness. This graph has all the major features of Figure 4.34, including the correspondences between the threshold field and the coercive field. In addition, this behaviour in Rochelle salt has been correlated with visual observations of the domain structure in this material. These observations are described in greater detail in Chapter 5. Because of the poor contrast between antiparallel domains in this material, it was not possible to obtain satisfactory photographs of the domain structure of Rochelle salt, so no photographic evidence is available to back up the visual observations described below.

When viewed down the polar axis, the domain structure of Rochelle salt consists of a number of long, thin parallel-sided domains (Jona and Shirane 1962). In the five thinnest samples of this material, the domain structure on one face was found to be very similar to that on the opposite face, indicating that the domain walls generally extended right through the thickness of the crystal. These samples all had a similar threshold field. In the thicker samples, where the threshold field varies linearly with 1/d, the domain structure on the two opposite faces was found to differ considerably, indicating a layered structure in the material. This layered structure would produce a highly non-uniform electric field within the material, which might account for the observed drop in the threshold field in thicker samples. A similar correlation between the domain structure and the behaviour of the threshold field was also searched for in lead germanate. However, as the domain

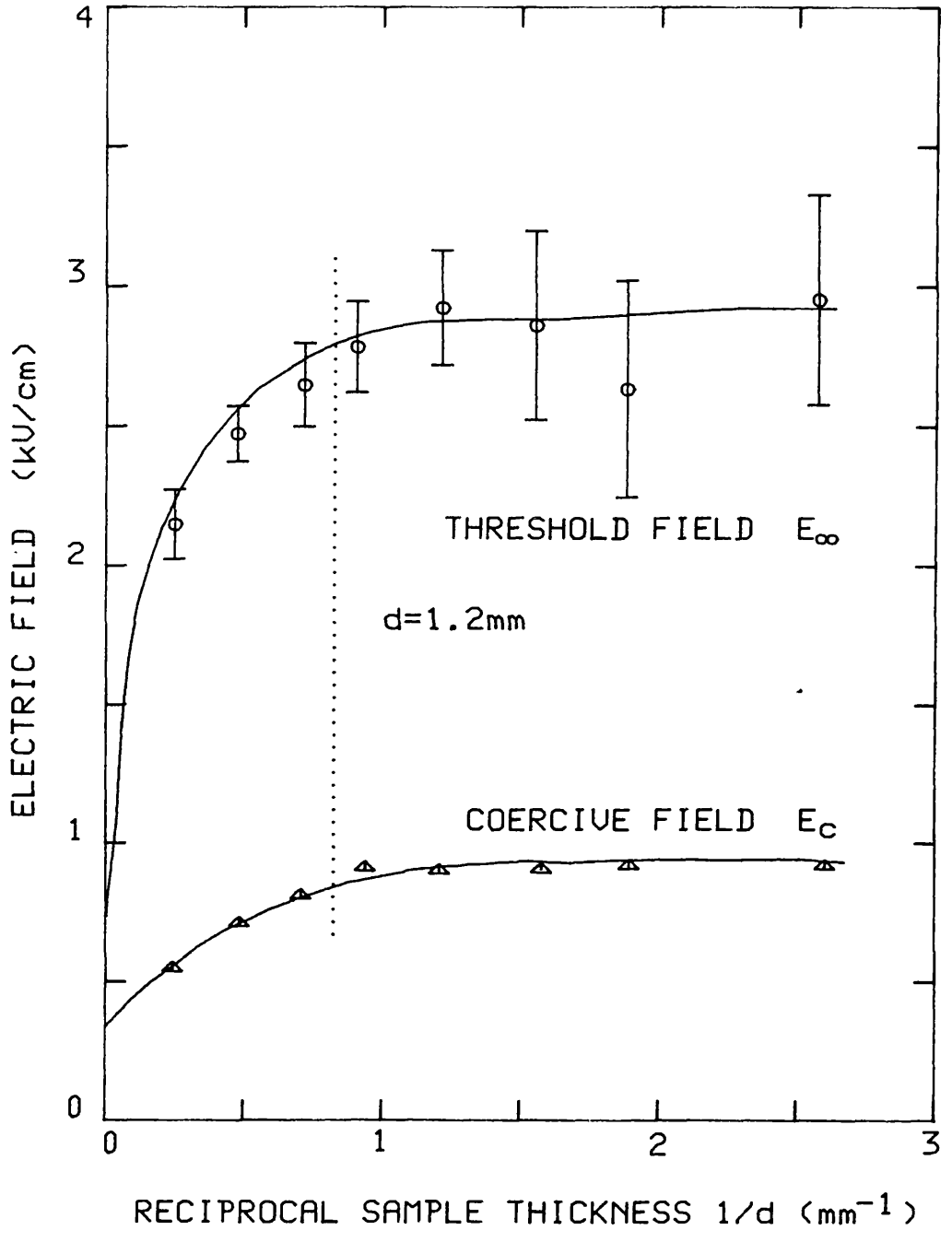

FIGURE 4.36 - Threshold field and coercive field plotted as a function of reciprocal sample thickness for Rochelle salt at 20°C.

structure of this material consists of a large number of tiny, cylindrical domains scattered more or less evenly throughout the crystals, matching the patterns on opposite faces of the sample proved almost impossible, and no definate conclusions could be drawn from this study.

Due to the small quantities of material available, it was only possible to prepare gadolinium molybdate samples over a small range of sample thicknesses. Both the threshold field and the coercive field were found to be constant over this limited range (0.64mm to 1.88mm). This is shown in Figure 4.37. The large strain energy associated with domain walls in gadolinium molybdate means that samples of this material usually contain only a small number of domain walls which generally extend right through the crystal between two opposite faces, both along the polar axis and perpendicular to it (Kumada 1972). Therefore, this finding does not contradict the observations made in Rochelle salt, where a single layer of domains was correlated with a large, constant threshold field independent of sample thickness.

4.10 The Dependence of the AE upon Sample Temperature.

Most ferroelectrics cease to be ferroelectric above a transition temperature, also called the Curie temperature by analogy with ferromagnetic materials. The fact that no AE can be observed at temperatures above the Curie point, even at the highest voltages that could be applied, is a strong indication that the source of the AE is connected with the ferroelectric nature of the material. Therefore a study of the AE in the vicinity of the phase transition should shed some light on the nature of the AE source. The ferroelectric phase transition is a structural phase change with the special property that the ferroelectric phase has a spontaneous polarisation. In most

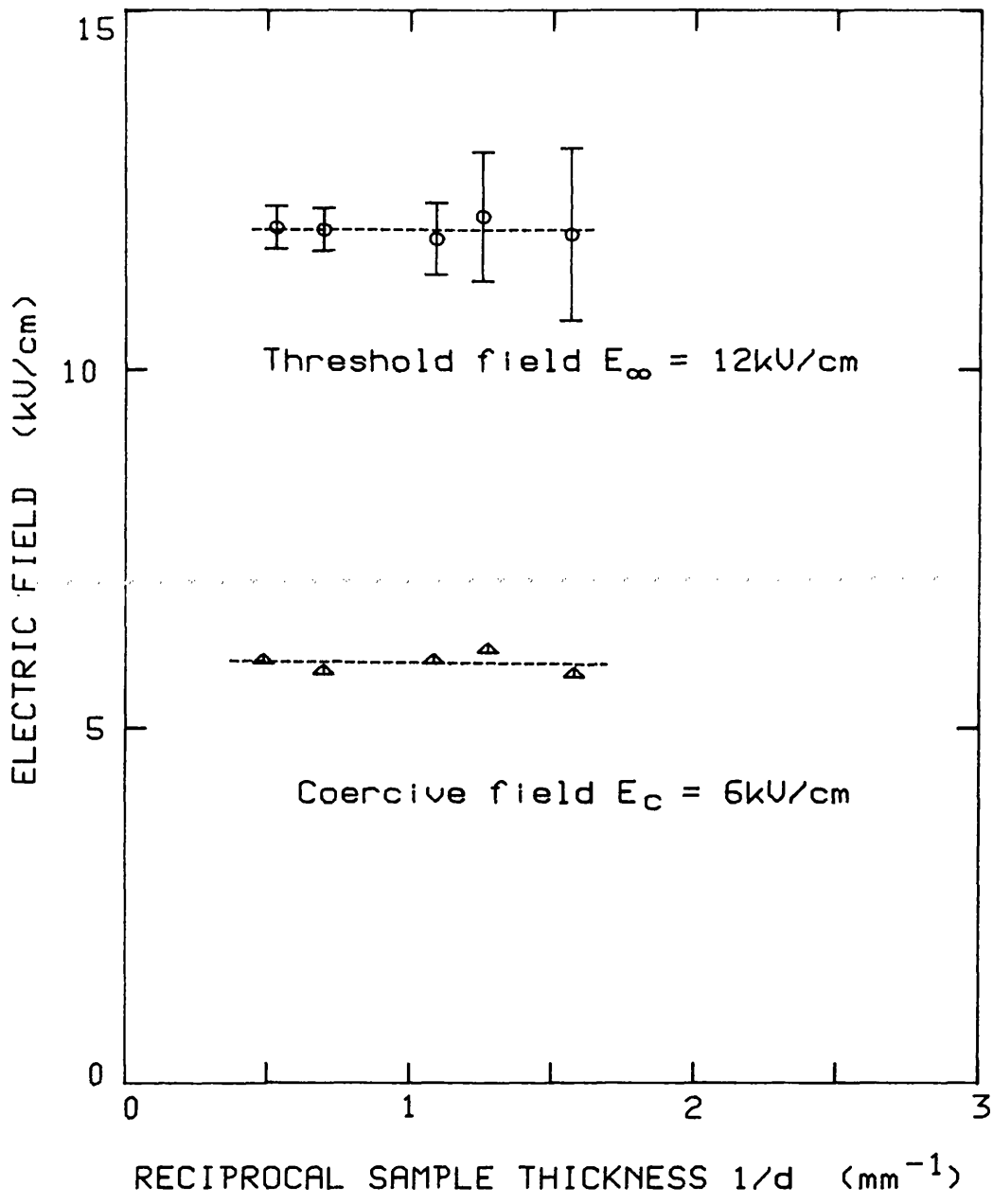

FIGURE 4.37 - Threshold field and coercive field in gadolinium molybdate plotted as a function of sample thickness. Both quantities remain essentially constant over the range of thicknesses investigated.

cases, the crystal is ferroelectric below the transition temperature: however transitions from non-polar to polar phases with increasing temperature are also known to occur (eg in Rochelle salt). Many properties of the material show anomalous behaviour in the vicinity of this phase change. In particular, most transitions of this type are characterised by an anomaly in one or more of the dielectric constants of the material. As the transition temperature is approached, the dielectric constant increases rapidly, often by several orders of magnitude. The measurement of the small-signal dielectric constant by an AC bridge (at a frequency of around 1kHz) provides a simple, effective means of determining the transition temperature in most ferroelectric materials.

The AE count rate and the threshold field have been measured as a function of sample temperature for a number of different ferroelectric materials. The following measurements were made on a lead germanate sample 1.13mm thick. The sample was mounted on an aluminium acoustic waveguide and placed in a vertical furnace as described in Section 3.9. The capacitance of the sample was measured as a function of temperature using a Wayne-Kerr B905 Autobalancing Bridge. Since the electrodes were applied to the faces of the sample perpendicular to the polar c-axis, this capacitance is proportional to the dielectric constant ϵ_{33}. These results, shown in Figure 4.38, give a Curie temperature of 178°C. The data in Figure 4.38 were measured as a function of increasing temperature. Measurements were also taken during the cooling cycle, with close agreement between the two sets of results. During cooling, the anomaly in the dielectric constant was found to occur at 177°C, giving a thermal hysteresis of about 1°C.

The AE ringdown count rate from this lead germanate sample at an applied electric field of 10kV/cm peak and an amplifier gain of 70dB is shown as a function of temperature in Figure 4.39. The count rate initially rises with increasing temperature, reaching a maximum at about 60°C, but then falls rapidly to zero at 127°C. At a slightly higher value of the applied field

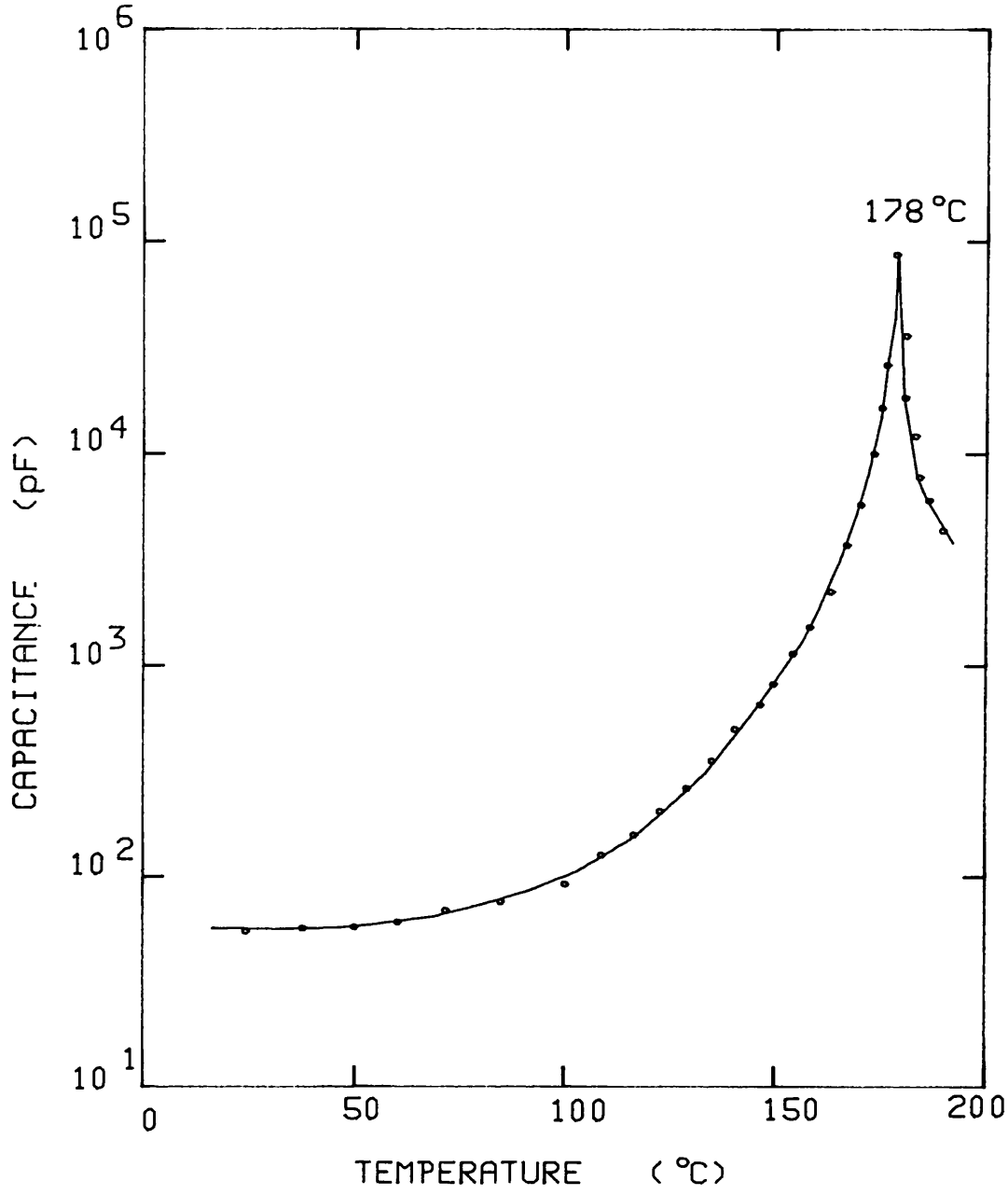

FIGURE 4.38 - Capacitance of a lead germanate sample (1.13mm thick, electrode area 78mm^2) as a function of temperature. The peak in the capacitance gives the Curie temperature as 178°C.

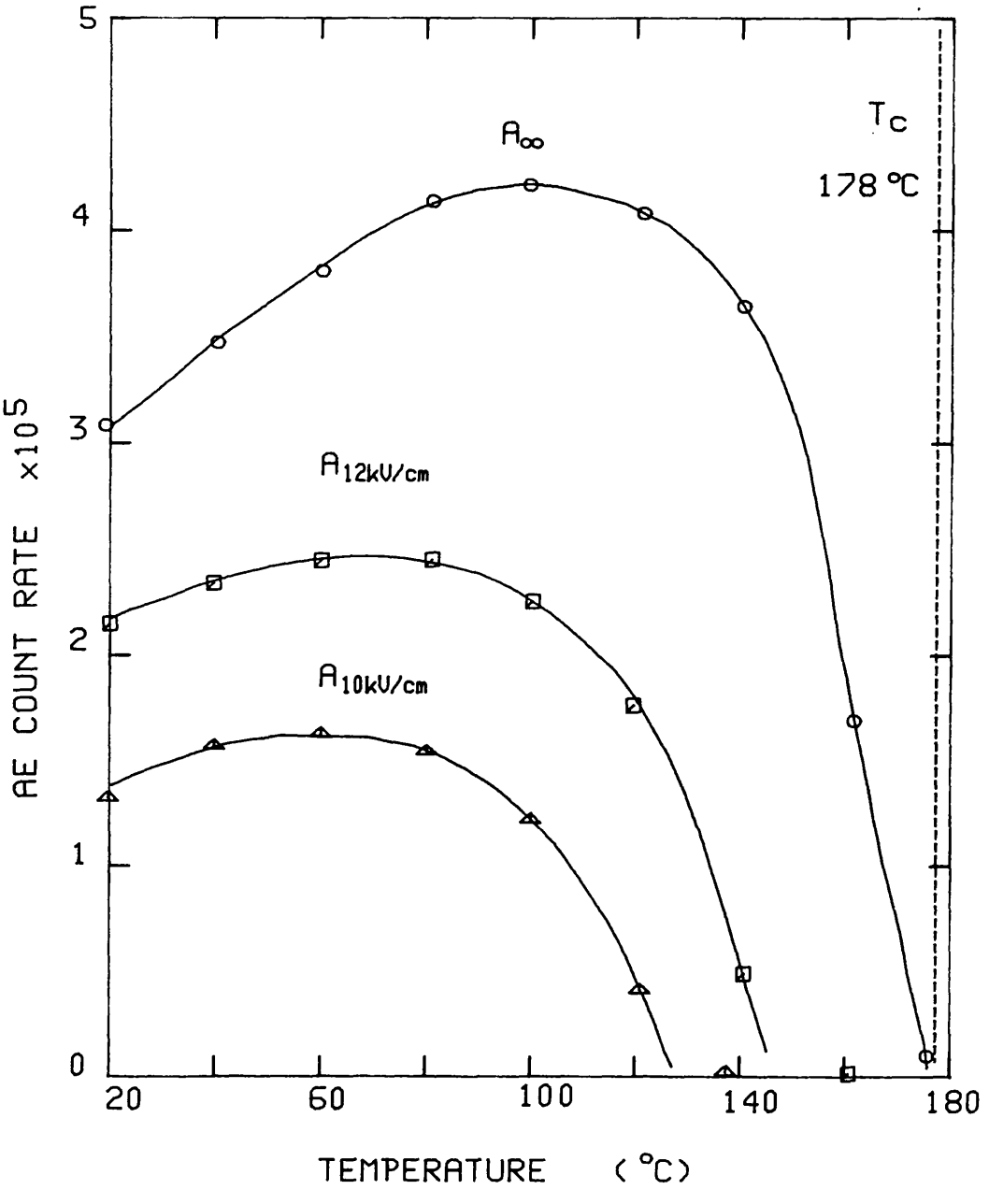

FIGURE 4.39 - AE count rate as a function of temperature for a lead germanate sample 1.13mm thick.

(12kV/cm), the count rate behaves similarly but falls to zero at a higher temperature. This behaviour can be explained if the threshold field increases with temperature, which forces the count rate to zero when the threshold field exceeds the applied field. A better estimate of the AE activity is provided by the count rate extrapolated towards infinite applied field, defined in Section 4.5 as A_∞ (also shown in Figure 4.39). This curve has the same features as the preceding ones but goes to zero near the Curie temperature of 178°C. This result has been observed in a number of lead germanate samples of different size and history: in all cases the limiting AE count rate A_∞ goes to zero at a temperature very close to the Curie point.

The dependence of the threshold field upon the sample temperature is shown in Figure 4.40. These measurements were made as a function of increasing temperature. As the Curie temperature is approached, the threshold field rises sharply. Clearly, if no AE is to be observed at and above the Curie temprature, at whatever value of the applied field, the threshold field must go to infinity as the transition is approached. (This happens as the transition is approached from below: the threshold field cannot be defined outside the ferroelectric region because no AE is produced there). As the threshold field increases, it becomes harder to measure accurately. As a general rule, AE is first detected (at an amplifier gain of 80dB) with an applied electric field some 1.3 times the threshold field, and the process of determining the threshold field requires the application of electric fields over and above this value to obtain sufficient data to enable a reliable extrapolation to be made. The limit on the highest voltage available from the equipment means that few data points are available when measuring very high threshold fields: this is reflected in the increasing length of the error bars in Figure 4.40 as the threshold field becomes larger.

In Section 4.9, the dependences of the threshold field for AE and the coercive field were compared. No such comparisons can be made in the case of the temperature dependences. The

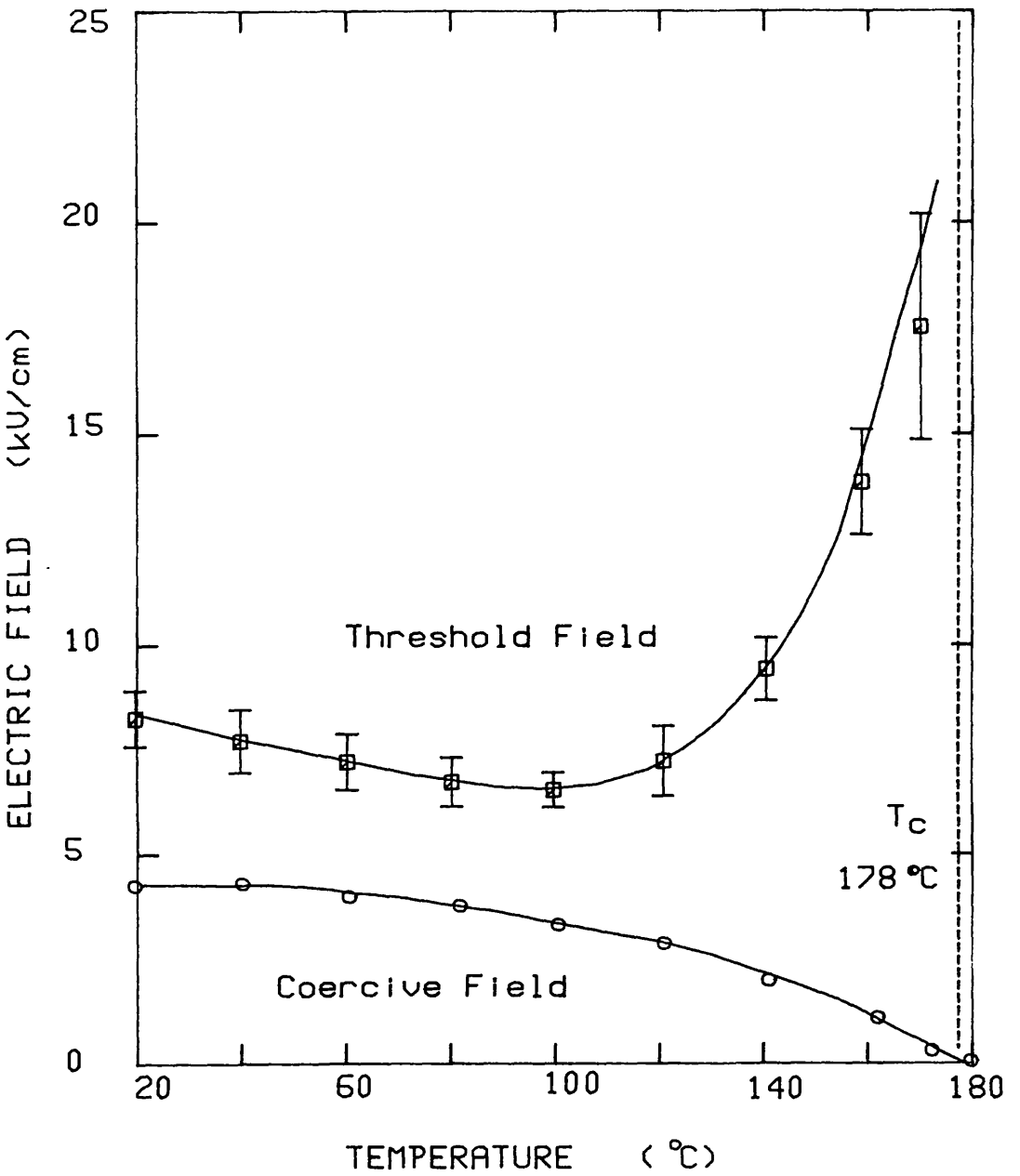

FIGURE 4.40 - Threshold field for acoustic emission and the coercive field plotted as a function of temperature for a lead germanate sample 1.13mm thick.

coercive field of the lead germanate sample was also measured as a function of temperature and is included in Figure 4.40. While the threshold field rises as the transition is approached, the coercive field goes to zero: this must occur because above the transition the P-E hysteresis loop collapses to a straight line passing through the origin, characteristic of a linear dielectric. In Section 4.9, it was shown that the threshold field tends towards the coercive field (at room temperature) for thick crystals: clearly this cannot happen at high temperatures where the two curves in Figure 4.40 diverge. To resolve this dilemma, an attempt was made to measure the thickness dependence of the threshold field at a temperature of 150°C: unfortunately the high values of the threshold field encountered led to large uncertainties in the results and no firm conclusions could be drawn. However, these experiments indicate that the limiting value of the threshold field for thick samples is always greater than that of the coercive field, and that while the two values are similar at room temperature they diverge rapidly as the transition is approached.

While Figure 4.40 represents a typical set of threshold field measurements, taking the sample through the phase transition was found to have a marked influence on the reproducibility of the results. These temperature runs were repeated several times, and although the curves obtained all show the same general features, details such as the threshold field at a given temperature were found to differ considerably from one run to another. These differences were also found in measurements made on heating and cooling cycles. Such a pair of curves is shown in Figure 4.41. The error bars have been omitted from this graph in the interests of clarity, but are generally similar to those in Figure 4.40. The "heating" curve in this figure may be compared with that in Figure 4.40: although the overall shape of the two curves is similar, they differ in detail. The minimum threshold field occurs at 100°C in Figure 4.40 and at about 70°C in Figure 4.41. The "cooling" curve also has the same general shape but shows a much lower minimum threshold field that occurs at about 90°C, which is higher than the temperature for minimum

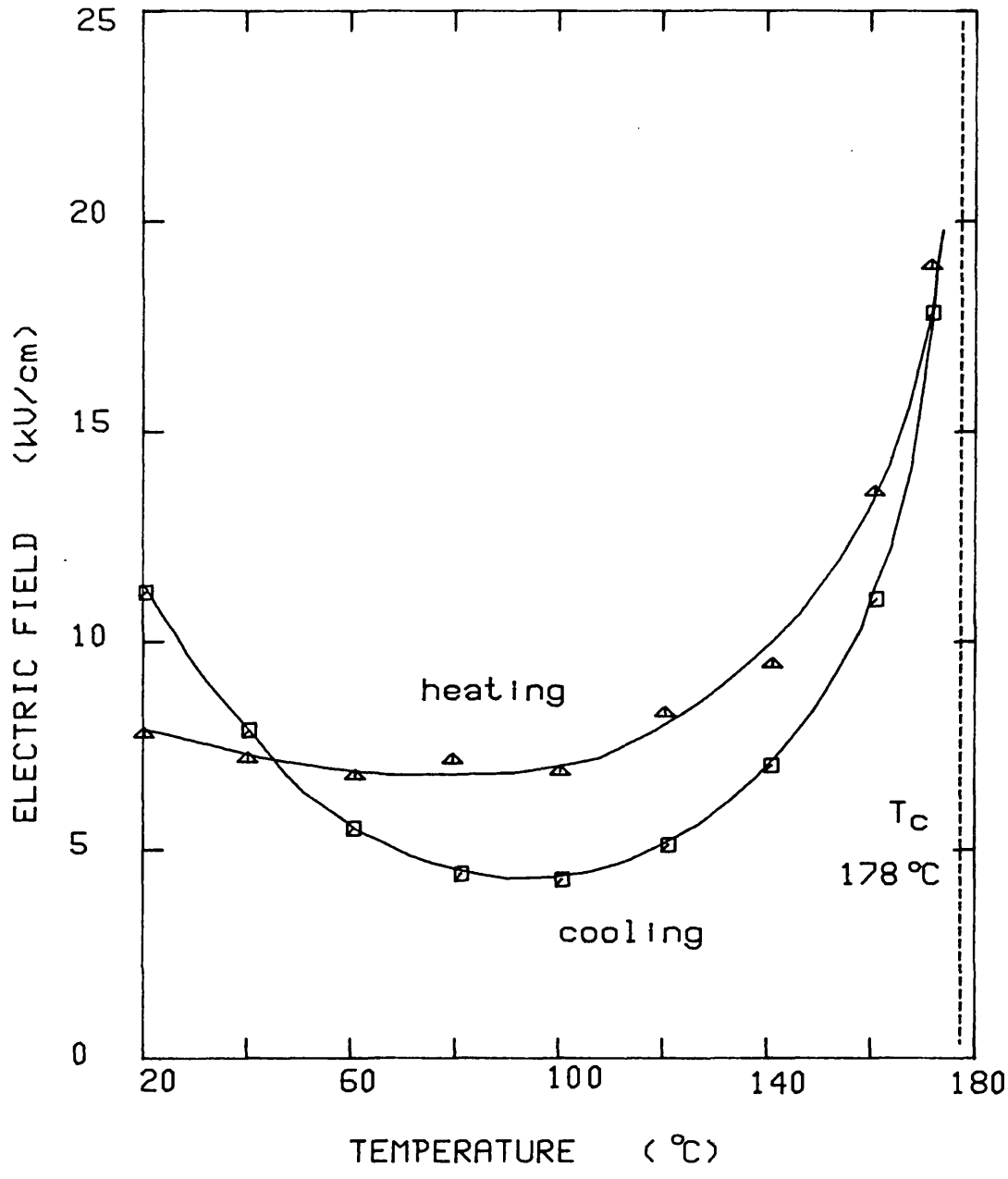

FIGURE 4.41 - Threshold field E_∞ as a function of temperature for heating and cooling cycles. The sample is the same as the one used to provide the data in Figure 4.40.

threshold field during the "heating" cycle. At a constant temperature, the measured threshold field is generally found to rise with time and repeated measurements (Section 4.7): this may account in part for the sharper rise in the threshold field at low temperatures during the "cooling" cycle. The variation in behaviour with time and repeated transitions through the Curie temperature is an interesting phenomenon, but a great many measurements would have to be taken for a thorough, statistical treatment of the matter. Although the heating-cooling process was repeated eight times, all that could be obtained from the data were the general remarks made above.

Gadolinium molybdate (GMO) and its isomorph terbium molybdate (TMO) have an abnormally low dielectric constant (about 10 at room temperature) which increases very little with temperature (by about 10% between room temperature and the Curie point) and shows no anomaly as the ferroelectric phase transition is approached (Cummins 1970). Therefore capacitance measurements cannot be used to determine the Curie temperature of these materials. Various sources give the transition temperature as between 159°C (Cummins 1970) and 163°C (Aizu et al 1969) for GMO and 157°C for TMO (Borchardt and Bierstedt 1967). The limiting AE count rates A_∞ for these materials are plotted as a function of sample temperature in Figure 4.42. As in lead germanate (Figure 4.39), in these materials A_∞ goes to zero near the Curie temperature: in fact in the absence of another method, the AE can be used to determine the Curie temperature. However, unlike the results for lead germanate, the curves in Figure 4.42 do not have a maximum: instead the limiting count rate A_∞ falls smoothly as the temperature is increased towards the transition. No measurements were made below room temperature, so it is possible that the AE activity falls at lower temperatures and that the curves do have a maximum like that in Figure 4.39: however the shape of the curves in Figure 4.42 does not give any indication that this is likely to happen.

The threshold field for AE in these materials also shows this behaviour (Figure 4.43). While the threshold field increases

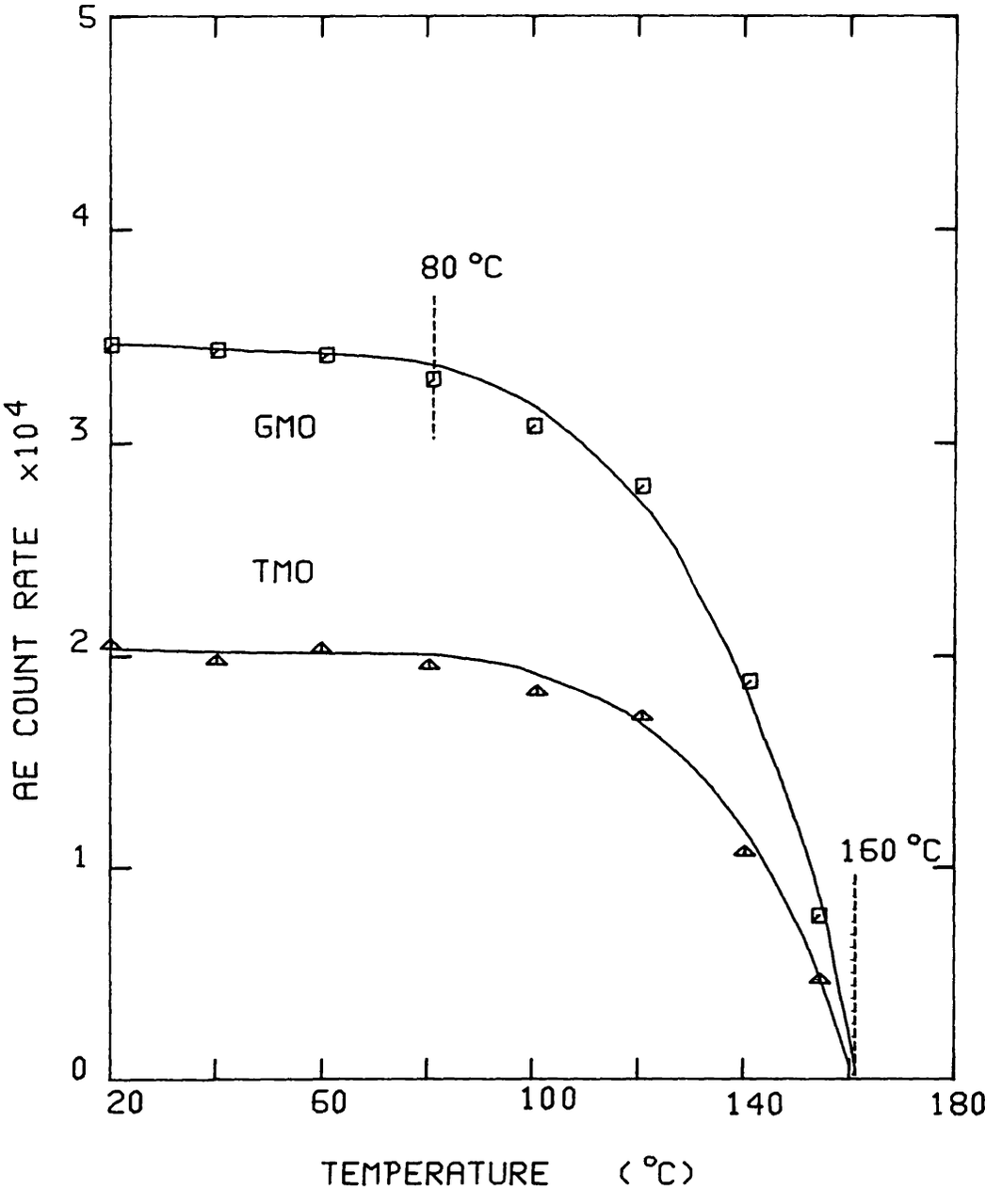

FIGURE 4.42 - Limiting AE count rate A_∞ as a function of temperature for samples of GMO (0.94mm thick) and TMO (1.01mm thick).

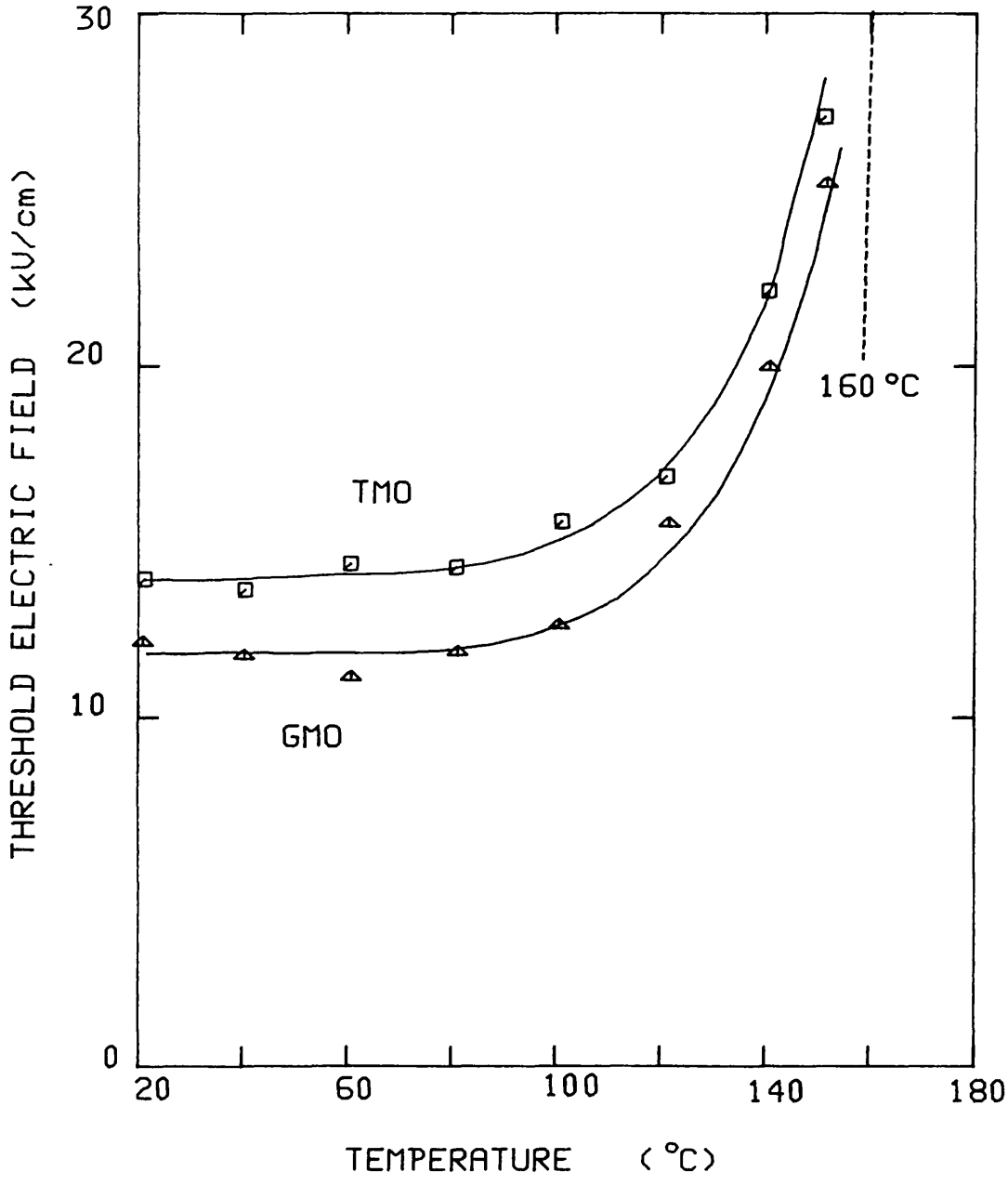

FIGURE 4.43 - Threshold field for acoustic emission plotted as a function of sample temperature for the same GMO and TMO samples used in Figure 4.42.

rapidly as the transition is approached, it is approximately constant at lower temperatures. This behaviour recalls the domain switching mobility in GMO measured as a function of temperature by Kumada (1972). He found that this mobility is constant below 80°C, but increases rapidly above this temperature. In Figure 4.43, the threshold field in GMO is constant at temperatures of up to about 80°C, which agrees with Kumada's observations. An increase in the threshold field means a decrease in AE activity, as a higher applied field is required to produce AE. Therefore an increase in domain wall mobility (which is defined as the sideways velocity of the domain wall divided by the magnitude of the applied (DC) electric field) is associated with a decrease in AE activity.

The case of Rochelle salt is particularly interesting because this material has two Curie points, being ferroelectric only between -18°C and +24°C. This is shown in Figure 4.44, where the capacitance of a typical AE sample (with electrodes perpendicular to the polar a-axis, therefore measuring ϵ_{11}) is shown as a function of temperature. These measurements were carried out on a sample 1.09mm thick mounted on a Pyrex glass waveguide and installed in a thermoelectrically cooled chamber, as described in Section 3.9. The measurement of the AE produced by this sample under the influence of an applied electric field posed some problems because the heat dissipated by the sample tended to upset the temperature stability in the sample enclosure. As described in Section 3.9, this was predominant at temperatures close to the transitions, and meant that no measurements could be taken within a few degrees of the Curie points.

The AE count rate at a constant value of the applied field is shown as a function of temperature in Figure 4.45. Although this count rate becomes very low as the transition points are approached, a significant count can still be detected outside the ferroelectric region. This is because of the background AE found in all the Rochelle salt samples prepared (Section 4.7). Once the measured count rates were corrected for this

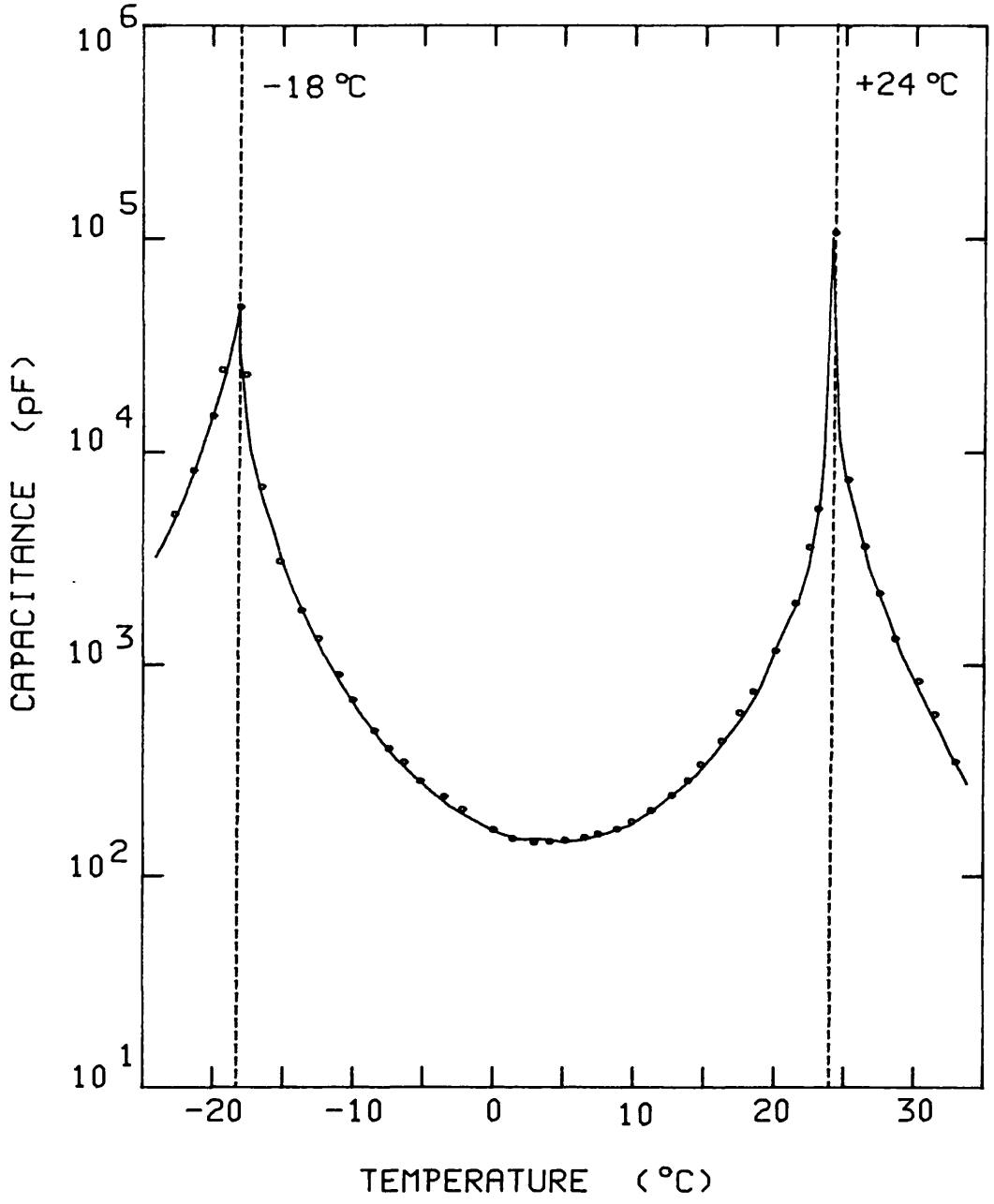

FIGURE 4.44 - Capacitance of a Rochelle salt sample 1.09mm thick (electrode area 78mm^2) plotted as a function of temperature. The capacitance peaks at the transition temperatures of -18°C and +24°C.

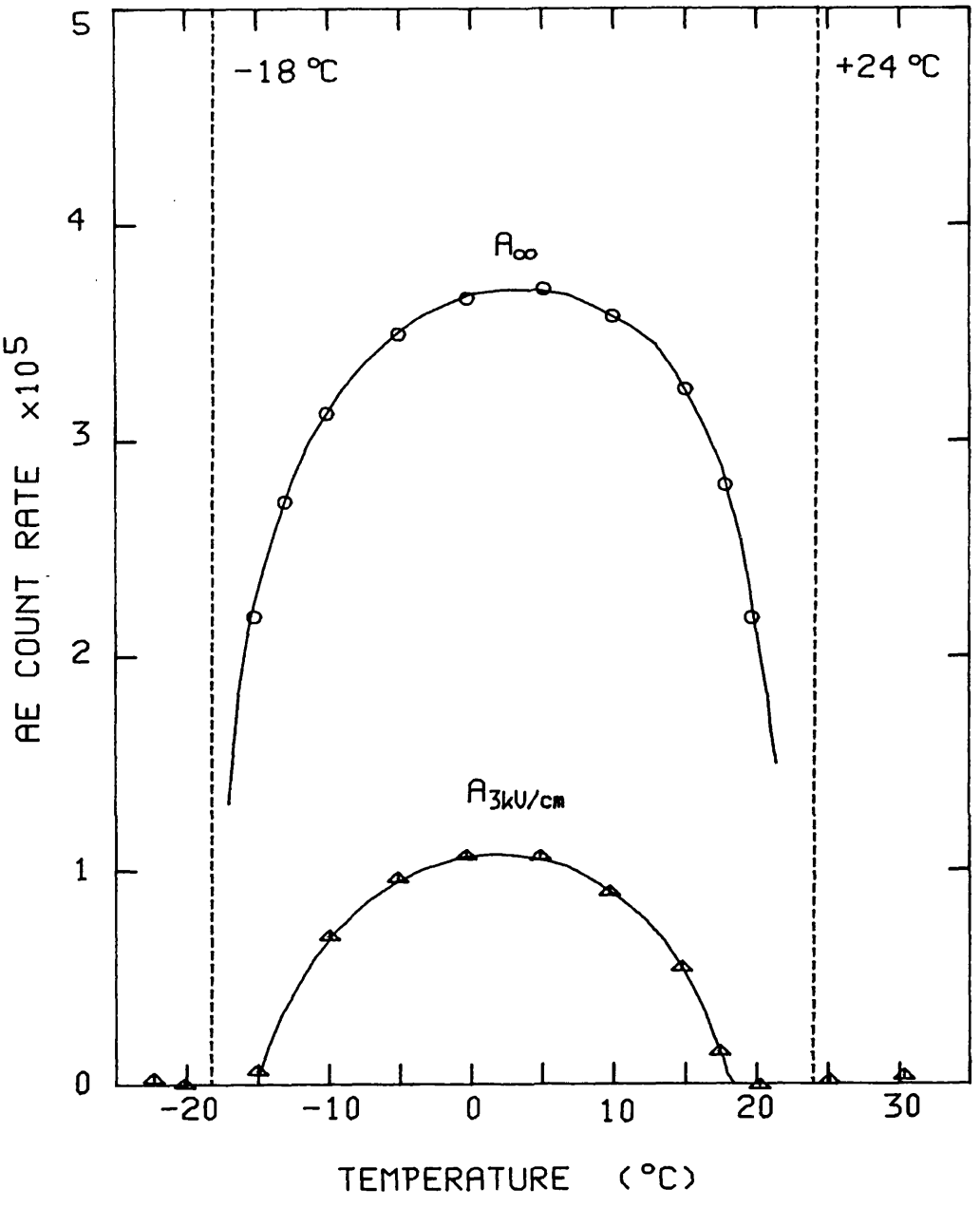

FIGURE 4.45 - AE count rate as a function of temperature for a Rochelle salt sample 1.09mm thick.

background, the limiting count rate A_∞ could be determined by extrapolation towards high field. This curve, which is also shown in Figure 4.45, goes to zero near the Curie points and has a maximum at about +4°C. The threshold field shows similar features (Figure 4.46), rising rapidly as both Curie temperatures are approached from within the ferroelectric region. This curve has a minimum at about +4°C, which agrees with the temperature for maximum AE activity (Figure 4.46). The mobility of domain walls in Rochelle salt as a function of temperature has been studied by Wieder (1958) who obtained curves similar in shape to the threshold field curve in Figure 4.46. Significantly, he obtained a minimum domain wall mobility at a temperature of +4°C.

As was the case in GMO, in Rochelle salt a high domain wall mobility is associated with a low AE activity, and vice-versa. This means that the source of AE cannot be the sideways motion of domain walls, otherwise the opposite correlation would be expected. On the other hand, a high domain wall mobility means that less nucleation of new domains is likely to occur, as the domains already present travel faster and so switch a greater fraction of the crystal volume. Therefore these observations are consistent with the hypothesis that the AE is produced by the nucleation of domains in the material, as suggested in Section 4.5.

4.11 The Dependence of the AE upon the Frequency and Risetime of the Applied Electric Field.

All the measurements described so far in this chapter were made with a 50Hz sinusoidal electric field applied across the sample. The electrical properties of ferroelectrics (such as the saturation polarisation and the coercive field) vary as a function of the frequency of the driving electric field. This

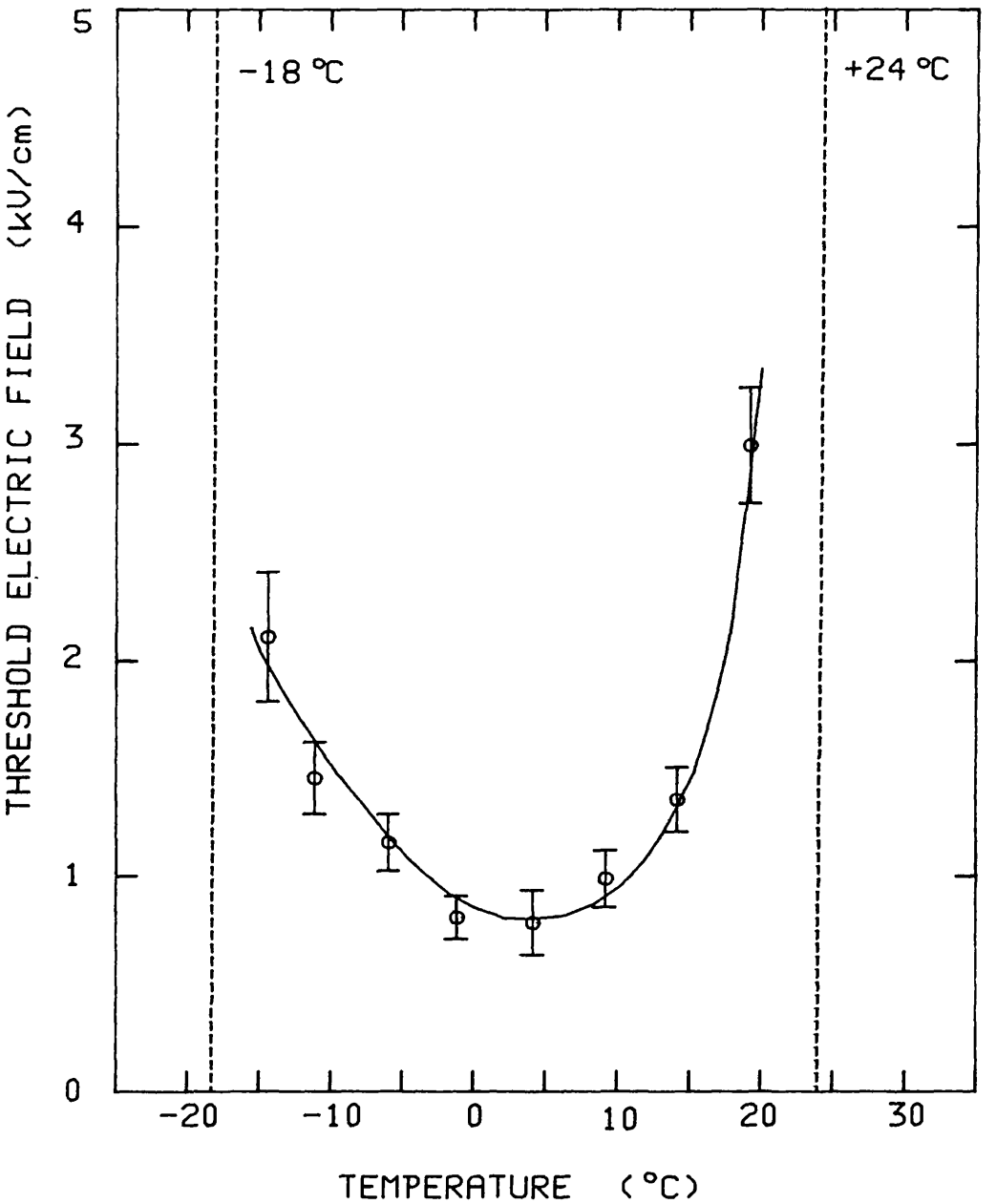

FIGURE 4.46 - Threshold field for acoustic emission plotted as a function of temperature for a Rochelle salt sample 1.09mm thick.

variation can be used to link measurements made from the hysteresis loop with the "steady-state" switching experiments made by applying a voltage step to the sample. Wieder (1957) has measured the frequency dependence of the coercive field E_c in barium titanate. He showed that this dependence can be explained by assuming that the switching starts at $E=E_c$ and that the switching time is the same as that measured in the "steady-state" experiments. However, very few measurements of this kind have appeared in the literature. This may partly be due to the difficulty of providing a suitable low-impedance source of the high voltages required over a wide range of frequencies.

This problem is even more acute if the AE from ferroelectrics is to be investigated as a function of frequency, as the threshold field for AE is typically several times greater than the coercive field in the material. The high-voltage operational power supply described in Section 3.8 was designed to provide a peak voltage of 1kV: for a typical sample thickness of 1mm this corresponds to an electric field of 10kV/cm. This means that the highest threshold field that can be reliably measured with this system is about 5kV/cm, so that of the four materials studied only Rochelle salt, which has the lowest threshold field (about 3kV/cm at room temperature), is really suitable. However, some measurements were also made on lead germanate by operating the system outside its design limits.

The AE count rate from a Rochelle salt sample as a function of the frequency of the 10kV/cm applied sinusoidal electric field is shown in Figure 4.47. The AE count per unit time rises as the frequency is increased: this is to be expected as a greater number of hysteresis cycles take place in unit time at higher frequencies. The AE count per hysteresis cycle is obtained by dividing the count rate (per unit time) by the frequency: this is also plotted in Figure 4.47. While this initially also increases with frequency, the curve reaches a maximum at about 250Hz. The frequency dependence of the threshold field for this sample is shown in Figure 4.48. For this experiment, the AE

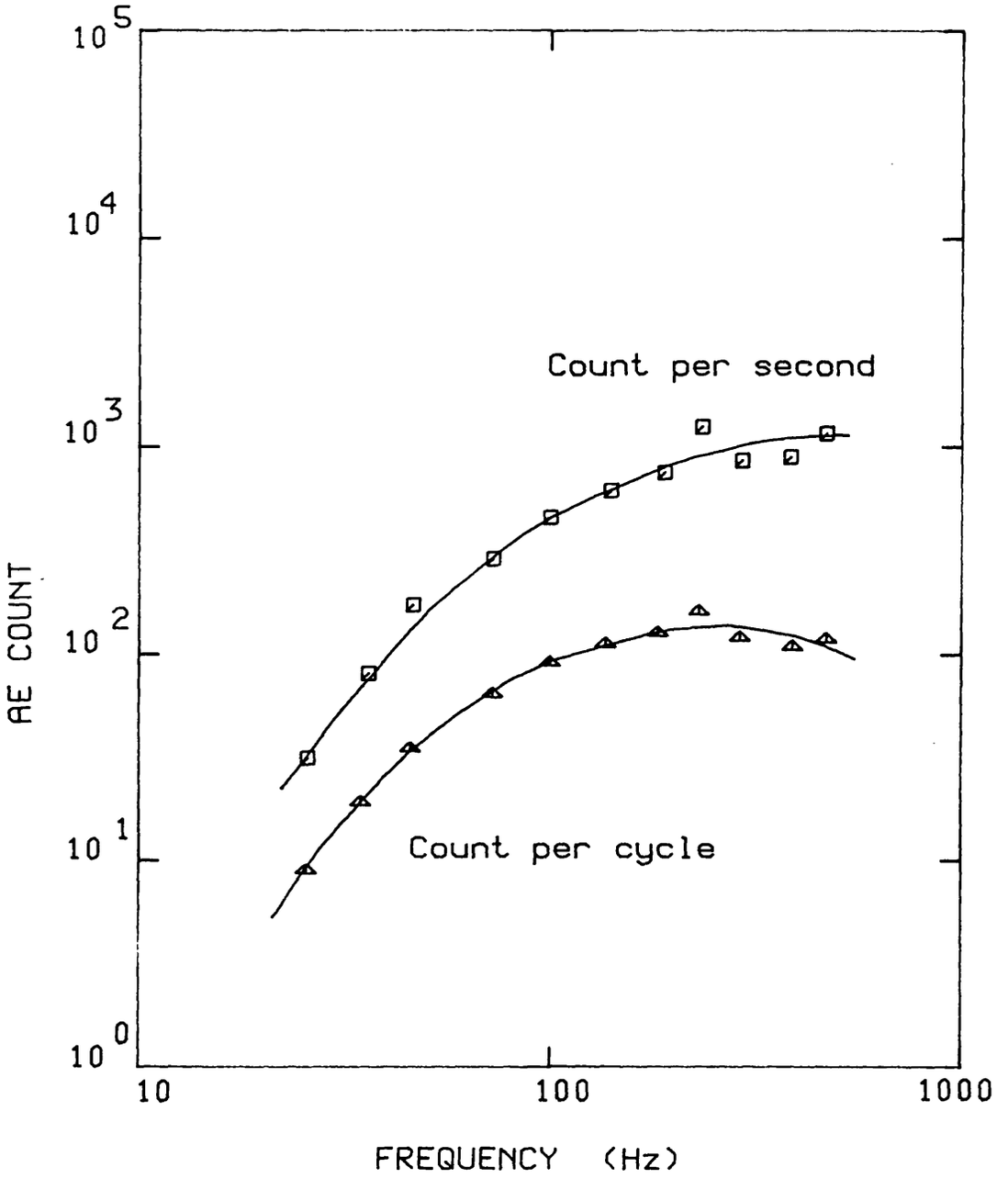

FIGURE 4.47 - AE count per second and AE count per hysteresis cycle as a function of the frequency of the 10kV/cm sinusoidal applied electric field for a Rochelle salt crystal 1.11mm thick at 20°C.

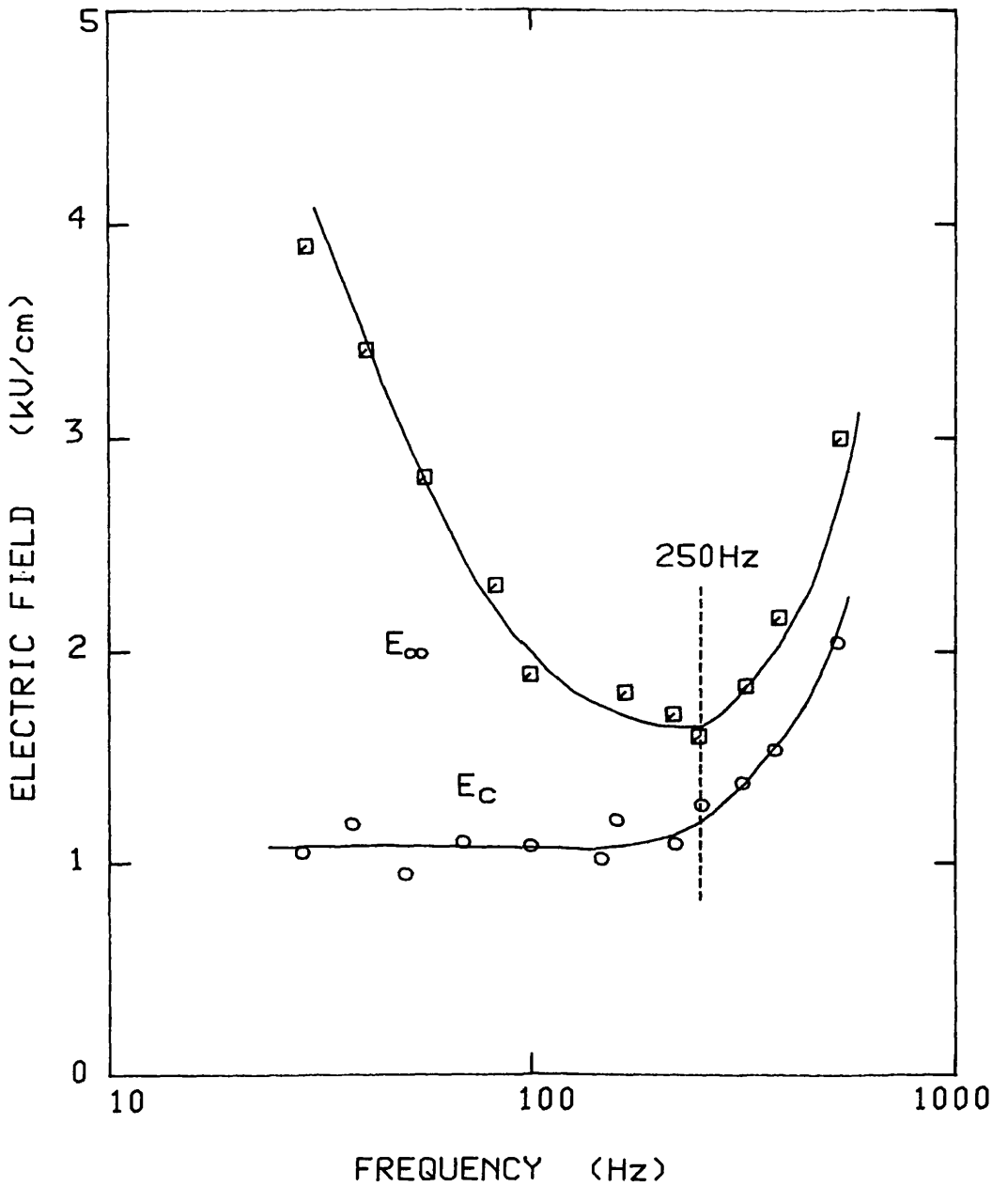

FIGURE 4.48 - Threshold field E_∞ and coercive field E_c plotted as a function of frequency for Rochelle salt. The sample is the same as that used to provide the data in Figure 4.47.

count rates were obtained by measuring over 5000 cycles - this takes only 100s at 50Hz but nearly ten minutes at 10Hz. As the frequency is increased, the threshold field becomes smaller, reaching a minimum again at about 250Hz. Above this frequency, the threshold field increases again. The operational power supply is slew-rate limited, so the available output voltage becomes less as the frequency is increased. This limited the number of measurements that could be made in this region.

The frequency dependence of the coercive field in this Rochelle salt sample is also shown in Figure 4.48. The coercive field is essentially constant at low frequencies, but rises rapidly above about 250Hz. This agrees qualitatively with the measurements of Wieder (1958) who measured the coercive field of Rochelle salt in the frequency range 1Hz to 3kHz. He found that the coercive field rises rapidly above about 200Hz, although his values for the coercive field are some ten times less than those found in this particular sample. At lower frequencies, Wieder found that the coercive field falls linearly with increasing (logarithmic) frequency. However, according to his measurements the coercive field only changes by about 10% between 10Hz and 200Hz: in Figure 4.48, the coercive field was measured off the oscilloscope screen with an accuracy of about 10%, so that this change would not be apparent.

Another interesting correlation between the threshold field and the coercive field is shown in Figure 4.49, where these quantities are plotted against the reciprocal of the frequency. At low frequencies, the threshold field increases linearly with $1/f$, while the coercive field is essentially constant. Ignoring the fact that the two curves depart from linearity at high frequencies, if the two straight lines are extrapolated towards $1/f=0$ (ie towards infinite frequency) they intersect the vertical axis at approximately the same point. In practice, this does not happen because both quantities increase at frequencies of over 200Hz. Wieder (1958) has attributed this rapid increase in the coercive field to the fact that since polarisation reversal is an adiabatic process, the temperature

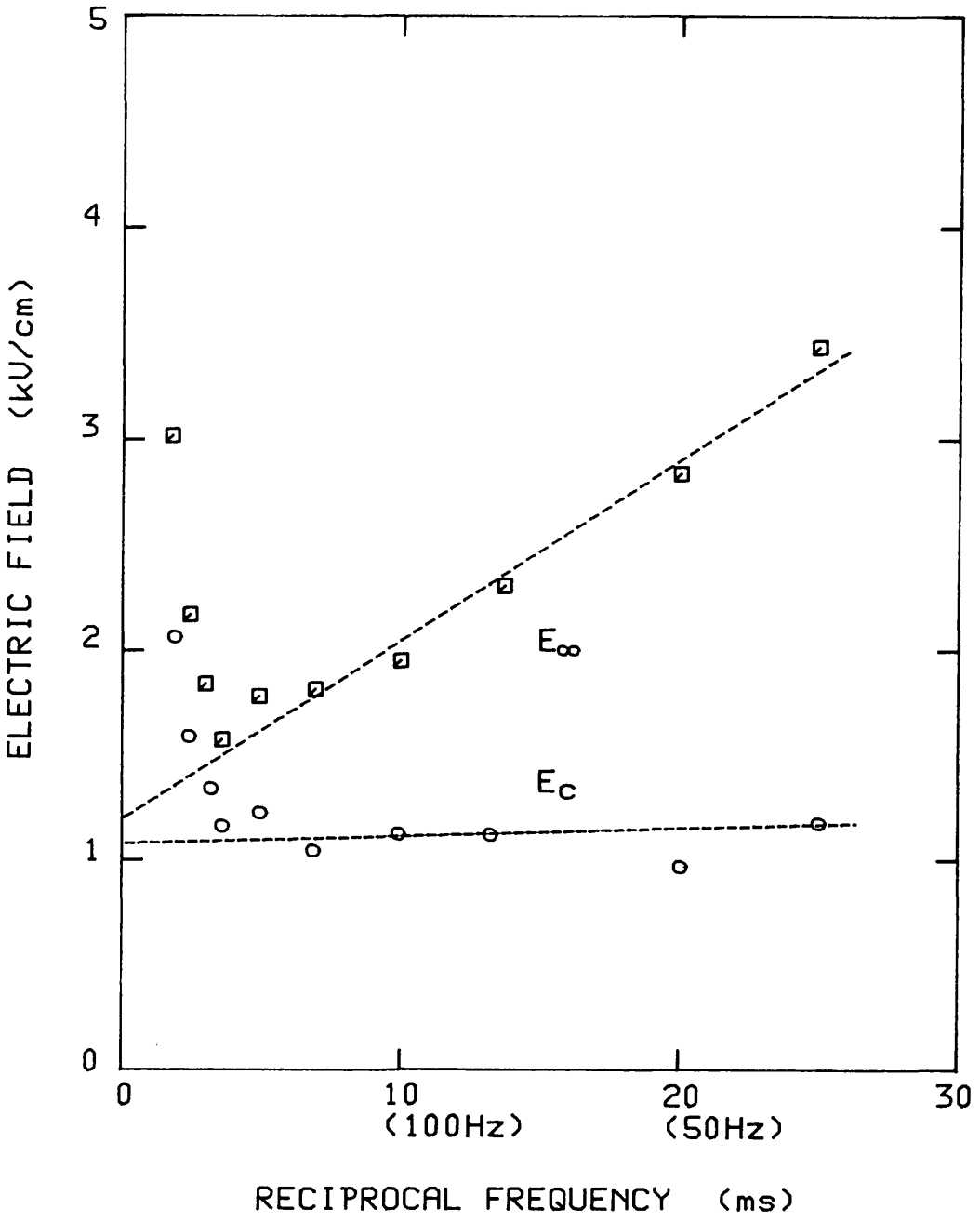

FIGURE 4.49 - Threshold field E_∞ and coercive field E_c plotted as a function of the reciprocal of the frequency of the applied field for Rochelle salt. The data is the same as that plotted in Figure 4.48.

of a ferroelectric crystal element would rise with the frequency of the driving field. He also noted that this increase occurs at higher frequencies as the ambient temperature decreases, and that it should not be possible to obtain a hysteresis loop at all with frequencies above about 100kHz as the temperature of the crystal would then exceed the Curie temperature.

The dependence of the coercive and threshold fields in lead germanate on the reciprocal of the frequency of the applied field is shown in Figure 4.50. The threshold field in this material is considerably higher than it is in Rochelle salt, and this means that very high voltages (over 1kV peak) had to be applied to the sample to make the measurements. In turn, this limited the highest frequency at which the required voltage could be supplied to about 120Hz. Both the coercive field and the threshold field were found to vary linearly with 1/f up to the highest frequency that could be applied, and as in Rochelle salt both curves extrapolate towards the same limit at high frequencies.

The threshold field in GMO and TMO is about 12kV/cm at 50Hz. The maximum voltage supplied by the operational power supply was not sufficient to produce any detectable AE from samples of these materials at frequencies of between 0.1Hz and 100Hz, indicating that the threshold field for AE is greater than 10kV/cm over this range. The coercive field in GMO (about 6kV/cm at 50Hz) has been measured as a function of frequency and is shown in Figure 4.51 - this curve agrees well with the results of Kumada (1972), who also measured the frequency dependence of the coercive field in this material. If the threshold field in GMO behaves as it does in Rochelle salt, it would be at its minimum at about 1Hz, where the coercive field starts to increase. Even if the threshold field at this frequency is lower than 10kV/cm, the AE count rate may have been too low to be measured.

The linear dependence of the threshold field on the reciprocal of the frequency shown in Figures 4.49 and 4.50 can be described

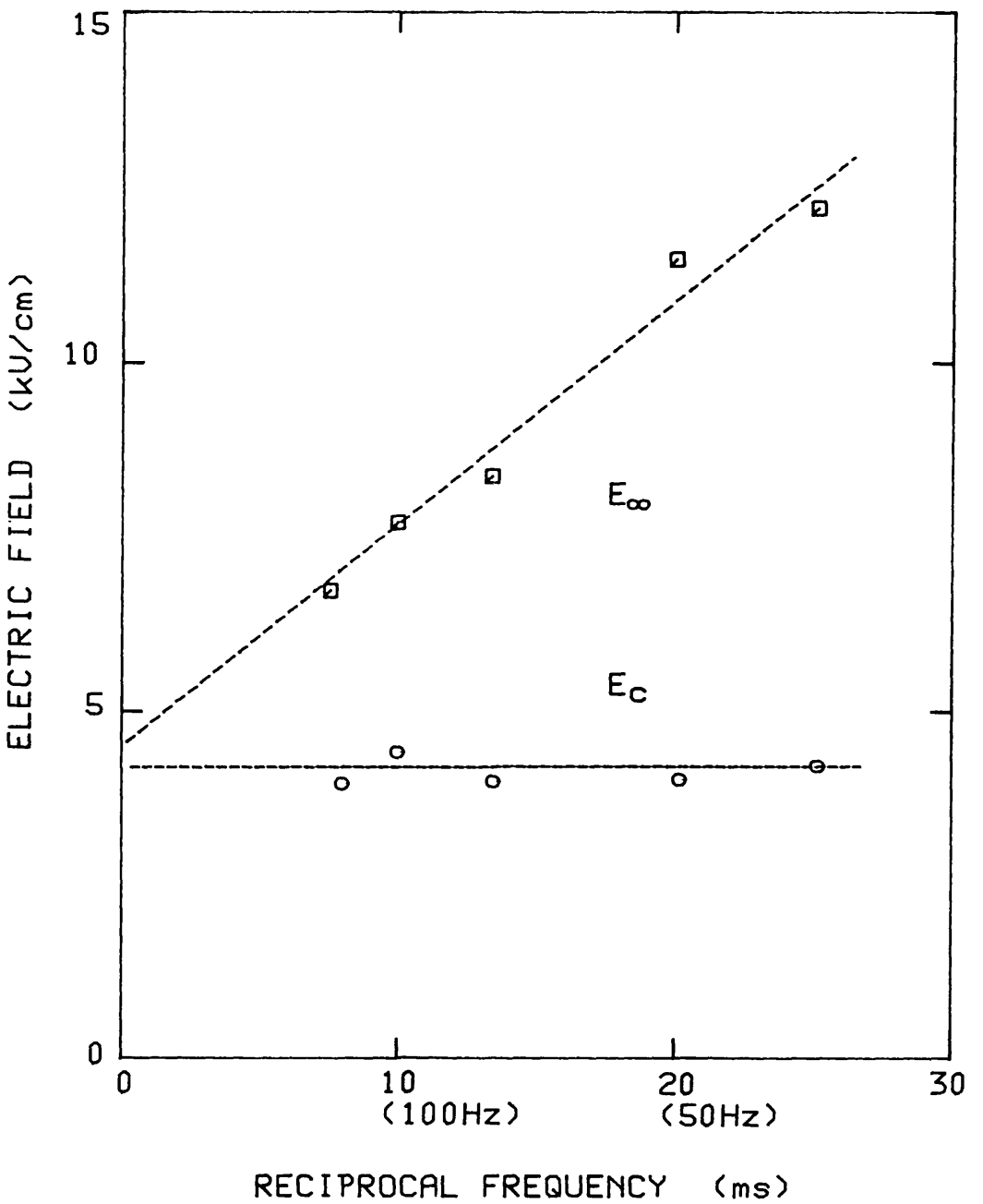

FIGURE 4.50 - Threshold field E_∞ and coercive field E_c plotted as a function of the reciprocal of the frequency of the applied field for a lead germanate sample 0.89mm thick at room temperature.

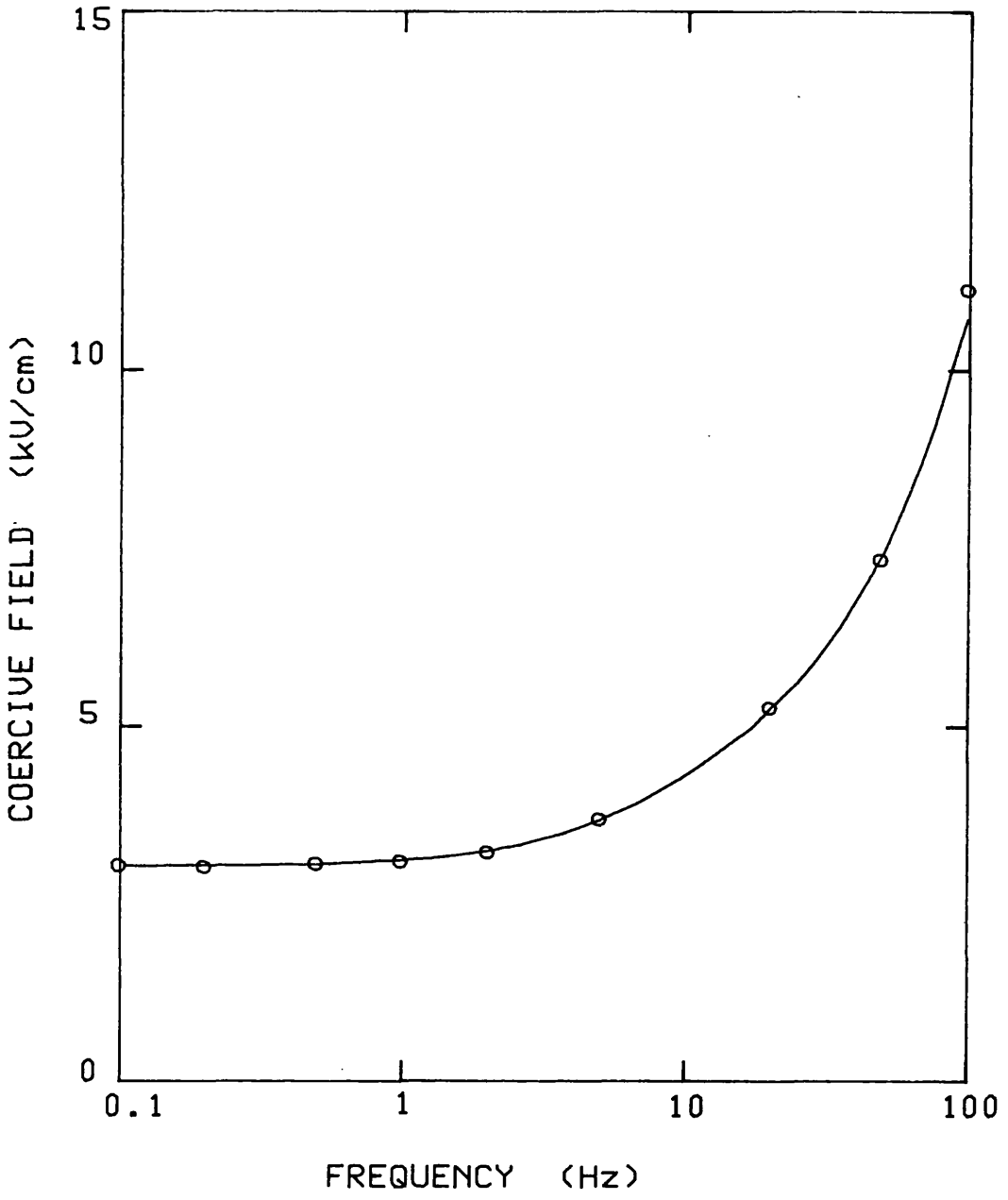

FIGURE 4.51 - Coercive field as a function of frequency for a gadolinium molybdate crystal 0.94mm thick at room temperature.

by an equation of the form:

$$E_{\infty}\ (f) = E_{o} + A/f$$

where E_o is the intercept of the line on the vertical axis (1/f=0) and to a first approximation is equal to the coercive field E_c (or its extrapolation to infinite frequency). The slope of the line is described by the constant A, which has the value 0.086 kV/cm/ms in Rochelle salt (Figure 4.49) and 0.32 kV/cm/ms in lead germanate (Figure 4.50). These values will of course change as a function of temperature and sample thickness. The dimensions of A - (kV/cm)/ms - are those of a rate of change of electric field, or slew rate. This indicates that the threshold field for AE is in some way related to the rate at which the applied field changes.

For a sinusoidal waveform, the slew rate is a function of the frequency and amplitude of the wave, and also varies with time within each cycle. To determine whether the frequency or the slew rate of the driving electric field is the important parameter, measurements were also made with a trapezoidal wave applied to the sample. For this waveform, the voltage changes linearly from one extreme to the other, and the time taken to switch (and hence the slew rate) can be varied from one-half the overall period of the signal (corresponding to a triangular wave) down to zero (corresponding to a square wave). In practice, this rise time could not actually reach zero, but was limited by the maximum slew rate of the operational power supply system to about 0.5ms.

The threshold and coercive fields in the lead germanate sample are plotted as a function of the risetime of the trapezoidal applied electric field in Figure 4.52. Both these quantities increase linearly with the risetime. Measurements were made at two different repetition rates of the trapezoidal waveform (10Hz and 30Hz), with no substantial differences between the results. This indicates that it is indeed the risetime and not the frequency of the signal that is the dominant factor in

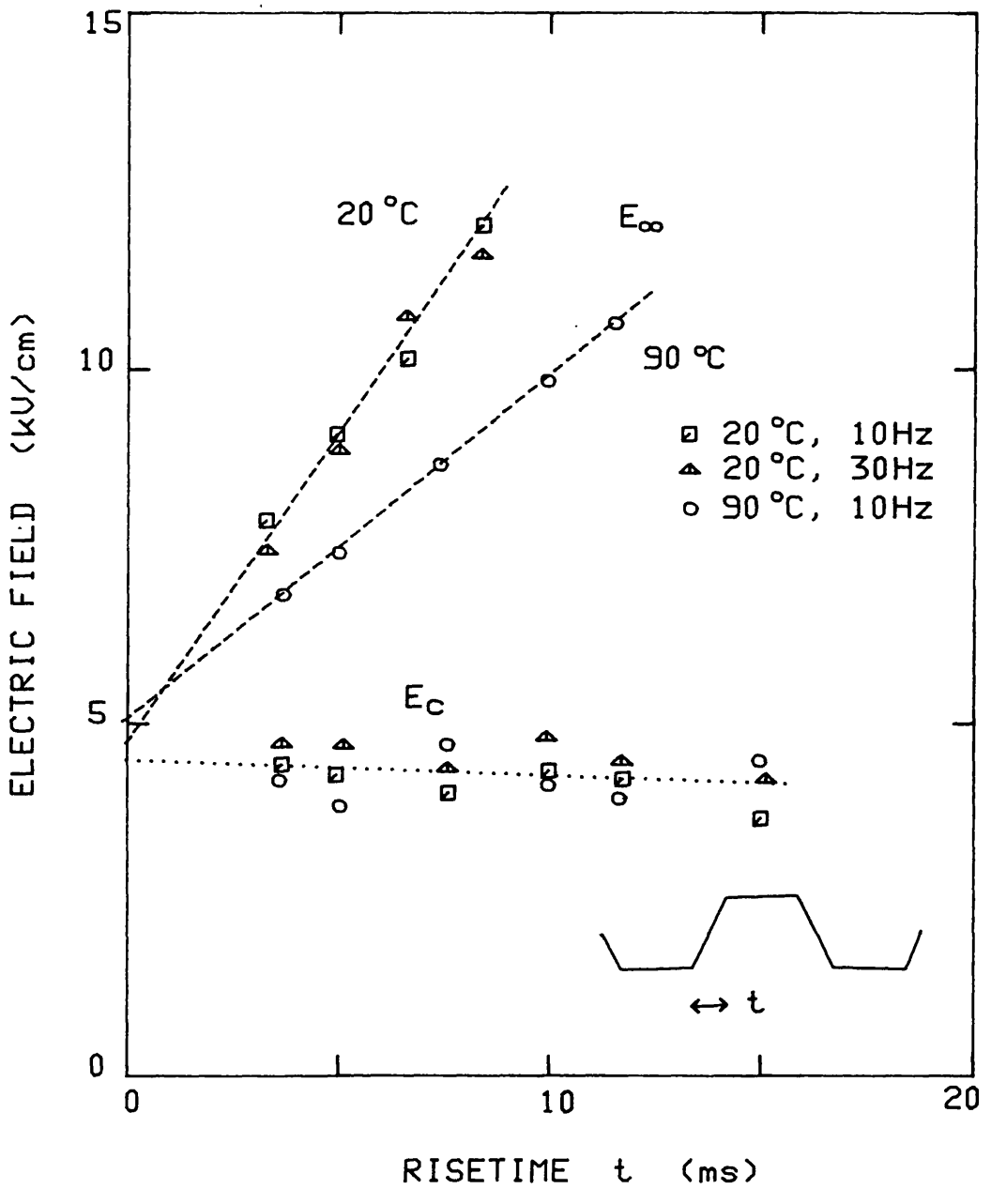

FIGURE 4.52 - Threshold field E_∞ and coercive field E_c plotted as a function of the risetime of the applied trapezoidal electric field at constant frequency. The lead germanate sample is the same as that used for Figure 4.50.

determining the threshold field. However, it is not possible to define a "critical slew rate" which must be exceeded for AE to be produced: if this were so, the threshold field would be proportional to the risetime and the line would pass through the origin. In Figure 4.52, this is clearly not the case, and the line makes a non-zero intercept E_o on the vertical axis. As in the case of a sinusoidal driving field, the coercive field also extrapolates towards this same limiting value. This value E_o (4.7kV/cm) is similar to that in Figure 4.51 for a sinusoidal electric field (E_o = 4.5kV/cm).

The dependence of the threshold field on the risetime has also been measured as a function of temperature. However, the maximum voltage available from the operational power supply severly limited the range over which these measurements could be made. In Figure 4.52, the threshold and coercive fields of lead germanate at 90°C are also shown. This temperature was chosen because the threshold field (at 50Hz) in this material reaches a minimum there (Figure 4.40). The linear relation is again evident, and although the slope of the line is lower than at room temperature, both lines extrapolate towards approximately the same limiting value at zero risetime.

In Figure 4.53, the threshold field in Rochelle salt (using the same sample described above) is plotted as a function of the risetime of the 20Hz trapezoidal applied field, for three different temperatures within the ferroelectric region. At each temperature there is a linear dependence on the rise time, and the slopes of the threshold field curves generally follow the temperature dependence of the 50Hz threshold field shown in Figure 4.46, being low at 4°C and increasing as the Curie temperatures are approached. Both the threshold field and the coercive field extrapolate towards the same limiting value, which is independent of the temperature.

This correlation between the limiting values of the threshold field and the coercive field again raises the dilemma of what happens as the transition temperatures are approached and the

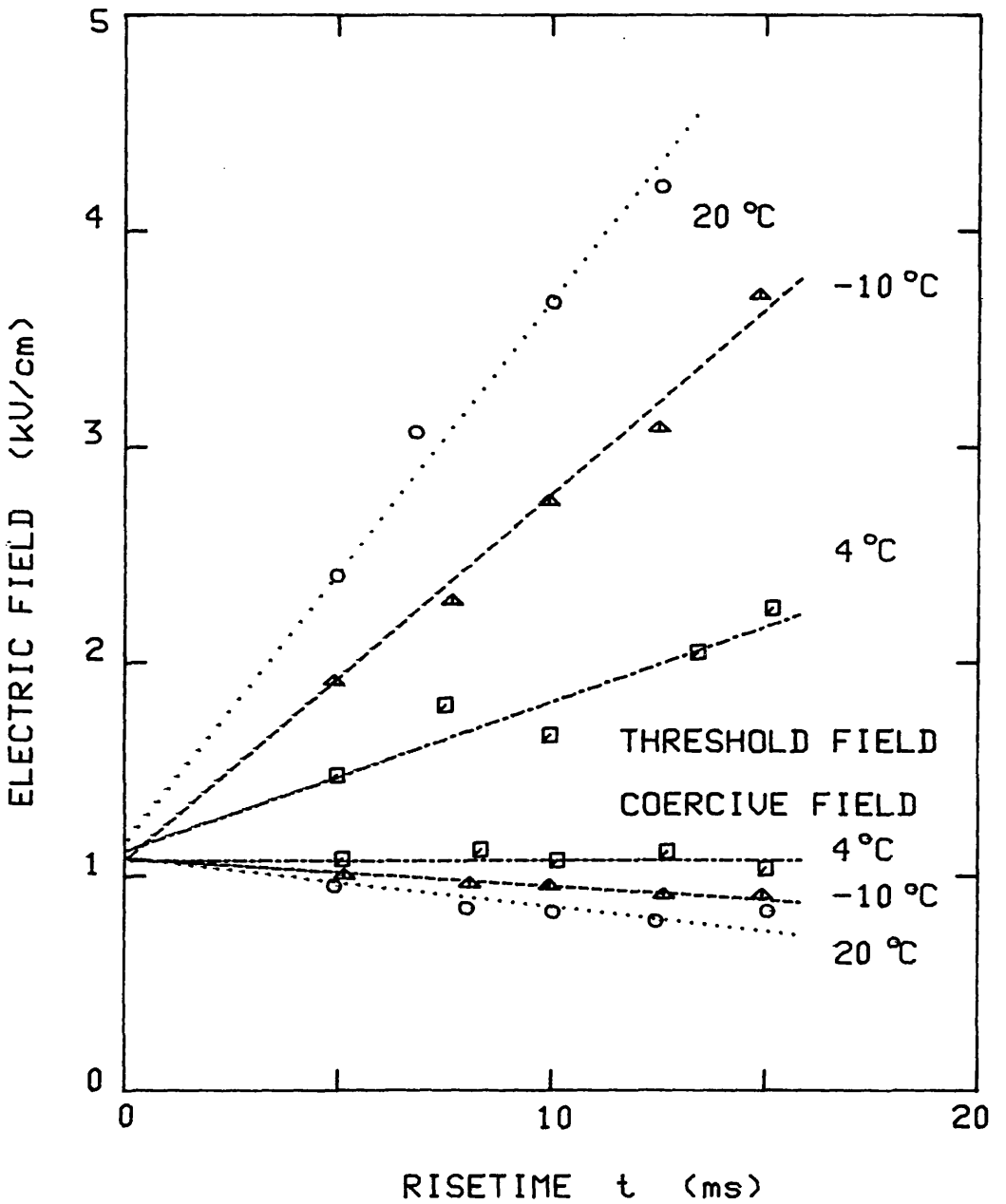

FIGURE 4.53 - Threshold and coercive fields in Rochelle salt (same sample as in Figure 4.47) plotted as a function of the risetime of the trapezoidal electric field.

threshold field (at a fixed frequency) goes to infinity while the coercive field vanishes. Figure 4.53 shows that this limiting value does not change appreciably with temperature between 20°C and -10°C. However, it is just outside this temperature range that the coercive and threshold fields begin to diverge rapidly. As the threshold field increases in these regions, the limitations of the equipment prevented any reliable measurements being made in these regions, exactly where any measurements would be most informative.

The variation of the threshold field in Figures 4.52 and 4.53 can be described by:

$$E_{\infty}(t) = E_{0} + B\,t$$

where the slope B also has the dimensions of a slew rate and should be related to the slope A of the line for a sinusoidal electric field by a geometrical factor taking into account the difference in the shapes of the two waveforms. For the lead germanate sample at room temperature (Figure 4.52), the slope B is 0.92 kV/cm/ms, which gives the ratio B/A as 2.9. For the Rochelle salt sample at 20°C (Figure 4.53), the slope B is 0.26kV/cm/ms. Comparing this with the slope A of the line in Figure 4.49 (for a sinusoidal electric field) gives a ratio B/A of about 3.0. This agrees well with the B/A factor obtained for lead germanate: if B/A is indeed a geometrical constant relating the two waveforms it should be independent of the material used. These measurements have been repeated on a number of Rochelle salt and lead germanate samples of different thicknesses and at different temperatures. In all cases, a value for B/A of between 2.8 and 3.3 was found.

The value of the B/A factor is close to π, which again indicates that the slew rate of the applied field influences the threshold field for AE. For the trapezoidal wave, the slew rate is constant over the sloping parts of the waveform (and zero elsewhere) and is given by:

$$\dot{E} = 2 E / t$$

where E is the peak value of the wave and t is the risetime. For a sine wave, the slew rate varies throughout the cycle, but its maximum value is given by:

$$\dot{E} = 2 \pi f E$$

where f is the frequency, or:

$$\dot{E} = \pi 2 E / t$$

where t is the period (reciprocal frequency) of the wave. Therefore the ratio between the amplitude of a trapezoidal wave of risetime t and the amplitude of a sinusoidal wave of frequency 1/t which has the same peak slew rate as the trapezoid is equal to π.

CHAPTER 5 - ELECTRICAL AND OPTICAL INVESTIGATION OF DOMAIN WALL DYNAMICS.

To back up the acoustic emission experiments described in the previous chapter, the switching process was also studied using electrical and optical methods. In this chapter, these techniques are described and the results related to the production of AE during polarisation reversal.

5.1 - Electrical Study of the Switching Process in Lead Germanate and Rochelle Salt.

The technique for electrical studies of polarisation reversal was briefly described in Section 2.4, and the basic circuit shown in Figure 2.4a. When an electric field is applied to a ferroelectric crystal so as to switch its polarisation, the resulting flow of current (proportional to the rate of change of polarisation) develops a voltage across a load resistor placed in series with the crystal. This voltage is recorded as a function of time, and gives the characteristic switching pulse shown in Figure 2.4c.

Although real voltage sources have a finite rise-time, the applied field is generally assumed to follow an ideal step function. For this assumption to be valid, this rise time should be much smaller than the duration of the switching process (the switching time). A rise-time of a fraction of a microsecond can be achieved with mechanical switching arrangements by using mercury-wetted relay contacts (Ravi et al 1980). In this work, the high-voltage operational power supply (Section 3.8, Figure 3.11) was used to provide the voltage steps. However, this equipment is limited to a slew-rate of about 10V/μs, which means that the rise-time of a 1kV step is

100μs. Fortunately, switching in lead germanate and gadolinium molybdate is relatively slow and a rise-time of at least one-tenth of the switching time could be maintained over a wide range of conditions. Rochelle salt switches appreciably faster, but requires lower voltages where the rise-time of the power supply is also reduced. Switching in gadolinium molybdate is significantly different from the other two materials, and is discussed in the following section.

A transient recorder (Section 3.6) was used to capture the switching pulses. A typical pulse is shown in Figure 5.1a for a voltage step of 500V across a 0.89mm thick lead germanate sample, giving an electric field of 5.6kV/cm. The shape of the pulse is similar to the "ideal" pulse sketched in Figure 2.4c, except that the initial transient due to the charging of the crystal capacitance is absent because of the loading effect of the input capacitance of the transient recorder. The flat top of the pulse means that the current is constant for most of the switching process: if the switching was carried out by a single domain wall, this would correspond to a constant wall velocity. However, in practice switching is carried out by the motion of a large number of domain walls, so the peak current cannot be simply related to the domain wall mobility. Figure 5.1b shows the switching pulse obtained at a higher applied field (800V or 9kV/cm), plotted to the same scale as Figure 5.1a. The switching time is now shorter, while the peak current is greater. The area under the switching curves remains constant at about 7.5mVμs, which dividing by the load resistance of 1kΩ gives the charge moved as about 7.5μC. This charge is equal to $2P_S A$ so for an electrode area A of 78mm² the spontaneous polarisation P_S is 4.8μC/cm². This is the value quoted in the literature for the spontaneous polarisation in lead germanate (Iwasaki et al 1972) showing that complete switching of the electroded area of the crystal occurs.

The switching time t_S will be defined as the time taken for the current to fall to 5% of its peak value. On this criterion, the switching time is about 90ms in Figure 5.1a and 25ms in

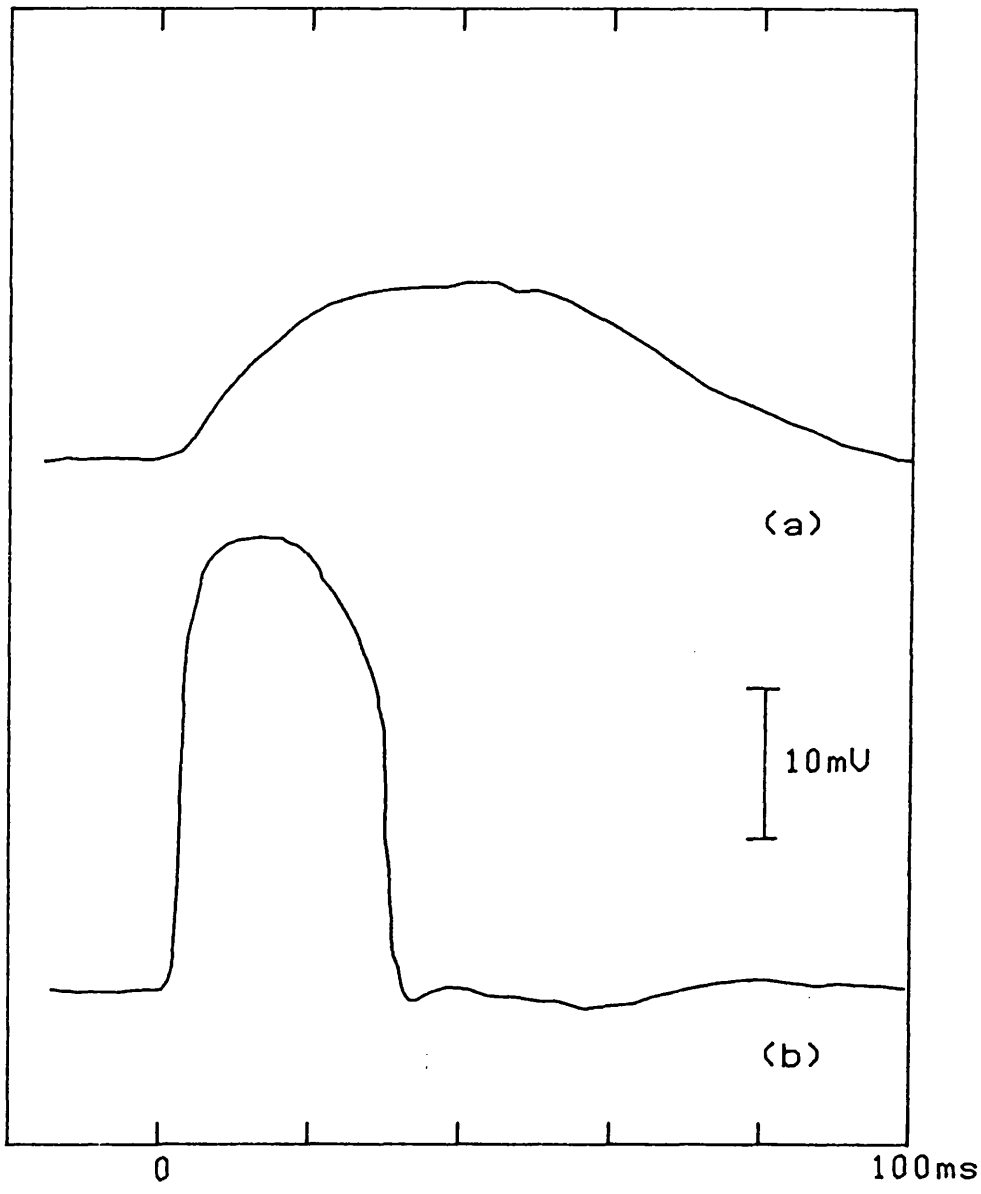

FIGURE 5.1 - Switching pulses from a lead germanate sample 0.89mm thick on applying a voltage step (at zero on the time axis) of (a) 500V and (b) 800V.

Figure 5.1b. The switching time is plotted as a function of the applied field in Figure 5.2, showing that switching occurs more rapidly at higher fields. The switching time rises rapidly at low fields, and no switching was observed for fields less than 4.5kV/cm (where the switching time is nearly half a second). This agrees with the results of Dougherty et al (1972) who observed no switching in lead germanate below about 3kV/cm.

If the reciprocal switching time (on a logarithmic scale) is plotted against the reciprocal of the applied field, a linear relation is found for fields between 5kV/cm and 12kV/cm (Figure 5.3). This linear relation is described by:

$$\log_{10}\left(\frac{1}{t_s}\right) = \log_{10}\left(\frac{1}{t_\infty}\right) - A / E$$

where the slope A is 6kV/cm. Converting to natural logarithms, the dependence of the switching time on the applied field can be described by the exponential relation:

$$\frac{1}{t_s} = \frac{1}{t_\infty} \exp\left(-\alpha/E\right)$$

where:

$$\alpha = A / \log_{10} e$$

and is equal to 13.8kV/cm. These results are similar to those of Suzuki et al (1978) who obtained a value for α of 19kV/cm for electric fields between 5kV/cm and 7kV/cm, again in lead germanate. At high fields the switching time decreases more rapidly, and the few points available in this region can be described by a similar equation but with a higher value for α. However, the limits on the maximum voltage that could be applied prevented measurements being made at fields above 15kV/cm, so the existence of a power law at these high fields (as observed by Suzuki et al) could not be verified.

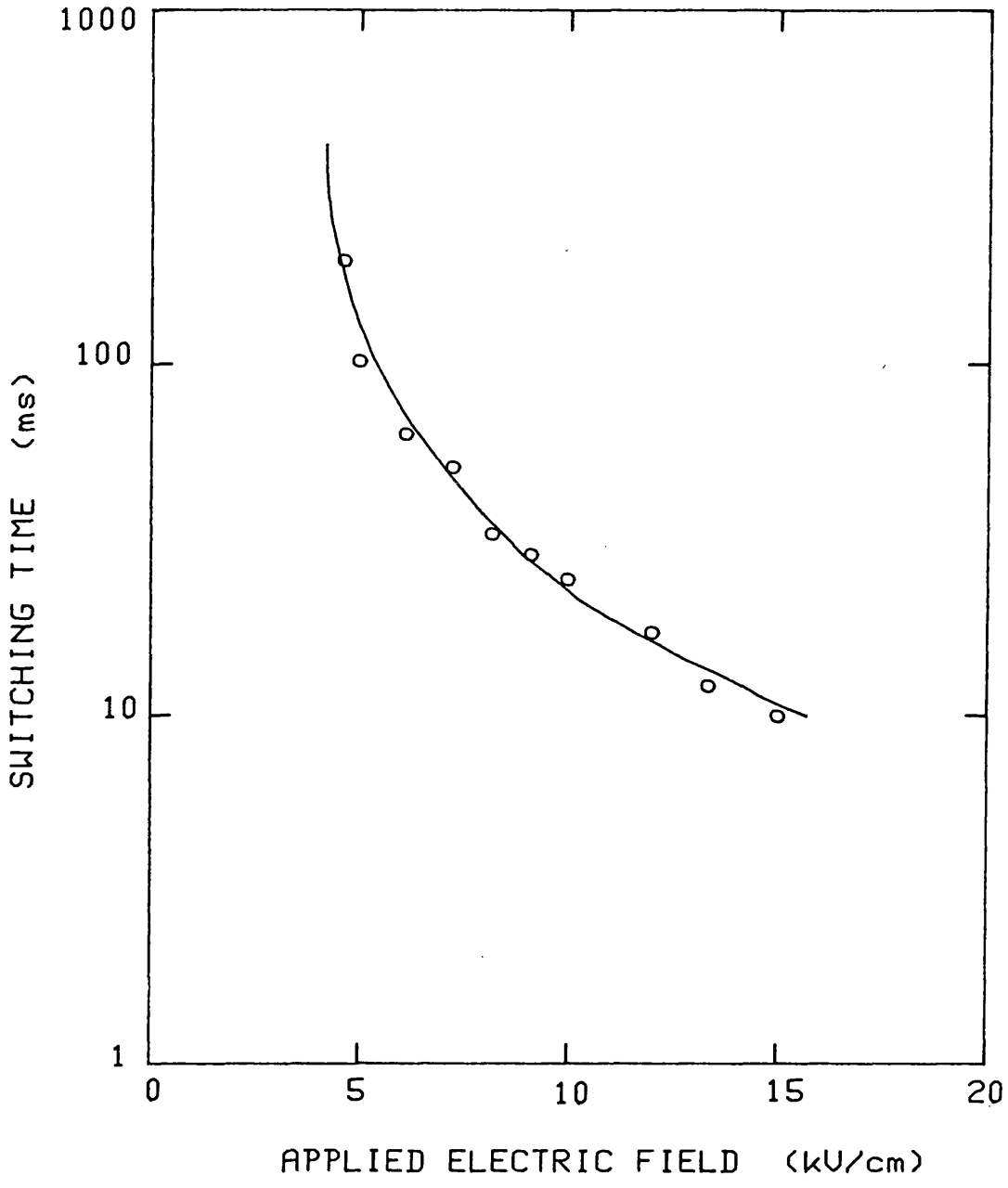

FIGURE 5.2 - Logarithmic switching time plotted as a function of the applied electric field for a lead germanate sample 0.89mm thick. No switching was observed for fields less than 4.5kV/cm.

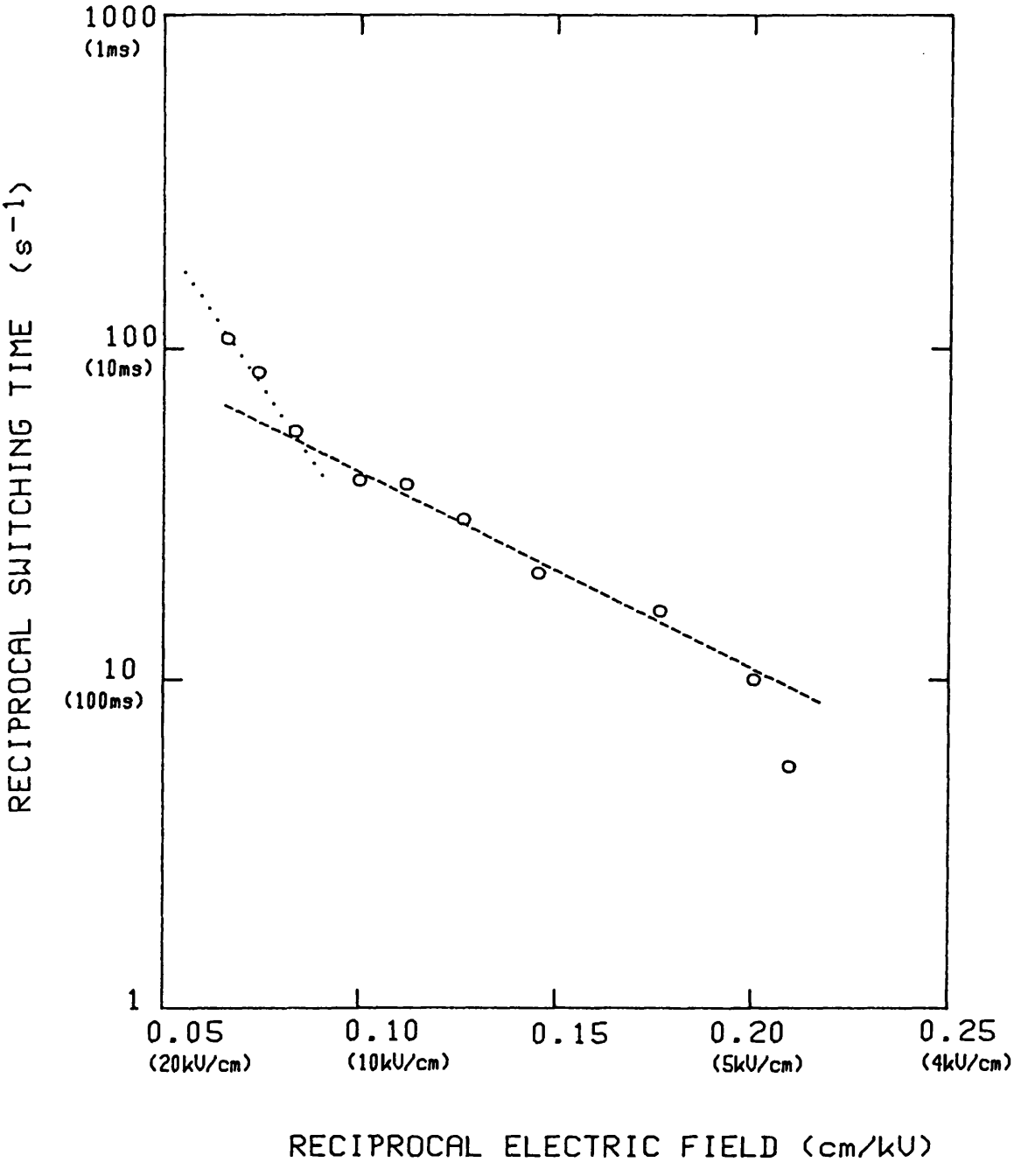

FIGURE 5.3 - Reciprocal switching time plotted against the reciprocal of the applied field for lead germanate. The data is the same as that in Figure 5.2. The curve departs from linearity for fields above 12kV/cm and below 5kV/cm.

The voltage steps applied to the sample can be considered as a trapezoidal waveform in the limit of low risetime and long repetition period. Using a trapezoidal waveform, the threshold field for acoustic emission and the coercive field were both found to extrapolate towards the same value - about 5kV/cm - in the limit of zero risetime (Section 4.11, Figure 4.52). This is close to the limiting field found in these switching experiments (which used the same sample) below which no switching was observed. If the curve in Figure 5.2 is extrapolated towards large switching times, a limiting electric field of about 4.5kV/cm can be found. Another correlation between the AE and the switching time was mentioned in Section 4.5: when the log count rate is plotted as a function of the reciprocal of the applied field, two linear dependences can be found with a knee at 12.5kV/cm (Figure 4.18). This agrees well with the value of 12kV/cm where a knee occurs in Figure 5.3, even though this curve refers to a different sample. These switching experiments were also carried out on the 1.13mm thick sample used to provide the data in Figure 4.18, with results very similar to those for the 0.89mm thick sample shown in Figures 5.2 and 5.3. In particular, a knee at 12kV/cm was also found for this sample.

The dependence of the switching time in Rochelle salt on the applied electric field is shown in Figure 5.4. This material does not have a true coercive field, with switching occurring even at very low values of the applied electric field. At higher fields, the reciprocal switching time varies linearly with the applied field, according to:

$$\frac{1}{t_s} = B\,(E - E_o)$$

where the intercept E_o is 0.93kV/cm. The departure from linearity occurs at about 1kV/cm, which agrees well with the limiting coercive and threshold fields at zero risetime of 1.1kV/cm found in Section 4.11 (Figure 4.53). The slope B of the linear portion, found to be 1.25cm/kV/ms, can be considered as the mobility of a hypothetical domain wall sweeping across the crystal: it is not a true domain wall mobility since

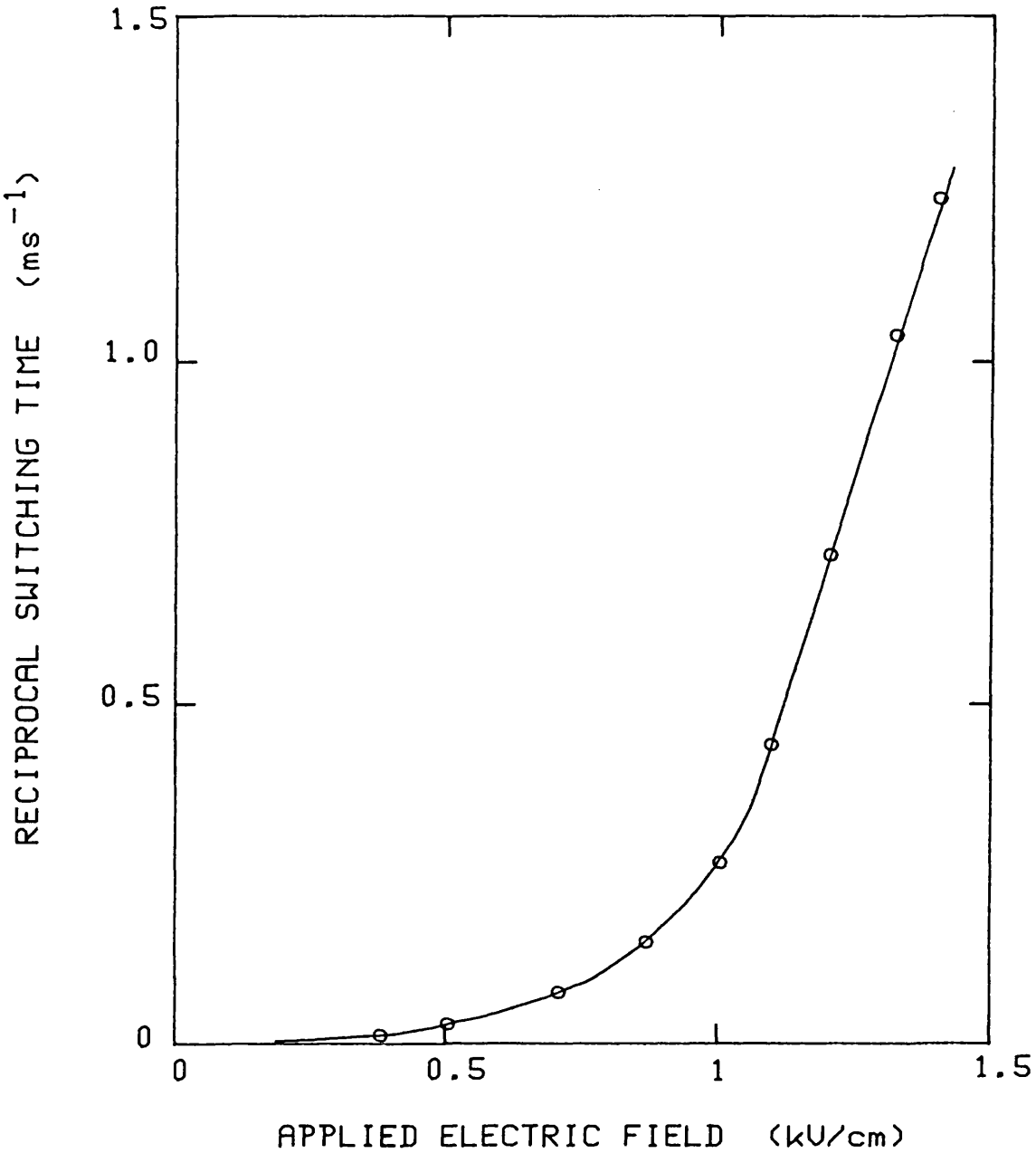

FIGURE 5.4 - Reciprocal switching time plotted against the applied electric field for a Rochelle salt sample 1.11mm thick at 20°C.

switching occurs through the motion of several domain walls.

These results are qualitatively similar to those of Wieder (1958). However, the intercept E_o is several times greater than the value of 0.19kV/cm reported by Wieder, and the mobility B is also several times less than his value. In Section 4.11 it was pointed out that the coercive field of these Rochelle salt samples was also found to be several times the values reported in the literature. Measurement of the area under the switching pulse gave a value for the spontaneous polarisation (by the method described above for lead germanate) of about $0.05\mu C/cm^2$, or about a quarter of the commonly accepted value. Microscopic observation of the domains in this sample showed that a number of domain walls did not move during switching, and that large areas - estimated at over half the total area of the crystal - remained unswitched. Other samples cut from the same crystal showed similar effects, as did samples cut from other crystals though to a different degree. These effects - reduction of the switchable polarisation, increase of the coercive field, increase in the switching time - are commonly associated with the phenomenon of ageing (Section 2.5). This particular Rochelle salt sample was cut from a large crystal of unknown vintage, and although ageing is usually associated with repeated reversals of polarisation, it also seems that the passage of a number of years over an undisturbed, large multidomain crystal can have similar effects.

5.2 Polarisation Reversal in Gadolinium Molybdate.

The switching behaviour of gadolinium molybdate was found to be critically dependent on the domain configuration of the sample. The following measurements were carried out on a number of GMO samples about 1mm thick with transparent aluminium electrodes which were used for the optical study of domains, which is

described in Section 5.4. Initial switching measurements on a multi-domain crystal invariably gave erratic, non-reproducible results: microscopic observation of the domains showed that the domain structure was rearranging, tending towards a single domain wall. Once only a single domain wall was left, the switching measurements became much more repeatable. Except at high fields, the switching was seen to be carried out through the motion of this one wall.

A typical switching pulse from a GMO sample is shown in Figure 5.5a. Since only one domain wall is involved in this case, it is possible to relate the peak current i_m to the domain wall velocity v, assuming that the length of the wall d is constant (ie that the crystal has a uniform cross-section) by the equation:

$$i_m = 2 P_s d v$$

P_s being the spontaneous polarisation. The switching pulse has rapid rise and fall times (for instance in comparison with lead germanate, Figure 5.1) which means that the domain wall accelerates and decelerates rapidly while most of the switching is carried out at constant velocity. The most reliable results were obtained using crystals which were not fully electroded, where the domain wall would come to rest under the edge of the electrode. With fully electroded crystals, the domain wall would disappear into the side of the crystal: upon reversing the applied electric field a few milliseconds would elapse before the domain started moving. This has the effect of delaying the switching pulse relative to the applied voltage step (Figure 5.5b), although good agreement was found between the domain wall velocities (ie peak switching currents) for fully and partially electroded crystals. The length of this delay is not reproducible and appears to be statistical in nature. At electric fields over about 10kV/cm, the nucleation of additional domains was found to occur: this gives rise to steps in the switching current as in Figure 5.5c. The voltage at which this happened was found to vary considerably from sample to sample,

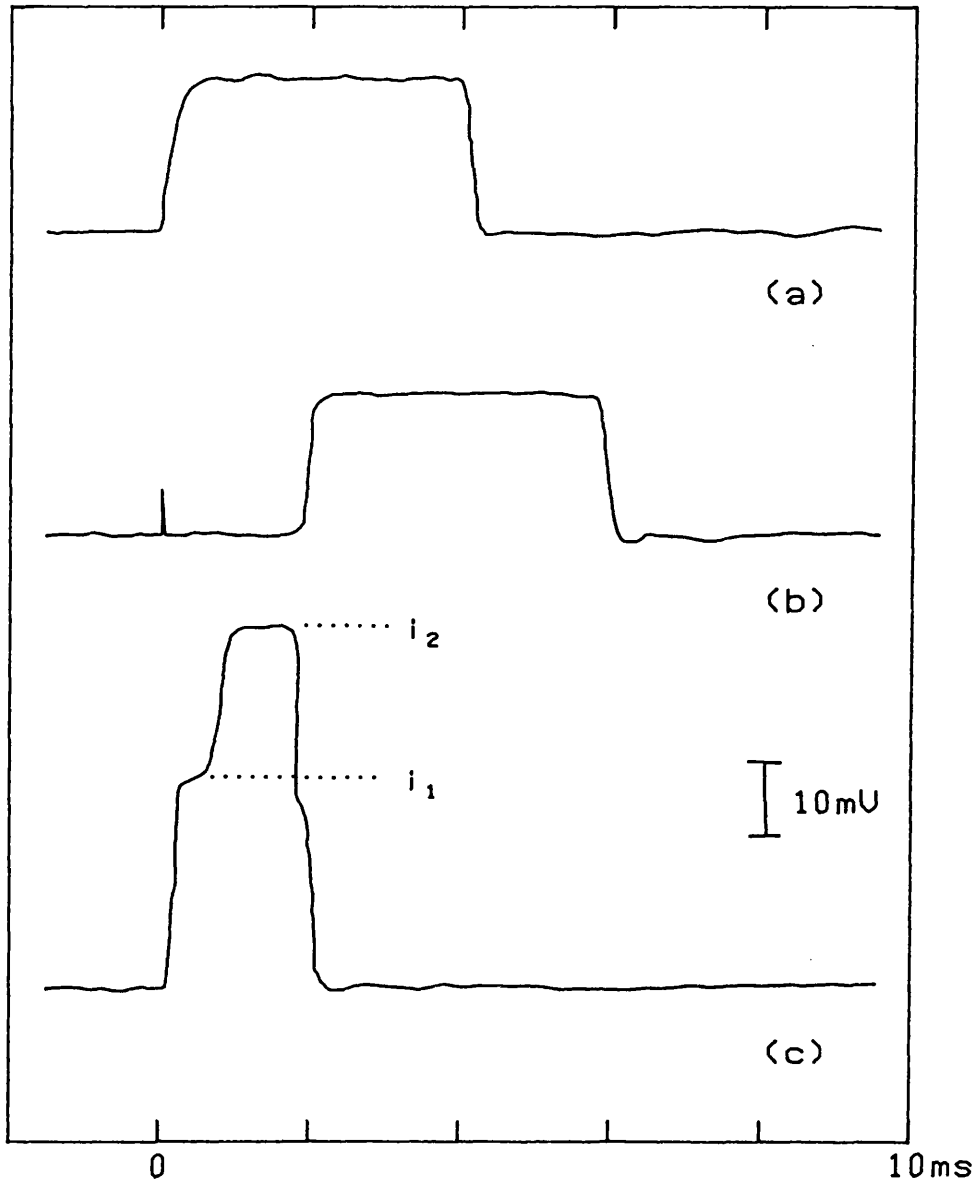

FIGURE 5.5 - Switching pulses from a gadolinium molybdate sample.
(a) Partially electroded, 8kV/cm.
(b) Fully electroded, 8kV/cm.
(c) Partially electroded, 12kV/cm.

and appears to depend on the surface finish of the crystal: in a scratched sample it was found to occur at only 5kV/cm. Microscopic observation of this damaged sample revealed the nucleation of domain walls under the scratch in the surface.

The dependence of the switching time on the applied field for a partially electroded GMO sample is shown in Figure 5.6. No switching was obtained for applied electric fields below about 1kV/cm. At higher fields than this, a linear relation between the reciprocal of the switching time and the applied electric field E was found, according to:

$$\frac{1}{t_s} = A\,(E - E_o)$$

the curve departs from linearity at field above about 10kV/cm where the nucleation of additional domains occurs.

Given the length of crystal traversed by the domain wall (ℓ =6mm), it is possible to calculate the domain wall velocity from the switching time, ignoring the acceleration and deceleration periods. Since the velocity is inversely proportional to the switching time, the dependence of the domain wall velocity v on the applied field E can also be described by a linear relation:

$$v = \mu\,(E - E_o)$$

where the mobility μ (or velocity per unit electric field) is related to the slope A of the switching time curve (Figure 5.6) by:

$$\mu = \ell A$$

The straight line of Figure 5.6 gives values of E_o and μ as 1kV/cm and 21.3cm^2/kV/s respectively. The actual mobility will be slightly higher than this because the acceleration and deceleration periods have been ignored. While the intercept E_o

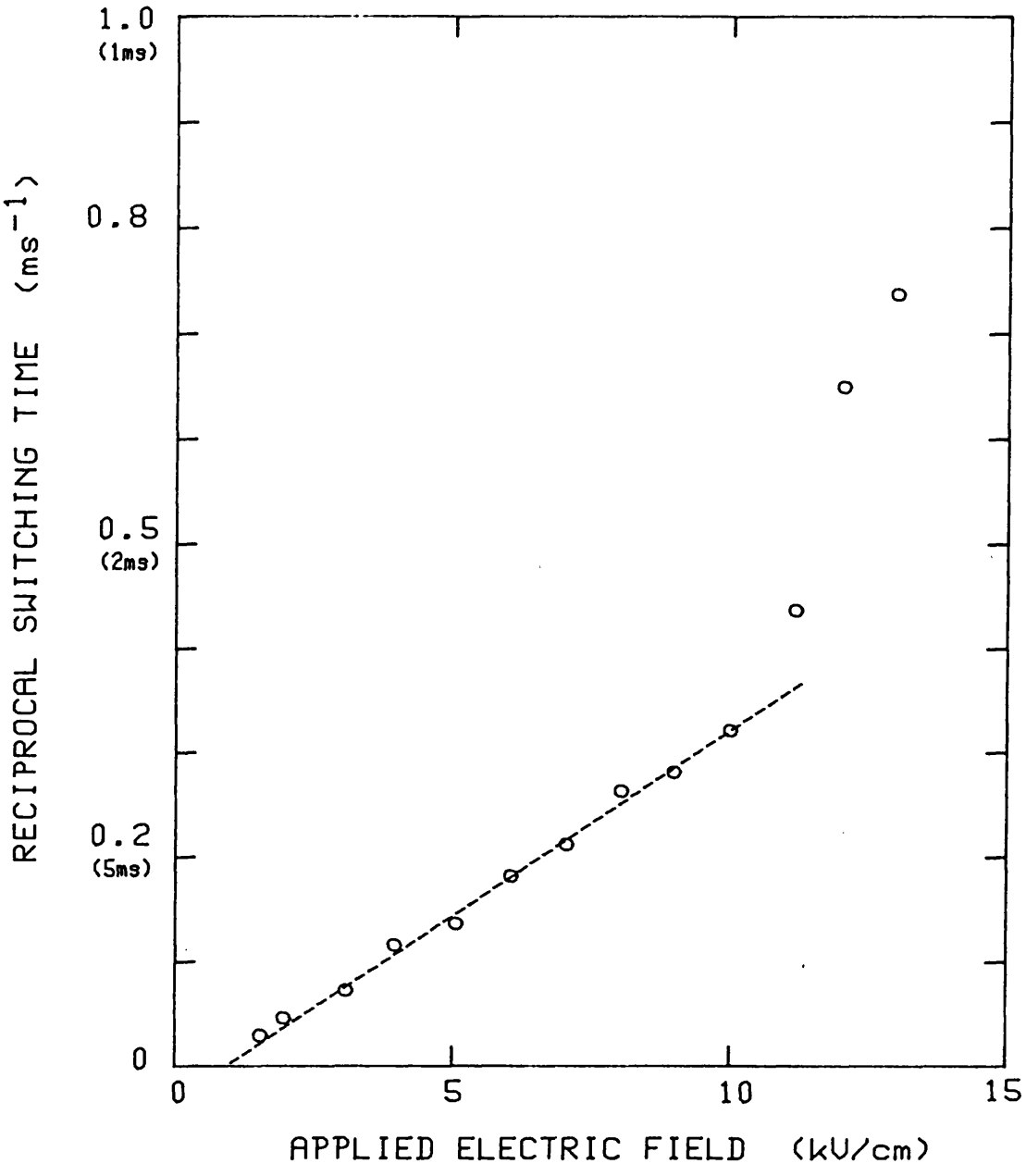

FIGURE 5.6 - Reciprocal switching time plotted against the applied electric field for a gadolinium molybdate sample 0.94mm thick.

varies from sample to sample (values from 0.8kV/cm to 2kV/cm were obtained), the mobility μ is surprisingly constant and appears to be independent of sample thickness, at least in the range 0.8mm to 1.9mm. Flippen (1975) measured the mobility of the domain walls in GMO using an optical method: the results obtained here agree closely with his values, the latter being 1.4kV/cm and 21cm^2/kV/s for E_o and μ respectively.

Another means of obtaining the domain wall velocity is through the peak switching current as described above. The peak switching current is shown as a function of the applied field (for the same GMO sample) in Figure 5.7a, which is also calibrated in terms of the domain wall velocity (proportional to the current). This graph is very similar to Figure 5.6, which is to be expected since for a rectangular switching pulse i_m is inversely proportional to t_s. The mobility is related to the slope B of this graph (in terms of current per unit applied field) by:

$$\mu = B / (2 P_s d)$$

the values of the spontaneous polarisation P_s and the electrode width d being 0.18μC/cm^2 and 4mm respectively. This gives a value for μ of 20.1cm^2/kV/s, in good agreement with the value obtained above.

The measurements taken above 10kV/cm all correspond to stepped switching pulses like that shown in Figure 5.5c. These data points were treated somewhat differently from the rest: rather than plotting out the peak current, the individual currents associated with each step (i_1 and i_2-i_1 in Figure 5.4c) were plotted in Figure 5.7a. In the case of the final measurement at 13kV/cm, the switching pulse showed three steps. These results indicate that there exists a limiting domain wall velocity (about 2m/s) which is not exceeded because additional nucleation occurs at higher fields rather than any further increase in domain wall velocity. This was also found by Flippen (1975).

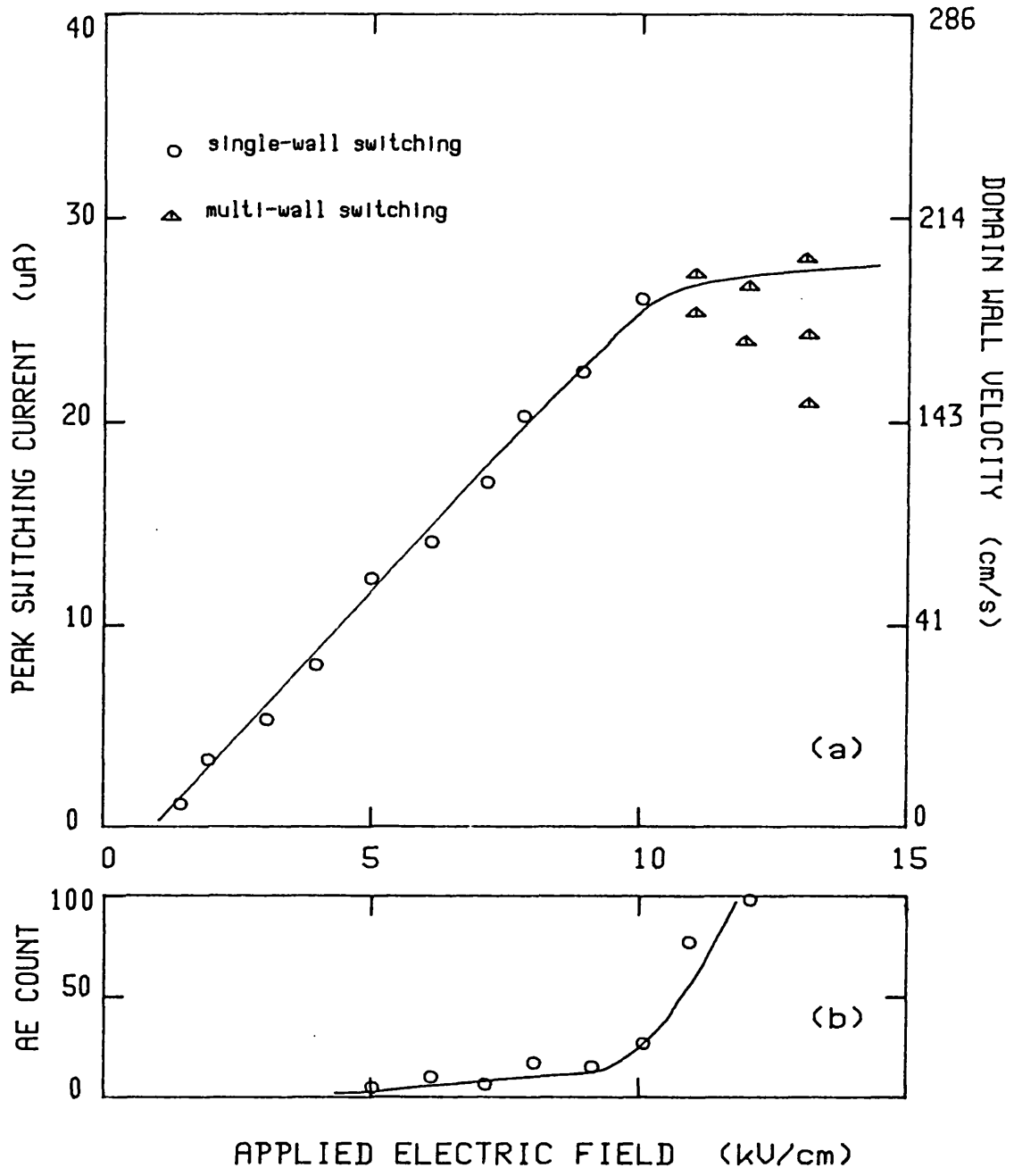

FIGURE 5.7(a) - Peak switching current plotted as a function of the applied electric field for the same GMO sample as used for Figure 5.6. The vertical axis is also calibrated in terms of the domain wall velocity.
(b) The AE count produced per polarisation reversal recorded simultaneously with the switching pulse.

By comparison with the results for lead germanate and Rochelle salt, the threshold field for acoustic emission and the coercive field for a trapezoidal waveform should at zero rise-time be about 10kV/cm, where the break in the switching time curve occurs. The threshold field at 50Hz is 12kV/cm in GMO: unfortunately it was not possible to obtain any AE from these samples when applying the highest permissible trapezoidal voltage (Section 4.11). Therefore these switching experiments were carried out with the sample mounted on an AE transducer, and any AE produced during switching monitored. This procedure is complicated by the fact that the current pulse on switching causes some spurious counts through electrical interference, even when the crystal is removed from direct contact with the transducer. The counts recorded during switching are shown in Figure 2.7b: there is a sharp increase above about 10kV/cm, which is where the switching current curve (Figure 5.7a) departs from linearity. Switching below this value occurs by sideways motion and produces little AE if any: it is with the onset of the nucleation of domain walls that large amounts of AE are produced.

5.3 - The Barkhausen Effect.

The current pulses produced by the switching of ferroelectric crystals are primarily due to the sideways motion of domain walls. However, a number of short, large-amplitude pulses are usually found superimposed on this relatively long and low-amplitude pulse. These transient impulses are referred to as Barkhausen pulses, and are generally attributed to the nucleation and forward growth of domains (Section 2.4). That these impulses are usually not evident when the switching pulse is displayed on an oscilloscope or transient recorder is simply due to the difference in scale: the duration of the Barkhausen pulses is of the order of microseconds, while to monitor the

switching pulse the timebase has to run for several milliseconds.

To record the Barkhausen impulses associated with polarisation reversal, the same basic setup used to measure the switching pulse was employed. The transient recorder or storage oscilloscope was set to a high timebase speed - typically 50μs per scan - and the triggering controls adjusted so that the relatively slow switching pulse would be ignored, while the high-amplitude Barkhausen pulses would initiate the scan. A selection of pulses from the switching of a lead germanate sample are shown in Figure 5.8a. The traces show steps which are due to the finite sampling rate of the transient recorder (50ns per step). Most of the pulses captured at a given switching voltage were found to be similar (both in terms of amplitude and area enclosed under the pulse), although this average size was found to increase with increasing voltage. However, it was found that the exponentially decaying "tail" of each pulse had a time constant of about 200ns, irrespective of the size of the pulse. This suggested that the "tail" may be due to the measuring equipment rather than to some property of the pulse itself. This will now be established.

When considering the circuit of Figure 2.4a for measuring the switching pulse, the effects of any shunting capacitance across the resistor R were ignored: in fact the transient recorder input, the connecting cable and the sample itself amount to a capacitance of some 150pF. With a value of 1k Ω for the load resistor, this gives an RC time constant of 150ns, short enough to be ignored in the context of the switching pulse (which is several milliseconds long), but close to the observed value of the decay "tail" of the Barkhausen pulses. In this case neither the duration nor the amplitude of the measured pulse reflect the duration and amplitude of the current through the sample. However, the area under the curve still gives the total charge switched, and assuming the Barkhausen current to be an ideal rectangular pulse, its duration is given by the rise-time of the measured pulse and its amplitude can then be obtained by dividing its area by this duration.

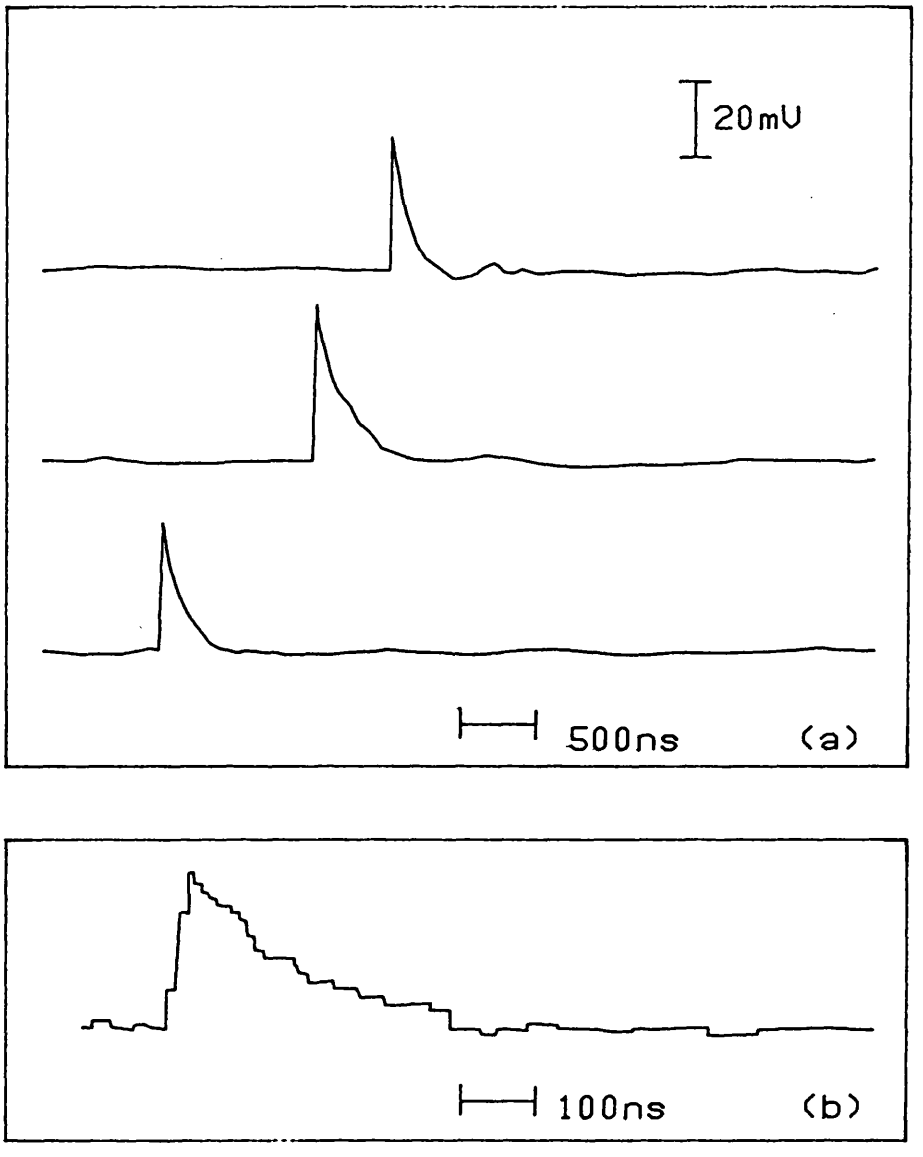

FIGURE 5.8 - Barkhausen pulses produced during polarisation reversal in a lead germanate sample. The traces in (a) were sampled at 20MHz while the trace in (b) was sampled at 100MHz (10ns per point) and is shown on an expanded horizontal scale.

On this basis, the duration of the Barkhausen events shown in Figure 5.8 is of the order of 50ns, which is the sampling time of the DL920 transient recorder. To measure this rise-time more accurately, a Biomation transient recorder with a 100MHz sampling rate (kindly made available by Dr. E.H. Putley of R.S.R.E. Malvern) was used, and a sample trace is shown in Figure 5.8c. The leading edge of the pulse shows three steps, giving a rise time of 30ns: this was found to be the average value for lead germanate, although some pulses were found with rise-times of up to 80ns. The area under the curve corresponds to a charge of only a few picocoulombs: the total charge involved in reversing the polarisation of the entire crystal is several microcoulombs (Section 5.1) so that even the several thousand Barkhausen pulses that may be associated with each polarisation reversal account for less than 0.1% of the total charge switched. This is in line with the observations of Chynoweth (1958) on barium titanate, though it should be pointed out that he obtained pulses several microseconds long in that material, whereas in lead germanate the pulses are only several nanoseconds long.

Since the transient recorder could only capture the first pulse with an amplitude sufficient to trigger it, this equipment could not be used to perform a statistical analysis of the pulses as performed by Chynoweth (1958) for barium titanate. However, by coupling the switching circuit to an electronic counter (Racal type 9838) through a small capacitor, the number of Barkhausen pulses (with an amplitude greater than the counter threshold) produced during each polarisation reversal could be obtained. The value of the coupling capacitor was chosen to be 50pF (giving a time constant of 50μs with the 1MΩ input impedance of the counter) to filter out the relatively slow switching pulse while passing the Barkhausen pulses. The way in which this count varies with the switching voltage is shown in Figure 5.9. A small count is observed at low fields (below 5kV/cm) where switching is known not to occur (Section 5.1) - this can be attributed to the counter registering the pulse caused by the

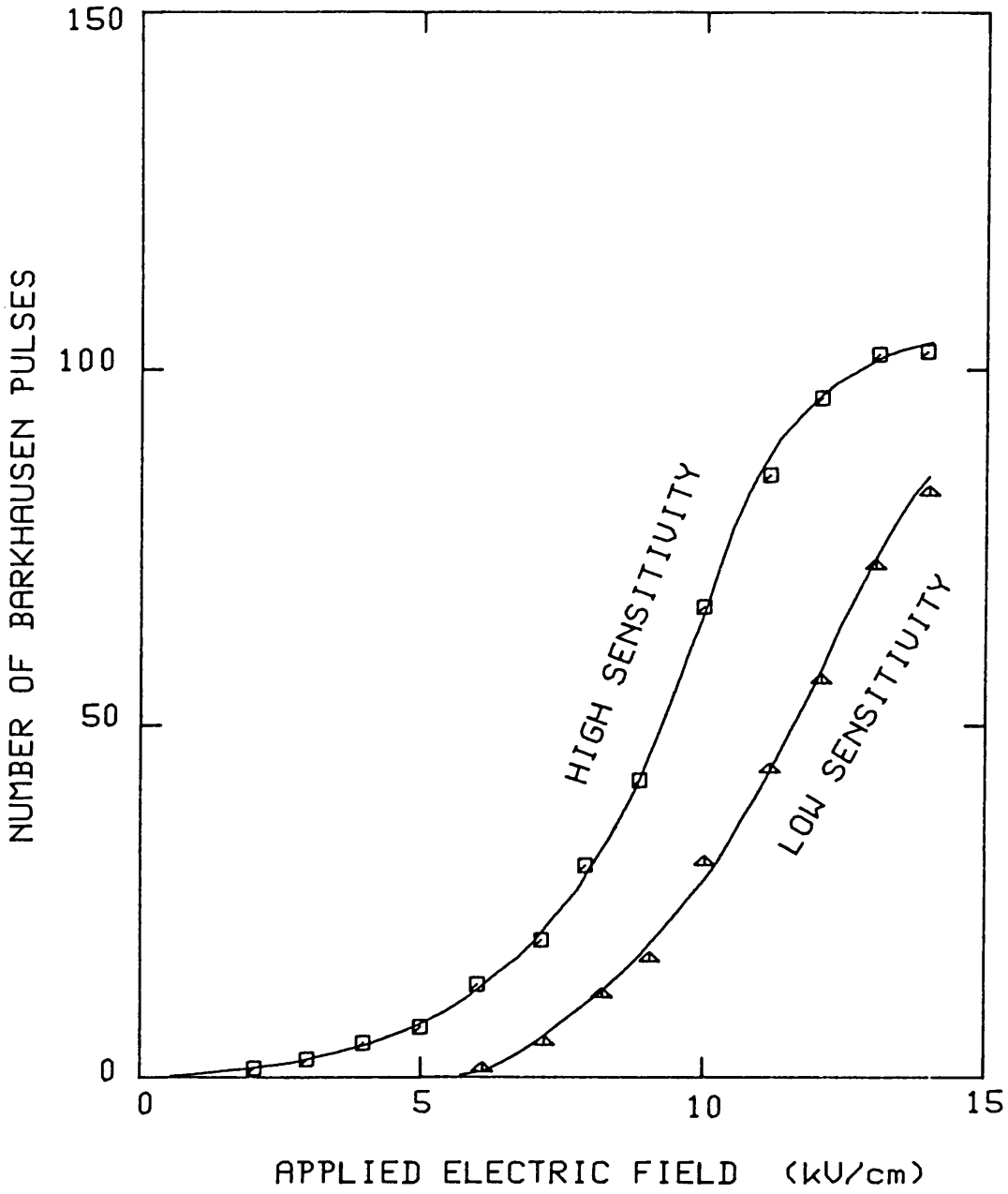

FIGURE 5.9 - Number of Barkhausen pulses per polarisation reversal plotted as a function of the switching field for a lead germanate sample 0.89mm thick. Measurements were made at two settings of the counter sensitivity.

charging of the crystal capacitance, or to electrical interference. The Barkhausen effect proper - pulses like those in Figure 5.8, occurring a short time after the voltage step is applied - is observed at fields greater than this value. The number of pulses increases with applied field, but levels out at high field. Since the amplitude of the pulses varies with the magnitude of the applied electric field, the count registered depends on the threshold level of the counter. Measurements made at a lower sensitivity are also shown in Figure 5.9. The situation is in fact similar to that encountered when measuring the threshold field for AE, and Figure 5.9 can be likened to the AE curves in Figure 4.15.

This similarity of behaviour inevitably poses the question of whether the electrical Barkhausen pulses and the ultrasonic AE impulses may be closely related. The lead germanate sample was mounted on an AE transducer during these switching experiments, so that any AE produced could be monitored. By simultaneously displaying the Barkhausen pulses and the AE signal on the two traces of a storage oscilloscope, the relation between the two could be investigated. However, the oscilloscope could not display the triggering impulse, so the only way to obtain a satisfactory trace was to use a slow timebase speed and a high switching voltage, to increase the chances of capturing a Barkhausen pulse produced after the one that triggered the oscilloscope sweep. To make the pulses visible at the low sweep speed, the oscilloscope input was shunted by a 1nF capacitor (which lengthened the decay "tail" of the pulses at the cost of reducing their amplitude). Typical oscillographs are shown in Figure 5.10, with the Barkhausen signal on the upper trace and the AE on the lower one: a one-to-one correspondence between the electrical and acoustic signals is evident. Of some 200 impulses captured in this way, this correlation was found for 94% of them. For about 75% of the recorded events, the sizes of the Barkhausen and AE impulses could also be correlated, although because of the limited frequency response of the AE detection system the amplitude of the measured AE signal does not necessarily reflect the energy of the source impulse

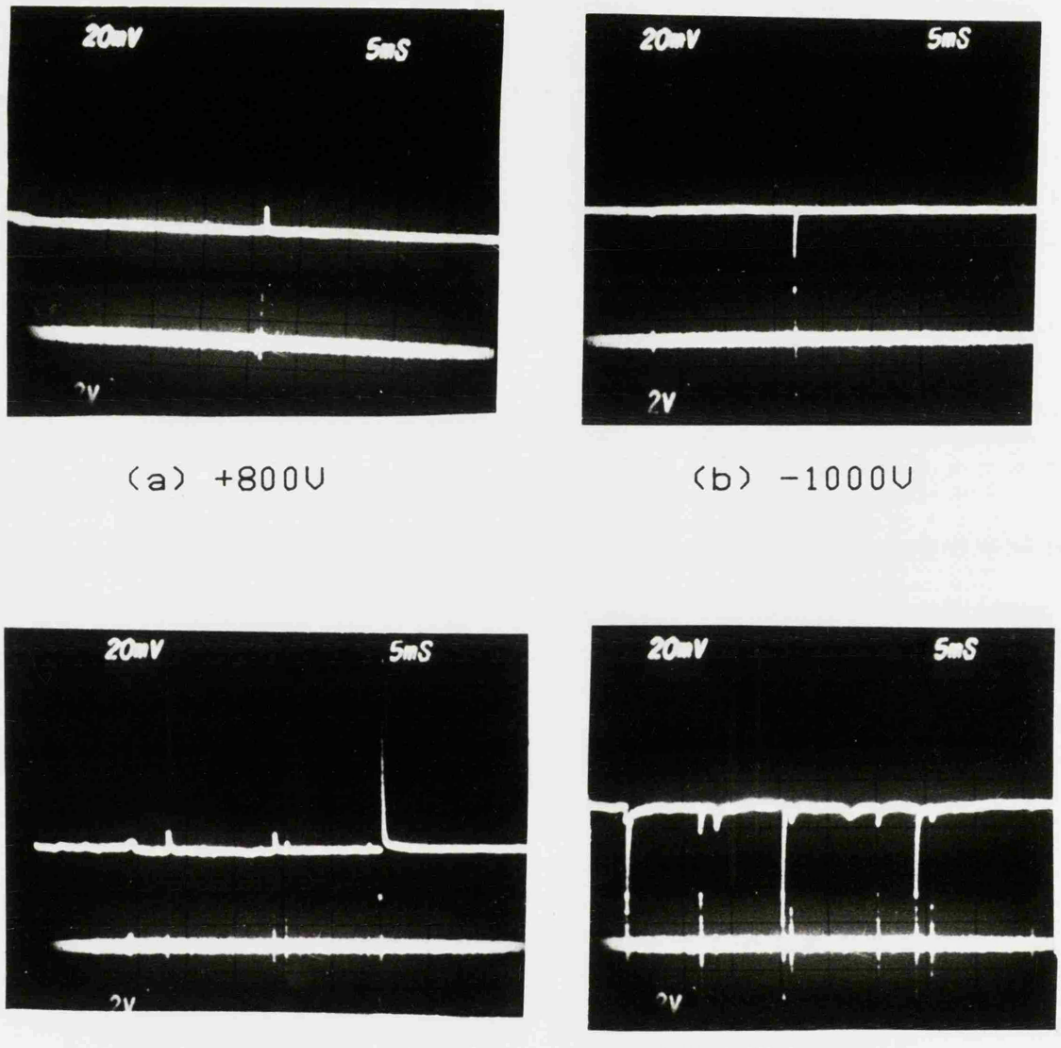

FIGURE 5.10 - Oscillographs showing the correlation between the electrical Barkhausen pulses (upper trace) and the ultrasonic AE bursts (lower trace) produced during polarisation reversal in a lead germanate sample, for different amplitudes and polarity of the applied voltage step.

charging of the crystal capacitance, or to electrical interference. The Barkhausen effect proper - pulses like those in Figure 5.8, occurring a short time after the voltage step is applied - is observed at fields greater than this value. The number of pulses increases with applied field, but levels out at high field. Since the amplitude of the pulses varies with the magnitude of the applied electric field, the count registered depends on the threshold level of the counter. Measurements made at a lower sensitivity are also shown in Figure 5.9. The situation is in fact similar to that encountered when measuring the threshold field for AE, and Figure 5.9 can be likened to the AE curves in Figure 4.15.

This similarity of behaviour inevitably poses the question of whether the electrical Barkhausen pulses and the ultrasonic AE impulses may be closely related. The lead germanate sample was mounted on an AE transducer during these switching experiments, so that any AE produced could be monitored. By simultaneously displaying the Barkhausen pulses and the AE signal on the two traces of a storage oscilloscope, the relation between the two could be investigated. However, the oscilloscope could not display the triggering impulse, so the only way to obtain a satisfactory trace was to use a slow timebase speed and a high switching voltage, to increase the chances of capturing a Barkhausen pulse produced after the one that triggered the oscilloscope sweep. To make the pulses visible at the low sweep speed, the oscilloscope input was shunted by a 1nF capacitor (which lengthened the decay "tail" of the pulses at the cost of reducing their amplitude). Typical oscillographs are shown in Figure 5.10, with the Barkhausen signal on the upper trace and the AE on the lower one: a one-to-one correspondence between the electrical and acoustic signals is evident. Of some 200 impulses captured in this way, this correlation was found for 94% of them. For about 75% of the recorded events, the sizes of the Barkhausen and AE impulses could also be correlated, although because of the limited frequency response of the AE detection system the amplitude of the measured AE signal does not necessarily reflect the energy of the source impulse

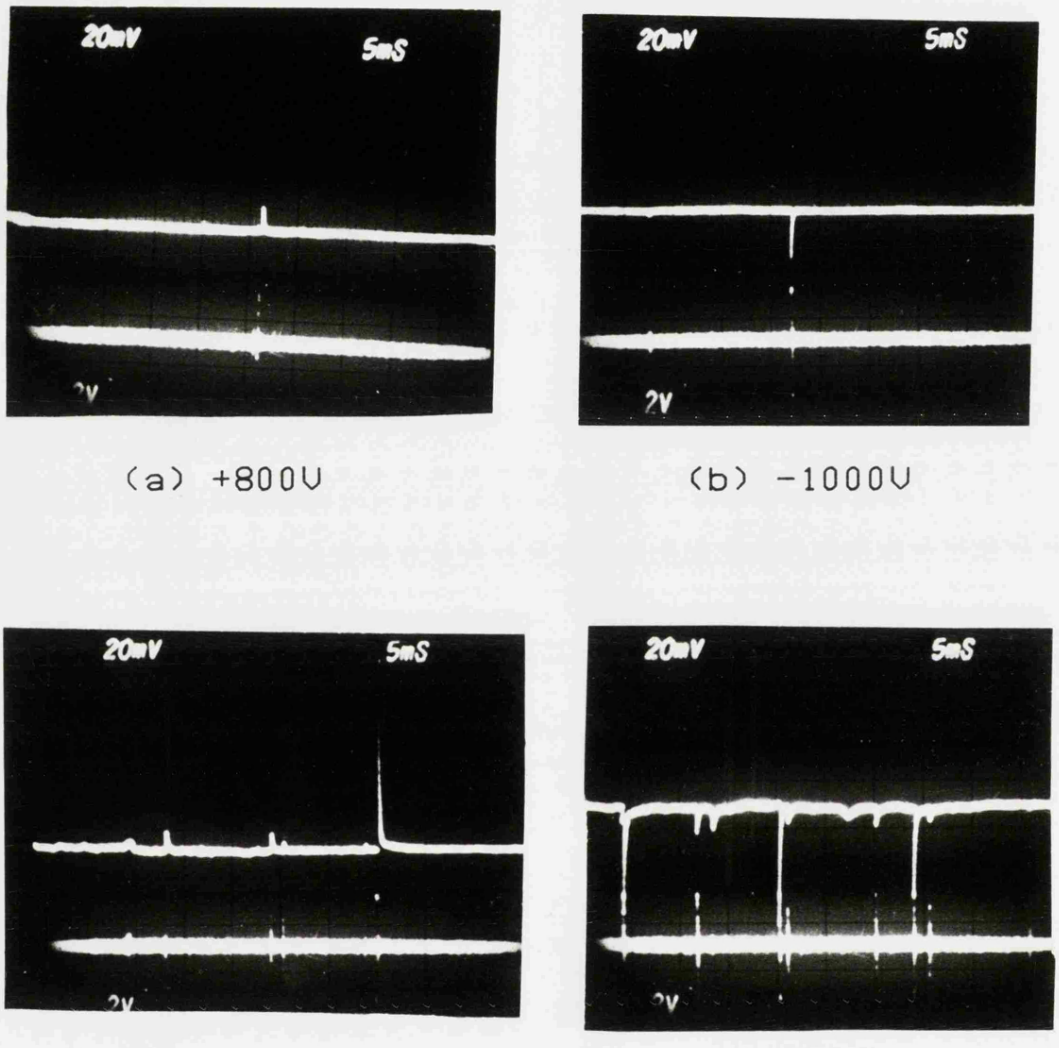

FIGURE 5.10 - Oscillographs showing the correlation between the electrical Barkhausen pulses (upper trace) and the ultrasonic AE bursts (lower trace) produced during polarisation reversal in a lead germanate sample, for different amplitudes and polarity of the applied voltage step.

(Section 4.2).

Although the Barkhausen and AE impulses appear to be simultaneous on the relatively slow timebase in the oscillographs in Figure 5.10, the ultrasonic signal is in fact delayed slightly by the acoustic transit time in the sample and transducer. Assuming that the two events are simultaneous, by measuring this delay the distribution of the AE sources along the thickness of the sample (ie along the polar axis) could be determined. This was done by displaying the AE signal on the transient recorder but triggering the instrument from the Barkhausen pulse. This cannot be a precise measurement, because of the difficulty of determining exactly where the AE signal starts (a typical AE signal was shown in Figure 4.3a). This delay was measured for a number of events, and the results plotted in histogram form in Figure 5.11. The delay within the transducer was measured by dropping a ball-bearing on to the transducer surface, thereby simulating a source at the surface. The signal to trigger the transient recorder was obtained by using the ball-bearing to complete a circuit to a silver-dag electrode painted on the surface of the transducer. The transit time equivalent of the crystal was obtained by dividing its thickness (0.89mm) by the speed of longitudinal waves in the material (3587m/s). With this information, the boundaries of the crystal (in units of time delay) can be marked in Figure 5.11. In Section 4.8, it was shown that the distribution of the AE sources in the plane perpendicular to the polar axis is uniform: however Figure 5.11 shows that the distribution along the polar axis is not uniform, the majority of the AE sources being located near to the sample surfaces. Since domain nucleation also generally occurs at surfaces, this supports the view that the two are related.

These experiments were repeated for Rochelle salt and GMO samples, with broadly similar results. The number of Barkhausen pulses produced while switching a GMO sample is plotted as a function of the applied field in Figure 5.12a. While only a few Barkhausen pulses are detected below 10kV/cm (this may again be

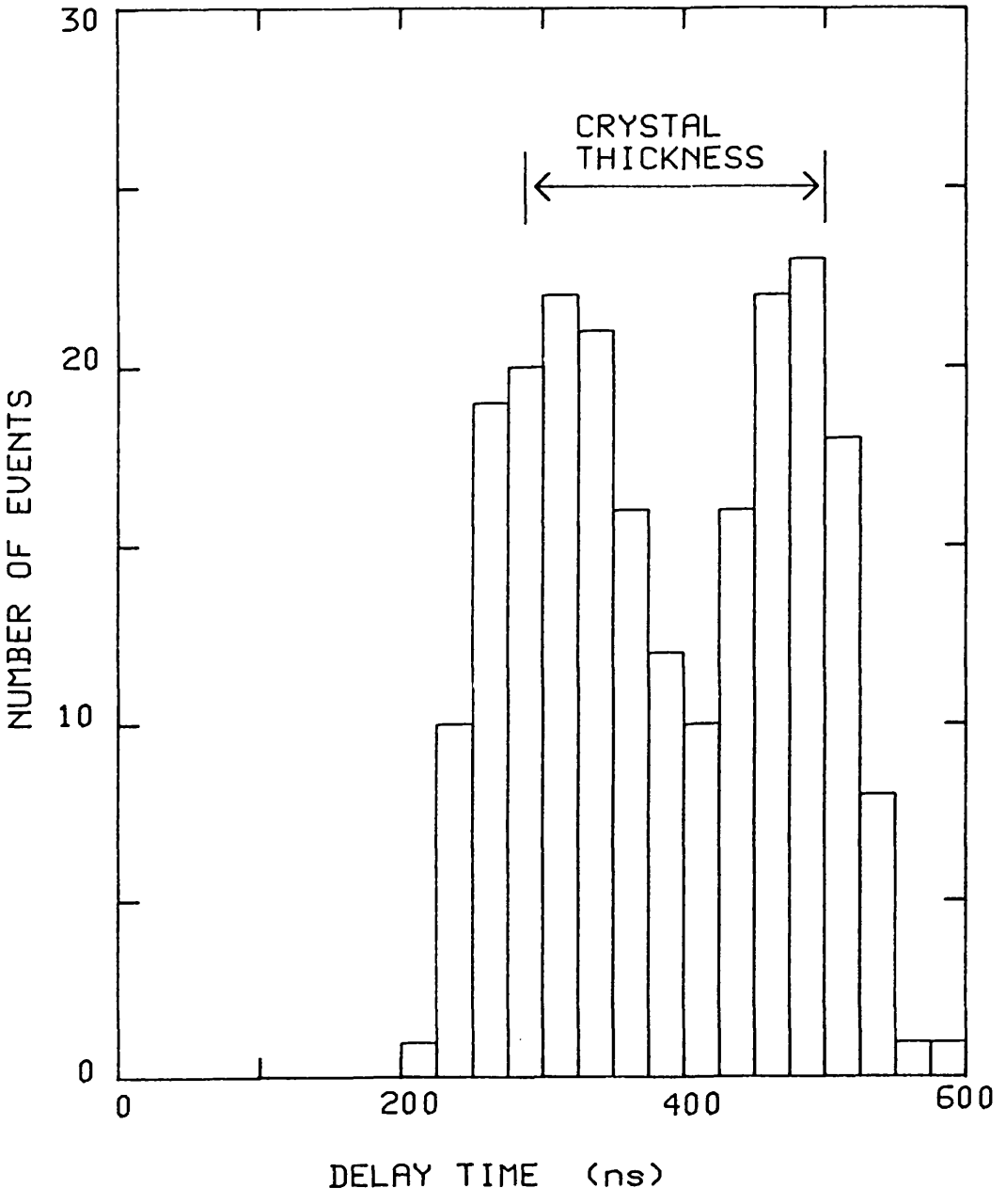

FIGURE 5.11 - Histogram showing the time delay between the Barkhausen pulses and the subsequent AE bursts, for a lead germanate crystal 0.89mm thick. Assuming the two events to occur simultaneously, this can be interpreted as the spatial distribution of the AE sources along the polar axis, showing that these are concentrated near the crystal surfaces.

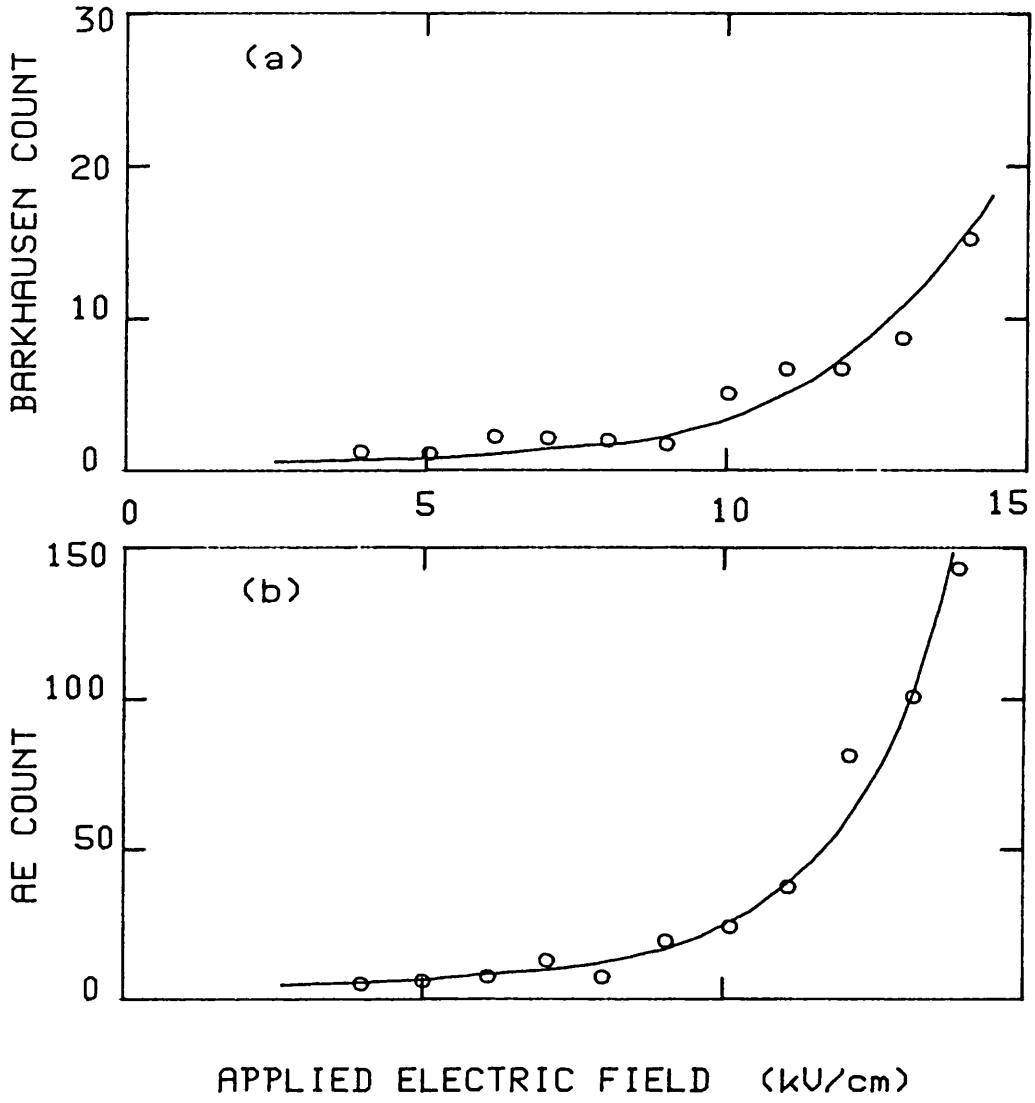

FIGURE 5.12(a) - Number of Barkhausen pulses per polarisation reversal as a function of the applied electric field for a gadolinium molybdate sample 0.94mm thick. The AE ringdown count was monitored simultaneously and is shown in (b).

attributed to counting the charging pulse or to electrical interference), the count increases dramatically at higher fields where the nucleation of additional domains is seen to occur. The AE count per polarisation reversal was also measured at the same time and is shown in Figure 5.12b (this is essentially identical to Figure 5.7b). The AE count also increases rapidly at fields above 10kV/cm. Chynoweth (1958) deduced that the Barkhausen effect in barium titanate is caused by the nucleation of domains: this has actually been observed here in GMO, and will be discussed next. The close correlation between the Barkhausen effect and the AE produced during polarisation reversal lends more weight to the argument that the AE can also be attributed to this cause.

5.4 Visual Observation of Domain Wall Motion.

The results described so far, particularly the correlation between the AE produced during polarisation reversal and the Barkhausen effect, indicate that the production of AE is closely related to the movement of domain walls within the crystal. Therefore it is useful to study how the domain pattern changes during polarisation reversal. Domains in all four ferroelectric materials studied are visible when viewed between crossed polarisers (Section 2.6). Of these materials, GMO and TMO proved to be the most suitable for an optical study of the dynamic behaviour of domain walls. These materials are transparent and can be readily polished to an optical finish. Furthermore, as they are ferroelastic the domain walls can be moved by applying a stress to the crystal surfaces, finger pressure being sufficient to switch the crystal. With practice, it was found possible to set up a desired initial domain configuration by squeezing the sample between two glass slides. Samples of these materials can be switched by the motion of a single domain wall traversing the crystal, which helps to keep

things simple.

To observe domain wall motion in these materials, the samples were coated with thin, transparent aluminium electrodes by vacuum deposition. Fine copper wires were connected to these electrodes by small drops of silver dag. The other ends of these wires were then connected to the usual switching circuit. The electrodes were liable to damage by scratching, and so were given a protective coat of transparent lacquer. The sample was placed between crossed polaroids on an optical bench, along with a collimated light source and a single-lens reflex camera which was used both for direct viewing of the domains and for taking still photographs. By mounting a cine camera on the optical bench, a cine film of the moving domain walls was taken. This film has been used with great success in seminars and conferences, and provides a graphic illustration of domain wall nucleation, sideways motion and annihilation, to far better effect than a sequence of still photographs like those given here.

As the sample was viewed down the polar axis (and hence perpendicular to the large faces of the plate), it was not possible to mount it on an AE transducer in the conventional manner. Instead, a transducer was placed in contact with one edge of the plate: this was found to give a low but detectable count rate when the crystal polarisation was switched. To correlate any AE produced with the visual observations, the audible output of the AE counter was used (Section 3.5).

For a crystal with a single domain wall, the application of an electric field of about 2kV/cm caused switching by the slow movement of this domain wall from one end of the electrode to the other. A sequence of photographs showing this is shown in Figure 5.13. In the first and last photographs of this sequence, the domain wall is lost in the glare near the edges of the crystal. Although about 2kV/cm was required to start the domain wall moving, this motion could then be sustained with fields down to 1kV/cm. At these low fields, the velocity of the

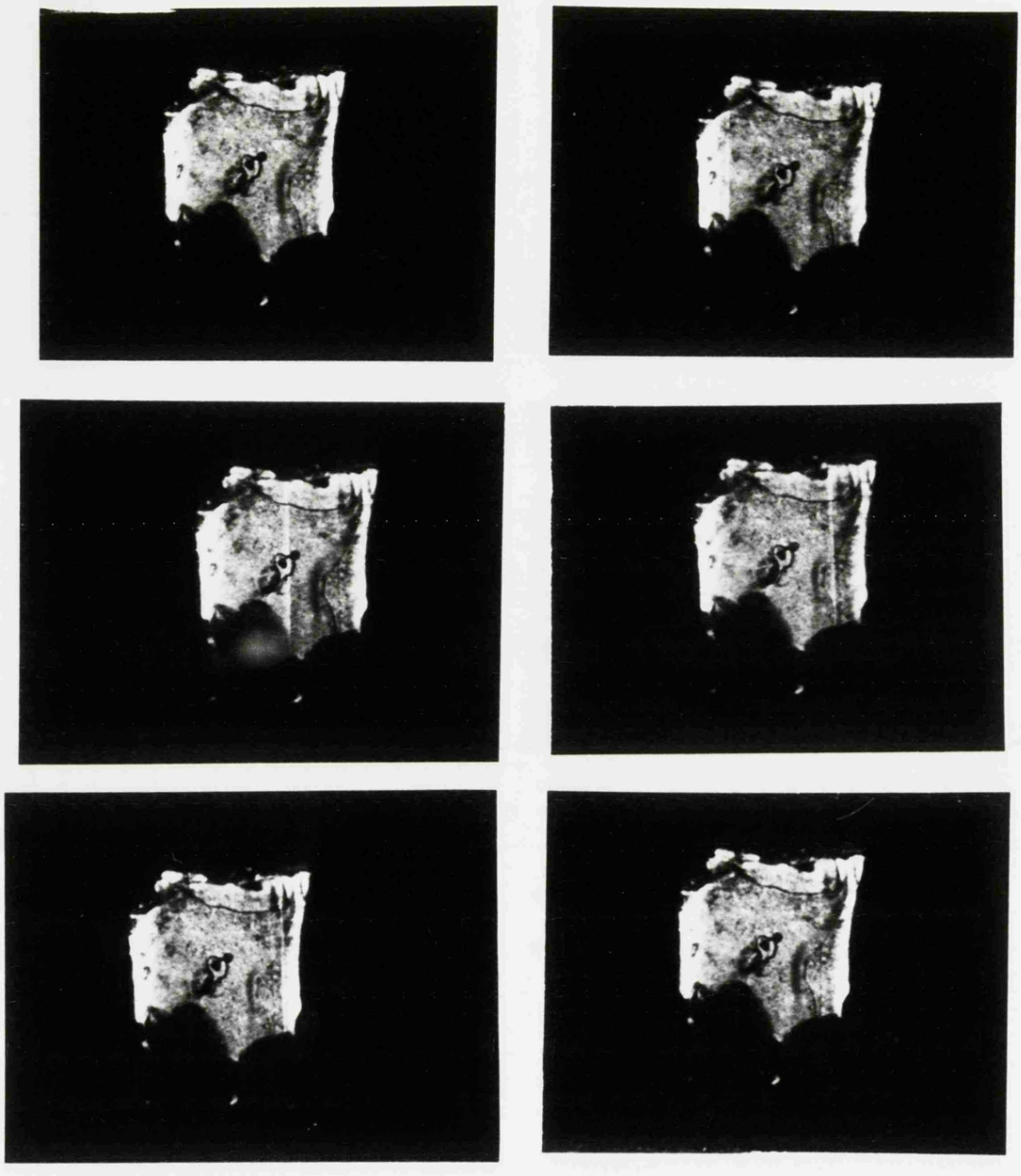

FIGURE 5.13 - Switching of a gadolinium molybdate crystal by the nucleation and subsequent sideways motion (from left to right) of a single domain wall, which appears as a bright vertical line. The dark areas at the bottom of the crystal are where the leads are connected to the electrodes with silver dag. The other marks on the crystal surface are irregularities in the protective lacquer coat applied over the electrodes.

domain wall could be estimated by timing it (using a stopwatch) over a measured distance between two marks on the crystal surface. These measurements gave results which agreed with those obtained from the switching pulse (Section 5.2, Figure 5.7). Although a small Barkhausen pulse was detected when the domain wall started to move, no further pulses were observed throughout the rest of the switching process. Small bursts of AE were sometimes found associated with these current spikes, but these bursts were barely above the threshold of detectability. At higher fields events occurred more rapidly and direct observation became impossible: however, switching was found to occur by the motion of this single domain wall for fields of up to 10kV/cm, above which the presence of additional domain walls at or near the electrode edges was observed after switching had taken place: since the switching process takes only a few milliseconds at these fields, the nucleation of these walls could not be observed directly. This high-field region was also distinguished by the production of large Barkhausen and AE impulses similar to those described previously.

Although these observations indicate that the AE and the Barkhausen pulses are caused by the nucleation of additional domains, this could not be confirmed since events happen too rapidly to observe the nucleation process proper. However, it was found possible to induce nucleation at far lower fields by introducing a suitable defect, such as a scratch near one end of the electrode. With a crystal prepared in this way, it was found that the nucleation of a domain at this defect was always accompanied by a Barkhausen pulse and a burst of AE. The size of the Barkhausen pulse (ie the volume of the domain nucleus) was found to be entirely repeatable and similar to those produced by switching at 10kV/cm. The subsequent motion of this "new" domain wall was again found to be "silent" in that no AE or Barkhausen pulses were produced.

A particularly interesting sequence of events is shown in Figure 5.14. As the voltage across the crystal is increased slowly, switching initially occurs by the motion of a

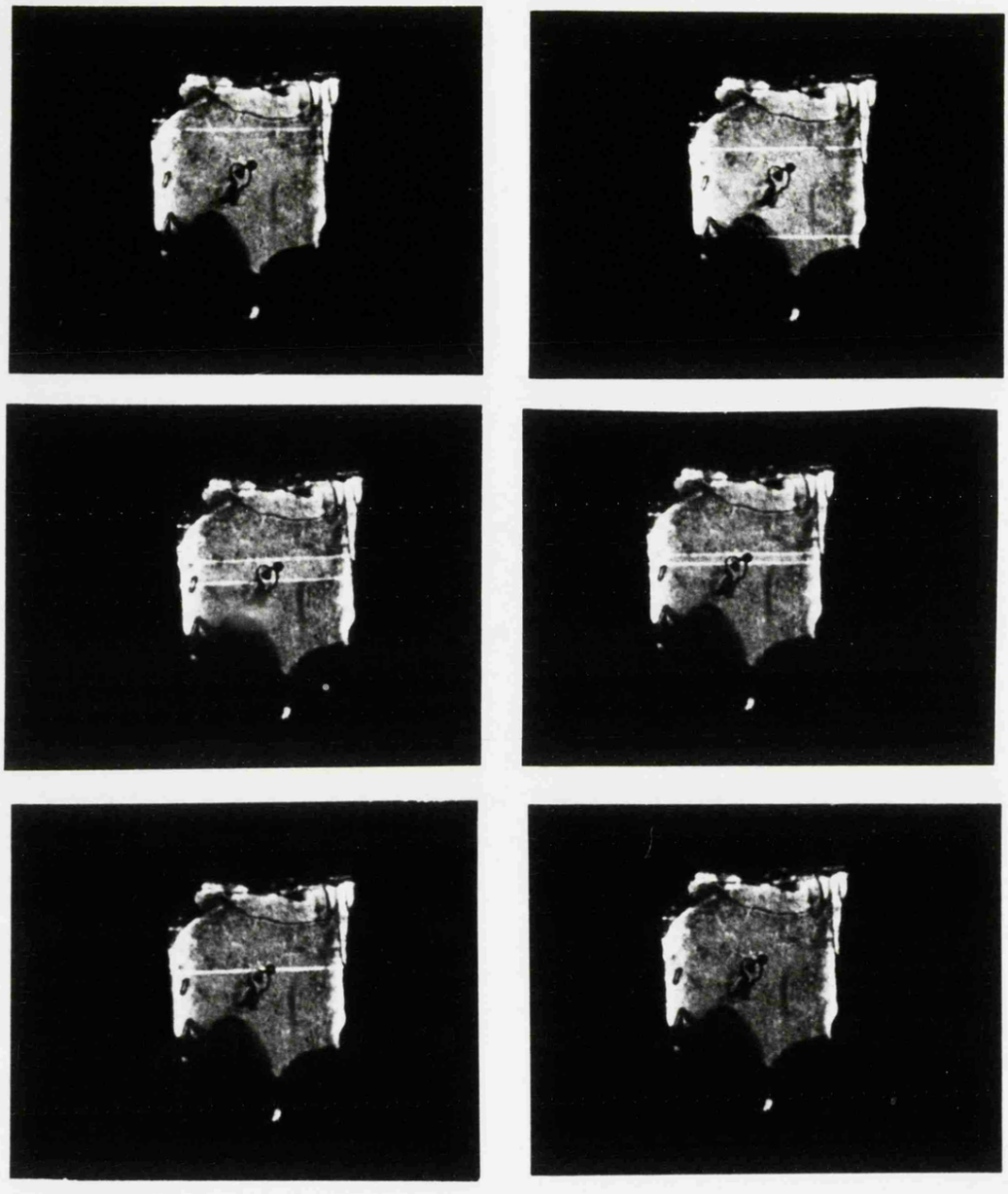

FIGURE 5.14 - Switching of a gadolinium molybdate crystal by the nucleation, sideways motion and final annihilation of two domain walls, which here appear as bright horizontal lines moving in a vertical direction.

pre-existing domain wall (which moves downwards in Figure 4.15). On further increasing the voltage, a second domain wall is nucleated at the scratch near the bottom of the crystal, accompanied by a Barkhausen pulse and a burst of AE. The two walls then move towards one another: this motion is "silent". As the two walls approach, they appear to repel one another, coming to a halt a small distance apart - this distance could not be measured at the low magnification used, and the two domain walls appeared to merge into a single, thick wall. After a short delay (which at low fields could be two or three seconds) the two walls suddenly vanish, again to the accompaniment of a burst of AE and a Barkhausen pulse. These observations show that, at least in GMO and TMO, AE is produced by the nucleation and annihilation of domain walls, while the sideways motion of these walls is "silent". While these experiments were also carried out on Rochelle salt and lead germanate samples, it was not possible to make such conclusive observations with these materials, because of the complicated domain structure and the large number of domains involved in each polarisation reversal.

As the above experiments were carried out with an essentially constant voltage across the sample, it is difficult to relate these results to what is happening when the ferroelectric is cycled at 50Hz, which is how most of the measurements described in Chapter 4 were made. The motion of domains when switching at this frequency can be observed in the same way as described above by illuminating the sample by a stroboscope synchronised to the driving electric field. The delayed pulse generator described in Section 3.7 was used to trigger the stroboscope: by varying the delay, the domain configuration at any point in the hysteresis cycle could be viewed. In all four materials, it was found that switching below the threshold field for AE was produced by the expansion and contraction of domains already present in the crystal, while above the threshold field the nucleation of new domains and the coalescence of domains to form large switched areas could be observed. This could be seen most clearly in lead germanate, and photographs of a sample coated with transparent tin oxide electrodes (kindly provided by Dr.

G.R. Jones of R.S.R.E. Malvern) are shown in Figure 5.15. The threshold field for this sample was found to be 4.8kV/cm. As the domains in lead germanate are small in size, these photographs were taken through a polarising microscope (a scale is provided in the diagram). The unswitched area at the upper left corner of each photograph (dark in sequence (a) but light in sequence (b) because the polarisers were adjusted between runs) is beyond the edge of the electrode. The first set of photographs (a) were taken at 4.2kV/cm: although switching occurs, some areas of the crystal are left unswitched and the same domains appear in all three photographs, even at saturation, albeit with different sizes. At an electric field of 5.5kV/cm, switching is almost complete and the creation of new domains in the photographs in sequence (b) is evident. Therefore the production of AE can be associated with the nucleation of new domains even when the crystal is switched by a 50Hz sinusoidal electric field.

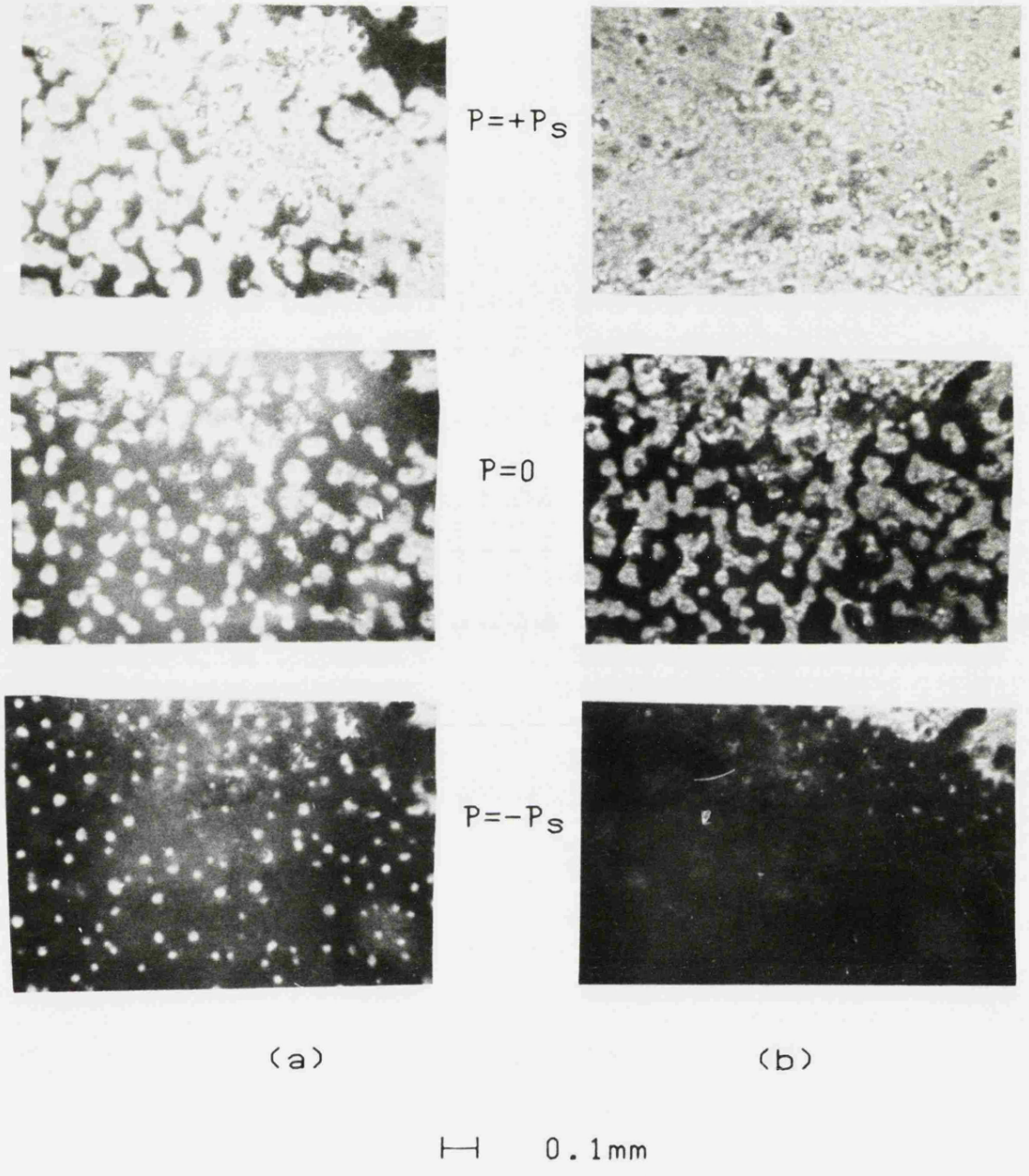

FIGURE 5.15 - Domain patterns in a lead germanate sample during switching at 50Hz. From top to bottom, the photographs were taken at peak positive voltage (positive saturation), at the coercive field, and at negative saturation. The peak applied field was 4.2kV/cm for set (a) and 5.5kV/cm for set (b), respectively below and above the threshold field for AE (4.8kV/cm).

CHAPTER 6 - DISCUSSION OF RESULTS.

In this final chapter, the experimental results described previously are reviewed in terms of domain wall motion as the source of the AE produced during polarisation reversal in ferroelectrics. A mechanism by which the ultrasonic stress waves may actually be produced is also discussed.

6.1 - Acoustic Emission and Domain Wall Motion.

Measurements of the AE produced when a ferroelectric crystal is cycled at 50Hz (as described in Chapter 4) clearly indicate that the source of the AE is closely connected with the process of polarisation reversal and therefore with domain wall motion. No AE was detected outside the ferroelectric region, where no switching can occur, and even when the material is ferroelectric it becomes more difficult to produce AE (ie the threshold field increases) as the Curie temperature is approached. Although the four materials investigated differ considerably in their microscopic properties, their behaviour as far as the production of AE is concerned is remarkably similar. Like the formation of a hysteresis loop and the Barkhausen effect, the production of AE during polarisation reversal must be associated with some macroscopic event (such as the motion of domain walls) rather than any individual characteristic of the material. However, the timing of the AE within the loop (Section 4.4) shows that the AE cannot be simply linked with domain wall motion, since the AE occurs near the ends of the hysteresis loop after the bulk of the crystal polarisation has been switched. Also, the materials studied exhibit a threshold field below which no AE is produced, even though switching still occurs. Therefore it is necessary to postulate two mechanisms for polarisation reversal, a 'silent' process through which most of the switching occurs

and an AE-generating process which is invoked at higher fields. The production of AE is closely related to the Barkhausen effect: not only is there a one-to-one correlation in number (Section 5.3) but the AE must be produced simultaneously with the electrical transient, otherwise the peaks in the histogram of Figure 5.11 would not agree so well with the computed extremities of the crystal. Furthermore, the AE event count shown in Figure 4.16 tends towards a fixed number of events at high field in the same way as the number of Barkhausen pulses produced per polarisation reversal (Figure 5.9): this latter observation is generally attributed to the existence of a limited number of sites where domain nucleation can occur. Together with the visual observation of domain wall motion during polarisation reversal (Section 5.4), these observations indicate that the two processes are respectively the sideways motion of domain walls and the nucleation and annihilation of domains.

On this basis, it is possible to explain, at least qualitatively, the features of the AE discussed in Chapter 4. Below the threshold field for AE, switching can occur through the sideways motion of domain walls already present in the crystal, which is only partially switched. Above the threshold field switching is more complete and nucleation and coalescence of domains occurs, which gives rise to the AE. The sequence of oscillographs in Figure 4.2 shows that although switching occurs below the threshold field, the saturation polarisation keeps increasing (ie the loop is not yet fully saturated) until the threshold field is reached. Figure 4.35 also shows this behaviour for the coercive field, which reaches its final, limiting value at the threshold field for AE. Therefore the threshold field represents a demarcation between partial and complete switching of the crystal at a given frequency of the applied field.

The temperature dependence of the threshold and coercive fields can also be explained on this basis. The threshold field represents the point at which nucleation becomes a favourable

mechanism for polarisation reversal in addition to sideways motion. The coercive field represents the voltage at which switching (by whatever mechanism) occurs: since the bulk of the switching occurs by sideways motion it gives a threshold for this kind of domain wall motion, and therefore decreases as the domain wall mobility increases near the Curie temperature. On the other hand, this increase in mobility means that the sideways motion can account for a greater proportion of the polarisation reversed during switching: therefore a higher voltage must be applied before the nucleation of domains becomes necessary to complete the switching process. The similarity in shape between the curves of the temperature dependences of the threshold field obtained here and the domain wall mobility published in the literature has been pointed out in Section 4.10: in all cases a high threshold field (ie low AE activity) is associated with a large domain wall mobility.

Figure 4.1 shows that the AE is only produced near the extremities of the hysteresis loop, after the bulk of the switching has taken place. This indicates that the AE-generating process is only invoked when the sideways motion of domains cannot switch a sufficient portion of the crystal polarisation. At a given frequency the threshold field defines where this happens: as the frequency is increased, the threshold field drops because switching has to occur in a shorter time and so the faster nucleation process is invoked at a lower voltage.

If the threshold field is to be attributed to the nucleation of domains competing with the sideways motion of domain walls as a mechanism for polarisation reversal, it is clear that the value of the threshold field will depend on a number of factors such as the number of nucleation sites, their spatial distribution (which influences the interaction and coalescence of domain walls) and the number and distribution of any defects which may impede the motion of the domain walls. In practical terms this means the purity and perfection of a crystal, its surface finish and its past history (since the stresses associated with repeated cycling may also introduce defects into the crystal).

All of these factors have been found to influence the switching behaviour of a ferroelectric sample and the AE it produces, and may account for the difficulty of obtaining reproducible results. They also make the modelling of the switching process extremely difficult, and most such calculations ignore them. While early attempts to model the switching current ignored the interaction between adjacent domain walls (eg Chynoweth 1958), this interaction can be estimated statistically by assuming a uniform random distribution for the nucleation centres (Avrami 1939, Dalton et al 1971). However, these calculations assume initial, rapid nucleation and concentrate on the subsequent sideways expansion of the domains. Therefore they do not relate to the situation actually observed here, where most of the switching is carried out by the expansion of domains already present in the crystal with nucleation and annihilation (and therefore the production of AE) only occurring towards the end of the cycle.

6.2 The Source of AE in Ferroelectrics.

Now that the source of the AE produced during polarisation reversal has been associated with the nucleation and collapse of domains within the material, it is possible to make some comments about how the stress waves may actually be generated. The papers in the literature dealing with AE sources can be divided into two classes: some give a quantitative mathematical treatment assuming some idealised source (such as the point force step of Pao et al (1979)) which unfortunately bears little relation to real results, while others give more descriptive (but somewhat less informative) statements of the type 'as the dislocation moves away from one minimum-energy position the elastic lattice strain increases until the "over-centre" position is reached: the increment of elastic strain is then suddenly released to produce a vibrational wave in the lattice'.

However, the vast majority of these publications refer to crack growth and dislocation motion, and their arguments are not directly applicable to the case of the AE produced by ferroelectric crystals.

AE has been observed during stress-induced twinning in a number of materials, including single-crystal indium (Van Doren et al 1976) and zinc (Toronchuk 1977). Recalling that ferroelectric domains may also be regarded as crystallographic twins, it is likely that the AE in these cases is due to a similar cause. Since twins differ in the orientation of crystal planes, the creation of a twinned region demands the movement of atoms: this displacement should give rise to an acoustic wave in the crystal lattice. The geometry is particularly simple in the case of gadolinium molybdate (Section 2.6c, Figure 2.5). In this material, the a- and b- axes of the unit cell differ in length by some 0.3%, or 3 picometres. On polarisation reversal, the a- and b- axes are interchanged, so viewed from an outside frame of reference this unit cell elongates by 3 picometres in one direction and contracts by an equal amount in a perpendicular direction. The area under the Barkhausen pulses in GMO gives the area of the domain nucleus as about 5×10^{-4} mm : assuming a cylindrical shape for the domain nucleus its radius would be of the order of 10μm, or about 10^4 lattice spacings. Thus the formation of such a nucleus would involve a displacement of several nanometres at its boundary. Since the formation of the nucleus is rapid - the rise-time of the Barkhausen pulses places this at some tens of nanoseconds - this source approximates to an ideal displacement step along the lines considered by Pao et al (1979).

Although the formation of a domain nucleus has been considered as the AE source in the above discussion, this nucleus is unstable because of the large depolarising energy associated with it and rapidly expands through the thickness of the crystal. The rate of this forward growth cannot be measured from the switching current since no external charge flow is associated with it. This process can be considered as a

continuation of the initial nucleation, and is likely to produce stress waves in the same way. In fact, the large number of atoms involved in a displacement step travelling through the crystal makes it a more plausible source for a detectable level of AE than a small nucleus only a few unit cells thick. Furthermore, the velocity of this forward growth is likely to depend on the magnitude of the applied electric field, and may therefore account for the observed increase in the amplitude of the AE produced with high applied fields (Sections 4.3, 4.6). The increase in the size of the Barkhausen pulses at high fields (Section 5.3) means that the domain nucleus is also larger, but this increase is not as dramatic as the observed increase in AE amplitude. Although this discussion has so far concentrated on domain nucleation, it should be pointed out that the annihilation of a domain (also observed to be a source of AE) is a similar process, involving the rapid change of orientation of a small volume of crystal.

If the source of AE in ferroelectrics lies in the change in strain resulting from polarisation reversal, the question arises of why the sideways expansion of domains, which is responsible for switching large volumes of material, does not produce any detectable AE. The emphasis here should perhaps be on the word 'detectable', as the two processes have different time-scales. The nucleation of a 10μm-wide domain in 50ns is equivalent to a sideways velocity of 200m/s, while the limiting domain wall velocity observed in GMO is only about 2m/s (Section 5.4). Therefore even if the processes are microscopically identical, the rate of energy release will be quite different, being much lower in the case of sideways motion. Another important difference lies in the fact that according to the Miller-Weinreich model the sideways motion occurs by preferential nucleation on an existing domain wall: this wall is a region of intermediate structure between the two opposed domains and therefore the strains involved are likely to be much lower than in the case of the nucleation of a new domain.

The stress waves emitted by such a source potentially carry

much information that can be used to determine the nature of the source. However, the AE arriving at the surface of the transducer is dominated by the mechanical resonances of the sample (Section 4.2), and much of this information is lost. To be able to excite these resonances the source event must have a short duration relative to the period of the resonant frequency: this is amply satisfied by the initial nucleation of a domain and can also be satisfied for the forward growth if this occurs at a velocity close to the speed of sound in the crystal. Pao et al (1979) have shown that even simple, ideal sources in plate-shaped solids can give rise to complicated waveshapes at the surface of the plate because of the different transit paths the disturbance can take. The waveform is further distorted by the limited response of the transducer and associated electronics. While it is possible to account for the transfer function of the measuring system by deconvolution (Sachse and Ceranoglu 1979), this is really only practical in the case of transducers with a simple transfer function, such as capacitance transducers (Scruby et al 1978). The wide bandwith of these systems also makes it possible to resolve details in the time domain which can help in characterising the AE source. It is likely that further work with such a system will clarify the nature of the source of AE in ferroelectrics, and may confirm some of the speculations made above.

6.3 Conclusion.

The AE produced during polarisation reversal in a number of ferroelectric materials has been investigated as a function of sample size and temperature and of the magnitude and frequency of the applied electric field. A one-to-one correspondence has been established between these acoustic impulses and the electrical Barkhausen pulses also produced during polarisation reversal. The hypothesis that the nucleation and collapse of domains are responsible for the AE is supported by this

correlation, and has been confirmed by the visual observation of the domains during switching while simultaneously monitoring the AE produced. The sideways movement of domain walls, which accounts for the bulk of the polarisation reversed during switching, does not produce any detectable AE. On this basis, the major features of the AE produced during polarisation reversal, such as the existence of a threshold electric field below which no AE is produced and the rapid increase of this threshold field as the Curie temperature of the material is approached, have been qualitatively explained. The way in which the nucleation and annihilation of domains may couple ultrasonic energy to the lattice has also been discussed. Acoustic emission provides a powerful technique, complementary to the conventional electrical and optical methods, of investigating the process of polarisation reversal in ferroelectrics.

APPENDIX A

The Hewlett-Packard 9825A Programmable Calculator and 98032A 16-bit Parallel Interface.

A Hewlett-Packard 9825A microcomputer was extensively used to collect and analyse the AE data discussed in this thesis. While the analysis of the results was fairly straightforward and was mainly carried out using the excellent suite of library programs available for this machine, in order to collect the data the calculator had to be interfaced to a variety of instruments, most of which were not designed for computer control. The interfacing of the 9825A to an AE monitoring system and a transient recorder is described in Appendices B and C: however it is proper to start with a brief description of the calculator and its interfaces. For a more detailed description refer to the Users' Manuals for these units.

The HP 9825A Programmable Calculator is a desktop computer with 16 kilobytes of memory which is capable of being programmed in a high-level language. This language, which is proprietary to Hewlett-Packard, is known as HPL and bears certain similarities to the BASIC language supported by the large number of microcomputers which abound today. One obvious difference from BASIC is that in HPL the destination variable in an assignment statement appears to the right of the expression whose value is to be assigned to it. The assignment operator (right arrow) appears as '}' in the listings given here. The basic language can be enhanced by the addition of plug-in ROM packs which add extra commands to the repertoire of the machine. The system used included the Advanced Programming, String Programming, General I/O and Extended I/O ROMs. Most of the additional features provided by these ROMs are used in the programs described here.

The 9825A has a number of built-in peripheral devices, such as a 32-character LED display, a magnetic tape drive for program

and data storage and a 16-column thermal printer. For external interfacing, there are three sockets at the rear of the unit. These sockets carry the internal bus of the calculator, and an additional interface unit is required to transform these signals into a more suitable form. For interfacing to dedicated computer peripherals such as printers and plotters, the 98034A interface provides full HP-IB (IEEE 488) capability. However, the versatility (and therefore complexity) of this interface makes it difficult to use in non-standard applications. Therefore a 98032A 16-bit parallel interface was used in the applications described here.

The 98032A interface provides 16 input lines (DI0-DI15), 16 output lines (DO0-DO15) and a number of miscellaneous control lines, most of which can be directly controlled by the calculator in HPL. The 32 input-output (I/O) lines can be considered either collectively to handle 8- or 16-bit words of data, or separately to provide on/off control of relays, for example. The other I/O lines available from the interface are used to provide control functions such as handshaking (I/O, PCTL, PFLG), reset (PRST) and indication of peripheral status (PSTS). Additionally, four uncommitted control and status lines (CTL0, CTL1, STS0, STS1), which can be directly controlled by the computer, are provided for user-defined functions.

The 98032A comes with an unterminated 48-way cable. This was terminated in a 50-way plug (Mc-Murdo 'D' series). The pin connections on this plug are given in Table A-1. The interface is also provided with 15 internal jumper links which can be set to provide the required functions on the I/O, control and status lines. The setting of these jumpers is given in Table A-2. The setting of the handshake control jumpers was chosen so that the interface could function without handshaking by connecting the PCTL and PFLG lines together.

Programming I/O through the 98032A interface is quite simple in HPL. The interface is assigned select code 2 by means of an internal switch. The 16 output lines can be set to any state by

Pin	Description	Pin	Description
1	DO 15	26	I/O
2	DO 14	27	PSTS
3	DO 13	28	GND
4	DO 12	29	GND
5	DO 11	30	GND
6	DO 10	31	GND
7	DO 9	32	GND
8	DO 8	33	GND
9	DO 7	34	DI 15
10	DO 6	35	DI 14
11	DO 5	36	DI 13
12	DO 4	37	DI 12
13	DO 3	38	DI 11
14	DO 2	39	DI 10
15	DO 1	40	DI 9
16	DO 0	41	DI 8
17	GND	42	DI 7
18	STS 1	43	DI 6
19	STS 0	44	DI 5
20	CTL 1	45	DI 4
21	CTL 0	46	DI 3
22	EIR	47	DI 2
23	PRST	48	DI 1
24	PFLG	49	DI 0
25	PCTL	50	GND

TABLE A-1 - Pin connections for the HP 98032A interface cable terminated on a McMurdo D-50 plug. DO refers to data output, DI to data input. DO15 and DI15 are the most significant bits while DO0 and DI0 are the least significant.

Jumper Reference	Status	Function
1	In	Sets data input lines to positive true.
2	In	Sets data output lines to positive true.
3	In	Defines PCTL as active high.
4	Out	Defines PFLG as active high.
5	In	Defines PSTS as active low.
6	Out	Sets pulse handshake mode.
7	Out	Activates DMA mode.
8	Out	Clocks high input byte on PFLG leading edge.
9	In	Clocks high input byte on PFLG trailing edge.
A	Out	Clocks high input byte on calculator internal clock.
B	In	Selects word input mode
C	Out	Clocks low input byte on calculator internal clock.
D	In	Clocks low input byte on PFLG trailing edge.
E	Out	Clocks low input byte on PFLG leading edge.
F	In	Selects word output mode

TABLE A-2 - Description and settings of the internal configuration jumpers of the HP 98032A 16-bit parallel interface.

a statement of the form:

```
wtb 2 , X
```

where the number X contains the binary representation of the required combination of 1's and 0's. The state of the input lines can be read through the function rdb(2). The control and status lines can be accessed through a similar pair of keywords, wtc (write control) and rds (read status). The control/status word is such that bits 0 and 1 control (or return the status of) the lines CTL0 and CLT1 (or STS0 and STS1) respectively. Setting bit 5 of the control word pulses the PRST line to reset the peripheral device.

APPENDIX B
Interfacing the HP 9825A Programmable Calculator to the AECL 105 AE Processor.

The Acoustic Emission Consultants Ltd. Model 105 Stress Wave Processor is a typical AE monitoring device consisting of a variable gain amplifier, a variable filter and a counter unit. This instrument is described in some detail in Section 3.5. Although the outputs of the counter are available in binary-coded-digital (BCD) form on a connector at the rear of this unit, the only provision for remote control is in starting, stopping and resetting the counter. It was often required to measure the AE count rate at different settings of the amplifier gain, so it was desirable that this too should be under computer control. Although the amplifier gain can be selected from a bank of seven push-button switches on the front panel of the AECL 105, there was no provision for this to be remotely controlled.

The major modification made to the AE counter unit was to solder miniature reed relays directly across the front-panel switches which select the amplifier gain. This resulted in a slight increase in the noise level of the counter, reducing the maximum usable gain from over 90dB to about 84dB. The accuracy of the gain settings was unaffected by this modification: this was verified by comparison with a similar but unmodified instrument. The open-collector outputs of the 98032A interface are capable of driving the relays directly. Light-emitting diodes were installed on the front panel of the AECL105 to monitor the operation of the instrument. These indicators can be seen in the photograph of Figure 3.2a.

A 25-way socket (Mc-Murdo 'D' series) was installed on the rear panel of the AECL 105 and a cable made up to mate this to the 98032A interface. The connections on this socket, and the corresponding connections to the computer interface, are given in Table B-1. The three decades of BCD output from the counter

Pin Number	Function	9825A Connection
1	x100 Range Select	DO 0
2	x10 Range Select	DO 1
3	1dB Gain Select	DO 2
4	2dB Gain Select	DO 3
5	4dB Gain Select	DO 4
6	8dB Gain Select	DO 5
7	10dB Gain Select	DO 6
8	20dB Gain Select (1)	DO 7
9	20dB Gain select (2)	DO 8
10	Counter HOLD	CTL 0
11	Counter RESET	CTL 1
12	Counter Overflow	STS 0
13	GROUND (common)	GND
14	DO 11 (MSB)	DI 11
15	DO 10	DI 10
16	DO 9	DI 9
17	DO 8	DI 8
18	DO 7	DI 7
19	DO 6	DI 6
20	DO 5	DI 5
21	DO 4	DI 4
22	DO 3	DI 3
23	DO 2	DI 2
24	DO 1	DI 1
25	DO 0 (LSB)	DI 0

TABLE B-1 - Pin connections for the McMurdo 25-way socket on the rear of the modified AECL 105 Stress Wave Processor and the respective connections to the HP 98032A 16-bit parallel interface. In addition to the connections given above, PCTL and PFLG on the interface are connected together to enable auto-handshake and PSTS is connected to GND to indicate that the peripheral is active.

are connected directly to the computer inputs. Reference to Figure 3.6 shows that the AECL105 has a six-decade counter although only three decades are displayed and output at any time. The decades output can be selected via front-panel switches on the instrument. Computer output lines DO0 and DO1 were connected to these switches to enable remote control of this function also. Output lines DO2 to DO8 control the amplifier gain. These lines are active low, ie a "0" on the line is equivalent to depressing the appropriate front-panel push-button. Counter control (hold and reset) is provided over the auxiliary control lines CTL0 and CTL1, while STS0 provides indication of overflow. These lines are active high. For the remote functions to work as described, the relevant push-buttons on the AECL105 must be in the inoperative state (out).

The counter can be controlled through a set of three subroutines which are given in Listing B-1. These subroutines all use local variables (p-variables) whenever possible: the only global variables used are the system gain G, scale factor M and a general loop counter I. A flag (flg0) is set to indicate an error such as a parameter out of range or a counter overflow condition. The fundamental subroutine is called 'SET' and outputs the required binary code to the interface to set the gain and output scale. This subroutine must be called via a statement of the form:

```
cll 'SET' (G,M)
```

where G is the gain in dB (0-65) and M the scale factor as a power of ten (0-3). Note that in this context the gain refers to the setting on the main amplifier and does not include the fixed 40dB gain of the preamplifier. A short time delay is incorporated in the last line of this routine to avoid problems associated with contact bounce in the reed relays. The function 'READ' returns the six-figure decimal integer recorded in the counter: it does this by reading the BCD outputs with the scale factor set first at xl and then at xl000, converting these values to decimal and combining the two results. Finally, the

```
45: "*****************************************************":
46: "*                                                   *":
47: "* LISTING B-1                                       *":
48: "*                                                   *":
49: "* Driver subroutines for the                        *":
50: "* AECL 105 AE Processor interface                   *":
51: "*                                                   *":
52: "*****************************************************":
53: "* Subroutine SET (G,M)                              *":
54: "* p1 = Gain    p2 = Multiplier   flg0 = error flag *":
55: "* This routine sets the AECL 105 to the             *":
56: "* requested gain and scale settings.                *":
57: "*****************************************************":
58: "":
59: "SET":cfg 0
60: if p1<0 or p1>65 or p2<0 or p2>3;sfg 0;0}p1}p2
61: p1}p3;0}p4
62: if p3>=45;p3-20}p3;p4+256}p4
63: if p3>=20;p3-20}p3;p4+128}p4
64: if p3>=10;p3-10}p3;p4+64}p4
65: if p3>=8;p3-8}p3;p4+32}p4
66: if p3>=4;p3-4}p3;p4+16}p4
67: if p3>=2;p3-2}p3;p4+8}p4
68: if p3>=1;p4+4}p4
69: p2}p3;if p3>=2;p3-2}p3;p4+2}p4
70: if p3>=1;p4+1}p4
71: wtb 2,cmpp4;wait 50
72: ret
*3375
```

```
73: "Listing B1 continued":
74: "*****************************************************":
75: "* Function READ                                      *":
76: "* This routine reads the contents of the             *":
77: "* counter in the AECL 105                            *":
78: "*  G = Gain     M = Multiplier   flg0 = error flag *":
79: "* I is used as a loop counter                        *":
80: "*****************************************************":
81: "":
82: "READ":cfg 0
83: if bit(0,rds(2))=1;sfg 0;ret 999999
84: cll 'SET'(G,3);if flg0;ret 0
85: wait 100;rdb(2)}p1
86: cll 'SET'(G,3);wait 100;rdb(2)}p2
87: cll 'SET'(G,M)
88: ret 'BCD'(p1)+1000*'BCD'(p2)
89: "":
90: "This routine converts a 12-bit BCD number":
91: "to its decimal equivalent":
92: "BCD":0}p2;for I=0 to 3
93: tn^I*band(15,shf(p1,4*I))+p2}p2
94: next I;ret p2
95: "":
96: "":
97: "*****************************************************":
98: "* Subroutine COUNT                                  *":
99: "* This routine enables the counter for p1 seconds   *":
100: "*  G = Gain     M = Multiplier   flg0 = error flag *":
101: "* I is used as a loop counter                        *":
102: "*****************************************************":
103: "":
104: "reset":wtc 2,3
105: cll 'SET'(G,0)
106: "start":wtc 2,0
107: for I=1 to p1;wait 968;next I
108: "stop":wtc 2,1
109: ret
*847
```

subroutine 'COUNT' enables the counter for a given time. This subroutine is normally followed by a call to 'READ' to return the AE count over that interval.

The program used to collect and store on tape the AE data required to determine the threshold field in a ferroelectric sample is given in Listing B-2. The subroutines in Listing B-1 are not included in this listing and must be appended to the program if it is to run. As described in Section 4.6, the data required for a threshold field determination is a sequence of AE count rates as a function of the peak applied voltage, repeated for a number of amplifier gain settings. The sample voltage has to be set by the operator, but all the other adjustments and measurements are performed automatically. The program computes a running mean from the measured count rates and displays this along with the standard deviation. As described in Section 3.10, if the standard deviation exceeds 20% of the mean the measurement is regarded as unreliable and the operator is given the option of retaking the measurement or ignoring it. At the end of each measurement, the results are printed out to provide a permanent record of the experiment. At the end of the run, the results are collected in the matrix A and saved on magnetic tape. Each row of the matrix contains measurements made at the same gain while each column contains measurements made at the same voltage. The first row and column of the array (A(0,X) and A(X,0)) are used to record the voltage and gain respectively referring to the particular column or row of data. The otherwise unused array element A(0,0) is used to hold an identification code code, derived from the date on which the experiment was performed, for the data set.

```
10: "*****************************************************":
11: "* LISTING B-2                                       *":
12: "* Threshold field determination - data acquisition *":
13: "* Note that the subroutines in Listing B-1          *":
14: "* must be appended to this program                  *":
15: "*****************************************************":
16: "":
17: fmt 1,f4.0,2x,fz6.0,2x,f2.0;fxd 0;dim A[0:15,0:15]
18: ent "ID number?",A[0,0];prt "ID=",A[0,0];spc 2
19: ent "Number of runs?",N;if N<0;jmp 0
20: ent "Time per run?",T;if T<0;jmp 0
21: ent "Number of Voltages?",r1;if r1<1 or r1>15;jmp 0
22: ent "Number of Gain Settings?",r2;if r2<1 or r2>15;jmp 0
23: for W=1 to r2
24: dsp "Gain setting #",W," (dB)?";ent "",G
25: int(G-40)}G}A[W,0];cll 'SET'(G,0);if flg0;gto -1
26: prt "GAIN=",G;prt "****************"
27: prt "Volts  Count SD%";for V=1 to r1;if V>1;gto +3
28: dsp "Voltage #",V," ?";ent "",A[0,V]
29: dsp "press CONTINUE when ready";gto +2
30: dsp "Set Voltage to",A[0,V]," (#",V,")"
31: stp
32: "rep":0}A}B;dsp "N=0";for P=1 to N
33: cll 'SET'(G,0);cll 'RUN'(T);'READ'}C
34: if flg0;C}A[W,V];100}F;2*N}P;gto +2
35: A+C}A;B+C*C}B;A/P}E;√((P*B-A*A)/(P*P*P))}F
36: dsp "N=",P,char(12)&"=",E,char(9)&"=",F;wait 500
37: next P;E}A[W,V];100*F/E}F
38: wrt 16.1,A[0,V],E,F;if F<=20;gto +2
39: ent "ERROR:  1-Abort,2-Repeat,3-Cont",H
40: gto "end";if H>1;gto "rep";if H>2;gto +1
41: next V;prt "****************";spc 2;next W
42: spc 3;ent "RUN FINISHED - FILE NO?",F;ent "track",T
43: trk T;rcf F,A[*];dsp "READY"
44: "end":end
*2182
```

APPENDIX C

Interfacing the HP 9825A Programmable Calculator to the Datalab DL920 Transient Recorder.

The DL 920 transient recorder is equipped with an 8-bit parallel interface which enables it to communicate with the DL Micro4 signal processing unit described in Section 3.6. The timing diagram in the DL920 User Manual indicated that only a small amount of logic is necessary to enable the HP microcomputer to access the transient recorder memory, either by listening in on data transfers between the DL920 and the DL Micro4 or by supplying the necessary signals to the transient recorder. The interface was also designed with the capability to output data from the HP to the DL Micro4, though this facility did not prove particularly useful.

A schematic diagram of the interface is shown in Figure C-1. As the HP has separate input and output lines, a multiplexer is required to channel data from the required output to the paralleled inputs. The remainder of the circuitry is accociated with the handshaking of the three units. The interface requires +5V at 50mA which is obtained from the transient recorder via an unused pin in the rear panel connector. Three switches are used to set the mode of operation of the interface. One switch (S1) determines whether the HP computer takes any part in the data transfer: another (S2) performs the same function for the DL Micro4. The third switch (S3) determines which unit arms the transient recorder to prepare it to capture another signal. The three modes of operation provided by these switches are summarised in Table C-1.

In all modes, the computer can trigger the transient recorder via a pulse on the CTL1 line and has access to its status on STS0. STS0 is high (logic 1) when the transient recorder is busy (armed and awaiting a trigger pulse). The transient recorder should be in the single-shot mode if the interface is to function correctly. In Modes 2 and 3, the HP can control the

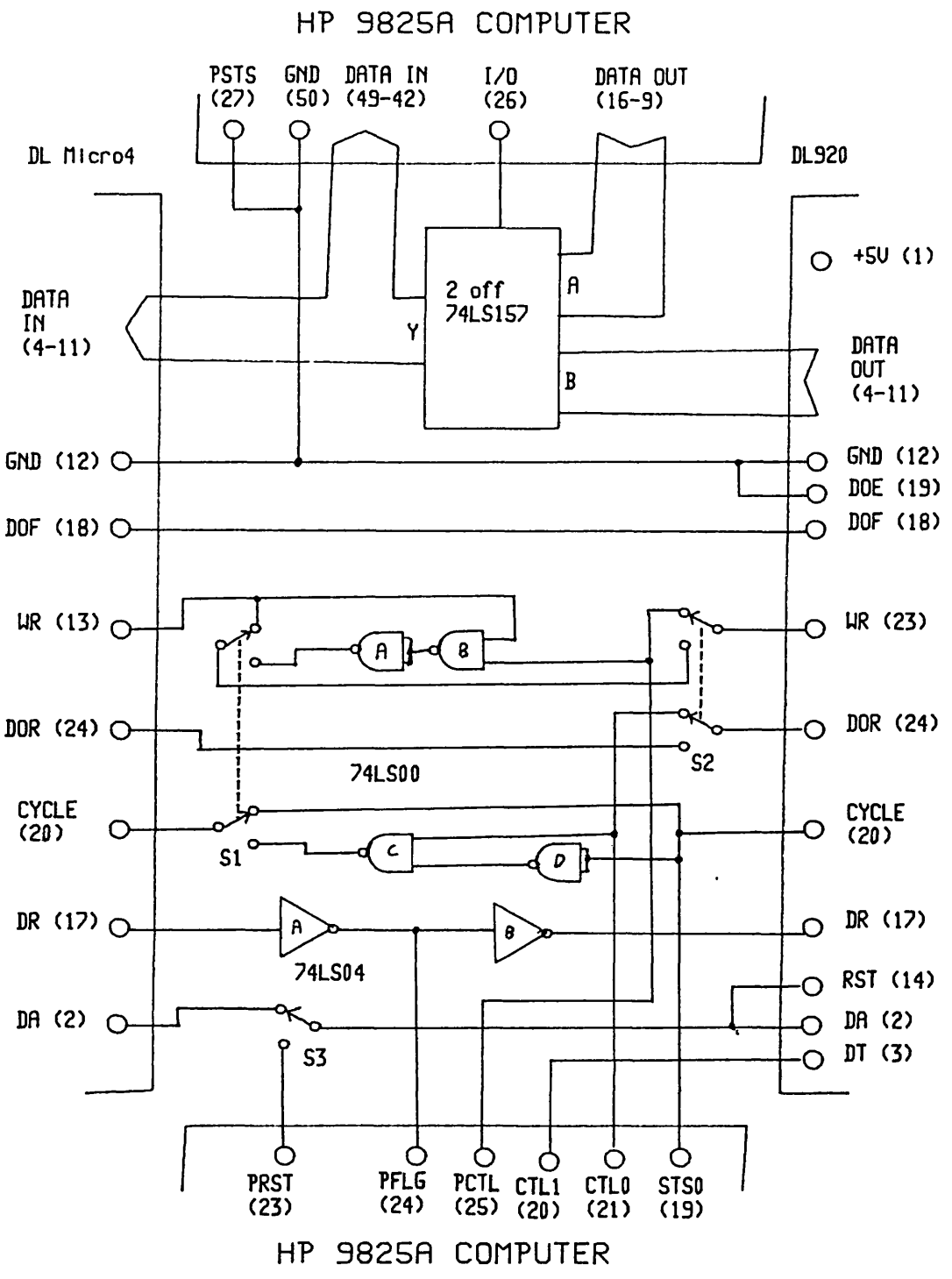

FIGURE C-1 - Circuit diagram of the interface between the HP 9825A computer, the DL920 transient recorder and the DL Micro4 signal processing unit. The three switches S1, S2 and S3 which set the mode of operation are shown in the inactive (UP) position.

Mode	Switch Settings	Function
1	S1 - up S2 - down S3 - up	In this mode, the HP computer is locked out and the DL920 and DL Micro4 units function normally.
2	S1 - down S2 - up S3 - down	In this mode the DL Micro4 is locked out and the HP 9825 supplies all the signals to the transient recorder. The DL920 can be armed via a PRST pulse and a data transfer initiated by a high-to-low transition on CTL0.
3	S1 - down S2 - down S3 - down	In this mode all three units function interactively. The DL920 must still be armed from the HP but a data transfer will initiate automatically on triggering if CTL0 is high. Data transfer can still be initiated by pulsing CTL0. In this mode, the HP can transfer data to the DL Micro4 by using WRITE commands.

TABLE C-1 - The three modes of operation available on the HP9825A - DL920 transient recorder interface unit and the switch settings required to set each mode.

data transfers via the CTL0 line. As the transient recorder transfers data in lots of 4096 bytes, the HP program in Listing C-1 makes use of the high speed buffered I/O facility provided by the Extended I/O Programming ROM. The data transfer can be terminated at any time by outputting a PRST pulse from the HP, which also arms the transient recorder. This process risks corrupting the transient recorder memory, but this is not important once the data transfer has taken place. The buffered I/O data transfer has a tendency to lock-up the transient recorder after reading the last byte: for this reason the program outputs a PRST pulse when the transfer is complete.

The program in Listing C-1 stores the transient recorder data in a string: the elements of this string can be converted to their numeric equivalents by the num function. Alternatively, the data can be read in numeric form from the buffer by the rdb function. The program gives the user the option of recording a signal and saving it on tape or loading previously recorded data from tape and transferring it to the DL Micro4 unit. In this latter mode the transient recorder merely provides the handshaking signals while the HP transfers data across the common bus.

```
10: "*****************************************************":
11: "* LISTING C-1                                       *":
12: "* Transient Recorder Interface Driver               *":
13: "* This program is for use in Interface Mode 3       *":
14: "* (all three switches DOWN)                         *":
15: "* The TR must be in the Single-shot mode            *":
16: "*****************************************************":
17: "":
18: dim A$[32],B$[4096+16],C$[16]
19: buf "tr",B$,3;gto +2
20: "wait":stp
21: "menu":ent "Load save Record Dump ?",C$;cap(C$[1,1])⟩C$
22: gto "load";if C$#"L";gto "save";if C$#"S";gto +1
23: gto "record";if C$#"R";gto "dump";if C$#"D";gto -2
24: "********":
25: "load":ent "file?",F,"track?",T;trk T
26: ldf F,A$,B$;dsp A$;gto "wait"
27: "********":
28: "save":if rds("tr")=0;dsp "BUFFER EMPTY";gto "wait"
29: ent "file?",F,"track?",T;trk T
30: ent "file header?",A$
31: rcf F,A$,B$;gto "menu"
32: "********":
33: "record":buf "tr"
34: wtc 2,32;dsp "TRANSIENT RECORDER ARMED"
35: dsp "HUNG UP";tfr 2,"tr";gto "menu"
36: "********":
37: "dump":
38: if rds("tr")#4096;dsp "BUFFER STATUS ERROR";gto "wait"
39: wtc 2,1;if bit(0,rds(2))=0;wtc 2,33
40: dsp "HUNG UP";wtc 2,32;tfr "tr",2;gto "menu"
*4987
```

REFERENCES

ASTM (1972) - 'Acoustic Emission', American Society for Testing and Materials, STP505.

ASTM (1975) - 'Monitoring Structural Integrity by Acoustic Emission', American Society for Testing and Materials, STP571.

ABE R. (1956) - J. Phys. Soc. Jap. 11, 104.

ABEY A.E. (1979) - Private Communication.

AIZU K. (1969) - J. Phys. Soc. Jap. 27, 367.

AIZU K. (1970) - Phys. Rev. B 2, 754.

AIZU K., KUMADA A., YAMOTO H. and ASHIDA S. (1969) - J. Phys. Soc. Jap. 27, 511.

ANDERSON L.K. (1972) - Ferroelectrics 3, 69.

ANDERSON L.K. (1974) - Ferroelectrics 7, 55.

ANDERSON P.W. (1960) - 'Fizika Dielektrikov', Akad. Nauk. S.S.R., Moscow.

AVRAMI M. (1939) - J. Chem. Phys. 7, 1103.

AXE J.D., DORNER B. and SHIRANE G. (1972) - Phys. Rev. B 6, 1950.

BEATTIE A.G. (1971) - Bull. Amer. Phys. Soc. (2) 16, 385.

BEEVERS L.A. and HUGHES W. (1941) - Proc. Roy. Soc. A 177, 251.

BILLETER T.R., GIAROLA A.J. and BJORKSTAM J.L. (1964) - J. Appl. Phys. 35, 2159.

BLINC R. and ZEKS B. (1974) - 'Soft Modes in Ferroelectrics and Antiferroelectrics', Elsevier, New York.

BORCHARDT H.J. and BIERSTEDT P.E. (1966) - Appl. Phys. Lett. 8, 50.

BORCHARDT H.J. and BIERSTEDT P.E. (1967) - J. Appl. Phys. 38, 2057.

BREKENRIDGE F.R., TCHIEGG C.E. and GREENPAR M. (1978) - J. Ac. Soc. Amer. 57, 626.

BRIGHAM E.O. (1974) - 'The Fast Fourier Transform', Prentice-Hall International, London.

BROWN A.F. and WEIGHT J.P. (1974) - Ultrasonics 2, 161.

BUCHMAN P. (1972) - Solid State Electronics 15, 142.

BURFOOT J.C. (1967) - 'Ferroelectrics', Van Nostrand, London.

BUSCH G. and SCHERRER P. (1935) - Naturwiss. 23, 737.

CADY W.G. (1946) - 'Piezoelectricity', McGraw-Hill, New York.

CALLABY D.R. (1966) - J. Appl. Phys. 37, 2295.

CAMLIBEL I. (1969) - J. Appl. Phys. 40, 1690.

CHYNOWETH A.G. (1958) - Phys. Rev. 110, 1316.

CHYNOWETH A.G. and FELDMANN W.L. (1960) - J. Phys. Chem. Sol. 15, 225.

COCHRAN W. (1960) - Adv. Phys. 9, 387.

CONNOLLY T.F., TURNER E. and HAWKINS D.T. (1970, 1974) - 'Solid State Physics Literature Guides' Vols. 1 and 6, Plenum Press, New York.

CRANGLE T. (1977) - 'The Magnetic Properties of Solids', Edward Arnold (Publishers) Ltd., London.

CROSS L.E., FOUSKOVA A. and CUMMINS S.E. (1968) - Phys. Rev. Lett. 21, 812.

CUMMINS S.E. (1970) - Ferroelectrics 1, 11.

DALTON N.W., JACOBS J.T. and SILVERMAN B.D. (1971) - Ferroelectrics 2, 21.

DEVONSHIRE A.F. (1949) - Phil. Mag. 40, 1040.

DEVONSHIRE A.F. (1954) - Adv. Phys. 3, 85.

DIDOMENICO M., JOHNSON D.A. and PAMBELL R.H. (1962) - J. Appl. Phys. 33, 1697.

DIDOMENICO M. and WEMPLE S.H. (1967) - Phys. Rev. 155, 539.

DOUGHERTY J.P., SAWAGUCHI E. and CROSS L.E. (1972) - Appl. Phys. Lett. 20, 364.

DROUILLARD T.F. (1979) - 'Acoustic Emission, a Bibliography', IFI/Plenum, New York.

DUNEGAN H.L., TATRO C.A. and HARRIS D.O. (1964) - Report UCID-4468, Lawrence Radiation Laboratory, Livermore, California, USA.

DUNEGAN H.L. and HARRIS D.O. (1969) - Ultrasonics 7, 160.

DUNEGAN H.L., HARRIS D.O. and TETELMAN A.S. (1970) - Mater. Eval. 28, 221.

ENGLE D.M. and TATRO C.A. (1967) - J. Ac. Soc. Amer. 41, 321.

ENGLE D.M. and BROWN A.E. (1975) - J. Ac. Soc. Amer. 57, 591.

FATUZZO E. and MERZ W.J. (1967) - 'Ferroelectricity', North-Holland, Amsterdam.

FLIPPEN R.B. (1975) - J. Appl. Phys. 46, 1068.

FOUSEK J. and JANOVEC V. (1969) - J. Appl. Phys. 40, 135.

FOWLER R.H. (1935) - Proc. Roy. Soc. 149, 1.

FRAZER B.C., MCKEOWN M. and PEPINSKY R. (1954) - Phys. Rev. 94, 1435.

GINZBURG V.L. (1949) - Zh. Eksp. Teor. Fiz. 19, 36.

GOPAL R., SMITH J.R. and RAO G.V. (1976) - Inst. Mech. Eng. Paper C194/76.

GRAHAM L.J. and ALERS G.A. (1975) - STP 571, ASTM, p11.

GUILD F.J., PHILLIPS M.G. and HARRIS B. (1980) - NDT Int. 13, 209.

HAAS C.W. and JAEP W.F. (1974) - Phys. Lett. 49A, 77.

HADNI A., HENNINGER Y., THOMAS R., VERGNAT P. and WYNCKE B. (1965) - J. Phys. Paris 26, 345.

HARDY H.R. (1972) - STP 505, ASTM, p41.

HARRIS D.O. and BELL R.L. (1977) - Expt. Mech. 17, 347.

HAYASHI M. (1972) - J. Phys. Soc. Jap. 33, 616.

HILL R. and EL-DARIDY S.M.A. (1977) - 'Physical and Metallurgical Applications of Acoustic Emission', Dec. 1977, Chelsea College, London.

HINZ H. (1939) - Zeitschrift fur Physik 111, 617.

HOCHLI U.T. (1971) - Phys. Rev. B 6, 1819.

HOLT J. and PALMER I.G. (1974) - Inst. Mech. Eng., Paper C80/74.

HOOTON J.A. and MERZ W.J. (1955) - Phys. Rev. 98, 409.

HUTTON P.H. and SKERPIK J.K. (1981) - ISA Trans. 20, 79.

HOULTON M.R., JONES G.R. and ROBERTSON D.S. (1975) - J. Phys D. (Appl. Phys.) 8, 217.

HSU N.N., SIMMONS J.A. and HARDY S.C. (1977) - Mater. Eval. 35, 106.

IWASAKI H., SUGII K, YAMADA T. and NIIZEKI N. (1971) - Appl. Phys. Lett. 18, 444.

IWATA Y. (1977) - J. Phys. Soc. Jap. 43, 961.

JANTA I. (1971) - Ferroelectrics 2, 299.

JEITSCHKO W. (1971) - Acta. Cryst. B 28, 60.

JONA F. and SHIRANE G. (1962) - 'Ferroelectric Crystals', Macmillan, New York.

KAISER J. (1950) - PhD Thesis, Technische Hochschule, Munich, Germany.

KANZIG W. (1957) - 'Ferroelectrics and Antiferroelectrics', Academic Press, New York.

KAWASHIMA R. and TATSUZAKI T. (1973) - Phys. Lett. 56A, 43.

KELLY M.P., HARRIS D.O. and POLLOCK A.A. (1975) - STP 575, ASTM, p221.

KEVE E.T., ABRAHAMS S.C. and BERNSTEIN J.G. (1971) - J. Chem. Phys. 54, 3185.

KHOLODENKO L.P. (1961) - Solid State 3, 3142 (translation in Soviet Physics 3, 2284).

KLINE R.A. and GREEN R.E. (1978) - J. Ac. Soc. Amer. 64, 1633.

KOBAYASHI J., YAMADA N. and NAKAMURA T. (1963) - Phys. Rev. Lett. 11, 508.

KUMADA A. (1969) - Phys. Lett. 30A, 186.

KUMADA A. (1972) - Ferroelectrics 3, 115.

KURCHATOV L.P. (1933) - Segnetoelektriki Moscow: C-M GTTI (abbreviated French translation published by Hermann and Cie, Paris, 1936).

LAMBSON E.F., LINZ A., MADHAVA M.R., MOHAMAD I.J., UNDERHILL C. and SAUNDERS G.A. (1977) - Proc. Inst. Ac. 4, 1.

LANDAUER R. (1957) - J. Appl. Phys. 28, 227.

LAUGHNER J.W., CLINE T.W., NEWNHAM R.E. and CROSS L.E. (1979a) - Phys. and Chem. Miner. 4, 129.

LAUGHNER J.W., NEWNHAM R.E. and CROSS L.E. (1979b) - Phys. Stat. Sol. A 56, K83.

LEMONS R.A., GEARY J.M., COLDREN L.A. and MATTES H.G. (1978) - Appl. Phys. Lett. 33, 373.

LINES M.E. and GLASS A.M. (1977) - 'Principles and Applications of Ferroelectrics', Oxford University Press, Oxford, UK.

LIPTAI R.G., DUNEGAN H.L. and TATRO C.A. (1969) - Int. J. NDT 1, 213.

LORD A.E. (1967) - Acustica 18, 187.

LORD A.E. (1975) - 'Physical Acoustics' Vol. 11 (ed. Mason W.P. and Thurston R.N.), Academic Press, New York.

MAKER P.D., TERHUNE R.W., NISENOFF M. and SAVAGE C.M. (1962) - Phys. Rev. Lett. 8, 21.

MARATUKE M. (1925) - J. Phys. Soc. Jap. 7, 25.

MASON W.P. (1950) - 'Piezoelectric Crystals and their Application to Ultrasonics', Van Nostrand, New York.

MEHAN R.L. and MULLEN J.V. (1971) - J. Composite Materials 5, 266.

MERZ W.J. (1954) - Phys. Rev. 95, 690.

MERZ W.J. (1956) - J. Appl. Phys. 27, 938.

MILLER A.J. and SAUNDERS G.A. (1979) - Private Communication.

MILLER R.C. (1958) - Phys. Rev. 111, 736.

MILLER R.C. (1960) - J. Phys. Chem. Solids 17, 93.

MILLER R.C. and SAVAGE A. (1958) - Phys. Rev. 112, 755.

MILLER R.C. and WEINREICH G. (1960) - Phys. Rev. 117, 1460.

MITSUI T. and FURUICHI J. (1953) - Phys. Rev. 90, 193.

MOHAMAD I.J. (1980) - PhD Thesis, School of Physics, University of Bath, UK.

MOHAMAD I.J., LAMBSON E.F., MILLER A.J. and SAUNDERS G.A. (1979) - Phys. Lett. 71A, 115.

MORAIS C.F. and GREEN A.T. (1975) - STP 571, ASTM, p184.

MUELLER H. (1940) - Phys. Rev. 57, 829.

MUENOW R.A. (1971) - 'Uses of Acoustic Emission in Construction', Symposium on Acoustic Emission, Dec. 71, Bal Harbor, Florida, USA.

NAKAMURA T., VEACH C.L. and MCCAULY B.O. (1972) - ASTM, STP505, 164.

NANAMATSU S., SUGIYAMA H., POI K. and KONDO Y. (1971) - J. Phys. Soc. Jap. 31, 616.

NEWNHAM R.E. (1974) - Amer. Minerologist 59, 906.

NEWNHAM R.E., WOLFE R.W. and DARLINGTON C.N.W. (1973) - J. Solid State Chem. 6, 378.

NIELSEN A. (1980) - 'Acoustic Emission Source Based on Pencil Lead Breaking', Svejsecentralen, Copenhagen. Pub. 80.15.

NIELSEN J. (1977) - J. Test. and Eval. 5, 476.

NICHOLS R.W. (1970) - 'Acoustic Emission', Applied Science, Barking, UK.

NOTVEST K. (1966) - Weld. J. 45, 173.

OBERT L. (1941) - US Bur. Mines, Rep. Invest. R1-3555.

OBERT L. and DUVALL W. (1945) - US Bur. Mines, Rep. Invest. R1-3803.

PAIN H.J. (1970) - 'The Physics of Vibrations and Waves', J. Wiley and Sons, London.

PAO Y.H., GAJEWSKI R.R. and CERANOGLU A.N. (1979) - J. Ac. Soc. Amer. 65, 96

PARRY D. and ROBINSON D. (1970) - Report IN-1398, Idaho Nuclear

Corp., Idaho Falls, Idaho, USA.

PEARSON G.L. and FELDMANN W.L. (1959) - J. Phys. Chem Sol. 9, 28.

PETZELT J. and DVORAK V. (1971) - Phys. Stat. Sol. 46B, 413.

PYTTE E. (1970) - Commun. Solid State Phys. 8, 2101.

RAVI R., SANGUNNI K.S. and NARAYUNAN P.S. (1980) - J. Phys. E. (Sci. Instrum.) 13, 585.

RUDYAK V.M., KUDZIN A.Y. and PANCHENKO T.V. (1968) - Fiz. Tverd. Tela 9, 3336 (translation in Soviet Physics Solid State 9, 2624).

SACHSE W. and CERANOGLU A.N. (1979) - 1979 Ultrason. Symp. Proc., New Orleans, USA (Sept. 1979), p138.

SAWYER C.B. and TOWER C.H. (1930) - Phys. Rev. 35, 269.

SCHOFIELD B.H. (1971) - STP 505, ASTM, p11.

SCHOFIELD B.H., BAREISS R.A. and KYALA A.A. (1958) - ASTIA Doc. AD155674.

SCHWERK E.B. and SCHEARER G.D. (1973) - NDT Int. 6, 29.

SCRUBY C.B. and WADLEY H.N.G. (1978) - J. Phys. D. (Appl. Phys.) 11, 1487.

SCRUBY C.B., WADLEY H. and SINCLAIR J.E. (1981) - Phil. Mag. A 44, 249.

SHEPHERD I.W. and BARKLEY J.R. (1972) - Commun. Solid State Phys. 10, 123.

SINCLAIR A.C.E. (1977) - CEGB Berkley Nuclear Laboratory Report RD/B/N4066.

SINGER B. and LALAK J. (1976) - Ferroelectrics 10, 103.

SLATER J.C. (1941) - J. Chem. Phys. 9, 16.

SLATER J.C. (1950) - Phys. Rev. 78, 748.

SMITH A.W. and BURNS G. (1969) - Phys. Lett. 28A, 501.

SPANNER J.C. (1970) - MS Thesis, Dept. of Metallurgy, Washington State University, USA.

SPENCER E.C., LENKO P.V. and BALLMAN A.A. (1967) - Proc. IEEE 55, 2074.

STADLER H.L. (1958) - J. Appl. Phys. 29, 1485.

STADLER H.L. and ZACHMANDIS P.J. (1963) - J. Appl. Phys. 34, 3255.

STRAUBEL-FISCHER E. (1957) - Naturwiss. 44, 230.

SUZUKI T., NAKAMURA T. and SATOU M. (1978) - Jap. J. Appl. Phys. 17, 1431.

TANAKA M. and HONJO G. (1964) - J. Phys. Soc. Jap. 19, 954.

TATRO C.A. and LIPTAI R.G. (1962) - Proc. 1962 Symp. Physics and NDT, South-West Research Institute, San Antonio, Texas, USA, p145.

TORONCHUK J.P. (1977) - Mater. Eval. 35, 51.

UBBELOHDE A.R. and WOODWARD I. (1946) - Proc. Roy. Soc. A 185, 448.

VALASEK J. (1920) - Phys. Rev. 15, 537.

VALASEK J. (1921) - Phys. rev. 17, 475.

VAN DOREN S.L., POND R.B. and GREEN R.E. (1976) - J. Appl. Phys. 47, 4343.

WATTON R., SMITH C. and JONES G.R. (1976) - Ferroelectrics 14, 719.

WIEDER H.H. (1957) - J. Appl. Phys. 28, 367.

WIEDER H.H. (1958) - Phys. Rev. 110, 129.

WILLIAMS R.V. (1980) - 'Acoustic Emission', Adam Hilger Ltd., London.

WOOD A. (1944) - 'The Physics of Music', Methuen, London.

WUL B. and GOLDMAN I.N. (1948) - C.R. Akad. Sci. URSS 46, 139.

YAKUNIN S.I., SHAKMANOV V.V., SPIVAK G.V. and VASIL'EVA N.V. (1972) - Fiz. Tverd. Tela 14, 373 (translation in Soviet Physics Solid State 14, 310).

YAMADA T., IWASAKI H. and NIIZEKI N. (1972) - J. Appl. Phys. 43, 771.

YARWOOD T.M. and CASTLE F. (1980) - 'Physical and Mathematical Tables', Macmillan, London.

YING S.P. (1973) - CRC Crit. Rev. Solid State Sci. 4, 75.

YOON H.S., CORACA B., KUAR H. and KATZ J.L. (1980) - Ultrason. Symp. Proc., Boston, Mass., USA, p1067.

ZHIRNOV V.A. (1958) - J. Exp. Teor. Fiz. 35, 1175 (translation in Soviet Physics 35, 822).